

# Very high energy gamma-ray emission from pulsars and pulsars wind nebulae observed by MAGIC telescopes

---

Šnidarić, Iva

Doctoral thesis / Disertacija

2023

Degree Grantor / Ustanova koja je dodijelila akademski / stručni stupanj: **University of Zagreb, Faculty of Science / Sveučilište u Zagrebu, Prirodoslovno-matematički fakultet**

Permanent link / Trajna poveznica: <https://um.nsk.hr/um:nbn:hr:217:270946>

Rights / Prava: [In copyright](#)/[Zaštićeno autorskim pravom.](#)

Download date / Datum preuzimanja: **2024-08-18**



Repository / Repozitorij:

[Repository of the Faculty of Science - University of Zagreb](#)





University of Zagreb  
Faculty of Science  
Department of Physics

Iva Šnidarić

**Very high energy gamma-ray emission from  
pulsars and pulsars wind nebulae observed  
by MAGIC telescopes**

DOCTORAL DISSERTATION

Zagreb, 2023





University of Zagreb  
Faculty of Science  
Department of Physics

Iva Šnidarić

**Very high energy gamma-ray emission from  
pulsars and pulsars wind nebulae observed  
by MAGIC telescopes**

DOCTORAL DISSERTATION

Supervisors:

dr. sc. Tihomir Surić, dr. sc. Vibor Jelić

Zagreb, 2023





Sveučilište u Zagrebu  
Prirodoslovno-matematički fakultet  
Fizički odsjek

Iva Šnidarić

**Visokoenergijsko gama-zračenje pulsara i  
maglica pulsarovog vjetra opažanih  
teleskopima MAGIC**

DOKTORSKI RAD

Mentori:

dr. sc. Tihomir Surić, dr. sc. Vibor Jelić

Zagreb, 2023.



# Supervisor information

Tihomir Surić is a Senior Research Associate at the Experimental Physics Division of the Ruđer Bošković Institute in Zagreb, Croatia. He received his PhD from the University of Zagreb in 1991. His main scientific interests are in theoretical high energy atomic physics - interaction of radiation with matter, and in astroparticle physics in very high energy gamma ray astronomy - pulsars and pulsar wind nebulae. He is a member of international collaborations in high energy gamma ray astronomy: MAGIC (since 2008) and CTA (since 2010).

Vibor Jelić is a Senior Research Associate and Head of the Laboratory for Astroparticle Physics and Astrophysics (Division of Experimental Physics) at the Ruđer Bošković Institute in Zagreb, Croatia. He is also affiliated with the University of Zagreb as an Associate Professor in Astronomy and Astrophysics at the Faculty of Science (Department of Physics). He received his PhD from the University of Groningen in 2010, and subsequently was a postdoctoral researcher at the Netherlands Institute for Radio Astronomy (ASTRON) and Kapteyn Astronomical Institute, University of Groningen. His scientific interests are towards the understanding of the interplay between the interstellar medium and magnetic fields in the Milky Way and towards detecting the cosmological 21 cm emission from the Cosmic Dawn and the Epoch of Reionization. In his research, he combines radio (polarimetric) observations with numerical simulations and observations at other wavelengths.



# Acknowledgements

Astrophysics is my long pursued passion. During the process of studying and then working on this thesis, I have come across or met some people who inspired me or helped me in many different ways. First and foremost, I would like to acknowledge Stephen Hawking for writing outstanding books that inspired me at my earliest age and because of whom I fell in love with the Universe. During my PhD, I had a pleasure to be part of the international MAGIC collaboration and came to know many dear and interesting people. Also, being a part of the shift crew at Roque de los Muchachos Observatory and operate the MAGIC telescopes is an experience I will never forget, and a dream come true. I thank my Croatian colleagues who accepted me in the MAGIC team. I thank my supervisor Tiho for the support and opportunities during my PhD years. I am especially thankful to dr. sc. Ana Babić who supported me, helped me with any problem I encountered and without whom this thesis would be certainly of a less quality. In addition, I am truly thankful to my MAGIC colleagues with whom I've collaborated directly: Takayuki Saito, Pierre Colin, Tomislav Terzić, Abelardo Moralejo, Ignasi Reichardt, Gianluca Giavitto, Stefan Klepser, Jezabel Rodriguez, Marcos Lopez and Karsten Berger - thank you for the help, patience and support. I am also thankful to late dr. sc. Eckart Lorenz for his inspiring passion for physics and a good deal of wise advice he shared with us within the MAGIC collaboration. I would also like to say a huge thank you to dr. sc. Vibor Jelić - I thank him for the positive attitude from the beginning and for the opportunity to collaborate with him on the paper, for the support, help and without whom all this work would never see the light of day. Kind thank you also to dr. sc. Vernesa Smolčić for positivity, overall student support and inspiration. Personal thanks also to my colleagues who supported me during this latest and hardest stage of my PhD: Ana, Lana, Marta, Tea, Lovro and Luka. To my dear parents, thank you for the love and support over all these years. Last but not least, I am grateful to my better half - Tomi, thank you for believing in me, for being my rock('n roll) and for helping me see the right perspective in life.

This thesis is dedicated to my three little knights: Matija, Noel and Oliver - pursue your passion and never ever give up!

# Abstract

A pulsar wind nebula (PWN) is a system with a central rotating object, a pulsar, which powers a surrounding nebula. This complex system is observed to emit radiation throughout the electromagnetic spectrum, from radio to gamma rays. In this thesis I explored the gamma-ray emission from pulsars, their respective nebulae and one PWN candidate at very high energies (VHE,  $E > 100$  GeV) using the Major Atmospheric Gamma-ray Imaging Cherenkov (MAGIC) telescopes. At the beginning of this research, only one pulsar, the Crab pulsar, was known to emit at VHE, challenging the theoretical models. The observed electromagnetic radiation from the pulsar-nebula system implies the presence of a mechanism that accelerates charged particles to ultra-relativistic energies. However, this mechanism is poorly understood, thus VHE pulsar observations are relevant not only as information for emission modelling but also as a contribution for better characterization of fundamental properties of these complex astrophysical systems. The MAGIC telescopes, with its novel trigger especially developed for pulsar observation, is the most suitable instrument to search for new VHE pulsars. In this thesis, I present the observations and analysis of two galactic sources: Crab (PSR J0534+2200) and Dragonfly (PSR J2021+3651) pulsars. For the well-known and previously detected Crab pulsar, the analysis shows the expected results and is used as a performance check of the method. The same method is then used to search for VHE emission from the Dragonfly pulsar, proposed as a very likely VHE pulsar candidate due to its similar characteristics to the Crab pulsar. I found no significant pulsed emission from Dragonfly pulsar in low  $E_\gamma$ -range ( $50 \text{ GeV} < E < 200 \text{ GeV}$ ) neither in the full  $E_\gamma$ -range ( $E > 200 \text{ GeV}$ ), only upper limits were derived. However, with the same set of data, the Dragonfly nebula surrounding the pulsar was detected. I also present the study of the unidentified TeV source, HESS J1858+020, that was put forward as a relic PWN candidate using the archival data collected from the MAGIC telescopes where this source was relatively far from the centre of the camera implying decrease in detection sensitivity. Nevertheless, the source was detected, source extension estimated and the spectrum between 300 GeV and 10 TeV was constrained, but morphological or other details were not discerned. Neither the PWN scenario could be refuted nor confirmed. Overall, detail studies of the VHE gamma-ray

---

emission from pulsars and nebulae seem more challenging than expected, and longer observations are needed for pulsed detection or for morphological characterization of nebulae. The next-generation Cherenkov telescope array (CTA) with an order of magnitude better sensitivity and with 1 arcminute resolution, will certainly allow detail morphological and spectral studies of this kind of sources.

Furthermore, I also studied a faint component of the Galactic diffuse synchrotron emission at low-radio frequencies by using multiple polarimetric observations with the LOW Frequency ARray (LOFAR). Before stacking them, these observations first needed to be corrected for the Faraday rotation in the Earth's ionosphere, otherwise the observed polarized emission may be either partially or in exceptional cases fully depolarized. I used the observed polarized diffuse synchrotron emission to characterize and additionally to correct for the ionospheric Faraday rotation. After stacking twenty observations, the noise was reduced by  $\sim \sqrt{20}$ , as expected. Higher signal-to-noise ratio achieved with this method, enables a study of the faint component of the Galactic diffuse emission, which was not visible in a single reference observation. Moreover, applied technique can also be used for studies of the faint polarized sources, including pulsars.

Keywords: gamma-rays: stars - pulsars: general - pulsars: individual: PSR J2021+3651: acceleration of particles - gamma rays: ISM - clouds: HII regions: ISM - individual objects: HESS J1858+020: radio continuum: ISM -techniques: interferometric, polarimetric - cosmology: observations, diffuse radiation.

# Prošireni sažetak

Glavna tema ovog rada je proučavanje visokoenergijskog gama-zračenja iz pulsara i maglica pulsarovog vjetra opažanih teleskopima MAGIC (engl. *Major Atmospheric Gamma Imaging Cherenkov*). Gama-astronomija proučava procese u svemiru koji se odvijaju u uvjetima ekstremno velikih energija i gustoća. Podrijetlo kozmičkog gama-zračenja vrlo visokih energija ( $100 \text{ GeV} < E < 100 \text{ TeV}$ ) su netermički procesi koji nose informaciju o galaktičkim i izvangalaktičkim izvorima. Galaktički izvori su ostaci supernova (engl. *supernova remnants*), pulsari, maglice pulsarovog vjetra (engl. *pulsar wind nebulae*), dvojni gama-sustavi (engl. *binary systems*) te magnetari, dok su izvangalaktički izvori npr. aktivne galaktičke jezgre, provale gama-zračenja (engl. *gamma ray burst, GRB*) i tamna tvar - koja je potencijalno i galaktički izvor. U prošlom desetljeću, opažanjima opservatorija na energijama u području TeV (MAGIC, VERITAS, HESS, Milagro) otkriven je velik broj izvora u galaktičkoj ravnini, među kojima su maglice pulsarovog vjetra dominantna populacija.

Maglica pulsarovog vjetra je kompleksni sustav s pulsarom kao središnjim rotirajućim objektom koji napaja okolnu maglicu. U prvom dijelu disertacije proučavam visokoenergijsko gama-zračenje iz pulsara i njihovih maglica opaženih Čerenkovljevim teleskopima MAGIC. Samo je jedan pulsar (pulsar Rakovice) opažen u području visokoenergijskog gama-zračenja u trenutku kada je istraživanje vezano za ovu disertaciju otpočelo. Glavno pitanje je bilo postoje li pulsari slični pulsaru Rakovice koji također emitiraju na energijama  $E > 100 \text{ GeV}$  ili je on jedinstvenih karakteristika. Promatranja ukazuju da kompleksni sustav pulsara i njegove maglice zrači na svim valnim duljinama, od radiozračenja do visokoenergijskog gama-zračenja. To je ukazivalo na postojanje mehanizma ubrzanja kojim su nabijene čestice ubrzane do ultrarelativističkih energija. Sam mehanizam, odnosno način pretvorbe rotacijske energije pulsara u opaženo elektromagnetsko zračenje je za sada slabo poznat. Visokoenergijska gama-opažanja od iznimne su važnosti za modeliranje zračenja iz pulsara te pružaju jedinstveni uvid u astrofizičke procese koji se odvijaju u tim kompleksnim objektima. U disertaciji su predstavljena opažanja i analiza podataka pulsara Rakovice (PSR J0534+2200) i pulsara Vilin konjic (PSR J2021+3651). Analiza dobro poznatog pulsara Rakovice ovdje je korištena kao metoda provjere tehničkih

karakteristika teleskopa MAGIC. Iste metode analize su primjenjene u potrazi za visokoenergijskim gama-zračenjem iz pulsara Vilin konjic koji je predložen kao vrlo izgledni kandidat za opažanje takve emisije. Također, predstavljeno je opažanje i analiza neidentificiranog izvora, HESS J1858+020, koji je klasificiran kao moguća starija maglica pulsarovog vjetra s mogućim odmakom od roditeljskog pulsara (engl. *parent pulsar*).

Osim opažanja pulsara i njihovih maglica u području visokih energija, u disertaciji se istražuje difuzno polarizirano zračenje iz naše Galaksije na niskim radiofrekvencijama (115-180 MHz) te je pritom razvijena metoda slaganja kako bi dubokim polarimetrijskim promatranjima difuzne emisije slabog sjaja bili u mogućnosti opaziti objekte slabog sjaja (npr. pulsari).

Ključne riječi: visokoenergijsko gama-zračenje, zvijezde - pulsari: individualno: PSR J2021+3651: akceleracija čestica - gama-zračenje: međuzvjezdana tvar - oblaci: područja HII: individualno: HESS J1858+020, radio-kontinuum, polarimetrijska opažanja, difuzna radioemisija iz Galaksije.

## Pulsari i maglice pulsarovog vjetra

J. Bell Burnell i A. Hewish otkrili su prvi radiopulsar (Hewish et al., 1968) još davne 1967. godine. Danas, više od 50 godina od otkrića prvog pulsara, otkriveno je više od 2900 radiopulsara (Manchester et al., 2005), stoga da se i na drugim valnim duljinama broj otkrivenih pulsara kontinuirano povećava. Populacija pulsara procijenjena je na  $10^5 - 10^6$  aktivnih pulsara unutar Galaksije, većina smještenih u ravnini Galaksije (Lyne & Graham-Smith, 2012). Periodi rotacije normalnih (kanonskih) pulsara koji svoju energiju dobivaju iz rotacijske energije nalaze se unutar 1 ms - 10 s. Postoji još jedna manja populacija pulsara koju zovemo milisekundni pulsari (engl. *millisecond pulsars*). Ovu populaciju čine starije neutronske zvijezde koje su ponovo ubrzane akrecijom materijala sa zvijezde pratioca. Na slici 1.8 prikazan je P –  $\dot{P}$  dijagram gdje su prikazane sve poznate populacije pulsara iz ATNF kataloga.<sup>1</sup> Opaža se da pulsari usporavaju tijekom vremena tako da se njihov period rotacije s vremenom povećava. Ovaj dijagram je dobar pokazatelj pulsarove starosti, sjajnosti te jačine magnetskog polja na površini te općenito pokazatelj životnog ciklusa pulsara: na početku svog života pulsar se pojavi u gornjem lijevom uglu dijagrama te kako s vremenom (tijekom nekoliko milijuna godina) usporava, pulsar se pomiče prema donjem desnom uglu dijagrama gdje se u konačnosti nalaze stari pulsari sa slabim magnetskim poljem te im pulsni signal postaje toliko slab da se više ne može ni opaziti. Milisekundni pulsari nalaze se u donjem lijevom kutu dijagrama.

---

<sup>1</sup>Katalog svih pulsara održava Australia Telescope National Facility (ATNF) i može se naći na sljedećoj web adresi: <https://www.atnf.csiro.au/research/pulsar/psrcat/>.

Opažanja pokazuju da se period vrtnje pulsara,  $P$ , definiran kao  $P = 2\pi/\Omega$ , gdje je  $\Omega$  kutna brzina, povećava s vremenom, što znači da pulsar postepeno usporava i gubi rotacijsku kinetičku energiju:

$$\frac{dE_{\text{rot}}}{dt} = \frac{d\left(\frac{1}{2}I\Omega^2\right)}{dt} = I\Omega\dot{\Omega} = \frac{4\pi^2 I\dot{P}}{P^3}, \quad (1)$$

gdje je  $I$  moment inercije neutronske zvijezde definiran kao  $I = 2/5MR^2$ . U najjednostavnijem modelu, ovo usporavanje odnosno gubitak energije usporavanjem (engl. *spindown luminosity*),  $\dot{E}$ , uzrokovano je zračenjem magnetskog dipola gdje je kut između magnetske i rotacijske osi,  $\chi$ , različit od nule,  $\chi \neq 0$ . Jedino kada je taj uvjet zadovoljen magnetski dipol ima komponentu promjenjivu u vremenu i emitira elektromagnetsko zračenje na frekvenciji  $\Omega$ . Dok optički teleskopi snime  $>100$  fotona u pulsu sa nekog pulsara, detektori gama-zračenja prime reda veličine tek jedan foton u satu. Iako proizvesti pulsni profil za više energije zahtjeva integraciju preko milijun pulsnih perioda, vremenska preciznost pulseva tijekom dužeg opažanja omogućuje detekciju periodičnosti pulsara i konstrukciju pulsnih profila. Svaki pulsni profil nekog pulsara je jedinstven, a proučavanje profila i njihove promjene kroz elektromagnetski spektar je ključ za razumijevanje geometrije, elektrodinamike i okoliša magnetosfere pulsara. Za pulsar Rakovice je karakteristično da pulsni profil kroz cijeli elektromagnetski spektar izgleda gotovo jednako što ukazuje da su populacije čestica koje uzrokuju opaženo zračenje smještene negdje u bliskim područjima. Za sada je pulsar Rakovice jedini takav slučaj. Pulsni profili mjenjaju se s energijom te se modeliraju u ovisnosti o geometriji kako bi razlikovali među više mehanizama emisije. Opažanja na različitim valnim duljinama doprinose razumijevanju ovih objekata. Pulsari u gama-području glavno su područje istraživanja ove disertacije. Lansiranje *Fermi* Gamma-ray Space Telescope koji je nosio Large Area Telescope (*Fermi-LAT*) 2008. godine označilo je novu eru za pulsare u gama-području. Prije *Fermi-LAT* ere samo je sedam gama-pulsara (iznad 100 MeV) bilo otkriveno satelitom EGRET (Energetic Gamma Ray Experiment Telescope), Fermijevim prethodnikom. *Fermi-LAT* tu je brojku povećao na 250 opaženih pulsara u području gama-energija od 100 MeV do nekoliko desetaka GeV. Kada se ova populacija pulsara otkrivenih *Fermi-LAT* satelitom stavi u  $P - \dot{P}$  dijagram (vidi sliku 1.8), uočava se da su svi otkriveni pulsari u gornjem lijevom kutu - što znači da su mladi i energični. Također, većina pulsara otkrivenih *Fermi-LAT* satelitom pokazuje slične spektralne karakteristike: svima je zajednički eksponencijalni prekid u spektru na energijama od nekoliko GeV do nekoliko desetaka GeV. Teorijski modeli predviđali su zakrivljeno sinkrotronsko zračenje (engl. *curvature radiation*) kao uzrok ovim prekidima u spektru na energijama u području GeV. Stoga, dugo vremena nije bilo očekivano pronaći zračenje iz pulsara na energijama iznad nekoliko desetaka GeV, što je

ujedno bio i energijski prag dostupan zemaljskim Čerenkovljevim teleskopima. Tek kada je 2008. godine pulsar Rakovice detektiran zemaljskim teleskopima MAGIC na energijama iznad 25 GeV (Aliu et al., 2008), počela je potraga za pulsarima koji zrače na vrlo visokim energijama (engl. *very high energy*, *VHE*). Drugi nađen pulsar na energijama do 100 GeV bio je Vela pulsar (H. E. S. S. Collaboration et al., 2018), a treći Geminga pulsar otkriven u rasponu energija od 15 GeV do 75 GeV (Acciari et al., 2020) te četvrti PSR B1706-44 (Spir-Jacob et al., 2019). Ovaj rad započet je u trenutku kada je samo jedan VHE pulsar bio poznat - pulsar Rakovice.

Maglica pulsarovog vjetra je maglica koja nastaje kad pulsarov vjetar dođe u interakciju sa okolnim ambijentalnim poljima. Maglica je kontinuirano napajana elektron-pozitron plazmom i magnetskim poljima s pulsara, tako da većina energije iz pulsara napaja maglicu. Maglica se nalazi unutar ostatka supernove (SNR) i razvija se zajedno s ostatkom supernove. Maglica se opaža u cijelom elektromagnetskom spektru, a opažena emisija se dogodi tek kada energija vjetra u udarnom valu (engl. *termination shock*) ubrza čestice na ultrarelativističke brzine koje onda u interakciji s poljima zrače sinkrotronskim ili inverznim Comptonovim zračenjem. Struktura maglice ovisi o energiji samog pulsara i strukturi okolnog medija u kojeg će se materijal širiti. Veličina maglice, morfologija te njen spektar ovisit će o parametrima centralnog "stroja" kao što su energija usporavanja, brzina pulsara, kut između rotacijske i magnetske osi, ali ovisit će i o uvjetima u okolini kao što su tlak te jačina magnetskog polja.

## Teleskopi MAGIC

Teleskopi MAGIC sustav su od dva Čerenkovljeva teleskopa, svaki promjera 17 m. Teleskopi su smješteni na kanarskom otoku La Palmi, na visini 2200 m, unutar observatorija Roque de los Muchachos. Za razliku od optičkih teleskopa, Čerenkovljevi teleskopi su specifični po tome što nemaju cijeloviti reflektor već segmentirani kako bi se dobila što veća sabirna površina ( $\sim 240 \text{ m}^2$ ). Veliki reflektor postavljen je na laganu konstrukciju od ugljikovih vlakana kako bi se teleskopi mogli vrlo brzo (40 s) usmjeriti u bilo koju točku na nebu. Brzo pozicioniranje je važno za opažanje provala gama-zraka gdje se u vrlo kratkom vremenu oslobodi iznimna količina energije. Kada visokoenergijska gama-zraka uđe u Zemljinu atmosferu dolazi do interakcija s molekulama u zraku te se razvija atmosferski pljusak čestica (engl. *extensive air shower*, *EAS*). Čestice, koje su u tom pljuskaju brže od svjetlosti u zraku, će emitirati kratkotrajne (nekoliko nanosekundi) bljeskove plavičaste svjetlosti - Čerenkovljevu svjetlost. Zrcalo će u kameru teleskopa reflektirati dio tog bljeska, a brza elektronika će snimiti taj događaj. U ovom slučaju Čerenkovljevo zračenje su niskoenergijski fotoni valnih duljina u ultraljubičastom dijelu spektra koji se emitiraju pod karakterističnim uskim kutom u odnosu na smjer nabijene čestice, ali i

---

primarne kozmičke gama-zrake. Ova usmjerenost i kratkotrajnost Čerenkovljevog zračenja iz atmosferskog pljuska optimalne su za indirektno opažanje kozmičkog gama-zračenja. Kamera Čerenkovljevog teleskopa sastoji se od fotomultiplikatora, fotosenzora koji su u mogućnosti zabilježiti signal kratkotrajnog bljeska Čerenkovljeve svjetlosti. Metodom analiziranja snimljenih slika (engl. *imaging*) moguće je rekonstruirati energiju i smjer upadnog gama-zračenja te time locirati visokoenergijski gama-izvor. Teleskopi kojima upravlja kolaboracija MAGIC optimalni su instrumenti za opažanje gama-zračenja iz pulsara te njihovih maglica osobito nakon što je snižen energijski prag teleskopa ugradnjom posebnog okidača tzv. *Sum-Trigger* koji je poboljšao osjetljivost teleskopa na energijama ispod 100 GeV što je posebno važno za opažanja pulsara zbog njihovog strmog spektra na tim energijama. Ovim posebnim okidačem se energijski prag teleskopa spustio sa standardnih 41 GeV na  $\sim 21$  GeV (Dazzi et al., 2021), vidi sliku 2.13.

## Opažanje visokoenergijskog gama-zračenja iz pulsara i maglice Rakovice teleskopima MAGIC

Maglica Rakovica (engl. *Crab Nebula*) je jedan od najčešće opažanih objekata u gama-astronomiji, posebno na vrlo visokim energijama ( $E > 100$  GeV). Ovaj izvor je bio prvi izvor opažen zemaljskim teleskopom Whipple pri energiji u području TeV (Weekes et al., 1989), označivši tako začetak visokoenergijske gama-astronomije. Maglica Rakovica je najsajjniji do sada poznati, kontinuirani izvor gama-zraka na nebu u području energija TeV te se smatra standardnom svijećom gama-astronomije, unatoč povremenim bljeskovima<sup>2</sup>. Kontinuirani sjaj maglice opažen duž elektromagnetskog spektra koristi se višestruko, npr. za kalibraciju teleskopa u X- i gama-području te za provjeru performanci teleskopa.

U središtu maglice Rakovice nalazi se pulsar, brzrotirajuća neutronska zvijezda koja je ostala nakon eksplozije supernove zabilježene 1054. godine. Ovaj pulsar je ujedno i prvi pulsar čije je pulsno zračenje opaženo na visokoenergijskim gama-energijama nekim zemaljskim teleskopima (Aliu et al., 2008, kolaboracija MAGIC). Nakon ovog otkrića uslijedila su nova opažanja pa je tako kolaboracija VERITAS razotkrila spektar pulsne emisije iz pulsara Rakovice do 400 GeV (VERITAS Collaboration et al., 2011), a kolaboracija MAGIC je nedavno otkrila da se pulsna emisija proteže čak do 1.5 TeV, bez nagovještaja prekida u spektru (Ansoldi

---

<sup>2</sup>Pojačan tok gama-zračenja iz maglice Rakovice opažen je u veljači 2009. godine satelitima *Fermi-LAT* i *Agile* kroz 16 dana. Tijekom tih bljeskova, opažen tok zračenja iz maglice bio je četiri do šest puta veći nego inače. S obzirom da je pojačan tok zračenja trajao relativno kratko vrijeme, pretpostavlja se da su PeV elektroni iz nekog manjeg područja odgovorni za emisiju opaženog sinkrotronskog zračenja (Abdo et al., 2011).



et al., 2016).

U ovoj su tezi, između ostaloga, opisana opažanja pulsara Rakovice te analiza tih podataka. Podaci su sakupljeni teleskopima MAGIC posebnim okidačem *Sum-Trigger* (Dazzi et al. 2015; Dazzi et al. 2021), napravljenim kako bi snizio energijski prag teleskopa. U svrhu provjere tehničkih karakteristika teleskopa s novim okidačem, prvo je provedena analiza zračenja Rakovice. Ukoliko ta analiza poluči očekivane rezultate, tada smo sigurni da promjene na hardveru nisu izmjenile performance teleskopa i da dobro razumijemo sistematske nepouzadnosti. Osim toga, kada je cilj detektirati pulsnu emisiju iz nekog novog pulsara tada analiza dobro poznatog pulsara Rakovice služi kao metodološka provjera. Budući da u analizi koristimo nestandardni okidač *Sum-Trigger*, pulsni signal se ne traži samo prostorno (prema koordinatama) već i vremenski (pulsni signal je periodičan).

Pulsar Rakovice je najmlađi ( $10^3$  godina) do sada pronađen pulsar, udaljen 2 kpc s periodom rotacije od 33 ms (Hester, 2008). Luminoznost usporavanja je najviši do sada opažen,  $4.6 \times 10^{38}$  erg s<sup>-1</sup> dok je pulsna emisija opažena kroz cijeli elektromagnetski spektar, od radiozračenja do visokoenergijskog gama-zračenja. Naime, opažanja su pokazala da pulsni signali iz pulsara Rakovice tijekom vremena usporavaju i to brzinom od 36 ns po danu. Pulsar usporava na način da gubi svoju rotacijsku kinetičku energiju tako što izbacuje relativističke čestice i time proizvodi magnetizirani pulsarov vjetar čiji ultrarelativistički elektroni i pozitroni u interakciji s okolnim poljima generiraju sinkrotronsku maglicu koju opažamo duž elektromagnetskog spektra (Buciantini, 2008).

Pulsar Rakovice opažan je teleskopima MAGIC u siječnju 2015. godine. Svi podaci snimljeni su koristeći oba teleskopa (stereo mode) i okidač *Sum-trigger* (Dazzi et al. 2015), kao i *wobble mode*<sup>3</sup> Koordinate pulsara Rakovice upotrebljene u analizi su (J2000): RA: 05<sup>h</sup>34<sup>m</sup>31.9<sup>s</sup>, Dec: 22°00'52.1'', dok je raspon zenitnih kuteva uzet od 5° do 25°. Pulsar je opažan tijekom 9 dana (13., 15. – 18. i 21. – 24. siječnja 2015. godine). Zbog loših vremenskih uvjeta ili tehničkih problema tri dana opažanja (13., 15. i 22. siječnja 2015. godine) je odbačeno kako bi skup podataka za analizu bio što kvalitetniji. Nakon selekcije, završni skup podataka sastojao se od 9.5 sati kvalitetnih podataka. Analiza je provedena koristeći standardni softver kolaboracije MAGIC *Analysis and Reconstruction Software* – MARS (verzija 2.14, Zanin, R., 2013). Također, koristila sam standardne Monte Carlo simulacije proizvedene za odgovarajući period,<sup>4</sup> ST03.05. Za hadronski uzorak koristila sam podatke prikupljene opažanjem pulsara

---

<sup>3</sup>*Wobble mode* (Fomin et al., 1994) je način snimanja gdje je izvor 0.4° od središta kamere (vidi Sliku 2.15), te se kružno izmjenjuju najčešće četiri takva položaja kako bi se smanjila mogućnost sistematskih grešaka pri upotrebi jedne polovice kamere za određivanje signala, a druge za procjenjivanje pozadine. Na taj način se istovremeno snima i pozadina te se tako štedi vrijeme opažanja i osiguravaju se jednaki uvjeti opažanja.

<sup>4</sup>Kolaboracija MAGIC interno uvodi nove periode u analizi koji su povezani sa značajnijim promjenama u performansama teleskopa. Novi setovi Monte Carlo simulacija se proizvode za svaki period.

---

Vilin konjic (engl. *Dragonfly pulsar*) iz ljeta 2014. godine. Javno dostupne podatke za period i promjenu perioda (ephemeris) za siječanj 2015. godine koristila sam sa zvjezdarnice Jodrell Bank<sup>5</sup> (Lyne et al., 1993). Kako bi se opazio pulsni signal, područje signala (P1 i P2) i pozadine (Bg) definirani su na sljedeći način, koristeći definicije iz Aleksić et al. (2012):  $P1=[0.983 - 0.026]$  i  $P2=[0.377 - 0.422]$  te  $Bg=[0.52 - 0.88]$ . Pulsni profil dobiven je za  $E < 200$  GeV (vidi Sliku 3.6), a statistička značajnost signala provjerena je preko  $Z_{10}^2$ -testa, H-testa i  $\chi^2$ -testa gdje nisu prisutne pretpostavke o položaju i obliku pulseva. To je suprotno Li&Ma testu signifikantnosti (vidi izraz 17, Li & Ma, 1983) gdje se *a priori* znaju položaji pulseva. Dva pulsna vrha opažaju se na svjetlosnoj krivulji. Prvi vrh, P1, je oko faze 0.0 opažen signifikantnošću  $\sim 4\sigma$  dok je drugi vrh, P2, oko faze 0.4, opažen signifikantnošću  $\sim 5\sigma$ .

Isti skup podataka koji je korišten za analizu pulsara Rakovice korišten je za određivanje kontinuirane emisije iz pripadajuće maglice gdje je i dalje izvor analiziran kao točkasti<sup>6</sup>. Obrada podataka izvršena je standardnim MAGIC softverom, MARS (verzija 2.14, Zanin, R., 2013). Iako su podaci snimani *Sum-trigger* okidačem, za obradu ovih podataka korištene su standardne Monte Carlo simulacije jer su bile jedine dostupne u to vrijeme. Sljedeći korake opisane u Albert et al. (2008a) dobivena je spektralna raspodjela energije (Slika 3.7). Raspodjela je dana za raspon energija od 60 GeV do  $\sim 7$  TeV nakon obrade 9.5 sati podataka. Prilagodnom analitičkog oblika zakrivljenog zakona potencije na dobivene podatke, kao rezultat su dobiveni faktor normalizacije  $f_0=(6.01 \pm 0.12) \times 10^{-10} \text{ cm}^{-2} \text{ s}^{-1} \text{ TeV}^{-1}$  te parametri  $a = (-2.36 \pm 0.02)$  i  $b = (-0.17 \pm 0.04)$ , vidi izraz 3.1. Za energije ispod  $10^3$  GeV emisija iz Rakovice slabi, dok za više energije emisija puno brže opada. Usporedbom dobivenih rezultata sa prijašnjim MAGIC rezultatima (npr. Albert et al., 2008a) ili spektrima dobivenim pomoću drugih IACT teleskopa (npr. teleskop HESS, Aharonian et al., 2006), zaključujem da su rezultati unutar statističkih nepouzdanosti, kao što je i bilo očekivano. Neznatne razlike u spektru posljedica su razlike u kalibraciji različitih IACT teleskopa, kao i sistematskih pogrešaka. Također, malo je vjerojatno da će jednostavni model poput zakona potencije moći opisati širokopojasnu emisiju iz maglice koja vjerojatno potječe od različitih populacija čestica (više o modeliranju Rakovice čitatelj se upućuje na Zhang et al., 2020). Analiza Rakovice, kao analiza dobro poznatog i stabilnog izvora, ovdje je korištena kao način provjere performanci teleskopa kako bi bili sigurni da dobro razumijemo sistematske nepouzdanosti. Provjera pulsne emisije pulsara Rakovice je način provjere da softver za analizu pulsarovog zračenja također daje ispravne rezultate. Ista analiza će biti primjenjena i u slučaju traganja za visokoenergijskim pulsним gama-zračenjem iz pulsara Vilin konjic, opisanim u sljedećem poglavlju.

---

<sup>5</sup><http://www.jb.man.ac.uk/research/pulsar/crab.html>

<sup>6</sup>H. E. S. S. Collaboration (2020) je nedavno HESS teleskopima razlučila Rakovicu i izmjerila proširenje od  $52''$  iznad 0.7 TeV.

## Opazanja pulsara PSR J2021 +3651 i njegove maglice teleskopima MAGIC

Pulsar PSR J2021+3651 ili pulsar Vilin konjic (engl. *Dragonfly pulsar*) je jedan od najsjajnijih pulsara na energijama iznad 10 GeV prema *Fermi*-LAT katalogu (Abdo et al., 2013). Prvotno je otkriven na 1.4 GHz Arecibo radioteleskopom (Roberts et al., 2002) u regiji *Cygnus* s koordinatama RA: 20<sup>h</sup>21<sup>m</sup>05<sup>s</sup>, Dec: 36°51'04". Period rotacije ovog pulsara je 103.7 ms, iz čega proizlazi karakteristična starost  $\tau = 17$  kyr i luminoznost usporavanja  $3.4 \times 10^{36}$  erg s<sup>-1</sup> (Roberts et al., 2002). Uzimajući u obzir njegovu udaljenost od 1.8 kpc (Kirichenko et al., 2015), pulsar Vilin konjic predstavlja vrlo izglednog kandidata za opazanja na vrlo visokim energijama ( $E > 100$  GeV) zbog visokog faktora detektibilnosti,  $\dot{E}/d^2$  (Carrigan et al., 2007). Također, nagovještaj pulsne emisije iznad 25 GeV spomenut je u *Fermi*-LAT katalogu izvora iznad 10 GeV (Ackermann et al., 2013).

Pulsar Vilin konjic je, osim u radiopodručju (Roberts et al., 2002), opažen u X-području (Hessels et al., 2004) te u gama-području sa satelitima *Fermi*-LAT i *Agile* (Abdo et al. 2009a; Halpern et al. 2008). Na temelju *Fermi*-LAT opazanja gdje se koristila vremenska informacija iz radiopromatranja, pulsni profil sastoji se od dva pulsa, gdje je prvi nađen u intervalu  $P1 = [0.13 - 0.20]$ , a drugi  $P2 = [0.58 - 0.68]$ . Na slici 4.4 pokazani su arhivski pulsni profili kroz cijeli elektromagnetski spektar: od radiozračenja do gama-zračenja (do energija  $E < 10$  GeV). Iz profila pulsne emisije uočava se trend da puls P1 s povećanjem energije slabi dok je P2 relativno stabilan.

Pulsar PSR J2021+3651 okružen je maglicom torusnog oblika koja je opažena u X-području satelitom *Chandra* (Etten et al., 2008), vidi sliku 4.6. Zbog specifične morfologije maglice koja podsjeća na vilin konjica, maglica se naziva maglica Vilin konjica (engl. *Dragonfly nebula*). Na energijama u području TeV opažen je proširen izvor ( $\sim 2^\circ$ ) MGRO J2019+37 koji se povezuje, između ostalog, s maglicom Vilin konjica (Aliu et al., 2014). VERITAS kolaboracija razlučila je ovaj proširen izvor u dva izvora, gdje spektar jednog izvora, VER J2019+368, nalikuje spektru tipične mlade maglice pulsarovog vjetra, a lokacija emisije odgovara položaju PSR J2021+3651.

Pulsar Vilin konjic opažan je teleskopima MAGIC u srpnju i kolovozu 2014. godine. Podaci su snimljeni u stereo modu okidačem *Sum-Trigger* (Dazzi et al., 2015). Tijekom opazanja korišten je *wobble mode* snimanja izvora. Koordinate izvora koje su korištene u analizi, preuzete iz opazanja u X-području (Hessels et al., 2004) su sljedeće: RA: 20<sup>h</sup>21<sup>m</sup>05<sup>s</sup>, Dec: 36°51'04" u rasponu zenitnih kutova od 5° to 35°. Pulsar Vilin konjic opažan je tijekom 18 noći (5., 6., 8., 10., 22. – 31. srpnja i 2. – 5. kolovoza 2014. godine). Tijekom tog perioda uspješno je prikup-

---

ljeno 35 sati opažanja<sup>7</sup>. Nakon uklanjanja podataka na koje su utjecali loši vremenski uvjeti ili tehničke poteškoće, na raspolaganju je ostalo  $\sim 27.6$  sati kvalitetnih podataka. Obrada podataka provedena je standardnim MAGIC softverom *MARS* kao i standardnim setom MC simulacija za period ST.03.05, što je jednaki set kojim se izvršila analiza podataka pulsara Rakovice. Podatke vezane za vremenske informacije o periodu, promjeni perioda i ostalo (*ephemeris*) osigurala je *Fermi*-LAT kolaboracija te smo, koristeći te podatke, *a priori* odredili područje signala (P1 i P2) te pozadine (Bg): P1=[0.08 – 0.15], P2=[0.5 – 0.63] i Bg=[0.65 – 0.9]. Svjetlosne krivulje izračunate su za niži energijski raspon energija ( $50 \text{ GeV} < E < 200 \text{ GeV}$ ) i za puni raspon (engl. *full  $E_\gamma$ -range*,  $E > 200 \text{ GeV}$ ) energija, gdje su rezultati prikazani na slici 4.10. Signifikantnost pulsog signala izračunat je za P1, P2 te za ukupni P1+P2, koristeći izraz 17 u Li & Ma (1983). Obradom podataka iz pulsara Vilin konjic nije nađen značajan pulsni signal, odnosno za ukupni pulsni signal (P1+P2) signifikantnost za energije ( $50 < E < 200$ ) GeV je jednaka  $-1.9\sigma$  te  $-1.6\sigma$  za energije  $E > 200 \text{ GeV}$ . Kako bi bolje odredili spektralnu raspodjelu energije pulsne emisije pulsara Vilin konjic, koristili smo javno dostupne podatke *Fermi*-LAT kolaboracije. Ti podaci prikupljeni su satelitom *Fermi*-LAT u periodu od 4.5 godina i pokrivaju raspon energija od 0.1 GeV do 10 GeV. Analizu tih podataka napravio je T. Saito, glavni istraživač (engl. *principal investigator*) za opažanja pulsara Vilin konjic teleskopima MAGIC. Primarno, temeljem već objavljenih rezultata *Fermi* kolaboracije (Abdo et al., 2009a) za isti izvor pretpostavljen je zakon potencije s prekidom u spektru (za energije  $0.1 \text{ GeV} < E < 10 \text{ GeV}$ ) gdje je za spektralni index pretpostavljen  $\Gamma = 4.0$ . Međutim, s obzirom na opažanja pulsara Rakovice na visokim energijama gdje nema naznaka prekida u spektru niti na energijama u području TeV, napravili smo prilagodbu funkcije na podatke prikupljene satelitom *Fermi* ( $E > 10 \text{ GeV}$ ) jednostavnim zakonom potencije (bez prekida), a dobiveni spektralni parametri prikazani su u tablici 4.3. Za podatke prikupljene teleskopima MAGIC izračunali smo gornje granice pulsne emisije za energije  $E > 200 \text{ GeV}$  pretpostavljajući jednostavni zakon potencije sa spektralnim indeksom  $\Gamma = 4.0$ . Ovaj rezultat potvrđuje i kolaboracija VERITAS koja je relativno nedavno objavila da analizom 58 sati podataka prikupljenih opažanjem pulsara Vilin konjic (Archer et al., 2019) također ne nalazi niti nagovještaj pulsne emisije. Temeljem dobivenih gornjih granica za  $E > 200 \text{ GeV}$  i strmog spektralnog indeksa možemo zaključiti da je ovaj pulsar slabiji od pulsara Rakovice jer će za detekciju statistički značajnog pulsog signala trebati puno više sati (u optimističnom scenariju  $\sim 200$  sati) opažanja nego što ih je u sklopu ove teze prikupljeno (zbog tehničkih poteškoća nije sakupljeno predviđenih 100 sati).

Kako bi se analizirala kontinuirana emisija iz maglice, korišten je isti skup podataka koji

---

<sup>7</sup>Kolaboracija MAGIC planirala je prikupiti 100 sati podataka s pulsara Vilin konjic, ali zbog tehničkih poteškoća prikupljeno je samo 35 sati podataka.

je korišten za analizu pulsno signal, dakle 35 sati podataka prikupljenih u srpnju i kolovozu 2014. godine. Opažanja su izvedena u standardnom *wobble* načinu snimanja, gdje je izvor  $0.4^\circ$  odmaknut od centra kamere što je prikladno za točkaste izvore. S pretpostavkom da je maglica pulsara Vilin konjic prošireni izvor (prema [Aliu et al. 2014](#)) koristili smo difuzne Monte Carlo simulacije prikladne za takav izvor i za odgovarajući period (ST03.05). Standardni *MARS* softver korišten je u obradi podataka. Za energije  $E > 1$  TeV određen je PSF instrumenta i iznosi  $PSF = 0.039^\circ$ , a *smearing kernel* je  $0.3^\circ$ . Na temelju opažanja, određen je položaj maglice RA  $20^h 18^m 56^s$ , Dec:  $+36^\circ 52' 01''$  i taj položaj se podudara s položajem VERITAS izvora VER J2019+37 ([Aliu et al., 2014](#)). Za energije  $E > 500$  GeV i  $E > 1$  TeV maglica je opažena sa  $> 5\sigma$  statističke značajnosti (vidi sliku 4.17). Na energijama iznad 5 TeV emisija iščezava kao i na niskim energijama  $100 < E < 300$  GeV (slika 4.16). Kako bi se izvor bolje razlučio i morfološki mogao analizirati, potreban je prikladniji način snimanja za proširene izvore. Prijedlog opažanja maglice na optimalan način predan je kolaboraciji MAGIC te je on usvojen, međutim u konačnosti nije sakupljen dovoljan broj sati promatranja zbog loših vremenskih uvjeta. Detalje maglice pulsara Vilin konjic bit će moguće razabrati opažanjima novom generacijom teleskopa kao što je primjerice niz Čerenkovljevih teleskopa, engl. *Cherenkov Telescope Array - North* (CTA - North, [Actis et al., 2011](#)).

## **Opazanje visokoenergijskog gama-zračenja iz neidentificiranog izvora HESS J1858+020 teleskopima MAGIC**

Izvori otkriveni u području energija TeV, koji emitiraju zračenje u visokoenergijskom gama-području ( $E > 100$  GeV) s neidentificiranim odgovarajućim izvorima na višim valnim duljinama (engl. *counterpart*) još su jedna poznata klasa izvora u ovom dijelu elektromagnetskog spektra. HESS J1858+020 (RA:  $18^h 58^m 20^s$ , Dec:  $2^\circ 05' 24''$ ) je neidentificirani prošireni izvor koji je otkriven u području energija TeV tijekom HESS pregleda neba ([Aharonian et al., 2008](#)) gdje je po izgledu spektra i veličini klasificiran kao kandidat za maglicu pulsarovog vjetra. Položaj ovog izvora podudara se s radioizvorom G35.6-0.4 (slika 5.1), identificiran kao ostatak supernove čija se starost procjenjuje na 30 000 godina. [Torres et al. \(2011\)](#) predložili su da opažena emisija u području TeV iz HESS J1858+020 proizlazi iz interakcije molekularnog oblaka nađenog u neposrednoj blizini spomenutog izvora i kozmičkih zraka ubrzanih na udarnoj fronti ostatka supernove. U vrijeme tih opažanja, unatoč očekivanjima, nije bio pronađen izvor niti u području GeV niti u području TeV. S druge pak strane, ako se radi o maglici pulsarovog vjetra, tada bi u blizini trebao biti pulsar koji je dovoljno snažan da objasni opaženu emisiju u području

---

TeV. Nađena su tri pulsara, PSR J1857+0212, PSR J1857+0210 i PSR J1858+020 koji su ili predaleko ili prestari ( $>10^5$  godina) da bi objasnili opaženu emisiju iz HESS J1858+020.

Analiza podataka iz izvora HESS J1858+020 prikupljenih teleskopima MAGIC opisana je u ovom poglavlju. S obzirom da na raspolaganju imamo dva velika seta podataka, gdje izvor HESS J1858+020 nije opažan direktno već je u polju opažanja drugih izvora (direktno opažani izvori su HESS J1857+026 i izvor W44) cilj je detektirati izvor, odrediti njegovu veličinu te proučiti morfologiju ako je to moguće. Prvi set podataka sastoji se od opažanja izvora HESS J1857 teleskopima MAGIC iz 2010. godine (od srpnja do listopada 2010.) s rasponom zenitnih kuteva od  $25^\circ$  do  $36^\circ$ . Izvor je opažan ukupno 50 sati. Izvor HESS J1857+026 (s koordinatama RA :  $18^{\text{h}}57^{\text{m}}27^{\text{s}}$  i Dec :  $02^\circ42'60''$ ) sniman je u standardnom *wobble* modu snimanja s četiri različita usmjerenja teleskopa koji su simetrični s obzirom na izvor, vidi lijevu sliku 5.4. Drugi set podataka sastoji se od opažanja ostatka supernove W44 teleskopima MAGIC iz 2013. i 2014. godine u rasponu zenitnih kuteva od  $25^\circ$  do  $45^\circ$ , vidi desnu sliku 5.4. Područje izvora W44 (koordinate RA :  $18^{\text{h}}54^{\text{m}}45^{\text{s}}$ , Dec :  $01^\circ53'59''$ ) promatrano je  $\sim 120$  sati. Podaci su analizirani u podgrupama prema odgovarajućim periodima te je ukupno na raspolaganju oko 170 sati podataka. Za krajnje rezultate svi podaci su objedinjeni. Obrada podataka napravljena je koristeći standardni MAGIC softver *MARS* (version 2.14, Zanin, R., 2013). Izvor je proširen (Aharonian et al., 2008) stoga su korištene Monte Carlo simulacije za proširene izvore. Podaci koji su snimljeni tijekom loših vremenskih uvjeta ili zahvaćeni tehničkim poteškoćama su odbačeni, tako da je na raspolaganju ostalo oko 160 sati kvalitetnih podataka. S obzirom da HESS J1858+020 nije opažan izravno već je u vidnom polju drugih opažanja, analizu je trebalo adekvatno prilagoditi jer je udaljenost između centra kamere i izvora od interesa veća od standardne udaljenosti. Osjetljivost instrumenta je manja što je izvor udaljeniji od smjera duž kojeg je teleskop postavljen tako da je za detekciju istog izvora potrebno više sati opažanja u odnosu kada se izvor opaža izravno. Kako bi se pak pozadina ispravno procijenila, koristi se nestandardna *Off from wobble partner (OfWP)* metoda opisana u poglavlju 2.4.10 kojom se određuje koji će *wobble* biti korišten za traženje signala, a koji za procijenu pozadine tako da izvori koji su bili opažani (HESS J1857 i W44) ne upadnu kao signal u pozadinu. Obradom svih podataka izvor HESS J1858+020 je opažen sa značajnošću od  $> 9\sigma$  za energije  $E > 200$  GeV, slika 5.8. Za isti raspon energija,  $E > 200$  GeV i uz PSF instrumenta  $0.071^\circ$  procijenjen položaj centra emisije nalazi se na koordinatama RA :  $18^{\text{h}}58^{\text{m}}8^{\text{s}}$  and Dec :  $02^\circ04'48''$  što je u skladu s rezultatom kolaboracije HESS (Aharonian et al., 2008). Procijenjena intrinzična proširenost izvora HESS J1858+020 je  $0.08 \pm 0.03$  deg, također u skladu s Aharonian et al. (2008). Spektralna raspodjela energije za HESS J1858+020 izračunata je za energije od 300 GeV do 10 TeV i prikazana na slici 5.10. Raspodjelu opisujemo zakonom potencije  $dN/dE = N_0[(E/1 \text{ TeV})]^{-\Gamma}$  gdje

je  $N_0 = (4.7 \pm 0.6) \times 10^{-13} \text{ TeV}^{-1} \text{ cm}^{-2} \text{ s}^{-1}$  sa spektralnim indeksom  $\Gamma = 2.29 \pm 0.13$ . Analiza proširenog izvora kakav je HESS J1858+020 koji nije primarna meta opažanja, već se nalazi u vidnom polju teleskopa (engl. *off-centred*), ima određenih ograničenja zbog toga što su Čerenkovljevi teleskopi prvenstveno namjenjeni direktnom opažanju točkastih izvora. U ovom slučaju izvor od interesa bio je na velikoj udaljenosti od centra kamere stoga je morfološke detalje bilo nemoguće razlučiti ovakvom metodom. Kasnije je razvijena metoda za opažanje proširenih i *off-centred* izvora (Vovk et al., 2018). Nedavno je nađen novi izvor u području energija GeV nadomak HESS J1858+020 (Cui et al., 2021) izvora čiji se SED glatko nastavlja na SED HESS J1858 izvora. Takav scenarij potencijalno može objasniti emisiju energija u području TeV na položaju HESS J1858+020 kao posljedicu bijega kozmičkih zraka iz obližnje supernove G35.6-0.4 i njihovu interakciju s molekularnim oblakom što bi odbacilo pretpostavku da je HESS J1858 maglica pulsarovog vjetra. Detaljnija opažanja u X-području su potrebna kako bi se objasnio nedostatak ove emisije.

## Proučavanje radioemisije slabog sjaja

Teleskop LOFAR (engl. *LOw Frequency ARray*, van Haarlem et al., 2013) je interferometrijski radioteleskop koji opaža nebo sjeverne hemisfere na niskim radiofrekvencijama (10 – 240 MHz). Opažanja se provode koristeći različite preglede neba kao što je primjerice aktualni LoTSS (engl. *LOFAR Two-meter Sky Survey*, Shimwell et al., 2017, 2019, 2022) na frekvencijama 120 – 168 MHz. LoTSS pregled neba uključuje i duboka polja koja su opažana više puta za redom, kao što je polje ELAIS-N1 (Sabater et al., 2021). Primarna svrha ovakvih opažanja je pretraživanje manje sjajne (engl. *fainter*) populacije radioizvora. U polarizaciji su inicijalnu analizu na LoTSS ELAIS-N1 polju proveli Herrera Ruiz et al. (2021). Oni su, koristeći 6 osmosatnih opažanja i primjenjujući metodu slaganja (engl. *stacking method*) pokazali uspješnost ove metode tako što su detektirali sedam dodatnih polariziranih izvora u objedinjenim podacima, koji se inače ne opažaju u pojedinačnoj noći postigavši tako incidenciju polariziranih izvora 1 po  $1,6 \text{ deg}^2$ . U ovom istraživanju koristit će se komplementarna metoda na podacima dubokog polja ELAIS-N1, pri čemu će se polarizirano sinkrotronsko zračenje Mliječne staze koristiti kao korekcija opažanja na promjene uzrokovane Faradayevom rotacijom u Zemljinoj ionosferi u svrhu detektiranja radioemisije slabog sjaja, ali i slabijih izvora (uključujući i pulsare). Kada se linearno polarizirani val, valne duljine  $\lambda$ , širi kroz magnetiziranu plazmu (među-

---

zvijezdane, ionosferu) dolazi do Faradayeve rotacije odnosno zakretanja kuta polarizacije:

$$\Delta\theta = RM\lambda^2 = 0.81\lambda^2 \int_{izvor}^{promatrac} n_e B_{\parallel} dl, \quad (2)$$

gdje je RM mjera rotacije (engl. *rotation measure*). Ovaj efekt proporcionalan je gustoći elektrona (engl. *total electron content*, TEC) integriranih duž linije gledanja i obrnuto proporcionalan kvadratu opažanih frekvencija (Thompson, 2008). Ako se promjene u kutu polarizacije događaju na vremenskoj skali kraćoj od vremena opažanja (osam sati), doći će do depolarizacije signala pa je potrebno napraviti određene korekcije. Jedna od metoda kojom se određuje na koji način Faradayeva rotacija u ionosferi utječe na podatke, odnosno koliko su opažanja međusobno relativno pomaknuta u prostoru Faradayevih dubina, koristi poznate polarizirane izvore (Herrera Ruiz et al., 2021) kao način kalibracije. Komplementarna metoda za provjeru relativnog pomaka između opažanja uzrokovanog Faradayevom rotacijom u ionosferi koristi polariziranu difuznu Galaktičku sinkrotronsku emisiju (Lenc et al., 2016; Brentjens, 2018). Ovaj je tip emisije na opažanim niskim radiofrekvencijama sveprisutan (npr. Erceg et al., 2022) i omogućuje analizu većeg dijela polja nasuprot korištenju jednog referentnog polariziranog izvora. Korekcije dobivene na ovaj način trebale bi poboljšati točnost do na  $\sim 0.01$  rad m<sup>2</sup>.

U ovom poglavlju koristim polariziranu difuznu sinkrotronsku emisiju za proučavanje utjecaja Faradayeve rotacije u ionosferi na podatke sakupljene iz 21 LOFAR opažanja polja ELAIS-N1. Metodu slaganja (engl. *stacking method*) primjenit ću na slike niske rezolucije (4.3') kako bih proučila strukture difuzne polarizirane emisije. ELAIS-N1 podaci korišteni u ovom poglavlju dio su LoTSS-Deep Fields Release 1 (Sabater et al., 2021). Korištena su 21 od 27 opažanja (10 opažanja iz Ciklusa 2 i 11 opažanja iz Ciklusa 4) provedena visokopojasnim antenama (engl. *High Band Antennas*) u razdoblju od svibnja do kolovoza 2014. i 2015. godine. Šum na svakoj frekvenciji, izračunat kao standardna devijacija u kutu svake slike, je u oba seta podataka usporediv, s tim da su podaci iz Ciklusa 4 jače zahvaćeni radiosmetnjama (engl. *Radio Frequency Interference*, RFI), vidi sliku 6.3. Za opažani raspon frekvencija, tipičan šum na frekvencijama koje nisu zahvaćene RFI-om jest  $\sim 3.3$  mJy PSF<sup>-1</sup> u setu Ciklusa 2 i  $\sim 2.7$  mJy PSF<sup>-1</sup> za Ciklus 4, gdje razlika dolazi od različitih širina frekvencijskih kanala. Za analizu podataka koristili smo Faradayeve kocke ELAIS-N1 polja nastale primjenom *rotation measure* (RM) metode (Burn, 1966; Brentjens & de Bruyn, 2005) na Stokes Q i U kocke u ovisnosti o frekvencijama. Ova metoda omogućuje dekompoziciju opažene polarizirane emisije po količini Faradayeve rotacije koja se dogodila duž doglednice te na taj način procjenjuje raspodjelu ionizirane međuzvijezdane tvari na tom putu kao i svojstva prisutnog magnetskog polja. Faradayeva dubina  $\Phi$  definirana je izrazom 6.3. Za određene koordinate na nebu, RM metoda daje nam raspodjelu opažene



polarizirane emisije po Faradeyevim dubinama. Taj Faradeyev spektar je Fourierov transformat kompleksne polarizacije opaženog signala,  $P(\lambda^2) = Q(\lambda^2) + iU(\lambda^2)$ , iz  $\lambda^2$ - prema  $\Phi$ -prostoru (Brentjens & de Bruyn, 2005) dan izrazom 6.4. Ako se RM sinteza primijeni na neko određeno područje neba, moguće je izvršiti Faradeyevu tomografiju odnosno proučiti morfologiju opaženog polariziranog zračenja na različitim Faradeyevim dubinama. Kao rezultat primjene RM sinteze i metode naslagivanja, difuzna emisija slabog sjaja detektirana je u rasponu Faradeyevih dubina od  $-16$  do  $+17 \text{ rad m}^{-2}$  te je karakteriziraju sljedeće značajke: emisija se, u manjem obimu, pojavljuje na sjeverozapadu slike na dubini  $-16 \text{ rad m}^{-2}$  te postepeno raste preko centra slike u smjeru jugozapada do dubine od  $-4 \text{ rad m}^{-2}$ . Na  $0.5 \text{ rad m}^{-2}$  polarizirana emisija je maksimalnog intenziteta. Prema višim Faradeyevim dubinama strukture difuzne emisije postaju nejednake i rupičaste te isčezavaju u potpunosti na  $+17 \text{ rad m}^{-2}$ . Uspoređujući strukture difuzne emisije slabog sjaja dobivene metodom naslagivanja 20 LOFAR opažanja (slika 6.5) sa istim strukturama dobivenih iz samo jednog opažanja (slika 7., Jelić et al., 2014) zaključujem da su strukture izražajnije i jasnije, posebice strukture dalje od centra slike te se strukture opažaju na širem rasponu Faradeyevih dubina. Također, opisanom metodom naslagivanja opažena je difuzna emisija slabog sjaja na višim Faradeyevim dubinama od  $+13$  do  $+17 \text{ rad m}^{-2}$  što u prijašnjim opažanjima nije bilo detektirano. Temperatura sjaja emisije slabog sjaja odgovara  $475 \text{ mK}$  što je gotovo red veličine slabije od najsajnije emisije prethodno opažene u tom polju. Nadalje, pokazano je da se difuzna polarizirana emisija može koristiti za određivanje relativnog pomaka (u prostoru Faradeyevih dubina) uzrokovanog Faradeyevom rotacijom u ionosferi s obzirom na neko referentno promatranje. Vjerodostojnost metode potvrđena je i za RM vrijednosti radioizvora uspješno detektiranih u konačnoj Faradeyevoj kocki s navedenim radioizvorima u katalogima (Herrera Ruiz et al., 2021) i Piras et al. (u pripremi) gdje se u oba slučaja koriste podaci više rezolucije ( $20''$  odnosno  $6'$ ). Opisanom metodom naslagivanja kombinirala sam 20 pojedinačnih promatranja objedinivši ih u skup podataka od 150 sati. U konačnoj Faradeyevoj kocki šum u polariziranom intenzitetu jest  $27 \mu\text{Jy PSF}^{-1} \text{ RMSF}^{-1}$  što je poboljšanje od  $\sim \sqrt{20}$  u odnosu na šum pojedinačnog promatranja u trajanju od  $5 - 8$  sati. Opisana metoda može biti korisna za buduća duboka polarimetrijska opažanja galaktičke sinkrotronske emisije na niskim frekvencijama s teleskopom LOFAR, SKA (Square Kilometre Array) te idućim generacijama radioteleskopa. Primjerice, mogla bi se primjeniti i na ostala LoTSS duboka polja (Lockman Hole i Boötes) kao i na GOODS-N (Great Observatories Origins Deep Survey- North) polje. Također, metoda bi mogla biti od koristi i u kozmološkim studijama gdje galaktička polarizirana emisija predstavlja zračenje iz prednjeg plana koje treba ukloniti (Carretti et al., 2022; Jelić et al., 2010; Asad et al., 2015; Spinelli et al., 2019).

# Contents

<b>1</b>	<b>Introduction</b>	<b>1</b>
1.1	Cosmic rays . . . . .	2
1.1.1	The origin of Galactic cosmic rays . . . . .	4
1.2	Production mechanisms of gamma rays . . . . .	7
1.2.1	Leptonic gamma-ray production mechanisms . . . . .	7
1.2.2	Hadronic gamma-ray production mechanisms . . . . .	10
1.3	Sources of Very-High-Energy Gamma Rays . . . . .	11
1.3.1	Galactic sources . . . . .	11
1.3.2	Extragalactic sources . . . . .	12
1.4	Detection techniques for high energy gamma rays . . . . .	13
1.5	Pulsars . . . . .	15
1.5.1	Discovery and overview . . . . .	15
1.5.2	Neutron stars . . . . .	18
1.5.3	Gamma-ray pulsars and observational revolution . . . . .	19
1.5.4	Pulsar physics . . . . .	21
1.5.5	Pulse profiles throughout the electromagnetic spectrum . . . . .	23
1.5.6	Pulsar magnetosphere and pulsar emission models . . . . .	25
1.6	Pulsar wind nebulae . . . . .	33
1.6.1	Overview . . . . .	33
1.6.2	The evolution of PWNe . . . . .	34
1.6.3	Observational properties of PWNe . . . . .	36
1.7	Short overview of supernova remnants . . . . .	39
1.8	This Thesis . . . . .	41
<b>2</b>	<b>Imaging Atmospheric Cherenkov Technique and MAGIC telescopes</b>	<b>43</b>
2.1	Introduction . . . . .	43
2.2	Imaging Atmospheric Cherenkov Technique . . . . .	43
2.2.1	Extensive Air showers . . . . .	44
2.2.2	Cherenkov radiation . . . . .	47
2.3	The MAGIC telescopes: hardware components . . . . .	50
2.3.1	Drive system and structure . . . . .	51
2.3.2	Mirrors . . . . .	52
2.3.3	Camera . . . . .	53
2.3.4	Receivers and triggers . . . . .	54

2.3.5	Sum-Trigger II . . . . .	56
2.3.6	The readout electronics . . . . .	57
2.3.7	Telescope observations . . . . .	58
2.4	MAGIC data analysis . . . . .	59
2.4.1	Pre-processing . . . . .	61
2.4.2	Calibration . . . . .	61
2.4.3	Image cleaning and parameters reconstruction . . . . .	62
2.4.4	Gamma Hadron separation and energy reconstruction . . . . .	64
2.4.5	Monte Carlo simulations . . . . .	65
2.4.6	Arrival reconstruction and signal extraction . . . . .	67
2.4.7	Spectrum and Light Curve . . . . .	69
2.4.8	Special case analysis - Pulsar detection . . . . .	71
2.4.9	Skymaps . . . . .	73
2.4.10	Notes on the non-standard observations . . . . .	74
2.5	MAGIC performance . . . . .	77
2.5.1	Upper limits . . . . .	80
2.5.2	Systematic uncertainties . . . . .	80
<b>3</b>	<b>Crab pulsar and its nebula observed at very high gamma-ray energies</b>	<b>82</b>
3.1	Introduction . . . . .	82
3.2	The source description . . . . .	84
3.2.1	The Crab pulsar . . . . .	84
3.2.2	The Crab nebula . . . . .	86
3.3	Crab pulsar and its nebula observed with the MAGIC telescopes . . . . .	88
3.3.1	Crab pulsar folded light curve . . . . .	89
3.3.2	Crab nebula spectral energy distribution . . . . .	91
3.4	Conclusions . . . . .	92
<b>4</b>	<b>Dragonfly pulsar and its nebula observed at very high gamma-ray energies</b>	<b>93</b>
4.1	Introduction . . . . .	93
4.2	The source description . . . . .	95
4.2.1	The Dragonfly pulsar . . . . .	95
4.2.2	The Dragonfly nebula . . . . .	99
4.3	Dragonfly pulsar and its nebula observed with the MAGIC telescopes . . . . .	102
4.4	Phase calculations for Dragonfly pulsar . . . . .	103
4.5	The spectrum of Dragonfly pulsar . . . . .	104
4.6	Updates on the Dragonfly pulsar . . . . .	106
4.7	Searching for an extended emission from Dragonfly's nebula . . . . .	109
4.8	Summary and future prospects . . . . .	112
<b>5</b>	<b>VHE observations of the unidentified TeV source HESS J1858+020</b>	<b>114</b>
5.1	Introduction . . . . .	114
5.2	The MAGIC observations and data sets . . . . .	118
5.3	Data analysis of HESS J1858+020 . . . . .	120

---

5.4	Results of the analysis on HESS J1858+020 . . . . .	123
5.4.1	Detection of HESS J1858+020 . . . . .	123
5.4.2	The spectrum of HESS J1858+020 . . . . .	125
5.5	Discussion and conclusions . . . . .	127
<b>6</b>	<b>Searching for the very faint radio emission</b>	<b>130</b>
6.1	Introduction . . . . .	130
6.2	Data and processing . . . . .	135
6.2.1	LoTSS-Deep Fields observations and very low-resolution images . . . . .	135
6.2.2	RM synthesis and Faraday depth cubes . . . . .	139
6.2.3	Comparison with a previous LOFAR commissioning observation . . . . .	142
6.3	Ionospheric Faraday rotation corrections . . . . .	143
6.3.1	Analysis of a relative shift in Faraday depth between different observations . . . . .	143
6.3.2	Restoring 011 observation using Galactic polarized emission . . . . .	145
6.4	Stacking a very low-resolution data . . . . .	149
6.5	The final stacked Faraday cube . . . . .	151
6.5.1	Cross-checking the detection of the radio sources . . . . .	151
6.5.2	Faint diffuse Galactic polarized emission . . . . .	152
6.6	Discussion on the faint polarized emission newly detected . . . . .	156
6.7	Summary and conclusions . . . . .	159
<b>7</b>	<b>Thesis summary and outlook</b>	<b>161</b>
	<b>Bibliography</b>	<b>164</b>
	<b>Curriculum vitae</b>	<b>172</b>

# List of Figures

1.1	The spectrum of cosmic rays measured by several ground-based experiments, as indicated in the legend. The position of the spectrum's characteristics, knee and ankle, are indicated with the arrows, as well as the equivalent laboratory LHC's energy. The figure is taken from <a href="#">Letessier-Selvon &amp; Stanev (2011)</a> . . . .	4
1.2	The first-order Fermi acceleration: when a charged particle crosses a shock front, it encounters a change in the magnetic field, which reflects it back through the shock wave at greater velocity. Credit: <a href="#">Saito (2011)</a> . . . . .	6
1.3	The spectrum of the synchrotron radiation, expressed as the total power radiated in all directions, is shown on linear (a) and logarithmic (b) scales. Figure taken from <a href="#">Longair (2011)</a> . . . . .	8
1.4	Electromagnetic spectrum and the corresponding detection techniques – in space and on the ground. The purple line indicates atmospheric electromagnetic opacity. Figure from ( <a href="#">Lopez-Coto, 2015</a> ). . . . .	13
1.5	Gamma-ray observatories: (a) satellite-borne telescope <i>Fermi</i> -LAT and ground-based instruments (b) MAGIC and (c) HAWC. . . . .	14
1.6	Jocelyn Bell (Burnell) pictured at the Mullard Radio Observatory (right) in 1967 with the pulsar chart (left). Image owned by Cavendish Laboratory. . . . .	16
1.7	Distribution of known pulsars in the Galactic plane, based on distance estimates derived from a model. The spiral arm structure, used in the electron density model, is indicated. The image shows the inner 15 kpc around the Galactic centre. Figure from <a href="#">Kramer et al. (2003)</a> . . . . .	17
1.8	Pulsars from the ATNF catalogue are shown in $P - \dot{P}$ space according to their properties discussed in Sec. 1.5.4. Rotation-powered gamma-ray pulsars are marked with blue, whereas millisecond ones are marked with red triangles. Radio pulsars are depicted as black dots. Figure from <a href="#">Carreto Fidalgo (2019)</a> . . . .	18
1.9	Inside the neutron star. The figure is taken from <a href="#">Page &amp; Reddy (2006)</a> . . . . .	19
1.10	The sky-map of known pulsars in Galactic coordinates obtained from <i>Fermi</i> -LAT observations where rotation-powered pulsars are divided into radio-loud (green dots) and radio-quiet (blue squares). Figure is taken from <a href="#">Abdo et al. (2013)</a> . . . . .	20
1.11	The folded light curves of the first seven gamma-ray pulsars (detected at HE gamma rays, up to a few tens of GeV with EGRET satellite) at different energies. A straight line indicates no pulsed emission found. Figure adapted from <a href="#">Thompson (2008)</a> by NASA. . . . .	23

1.12	Crab pulsar profiles throughout the spectrum (from radio to X-rays). Figure is taken from <a href="#">Moffett &amp; Hankins (1996)</a> . . . . .	24
1.13	Model of a pulsar rotating around its spin axis and emitting beams of radiation along its magnetic axis. Figure is taken from Yuri Lyubarsky. . . . .	26
1.14	Model showing pulsar electrodynamics with the co-rotating magnetosphere and the wind zone proposed by <a href="#">Goldreich &amp; Julian (1969)</a> . The model is for an aligned rotator where magnetic and rotational axes are aligned. Pulsar is at the lower left, with the illustrated poloidal magnetic-field structure. The particles attached to the closed magnetic-field lines corotate, and they are within the light cylinder (LC). The open magnetic-field lines are the ones that pass through the LC and charged particles stream out along them. Figure is taken from <a href="#">Goldreich &amp; Julian (1969)</a> . . . . .	27
1.15	Possible emission regions in the pulsar magnetosphere, as theorized in <a href="#">Hirotani (2011)</a> . The last closed field line (dark green) meets the light cylinder at the equatorial plane, at the $\Upsilon$ point. PC stands for polar cap region; slot gap (SG) is the region along the last closed line. Outer gap (OG) region extends from the null-surface (dashed line) to the LC; equatorial current sheet (ECS) extends from the $\Upsilon$ point to the outside of the LC. Figure from <a href="#">Ceribella (2021)</a> . . . . .	28
1.16	Model of a striped wind for an oblique rotator, which encloses the angle $\chi$ between the rotational and magnetic axes. The undulating current sheet (blue curve) in the meridional plane separates the stripes of opposite magnetic polarity. In the equatorial plane, the current sheet develops an Archimedean spiral. Figure from <a href="#">Mochol (2017)</a> . . . . .	29
1.17	Configuration of magnetic field lines for different oblique rotators (inclination angle $\alpha$ is indicated in the title of each plot) in the poloidal plane ( $\mu, \Omega$ ) obtained from simulations from a dissipative pulsar magnetosphere. The electric field $E_{\parallel}$ along the magnetic field lines is denoted by the colour scale, and the magnetic field is marked with streamlines. The rotation vector $\Omega$ is along the $Z$ -axis, where $Z$ and $X$ are given in the units of the light cylinder $R_{lc}$ marked with a vertical dashed line. Figure is taken from <a href="#">Kalapotharakos et al. (2014)</a> . . . . .	31
1.18	Model spectral energy distribution for the Crab pulsar for inclination angle $\alpha = 45^\circ$ , viewing angle $\zeta = 66^\circ$ (left), and for Geminga pulsar for inclination angle $\alpha = 75^\circ$ , viewing angle $\zeta = 50^\circ$ (right). The viewing angle chosen to best match the Fermi and VHE light curves. Differently coloured lines and points/symbols show results of simulation(s) and observations, as indicated in legends of left and right panels. Figures and data points are from the references in <a href="#">Harding et al. (2021)</a> . . . . .	32
1.19	Model spectral energy distribution for the Vela pulsar for inclination angle $\alpha = 75^\circ$ , viewing angle $\zeta = 50^\circ$ (left), and for PSR B1706-44 for inclination angle $\alpha = 45^\circ$ , viewing angle $\zeta = 53^\circ$ (right). Figures and data points are from the references in <a href="#">Harding et al. (2021)</a> . . . . .	32

1.20	Examples of PWN: a) multi-wavelength image of Crab nebula with X-ray emission (blue) from <i>Chandra</i> , optical emission (red and yellow) from Hubble Space Telescope, and IR emission (purple) from <i>Spitzer</i> ; b) multi-wavelength image of G54.1+0.3 with X-ray emission (blue) and IR emission (red-yellow) from the same detectors as in a). Images courtesy NASA/CXO. . . . .	33
1.21	Sketch of radiation zones in pulsar wind nebula: pulsar and its nebula radiate in a wide energy range, the unshocked wind is assumed to produce only GeV or TeV photons. Figure from <a href="#">Aharonian &amp; Bogovalov (2003)</a> . . . . .	35
1.22	The model of a composite SNR with a central neutron star (pulsar) and its nebula. The pulsar produces a cold, ultra-relativistic wind of particles. Wind flows (free expansion) up to the termination shock (denoted with $R_{pwn}$ , where particles are heated after crossing the shock to produce the shocked wind. The nebula is surrounded by the supernova remnant, itself imprisoned by the ambient medium. Figure adopted from <a href="#">Gelfand et al. (2007)</a> . . . . .	36
1.23	Modelled spectral energy distribution (SED) of the generic PWN: time evolution of the SED from 1 kyr - 200 kyr. The left component is the synchrotron and the right one is the Inverse Compton component of the emission. The decline of synchrotron energy flux with the increasing age of the system is more prominent than that of IC component, due to the synchrotron strong dependence on decaying magnetic field strength. Figure from <a href="#">Abdalla et al. (2018)</a> . . . . .	37
1.24	Population study shows some trends between pulsars and their nebulae. Left: Spin-down rate, $\dot{P}$ , and rotational period of pulsars with a firmly identified PWN, candidate PWN and without TeV counterpart (grey dots). Right: PWN extension versus characteristic time $\tau_c$ where the steeper part corresponds to the free expansion phase and the softer part to the interaction phase, but in general, one PWN expand with time until the age of a few tens of kiloyears. Figure from <a href="#">Abdalla et al. (2018)</a> . . . . .	38
1.25	Examples of the shell-type SNRs: a) Cassiopeia A b) Tycho's SNR c) Kepler's SNR d) RCW 103. Cas A and RCW are the result of the core collapse SN, while Tycho's and Kepler's are the remnants from SN Type Ia. (NASA) . . . . .	39
1.26	G11.2-0.3 is a circularly symmetric supernova remnant with a pulsar at its centre. <i>Chandra</i> 's X-ray image shows the pulsar and its pulsar wind nebula seen as high-energy X-rays (blue). A shell of heated gas from the outer layer of the exploded star (the supernova remnant) surrounds the PWN and is visible in the lower X-rays (red and green). Credit: NASA/CXC/Eureka Scientific/M.Roberts et al. . . . .	40
2.1	Simulations of air showers, from left to right: a) secondaries of a 50 GeV photon primary particle b) same, but only secondaries that produce Cherenkov light are plotted c) secondaries of a 200 GeV proton primary particle d) same, but only secondaries that produce Cherenkov light are plotted. In all figures, the particle type is colour coded: red = electrons, positrons, gamma rays; green = muons; blue = hadrons. Figure is taken from <a href="#">Hrupec (2008)</a> . . . . .	45

2.2	Longitudinal development of an EAS initiated by a gamma ray. The number of secondary electrons in relation to radiation length and the height above sea level for different photon energies is shown. The green lines indicate the shower age ( $s=0$ is the start of the shower, $s=1$ at the shower maximum). The altitude of the MAGIC telescopes is indicated. Figure is taken from <a href="#">Wagner (2006)</a> . . . . .	46
2.3	Scheme for the development of hadronic shower in the air. Figure is taken from <a href="#">Wagner (2006)</a> . . . . .	47
2.4	Left: Polarization of the medium with refractive index $n$ when a charged particle passes through. While the particle with $v < c/n$ produces symmetric polarization of the surrounding medium, particles with $v > c/n$ are faster than the electromagnetic information that induces the polarization. As a result, a photonic shock wave is produced and is emitted in the narrow cone along the incidental direction of the particle (right). Figure from <a href="#">de Naurois &amp; Mazin (2015)</a> . . . . .	48
2.5	IACT technique shown: telescopes detect Cherenkov light from the EAS. Shower images can be combined and stereo image parameters are obtained. Figure is taken from <a href="#">Fruck (2015)</a> . . . . .	48
2.6	Illustration of the reconstruction of the stereo parameters. Two cameras are shown, each with the characteristic image of the same shower. An orange star indicates the source position and a blue star is the reconstructed position. The angular distance between the sky position of the source and the reconstructed direction of the gamma ray is denoted $\theta$ . Figure is taken from <a href="#">Fruck (2015)</a> . . . . .	49
2.7	The MAGIC telescopes at the Roque de Los Muchachos Observatory, Canary Islands, Spain. Credit: Miguel Claro . . . . .	50
2.8	The MAGIC telescopes showing insets with the main hardware subsystems. Picture adapted from <a href="#">Fernandez Barral (2017)</a> . . . . .	52
2.9	The reflecting, parabolic surfaces are composed of mirrors: MAGIC I is on the left and MAGIC II on the right. Credit: R. Wagner. . . . .	53
2.10	MAGIC camera from the backside and from the front. Credit: R. Wagner. . . . .	54
2.11	The MAGIC camera and the trigger region: distribution of the L1 macrocells, each with 37 PMT pixels equipped with hexagonal Winston cones. The trigger FoV is $2.5^\circ$ diameter. The figure is taken from <a href="#">Fernandez Barral (2017)</a> . . . . .	55
2.12	The working principle of the Sum-Trigger: clipped channels from a macrocell are summed and then digitized. From <a href="#">Haefner et al. (2011)</a> . . . . .	56
2.13	Monte Carlo simulations show the energy threshold comparison for the Sum-Trigger and standard, digital trigger. From <a href="#">Dazzi et al. (2021)</a> . . . . .	57
2.14	Scheme of the electronic chain for the MAGIC telescopes, figure taken from <a href="#">Sitarek et al. (2013)</a> . . . . .	58



2.15	The observational <i>wobble</i> mode method where the telescopes are not pointing directly (like in ON/OFF observations) but slightly off from the source. The black circle marks the centre of the camera, located at $0.4^\circ$ from the source - ON region (green circle). Since the source is moving in the sky, it remains placed at this distance from the centre of the camera, resulting in a circular movement around the camera centre. The background is simultaneously observed from one region (left plot) or from three regions (right plot). When using 1 OFF region, it is taken $180^\circ$ from the source (at the opposite direction from the source), while when using 3 OFF regions the regions are separated the same distance one from the other, all of them $0.4^\circ$ from the camera centre at the angles $90^\circ$ , $180^\circ$ and $270^\circ$ counting clockwise from the ON region. Plot taken from <a href="#">Lopez-Coto (2015)</a> .	59
2.16	The observed data with the MAGIC telescopes is analysed with the software called MARS ( <b>M</b> agic <b>A</b> nalysis and <b>R</b> econstruction <b>S</b> oftware). In the above scheme, all the analysis steps are shown. The figure is taken from <a href="#">Fernandez Barral (2017)</a> .	60
2.17	An example of the PMT signal digitized by the readout. The readout counts are plotted on the y-axis and on the x-axis are the readout slices. As an artefact of the readout, a so-called <i>ringing</i> appears after the light pulse. The readout can also be triggered by the <i>afterpulses</i> from PMTs, which are large amplitude signals caused by an ion accelerated back to the PMT's photocathode. Credit: J. Sitarek.	62
2.18	Process of an image cleaning: for each event, charges (left) and arrival times (middle) are processed. If a pixel survives an image cleaning algorithm, it is shown in the cleaned image (right). Figure is taken from <a href="#">Giavitto (2013)</a> .	62
2.19	The reconstructed image of the shower in the camera is an ellipse which can be parametrized with the specific <i>Hillas parameters</i> . This method helps discriminate between gamma-like and hadron-like events. Figure is taken from <a href="#">Fernandez Barral (2017)</a> .	63
2.20	Two types of Monte Carlo gamma-ray simulations for the MAGIC telescopes are shown: <i>ringwobble</i> (left) and <i>diffuse</i> (right) MC. Figure from <a href="#">Lopez-Coto (2015)</a> .	66
2.21	<i>Doughnut</i> MC for the extended sources (or sources found at different off-axis angles) where the source extension and morphology is assumed a priori for the better precision of the MC files. From the MAGIC wiki pages.	67
2.22	<i>Disp</i> parameter: a) the shower impact point reconstruction has, in the case of mono observations, two possible degenerate solutions; b) in the case of stereo shower reconstruction, the degeneracy is removed by choosing the closest possible pair. Figure is taken from <a href="#">Fernandez Barral (2017)</a> .	67
2.23	Parameter $\theta$ is defined as the angular distance between the source position and the reconstructed position of the source. Right plot: an example of the $\theta^2$ distribution, where the vertical dashed line is the cut on the signal region. Figure is taken from <a href="#">Giavitto (2013)</a> .	68

2.24	Collection area of the MAGIC telescopes at the trigger level (dashed line) and after the cuts (solid lines). Thickness of the line depends on zenith angles. For comparison, the collection area before upgrade is shown with grey lines. Figure taken from <a href="#">Aleksić et al. (2016b)</a> . . . . .	70
2.25	Example of signal extraction from a light curve of a pulsar: signal (ON pulse phase) and background (OFF pulse phase). Figure taken from <a href="#">Saito (2011)</a> . . .	71
2.26	Left: Example of the skymap from the Crab Nebula analysis shows clear signal. Right: TS distribution shows a clear deviation from the null hypothesis (blue). Figure taken from <a href="#">Krause (2013)</a> . . . . .	73
2.27	Illustration how <i>Off from Wobble partner</i> method extracts the background in the case of an arbitrary source position. The black star marks the centre of the camera, located at $0.4^\circ$ from the nominal source (gray circle). The yellow star marks a source in the FoV aimed for analysis. While in W1 (left plot) the ON region for the source of interest is selected, W2- the wobble partner (right plot) is used to select the OFF region at the same position in the camera at which the source was located when in W1 wobble position. Afterwards, the procedure is repeated, but this time ON is taken from W2 and OFF from W1. Illustration adapted from <a href="#">Lopez-Coto (2015)</a> . . . . .	75
2.28	Scheme for the maximum possible extension for a source taken in the <i>wobble</i> mode with the MAGIC telescopes. Both <i>wobble</i> modes are shown here simultaneously. From W1, the ON region (green) is taken while from W2 one obtains the OFF (red) at the same distance, $d$ , from the camera centre. The normalization region is marked with green crosses between ON and OFF regions. Figure taken from <a href="#">Fernandez Barral (2017)</a> . . . . .	76
2.29	Left: energy resolution (solid lines) and bias (dashed lines) evaluated from MC simulations of $\gamma$ rays. Red lines represent low zenith angle; blue lines medium zenith angle; grey lines are pre-upgrade values. Right: rate of $\gamma$ rays after quality cuts for low and medium zenith angle. The peak of distribution marks the energy threshold, which is $\sim 75$ GeV for low zenith angles and $\sim 100$ GeV for medium zenith angles. Plots taken from <a href="#">Aleksić et al. (2016b)</a> . . . . .	77
2.30	MAGIC integral sensitivity as a function of energy threshold ( <i>left</i> ) and differential sensitivity as a function of energy ( <i>right</i> ) for different phases of the MAGIC experiment. Observations in MONO mode (only MAGIC I) are represented in light and dark grey. The black line represents the sensitivity for STEREO observations before the upgrade period. The current performance of the system for low and medium zenith angle is represented with red ( $Z_d < 30^\circ$ ) and blue ( $30^\circ < Z_d < 45^\circ$ ) lines. Plots were taken from <a href="#">Aleksić et al. (2016b)</a> . . . . .	78
2.31	Angular resolution of MAGIC telescopes as a function of the estimated energy obtained with the Crab Nebula data sample (points) and MC simulations (solid lines). 2D Gaussian fit with 68% containment radius. Plots taken from <a href="#">Aleksić et al. (2016b)</a> . . . . .	79
2.32	Integral sensitivity above 290 GeV for low zenith angle observations at different offsets from the camera centre. Plot from <a href="#">Aleksić et al. (2016b)</a> . . . . .	79

3.1	An example of pulsar wind nebula (PWN): multi-wavelength image of the Crab nebula. Credits: Radio: NRAO/AUI and M. Bietenholz; NRAO/AUI and J.M. Uson, T.J. Cornwell Infrared: NASA/JPL-Caltech/R. Gehrz (University of Minnesota) Visible: NASA, ESA, J. Hester and A. Loll (Arizona State University) Ultraviolet: NASA/Swift/E. Hoversten, PSU X-ray: NASA/CXC/SAO/F.Seward et al. Gamma: NASA/DOE/Fermi LAT/R . . . . .	83
3.2	The Crab pulsar light curves throughout the electromagnetic spectrum. The image is taken from <a href="#">Abdo et al. (2010)</a> . . . . .	84
3.3	Left: Pulse profile of the Crab pulsar for energies up to 400 GeV and beyond. Two rotational cycles are shown. The phase intervals of the two peaks are marked with yellow, off-pulse regions are marked with grey. Right: Phase-folded spectral energy density of the first peak P1 (filled black circle) and the second P2 (open blue circle). The power-law spectrum of P2 extends up to $\sim 2$ TeV, while P1 diminishes beyond 0.9 TeV. When comparing with the Crab nebula spectrum (open squares) at 1 TeV, one sees that the nebula energy flux is almost 3 orders of magnitude higher than that from the pulsar. For details, see <a href="#">Ansoldi et al. (2016)</a> . . . . .	85
3.4	Left: This image of the Crab nebula is the most detailed image to date. It was taken with the Hubble Space Telescope WFPC2 camera and assembled from 24 individual exposures, which presents the highest-resolution image of the entire Crab nebula ever made. Credit: NASA, ESA and Allison Loll, Jeff Hester (Arizona State University); acknowledgement: Davide De Martin (ESA, Hubble). Right: The composite image of the Crab nebula showing X-ray image from Chandra satellite in blue, visible light from Hubble in green and a VLA radio image in red. The pulsar is seen in the centre as a bright blue light. Image taken from <a href="#">Hester (2008)</a> . . . . .	86
3.5	Left: The full spectral energy distribution (SED) of the Crab nebula from radio band to the gamma rays. Lines represent the best fit results based on the theoretical models: thin lines represent the individual components of the electromagnetic spectrum, and the thick blue line is the overall emission. Right: SED of the Crab nebula only from the gamma-ray regime: MAGIC and <i>Fermi</i> -LAT data ( <a href="#">Aleksić et al., 2015</a> ). . . . .	87
3.6	Crab pulsar light curve for energies $E < 200$ GeV. Light curve is folded using monthly ephemeris publicly provided by the Jodrell Bank Observatory ( <a href="#">Lyne et al., 1993</a> ) covering MAGIC January observations. Two rotation cycles (green histogram) are shown for clarity. Two peak amplitudes (grey shaded area) are visible in the structure that correspond to the P1 and P2 emission: one around 0.0 (P1) and the other around 0.4 (P2). The black line is the constant background level derived from the off-region. . . . .	90

3.7	The spectral energy distribution of gamma-ray emission of the Crab nebula, obtained from the 9.5 hours of data observed with MAGIC telescopes in January 2015. Black data points represent this work (the upper limits indicated with black arrow) and agree well, within the systematic uncertainties, with the SED computed by H.E.S.S. (turquoise line) and within statistical uncertainties with previous MAGIC work (red dashed line, <a href="#">Albert et al., 2008b</a> ). . . . .	90
4.1	Pulsar spin-down rate $\dot{P}$ , versus the rotation period $P$ . Different pulsar classes are given in the legend and some ground-detected VHE pulsars and pulsar candidates are indicated in the Figure. Lines of constant characteristic age (blue), magnetic field strength (green) and spin-down luminosity (red) are displayed. Figure adapted from <a href="#">Abdo et al. (2013)</a> . . . . .	94
4.2	Pulse profiles of Crab, Vela, Geminga and PSR J2021+3651 (Dragonfly) produced after folding 5-years of <i>Fermi</i> -LAT data, where white, gray and black histograms denote events with energies $E > 100$ MeV, $E > 10$ GeV, $E > 25$ GeV respectively. Vertical dashed lines correspond to the on-peak, off-peak and bridge emission phase intervals for $E > 10$ GeV. Figure adapted from <a href="#">Burtovoi et al. (2017)</a> . . . . .	96
4.3	Left: 1.4 GHz radio pulse profile for Dragonfly pulsar, with the error bar representing $1\sigma$ uncertainty. Figure is taken from <a href="#">Roberts et al. (2002)</a> . Right: plot shows the polarization- and flux-calibrated profile for the same pulsar measured at Green Bank Telescope. The black line corresponds to the total intensity, the red to linear and the blue to circular polarization; polarization data imply magnetic inclination of $70^\circ$ , meaning that Dragonfly is close to the orthogonal rotator. Figure taken from <a href="#">Abdo et al. (2009a)</a> . Rotation and dispersion measure were determined from the radio observations and suggest a large distance of $\sim 12$ kpc. Later, optical data showed the distance was overestimated. For details see <a href="#">Kirichenko et al. 2015</a> . . . . .	97
4.4	Top frames: Dragonfly pulse profile for gamma rays with $E > 100$ MeV with <i>Fermi</i> -LAT; two rotation cycles are shown, the dashed line marks the average number of counts in the OFF region. Three following frames: light curves in specified energy ranges; second frame from the bottom: <i>Chandra</i> X-ray light curve; bottom frame: two radio profiles – upper obtained from Green Bank Telescope (1950 MHz) and the lower curve is the total intensity curve obtained from Arecibo. Figure adapted from <a href="#">Abdo et al. (2009a)</a> . . . . .	98
4.5	SED for PSR J2021+3651 from <i>Fermi</i> -LAT data: power-law spectrum with an exponential cutoff was assumed (for P1 – dotted, P2 – dot-dashed, Total pulse – solid). Figure adapted from <a href="#">Abdo et al. (2009a)</a> . . . . .	99
4.6	<i>Chandra</i> X-ray image of the axisymmetric Dragonfly nebula extending $20''$ and $10''$ with two ridges of emission from pulsar. Adapted from <a href="#">Etten et al. (2008)</a> . . . . .	99
4.7	<i>Chandra</i> X-ray images of Crab, Vela and Dragonfly nebula, for comparison. Credit: <a href="#">Kargaltsev et al. (2015)</a> . . . . .	100

4.8	VHE gamma-ray excess map of MGRO J2019+37 region (observed by VERITAS) above 600 GeV. Regions used for spectral analysis of VER J2019+368 (and the other sources) are defined by white dashed circles. The locations of possible counterparts are marked using different colours. The contour of significance ( $9\sigma$ ) of MGRO J2019+37 is overlaid in white. Two white “X” indicate the previous MAGIC wobble pointings (from July and August 2014) and two red “X” indicate newly proposed wobble pointing of 0.7 degrees offset from the camera centre. Adapted from <a href="#">Aliu et al. (2014)</a> . . . . .	101
4.9	Zenith angle distribution of Dragonfly data set taken from July to August 2014.	102
4.10	Light curves for Dragonfly pulsar obtained with the data from the MAGIC telescopes (this work) for different energy bands. Left to right: low-energy analysis ( $50\text{ GeV} < E < 200\text{ GeV}$ ), full $E_\gamma$ -range analysis ( $E \geq 200\text{ GeV}$ ). For clarity, two periods are shown. The bin width is 0.03, corresponding to $\sim 3$ ms of Dragonfly rotational period. The shaded area indicates positions of P1 (main pulse) and P2 (interpulse). No significant pulsed emission is detected. . . . .	104
4.11	Dragonfly SED for the pulsed emission of Dragonfly in terms of P1 (left), P2 (middle) and total pulse (right), respectively. The red line represents the SED computed using 4.5 years of <i>Fermi</i> -LAT data (analysis performed by T. Saito), assuming power law spectrum with the exponential cutoff. The blue line is a simple power-law fit to <i>Fermi</i> data above 10 GeV. The statistical error contour from the power-law fit is also plotted. The MAGIC analysis (this work) is done with the assumed spectral index of 4.0 (a simple power-law). The MAGIC upper limits are indicated with black arrows, where a line above an arrow indicates the bin width. . . . .	105
4.12	<i>Fermi</i> -LAT SED for Dragonfly pulsar (marked with black squares) combined with VERITAS differential flux upper limits (H-Test limits: red arrows, Rolke limits: blue arrows). With black solid line 1% Crab Nebula emission is noted, and grey area marks the Crab pulsar SED. Figure from <a href="#">Archer et al. (2019)</a> . . .	106
4.13	The SED of Dragonfly P2 (red) and Geminga P2 (blue) above 100 MeV obtained from <i>Fermi</i> -LAT data. . . . .	107
4.14	Expected Dragonfly’s SEDs produced from the official tool – MAGIC Source simulator for the MAGIC observations (left) and for the CTA (LST) observations (right). The assumed spectrum is a power-law with spectral index of 3.5. The simulator estimates 200 hours of observations are needed for Dragonfly pulsar detection with the MAGIC telescopes, that is 110 hours of CTA with the LST observations. . . . .	108
4.15	Distribution of squared angular distance $\theta^2$ between the direction of gamma-ray events and the source position where the applied $\theta^2$ – cut is $0.09\text{ deg}^2$ (vertical dashed line). The source position is obtained from skymaps and is found to be RA: $(20.3156 \pm 0.0067)\text{h}$ and Dec: $(36.8672 \pm 0.0776)^\circ$ . The distribution of $\theta^2$ for OFF positions is the grey-filled histogram. There is also a negative excess in $\theta^2$ -range above $0.2\text{ deg}^2$ which is the result of unsuitable wobble position, intended for a point source (pulsar observations) and not for the extended source (nebula). . . . .	109

- 
- 4.16 Dragonfly nebula Test Significance (TS) maps representing signal significance computed for the source location (grey star), for energies  $100 \text{ GeV} < E < 300 \text{ GeV}$  (left) and above  $5 \text{ TeV}$  (right). The position of the pulsar is indicated by a magenta square, VERITAS coordinates are indicated by the green cross and grey star indicates this work. The white circle indicates the point spread function. 110
- 4.17 Dragonfly nebula Test Significance (TS) maps representing signal significance computed for the source location (grey star), for energies above  $500 \text{ GeV}$  (left) and above  $1 \text{ TeV}$  (right). For both energy ranges significance is around  $6\sigma$ . Position of the pulsar is indicated by a magenta square, VERITAS coordinates are indicated by the green cross and grey star indicates this work. The white circle indicates the point spread function. . . . . 111
- 4.18 Dragonfly nebula gamma-ray flux map in arbitrary units for events with estimated energies above  $500 \text{ GeV}$  (left) and above  $1 \text{ TeV}$  (right). Overlaid are test statistic value contours in steps of 1, starting at 3, where the numbers approximately correspond to Gaussian significances. At the bottom-left the instrumental PSF is indicated (after smearing). . . . . 111
- 5.1 Left: VHE gamma-ray image of HESS J1858+020 and a larger nearby source J1857+026. Right: The HESS significance contours (black) and X-ray contours (green) overlaid on a radio image (grey-scale). Figures are taken from [Aharonian et al. \(2008\)](#). . . . . 115
- 5.2 Radio image (black contours) of the field containing the unidentified HESS J1858+020 obtained with GMRT at  $610 \text{ MHz}$ . The HESS significance contours ( $4.5\sigma$  and  $6\sigma$  in magenta) are overlaid. The red circles correspond to X-ray sources. Distinct radio sources are marked with R1,... R5, respectively. The shell-like structure of SNR G35.6-0.4 is visible in the upper right region of the Figure. *Fermi*-LAT gamma-ray source 2FGL J1857.6+0211 is marked with a blue ellipse. Three nearby pulsars are marked with the yellow crosses. Figure adapted from [Paredes et al. \(2014\)](#). . . . . 116
- 5.3 Infrared image obtained from Spitzer-IRAC ( $8\mu\text{m}$ ) of the area around SNR G35.6-0.4 with contours of radio continuum emission at  $20 \text{ cm}$ . The circle represents the position and the extension of HESS J1858+020. SNR is possibly partially superimposed over the HII region. For details, see [Paron et al. \(2011\)](#). 117
- 5.4 MAGIC observations of HESS J1857+026 (left) and W44 (right) where HESS J1858+020 is in the field of view of MAGIC camera. Different wobble positions of the MAGIC camera are marked with different colours and shapes. . . . . 119
- 5.5 Left: *Fermi*-LAT  $\gamma$ -ray count map for  $2\text{-}100 \text{ GeV}$  in units of counts per pixel in celestial coordinates (J2000) showing SNR W44 and its surrounding area. Right: The difference between the count map (left) and the best-fit model which includes diffuse emission, other sources, and SNR W44 represented by the radio map). SRC-1 and SRC-2 are areas of  $\gamma$ -ray excess emission, located in the vicinity of W44 (green contours represent a  $10 \text{ GHz}$  radio map of SNR W44). Figure is taken from [Uchiyama et al. \(2012\)](#). . . . . 121

5.6	<i>Doughnut</i> Monte Carlo produced for the HESS J1858+020 source. MC were adjusted for the assumed extension of the source, which is taken from <a href="#">Aharonian et al. (2008)</a> to be 0.08 deg. This particular MC is produced for the period ST0302 and for the wobbles with the same and similar distances from the camera centre (wobble positions 270, 260, 170 and 180). . . . .	123
5.7	Detection of the HESS J1858+020 (this work). Left: Test statistic (TS) value map (full $E_\gamma$ -range $E > 200$ GeV). TS value of the fitted position is $9.67\sigma$ . The source HESS J1858 is marked with the grey star (this work); Right: gamma-ray flux skymap (in arbitrary units) showing morphology of HESS J1858+020. Fitted source extension is $0.08 \pm 0.03$ deg. Overlaid TS contours start at $5\sigma$ and are in steps of $2\sigma$ and roughly correspond to Gaussian significances. In the bottom-left the instrument's PSF (0.05 deg) is shown along with the applied smearing kernel of the same value which gives the total PSF=0.071 deg . . . .	124
5.8	Distribution of squared angular distance $\theta^2$ between gamma-ray events and the position of HESS J1858+020 where the applied $\theta^2$ -cut is $0.03 \text{ deg}^2$ (black vertical dashed line). The distribution of $\theta^2$ for OFF positions is a grey-filled histogram. The normalization range used for the background estimation is $(0.06 - 0.12) \text{ deg}^2$ . There is a signal enhancement at $\theta^2 > 0.14 \text{ deg}^2$ due to a neighbouring bright source, HESS J1857+026. . . . .	124
5.9	The migration matrix shows the relation between the reconstructed and the true energy. For the points above 10 TeV, MC statistics is too low: the real data in the $E_{est}=20$ TeV bin would contain events with real energy above 30 TeV, which is not simulated. The estimated flux would contain a systematic error. . .	125
5.10	Spectral energy distribution of HESS J1858+020 obtained from MAGIC data (this work, green dots with power-law fit marked with green solid line). MAGIC measured the spectrum between 300 GeV and 10 TeV. SED from HESS ( <a href="#">Aharonian et al., 2008</a> ) of the same source with a power-law fit (blue solid line) is included for comparison. . . . .	126
5.11	The SED of HESS J1858+020. Blue, black and red dots show the hard (SrcX2) and soft <i>Fermi</i> -LAT (SrcX1) and HESS GeV observations, respectively. The solid green line is the joint fit for the <i>Fermi</i> -LAT data of SrcX2 and HESS data of HESSJ1858+020. Figure is taken from <a href="#">Cui et al. (2021)</a> . . . . .	128
6.1	The LOFAR stations across Europe (left) and LOFAR's central station, the so-called "superterp" (right). Images taken from <a href="https://science.astron.nl/">https://science.astron.nl/</a> . . . . .	132
6.2	Calculated $RM_{ion}$ corrections given at 30-minute intervals for different observations using the satellite-based TEC measurements and the global geomagnetic field model. The observed decrease of $RM_{ion}$ during each nighttime observation is due to recombination of plasma in the ionosphere, which happens after the sunset and decreases the TEC throughout night. . . . .	137
6.3	Noise in Stokes QU data cubes for observations from Cycle 2 (top plot) and Cycle 4 (bottom plot) as a function of frequency. Cycle 4 data are much more affected by broad RFI than Cycle 2 data, due to DABs and DVBS. . . . .	138

- 
- 6.4 RMSF for 10 observations in Cycle 2 (dashed) and 11 observations in Cycle 4 (solid line) of the ELAIS-N1 field. . . . . 140
- 6.5 Image of the highest peak of the Faraday depth spectrum in the polarized intensity (left) and a corresponding image of a Faraday depth of the highest peak (right) for the observation with the lowest noise (014, the reference observation for Cycle 2). The blue circle in the left image marks a randomly chosen location for which a Faraday spectrum is presented in Fig. 6.6. . . . . 143
- 6.6 Left panel: Example of a Faraday spectrum given in the polarized intensity for the 009 observation (blue line) and the reference (014) observation at a randomly chosen location marked with a blue circle in Fig. 6.5 (RA  $242^{\circ}18'03.60''$  and Dec  $56^{\circ}08'16.80''$ ). Right panel: Calculated modulus of the complex cross-correlation function  $|\zeta|$  (red line) for the given Faraday spectra, fitted with a Gaussian (blue dashed line) to estimate the misalignment between the two observations (black vertical line) at this specific location. . . . . 144
- 6.7 Calculated modulus of the averaged complex cross-correlation function for observations 009 and 014 (solid magenta line) and variations of the cross-correlation function across the field of view as measured by a standard deviation (dashed cyan line). A misalignment between two observations is determined by fitting a Gaussian to the peak (solid yellow line). . . . . 145
- 6.8 Example of an image in Faraday cube given in the polarized intensity at  $-2.25 \text{ rad m}^{-2}$  for the 011 observation (left image), which is not properly corrected for the  $RM_{\text{ion}}$ . There is almost no emission visible in comparison to the reference (014) observation (middle image), whose image is given at  $-3.25 \text{ rad m}^{-2}$  to account for a relative misalignment of  $+1.0 \text{ rad m}^{-2}$  between the two observations. The polarized emission is visible in the restored Faraday cube of the 011 observation (right image), which is corrected using the estimated  $\Delta\Phi_{\text{shift}}$  given in Fig. 6.9. . 146
- 6.9 Estimated relative shifts in Faraday depth ( $\Delta\Phi_{\text{shift}}$ ) of each 10-minute interval of the 011 observation with respect to the full eight-hour reference (014) observation (thick solid black line). The calculated  $RM_{\text{ion}}$  corrections based on the satellite TEC measurements are plotted with thick dashed black line. The thin solid colored lines give the  $\Delta\Phi_{\text{shift}}$  in the field of view quadrants. . . . . 147
- 6.10 Primary beam uncorrected Faraday spectrum at a location of a polarized source (ID 01 in [Herrera Ruiz et al., 2021](#)) in the high-resolution restored (solid black line) and unrestored (solid cyan line) Faraday cube of the 011 observation. The source should be present at Faraday depth of  $+(9.44 \pm 0.03) \text{ rad m}^{-2}$  (red vertical line), as reported by [Herrera Ruiz et al. \(2021\)](#). . . . . 148
- 6.11 Number of observations per frequency channel used in the stacked data cube from Cycle 2 (upper plot) and Cycle 4 (lower plot) data. Although the data cover the same frequency range, they have different frequency configurations and hence a different number of frequency channels (see Sec. 6.2.1). . . . . 150



6.12	Example of a successful (upper panels) and an unsuccessful detection of a polarized source (lower panels) in the presented Faraday cubes (sources with ID 10 and 07 in <a href="#">Herrera Ruiz et al., 2021</a> , respectively). Polarized intensity images in the reference (014, left images) and in the final stacked Faraday cube (middle images) are given at the closest available Faraday depth, such as that of the source. The location of the source in each image is marked with the red circle, while the corresponding Faraday spectra are given in plots on the right. A reported Faraday depth of the sources by <a href="#">Herrera Ruiz et al. (2021)</a> are marked with vertical red lines. . . . .	151
6.13	Images of the ELAIS-N1 field in the polarized intensity given at Faraday depths of -15.0, -10.0, -5.0, -3.0, -1.0, +1.0, +3.0, +5.0, +7.0, +10.0, +12.0 and +16.0 $\text{rad m}^{-2}$ of the final stacked Faraday cube. The cube is based on $\sim 150$ hours of the LOFAR observations in the frequency range from 114.9 to 177.4 MHz. Angular resolution of the images is $4.3'$ . These are primary beam uncorrected images with the noise of $27 \mu\text{Jy PSF}^{-1} \text{ RMSF}^{-1}$ . . . . .	154
6.14	Moments of the reference (014) (upper images) and the final stacked Faraday cube (lower images). The left images give $M_0$ , the middle ones show $M_1$ , and the right images give $\sqrt{M_2}$ . . . . .	155
6.15	Examples of the faint Galactic polarized emission, which is only clearly detected in the final stacked Faraday cube. The images are given in the polarized intensity at Faraday depths of +14.5 (upper images) and +16.25 $\text{rad m}^{-2}$ (lower images) for the reference (left images) and the final stacked cube (middle images). The corresponding Faraday spectra at a location of the red circle in the images are given in plots on the right. . . . .	156
6.16	The total Galactic RM in the area of the ELAIS-N1 field, extracted from the publicly available the Galactic Faraday Sky map by <a href="#">Hutschenreuter et al. (2022)</a> . . . . .	158

# List of Tables

4.1	Comparing Dragonfly pulsar with all four ground-detected VHE gamma-ray pulsars and their main characteristics: pulsar period (in milliseconds), distance in kiloparsec, age in kiloyears, spin-down luminosity ( $dE/dt$ ) in $\text{ergs}^{-1}$ and magnetic field strength in Gauss where $1 \text{ erg} = 1 \times 10^{-7} \text{ Joules}$ , $1 \text{ T} = 1 \times 10^4 \text{ Gauss}$ , $1 \text{ kpc} = 3261.5 \text{ ly}$ , $L_{\text{Sun}} = 3.846 \times 10^{33} \text{ ergs}^{-1}$ . . . . .	94
4.2	Significance computed for the signal regions P1, P2 and the sum of both peaks for the Dragonfly pulsar. The significances were computed using Li&Ma ( <a href="#">Li &amp; Ma, 1983</a> ). . . . .	104
4.3	Dragonfly’s spectral parameters corresponding to figure 4.11 obtained from <i>Fermi</i> -LAT and MAGIC data. For energy range from 0.1 – 100 GeV, power law spectrum with the cutoff was assumed: $dF/dE = F_0(E/E_0)^{-\Gamma} \exp(-E/E_c)$ with $E_0=868 \text{ MeV}$ (upper table). For energy range above 10 GeV, simple power law was assumed: $dF/dE = F_0(E/E_0)^{-\Gamma}$ with $E_0=20 \text{ GeV}$ (lower table). . . . .	105
5.1	Target sources with their coordinates and observational dates . . . . .	120
5.2	Distance (in degrees) between the MAGIC camera centre and the HESS J1858+020 source at 8 different wobble positions intended for W44 observations. . . . .	122
5.3	Distance (in degrees) between the MAGIC camera centre and the HESS J1858+020 source at 8 different wobble positions intended for HESS J1857+026 observations. . . . .	122
5.4	Point Spread Function (PSF) of the MAGIC telescope for the corresponding observational periods. . . . .	123
6.1	ELAIS-N1 observations. The table is marked with the following columns (i) ID - Internal ID code of the data set; (ii) LOFAR observation ID - standard LOFAR ID; (iii) Cycle - observing LOFAR cycle; (iv) Date - Date and time of the beginning of the observations; (v) Obs. time - Duration of the observations in seconds. The Figure is taken from ( <a href="#">Sabater et al., 2021</a> ). . . . .	136
6.2	Calculated noise in the Faraday cubes given for different observations and their relative shift in Faraday depth ( $\Delta\Phi_{\text{shift}}$ ) with respect to the reference observation (calculated in Sec. 6.3). An ID of each observation corresponds to the one given in Table 1 in <a href="#">Sabater et al. (2021)</a> . . . . .	141

# Chapter 1

## Introduction

A pulsar, remnant star of a core-collapse supernova, is an ultra-dense, rotating, magnetized neutron star that emits beams of radiation, from radio to very high energy gamma rays. If pulsar's emitted beams of radiation sweep over Earth, its emission will be detected as pulses - like a lighthouse effect. Predominantly, pulsars are detected in the radio band where over 2900 pulsars are found, but they are also detected in other wavebands, mainly in high energy (HE,  $E > 100\text{ MeV}$ ) gamma rays. Before 2008, there were only 7 HE gamma-ray emitting pulsars known and with the emergence of the *Fermi*-Large Area Telescope, that number climbed to the current 250 (and increases every year). The *Fermi*-LAT pulsars were all showing similar behaviour, exhibiting an exponential cutoff in their spectra around the GeV range. Yet, there were no pulsars detected, by the ground-based instruments, in the very high energy band (VHE,  $E > 100\text{ GeV}$ ) for a long time ([Breed et al., 2016](#)). Therefore, it was a long-held assumption that pulsars do not radiate in VHE gamma-ray band. The energy gap between satellite's upper threshold and Cherenkov telescopes' lower energy threshold, present at that time, contributed to the expectation that pulsars do not emit at VHE. Only after lowering the energy threshold, ground-based MAGIC telescopes discovered VHE pulsed emission from the Crab pulsar which marked the first such pulsar to be found, initiating a hunt for other VHE gamma-ray pulsars. With the detection of Crab pulsation above 400 GeV, and later even above 1 TeV, with no sign of an exponential cutoff like in all *Fermi*-LAT pulsars, revision of theoretical models was required to explain the VHE emission from this pulsar. While most of the emission models assumed the pulsed gamma-ray emission is due to the curvature radiation, Crab pulsar observations at VHE refute this scenario. Much later, three more pulsars were detected at VHE and the aim is to detect many more pulsars in VHE gamma rays to be able to use statistical methods and thus better characterize the fundamental properties of these objects and the acceleration mechanisms involved.

Most of the rotational energy from a pulsar is carried away by the relativistic particles, which interact with the ambient medium and produce powerful pulsar wind nebula (PWN). Only a percentage of that energy is in the form of the pulsed electromagnetic emission. Both pulsars and pulsar wind nebulae (PWNe) emit VHE gamma rays, but in contrast to pulsars which are rarely detected in VHE gamma rays, PWNe are the largest population of firmly identified galactic TeV sources. A nebula can be considered as a dynamical object around the pulsar, that keeps and displays the pulsar-powered output while at the same time going through its evolutionary phases inside the host supernova remnant (SNR). From the recent population study, it appears that young and energetic pulsars grow powerful PWNe.

By studying gamma rays, we can study the parent particles which produced the observed gamma rays, and these are very energetic charged particles - cosmic rays (CR). Combining multi-wavelength data is a tool for understanding the complete picture of all processes involved around one astrophysical source, which allows us to inspect populations and interactions of high energy particles. For example, high energy photons are produced by particles of even higher energies. In the vicinity of magnetic fields, these relativistic particles emit photons of different energies, from radio to gamma rays via different emission mechanisms: synchrotron, Compton scattering, Bremsstrahlung, pion production and decay. In recent times, the multi-messenger approach is also used, as some of the sources emit other messenger particles except photons and CR, like neutrinos or gravitational waves.

In this Thesis, in the following introductory Section 1.1, I will address the problem of the origin of galactic cosmic rays and the role of gamma rays as a powerful tracer of this particle population. One possible way how particles gain tremendous energies that we observe is via diffusive shock acceleration mechanism, assumed to be the best theory yet to explain the spectrum of the relativistic particles. In Section 1.2 production mechanisms for gamma rays will be explained, then in Section 1.3 I will introduce all known classes of galactic and extra-galactic VHE gamma-ray sources. Section 1.4 introduces detection techniques for high and very high gamma rays and differences among them. Pulsars, their discovery, and characteristics with basic pulsar emission models are described in Section 1.5. Basic overview of pulsar wind nebulae and supernova remnants are described in Sections 1.6 and 1.7, respectively. Last Section 1.8 is an overview of the major goals of this Thesis.

## 1.1 Cosmic rays

Particle astrophysics (or astroparticle physics) combines physical phenomena at the smallest and the largest scales of the Universe. The relevant discoveries in particle physics will imme-

diately affect our understanding of the Universe, and cosmological findings will alter particle theories. One of the unsolved questions in this field is: “what is the origin of cosmic rays?”. The doors of astroparticle physics were unintentionally opened by Victor Hess<sup>1</sup> in 1912. Using a charged electroscope onboard the ascended balloon, he discovered a special type of radiation that enters the Earth’s atmosphere from above. This discovery was confirmed by R. Millikan, who proved that these particles had an extraterrestrial origin, naming them cosmic rays (CR). These relativistic particles are deflected on their path to the Earth due to interaction with the magnetic field in the interstellar medium, which can cause the loss of information about their origin. However, their very high energies exceed those associated with typical stellar processes, indicating that these particles are messengers of the non-thermal Universe. Non-thermal particle population, like CRs, is (considered to be) produced by a collective mechanism, where the energy outflow is focused from the source onto a relatively small number of particles. The energy spectrum of cosmic rays (see Fig. 1.1) is measured by several detectors and shows how the rate changes with increasing energy.

Arriving from outside our atmosphere, CRs are charged particles, where 99% are the atomic nuclei and about 1% electrons. About 90% of the nuclei are protons (hydrogen nuclei), 9% are alpha particles (helium nuclei) and about 1% are the nuclei of heavier elements. The CRs cover a wide range of energies, from  $10^8$  up to  $10^{21}$  eV. Depending on their energy, they can be detected either directly or indirectly. While the balloon experiments and satellites are used to directly measure CRs with energies up to  $10^{14}$  eV, ground-based experiments are used to indirectly study CRs of higher energies. Indirect methods imply observations of Extended Air Showers (EAS) where a cascade of secondary particles are produced when a primary CR enters the Earth’s atmosphere and interacts with its molecules.

A spectrum of the CRs extends over a wide range of energies, as shown in Fig. 1.1. The spectrum can be approximated by a simple power law,  $dN/dE \propto E^{-\Gamma}$ , with different indices for different energy ranges. At the energy of  $\sim 10^{15}$  eV, there is a steepening in the spectrum, named *the knee*, where a photon index changes the value from  $\Gamma \sim 2.7$  to  $\sim 3.1$ , apparently due to the changes in the chemical composition of CR (heavy nuclei dominated). Another feature in the spectrum, called the *ankle*, is found between  $10^{16}$  and  $10^{18}$  eV and is followed by the spectral flattening with  $\Gamma \sim 2.6$ . Particles covering the spectrum up to the *knee* are thought to be accelerated within our Galaxy and the ones above the *ankle* could have an extra-galactic origin, while the origin of particles with energies between the knee and ankle is still poorly understood. The Greisen-Zatsepin-Kuzmin (GZK) cutoff occurs at energies above  $10^{20}$  eV, and presents a

---

<sup>1</sup>V. Hess was awarded the Nobel Prize for the discovery of cosmic rays in 1936, together with C. Anderson, who discovered the positron and the muon in the cosmic rays.

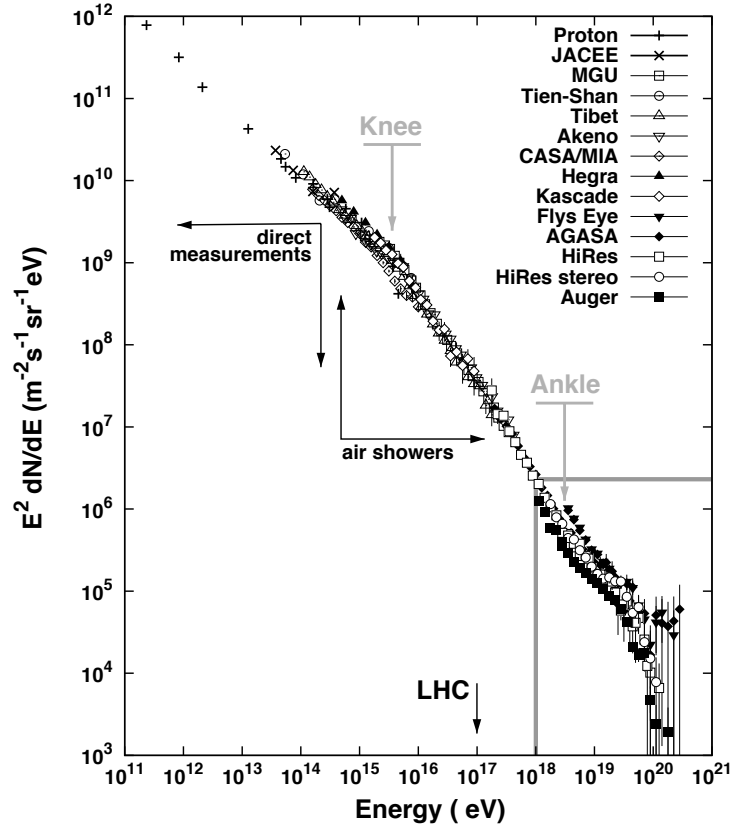


Figure 1.1: The spectrum of cosmic rays measured by several ground-based experiments, as indicated in the legend. The position of the spectrum’s characteristics, knee and ankle, are indicated with the arrows, as well as the equivalent laboratory LHC’s energy. The figure is taken from [Letessier-Selvon & Stanev \(2011\)](#).

sharp steepening of the spectrum caused by the pion photoproduction due to protons interacting with the Cosmic Microwave Background (CMB) field,  $p + \gamma_{CMB} \rightarrow \pi + p$ .<sup>2</sup>

### 1.1.1 The origin of Galactic cosmic rays

The widely accepted SNR paradigm states that the bulk of CRs is accelerated in SNRs in our Galaxy, i.e., SNRs are the main sources of galactic cosmic rays. There is increasing evidence to support this theory, with the most important being the possibility to explain the composition of CRs at the Earth by the acceleration of the interstellar medium (ISM) around the SNRs, the detection of the strong magnetic fields in supernova shock waves and the detection of HE and

<sup>2</sup>Theoretically, extra-galactic CR which are located more than 50 Mpc from the Earth and with energies above the GZK limit shouldn’t be observed on Earth.

VHE gamma rays emitted by SNRs. As previously mentioned, in the interaction of relativistic particles, gamma rays are produced as well. However, there are still several questions that need to be answered before accepting the SNRs as the main sites of CR creation. One such question is whether the SNR can accelerate protons and ions up to PeV energies, i.e., to the *knee* of the CR spectrum, for details see [Blasi \(2013\)](#). It is believed that charged particles are accelerated at a supernova shock wave via diffusive shock acceleration (DSA), also known as the Fermi acceleration ([Fermi, 1949](#)). The acceleration of the charged particle happens when the particle is repeatedly reflected, usually by a magnetic mirror<sup>3</sup>. There are two types of Fermi acceleration mechanism, namely the first and the second order Fermi acceleration:

**Second order Fermi acceleration** is a mechanism in which particles interact with moving magnetized clouds in the interstellar medium and are elastically reflected by magnetic mirrors. The clouds move randomly with velocity  $\beta = V/c$ , and the reflections increase the energy of the particles, but the average energy gain in one reflection is only second order in  $\beta$ :

$$\left\langle \frac{\Delta E}{E} \right\rangle \propto -\beta^2 \quad (1.1)$$

There is a maximum energy,  $E_{\max}$  that accelerated CR can gain this way:

$$E_{\max} = ZqBR, \quad (1.2)$$

where  $q$  is the electric charge of the particle,  $B$  is the magnetic field,  $R$  is the size of the accelerator region and  $Z$  is the atomic number of the particle. There is a geometrical criterion, the Hillas criterion, ([Hillas, 1984](#)) for all types of cosmic ray sources where for the Larmor radius of the particle is  $R_L = E_{\max}/(ZqB) \leq R$ . If the particle escapes the acceleration region, it will not be able to gain more energy. The energy spectrum of particles limited by this criterion is strongly dependent on the magnetic properties of the magnetized interstellar cloud serving as a magnetic mirror and cannot explain the observed CR spectrum ([Longair, 2011](#)).

**First-order Fermi acceleration mechanism** was proposed to better explain the CR energy spectrum. Within this mechanism, the CR particles gain energy through interaction with the changing magnetic field of shock waves. Shock waves are lumps of material with a velocity greater than the speed of sound in the medium through which they travel. These waves have moving magnetic inhomogeneities preceding and following them. When a charged particle travels through the shock wave (from the unshocked region, i.e., upstream, to the shocked region, i.e., downstream, see [Fig. 1.2](#)) and encounters a change in the magnetic field, it will move back

<sup>3</sup>A magnetic mirror is a static magnetic field that, within a localized region, has a shape such that approaching charged particles are repelled back along their path of approach.

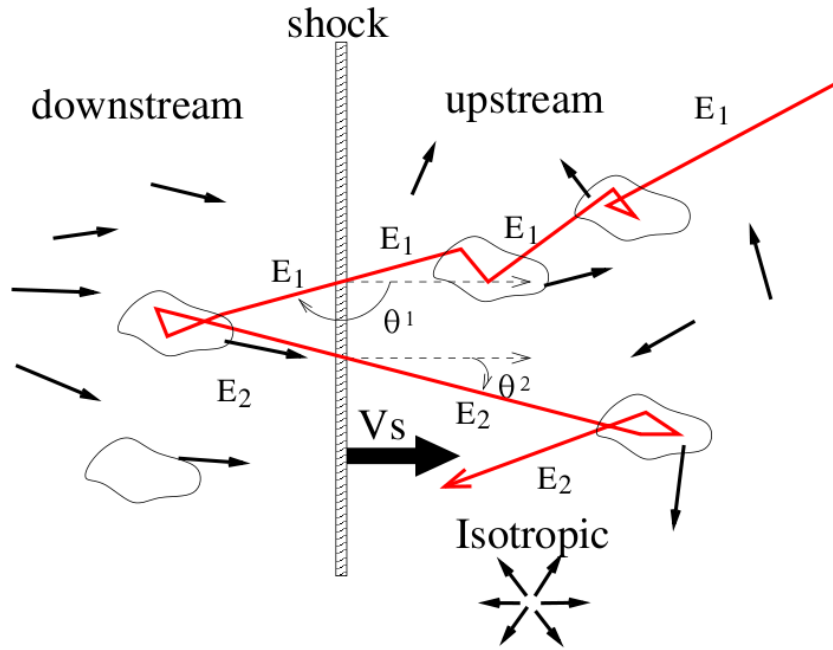


Figure 1.2: The first-order Fermi acceleration: when a charged particle crosses a shock front, it encounters a change in the magnetic field, which reflects it back through the shock wave at greater velocity. Credit: [Saito \(2011\)](#).

through the shock (downstream to upstream) at increased velocity. If multiple reflections occur, the result will be a significant increase in the energy of a particle. The energy gained by the particle depends linearly on the velocity ratio  $\beta = v_s/c$ , where  $v_s$  is the speed of the shock wave and  $c$  is the speed of light. The resulting energy spectrum of particles undergoing this process is a power-law:

$$\frac{dN(E)}{dE} \propto E^{-p}, \quad (1.3)$$

where the spectral index  $p \geq 2$  depends solely on the compression ratio<sup>4</sup> of the shock. This mechanism is much more efficient than the second-order Fermi acceleration, and it correctly predicts a power-law spectrum. Furthermore, this is considered to be the main mechanism for particles to reach the observed non-thermal energies in astrophysical shock waves. The current problem of this theory is the injection problem: only particles with energies much higher than the thermal energies can cross the shock front in the first place and begin the acceleration

<sup>4</sup>At the shock, waves are subjected to compression, so shock compression ratio is defined as  $p = U_1/U_2$ , where  $U_1, U_2$  are plasma velocities in the shock rest frame for upstream (1) and downstream (2) region, respectively.



process, and thus it is unclear what mechanism causes these particles to have such high energies. For details on particle acceleration by astrophysical shocks, see [Longair \(2011\)](#); [Blandford & Ostriker \(1978\)](#).

## 1.2 Production mechanisms of gamma rays

Very high energy photons are produced by radiative or collisional processes. For example, the interaction of cosmic rays (electrons, protons, or ions accelerated by the shock wave in the vicinity of some astrophysical source) with the nuclear targets (like in a molecular cloud) or radiation fields (magnetic or photon fields) will result in the production of gamma rays. Gamma rays can be produced either in leptonic or in hadronic processes. In hadronic processes, photons are secondary products of interactions. Models involving hadronic processes provide a direct link between high energy photons, the acceleration of cosmic rays and the production of neutrinos. Thus, the detection of neutrinos, which are also neutral and point towards the source, is a unique proof of hadronic acceleration.

### 1.2.1 Leptonic gamma-ray production mechanisms

Electrons accelerated to high energies can radiate high-energy photons through a variety of quantum electrodynamical processes, with synchrotron and inverse Compton radiation being the most common in astrophysical scenarios.

- **Synchrotron radiation**, also known as a **magnetobremssstrahlung**: the emission of high energy electrons in the magnetic field. This radiation is the main contributor to the radio emission of our Galaxy and extra-galactic radio sources. It is a non-thermal emission indicating a distribution of particles with a non-Maxwellian continuous energy spectrum. In a uniform static magnetic field  $\mathbf{B}$ , a charged particle moves with a constant speed along the magnetic field lines in a circular motion with constant pitch angle  $\alpha$ , which is the angle between the velocity vector and the field vector. For the non-relativistic case ( $v \ll c$ ), an electron (mass  $m_e$ , charge  $e$ ) emits energy at the non-relativistic gyro-frequency  $\nu_L = eB/2\pi m_e$ , called Larmor frequency, and the emission is called cyclotron emission. In the ultra-relativistic limit ( $v \approx c$ ) there is a spread of emitted frequencies in the observer's frame of reference (due to Doppler and aberration effects) thus the radiation becomes continuous and is called synchrotron. In this case, the gyro-frequency  $\nu_L$  is reduced to a value  $\nu_g$  by the relativistic factor<sup>5</sup>  $\gamma$ :  $\nu_g = \nu_L / \gamma = \nu_L (1 - \beta^2)^{1/2}$ . In other

---

<sup>5</sup>Relativistic or Lorentz factor expresses the amount by which a physical property of an object changes due to

words, a single electron gyrating perpendicular to the magnetic field and is observed in the plane of its orbit radiates an electric field. This field consists of pulses that are produced while the electron travels towards the observer. The duration of the pulse is of the order  $\delta t \sim 1/(\nu_g \gamma^3)$  and the characteristic frequency  $\nu_c$ , at which the spectrum is concentrated, is the inverse of the pulse duration:  $\nu_c \sim \gamma^3 \nu_g \sim \gamma^2 \nu_L$ . The total energy loss rate due to synchrotron emission is:

$$\frac{dE_{sync}}{dt} \propto -B^2 \gamma^2 \sin^2 \alpha, \quad (1.4)$$

where  $B$  is magnetic field strength,  $\gamma$  is a relativistic factor and  $\alpha$  is a pitch angle.

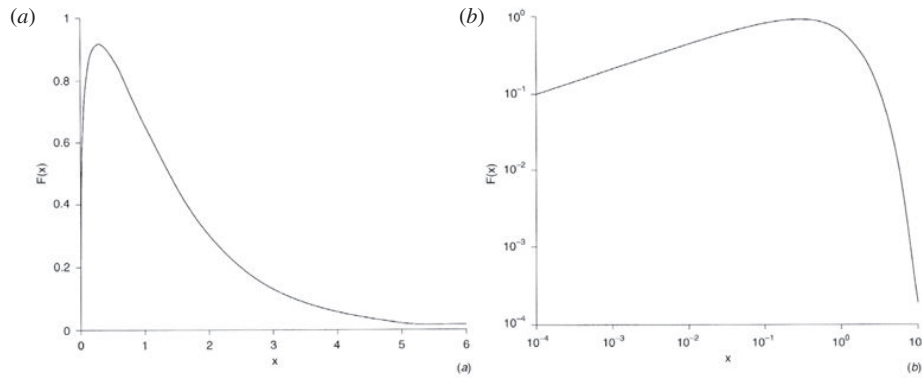


Figure 1.3: The spectrum of the synchrotron radiation, expressed as the total power radiated in all directions, is shown on linear (a) and logarithmic (b) scales. Figure taken from Longair (2011).

The spectrum of synchrotron radiation is shown in Figure 1.3. The maximum intensity is at frequency  $\nu_m$ , which is at approximately  $\nu_c/3$ . Below this frequency, the spectrum is a power-law proportional to  $\nu^{1/3}$  and above  $\nu_m$  falls exponentially as  $\exp(-\nu/\nu_c)$ . The total radiated power for a particle of energy  $E$  in a field  $B$  at the frequency  $\nu$  is:

$$P(\nu) = 4 \times 10^{-22} B \left( \frac{\nu}{\nu_c} \right)^{1/3} \exp\left(-\frac{\nu}{\nu_c}\right) \text{erg s}^{-1} \text{Hz}^{-1}, \quad (1.5)$$

The main characteristic of synchrotron radiation from astrophysical sources is a non-thermal power-law broadband spectrum (from radio to X-rays).

- **Curvature radiation:** in the environments like pulsar magnetosphere, which will be described in detail in Sec. 1.5, magnetic fields are especially strong ( $10^{11} - 10^{13}$  G), thus

---

its relativistic motion.

an electron/positron may be constrained to follow magnetic field lines, with a pitch angle nearly zero. In this case, the field line will generally be curved so the electron/positron is accelerated and will radiate. This radiation is similar to synchrotron radiation and is called curvature radiation. A necessary condition for the emission of this radiation are ultra-relativistic velocities of particles in the pulsar magnetosphere, which are obtained by strong electric fields induced by the rotation of a pulsar. These high energy particles follow a path with radius  $\rho$  and then radiate with gyro-frequency  $c/2\pi\rho$ . There is also a critical frequency  $\nu_c$ , like in synchrotron radiation, given by

$$\nu_c = \frac{3c}{4\pi\rho}\gamma^3, \quad (1.6)$$

where  $c$  is the speed of light,  $\rho$  is the radius of curvature and  $\gamma$  is a relativistic factor. The spectrum is also similar to the synchrotron: below  $\nu_c$  it follows a power-law  $\nu^{1/3}$ , while above  $\nu_c$  it falls exponentially. Therefore, the combination of high energy particles and small curvature radii of magnetic field lines near pulsar surface gives away high power of curvature radiation which is sufficient to explain X-ray and lower part of gamma-ray emission. Optical and radio emission, which have very high brightness temperature, could be explained by coherent emission mechanism<sup>6</sup>.

When an ensemble of electrons/positrons is considered, not just a single charged particle, particle energies are distributed as a power law with index  $s$ ,  $N(E) \propto E^s$  and the spectrum will follow a power-law as well,  $P(\nu) \propto \nu^\alpha$ , with the spectral index  $\alpha = (1 - s)/2$ . In the case of curvature radiation, this relation between particle energy spectrum and the spectral index of the radiated spectrum is given by  $s = 1 - 3\alpha$  instead of  $s = 1 - 2\alpha$  (Lyne & Graham-Smith, 2012).

- **Inverse Compton scattering:** in the classical Compton scattering, high-energy photons scatter on the low-energy electrons and emerge from the scattering with longer wavelengths. Inverse Compton scattering is the opposite process that involves the energy transfer from high-energy electrons to radiation. Specifically, the ultra-relativistic electron scatters a low energy photon of energy  $\epsilon$  to high energy photon with energy  $\epsilon'$  ( $\epsilon' > \epsilon$ ), where the energy gain is at the expense of kinetic energy of the electron. The maximum transfer of energy happens for head-on collisions of the photon and the electron. Photon energy after the scattering ( $\theta = 0$ , where  $\theta$  is the angle of incidence) is:

---

<sup>6</sup>Coherent emission cannot be explained in terms of individual particles which radiate independently of each other

$$\epsilon' = \frac{4\epsilon\gamma^2 m_e c^2}{m_e c^2 + 4\epsilon\gamma}, \quad (1.7)$$

where  $m_e$  is the rest mass of the electron,  $\gamma$  is the Lorentz factor. In the Thomson limit ( $\gamma\epsilon \ll m_e c^2$ ), the maximum energy of the scattered photon is  $\epsilon' \sim \gamma^2 \epsilon$  and in this case, the electron gradually loses energy. On the other hand, in Klein-Nishina limit ( $\gamma\epsilon \geq m_e c^2$ ) the maximum photon energy is  $\epsilon' = \gamma m_e c^2$ , thus the photon scatters and carries off most of the electron's energy in a single scattering process (Longair, 2011). The electron energy distribution is described with a power-law spectrum with a spectral index  $p$ , which after Inverse Compton scattering results in a power-law energy spectrum of photons with index  $(p-1)/2$ . So, this radiation mechanism for high-energy particles will increase the total flux of radiation energy and the emitted radiation will be shifted towards shorter wavelengths.

- **Synchrotron-Self-Compton emission:** there is also a process where ultra-relativistic electrons up-scatter low energy photons that were emitted by the same population of electrons and is called **Synchrotron-Self-Compton** radiation. This mechanism has been seen at work in the close environment of the astrophysical sources, like, e.g., SNR. Local magnetic fields are in interactions with the high energy electrons and cause the emission of synchrotron photons with a spectrum that peaks in the infrared-X-ray range. Then, these photons interact with their parent electron population via inverse Compton scattering and are boosted by a large Lorentz factor. A useful relation that approximately links electron's energy and scattered photon's energy is given by:

$$E_\gamma \simeq 6.5 \left( \frac{E_e}{TeV} \right)^2 \left( \frac{\eta}{MeV} \right) GeV \quad (1.8)$$

The inverse Compton component for the typical astrophysical source peaks at GeV-TeV energies.

## 1.2.2 Hadronic gamma-ray production mechanisms

Aside from the production of VHE photons via leptonic production mechanisms, they can also be produced if protons or nuclei (hadrons) are accelerated in the vicinity of extreme as-

astrophysical sources. The beam of accelerated hadrons has the potential for colliding with a target of nucleons within the molecular cloud or with the ambient photon field (synchrotron, electron bremsstrahlung or CMB). In these environments, the dominant gamma-ray production mechanism is the **neutral pion decay**. Neutral pions mostly originate from collisions of cosmic rays (mostly protons) and have a very short lifetime ( $8.4 \times 10^{-17}$  s) after which they decay into gamma rays,  $\pi^0 \rightarrow \gamma + \gamma$ . The produced gamma-ray spectrum follows the spectrum of pions which follows the spectrum of parent protons, therefore detecting and studying gamma rays is an efficient tool to better understand the acceleration of cosmic rays. Hadronic production mechanism of gamma rays has a special signature in the spectral energy distribution, the so-called pion bump, which is a peak at  $E \approx m_\pi c^2 / 2 \approx 67.5$  MeV. This peak is precisely the energy of both gamma rays produced from the decay of neutral pion, in pion's rest frame, with momentum opposite to each other. The *pion bump* has been detected in the data of galactic SNRs and in the galactic centre region, which supports the idea of a hadronic mechanism behind the production of cosmic rays at energies up to the knee ([Alessandro De Angelis, 2018](#)) of the cosmic ray spectrum (Fig. 1.1). The charged pions,  $\pi^+$  and  $\pi^-$ , also emerge from the interaction of cosmic rays with surroundings which then decay into positrons and electrons, accompanied by neutrinos. The detection of neutrinos is additional proof for a hadronic acceleration of cosmic rays, thus neutrino astronomy is also a promising window into the multi-messenger Universe.

## 1.3 Sources of Very-High-Energy Gamma Rays

The production mechanisms of gamma rays are believed to occur within astrophysical sources which are related to the stellar phenomena within the galaxies or the activity of central galactic regions of distant galaxies. These sites of gamma-ray production can be divided based on the place of origin into galactic and extragalactic sources.

### 1.3.1 Galactic sources

**Pulsars and pulsar wind nebulae** Pulsars are rotating and highly magnetized neutron stars which emit beams of electromagnetic radiation from radio to VHE gamma rays. These objects lose their rotational energy via relativistic winds comprised of relativistic particles and electromagnetic fields. This relativistic outflow, when interacting with the ambient medium, produces synchrotron and inverse Compton radiation, thereby generating luminous pulsar wind nebula. Pulsar-PWN systems will be described in detail later in this Chapter.

**Supernova remnants** A massive star, at the final stage of its life, undergoes in a supernova

explosion, leaving behind an expanding shell of ejected material, forming a supernova remnant (SNR). The SNR, during its expansion, sweeps the interstellar material forming shock fronts in which particles are assumed to be accelerated via diffusive shock acceleration. As previously discussed (see Sec. 1.1.1), the diffusive shock acceleration mechanism is very efficient in producing (V)HE gamma rays. For this reason, SNRs are discussed as primary candidates for sources of high-energy cosmic rays.

**Binary systems** A compact object (a black hole or a neutron star) and an orbiting low- or high-mass companion comprise a binary system. If the spectrum of a binary object is dominated by the gamma-ray emission, it is called a gamma-ray binary. Currently, there are only several known binaries in which the compact object was identified as a pulsar. In these objects, the VHE emission can be explained by the interaction of pulsar wind with the stellar wind of the companion star.

### 1.3.2 Extragalactic sources

**Active Galactic Nuclei** An active galactic nucleus (AGN) is the central region of a galaxy with an active supermassive black hole onto which the material accretes from the surroundings. In some AGNs, two relativistic jets are formed around the compact object perpendicular to the accretion disk. Within these jets, charged particles are accelerated and the gamma-ray emission is produced. These extragalactic sources account for 35% of all detected sources in the VHE sky (more than  $\sim 200$  sources) (Wakely & Horan, 2008). A special type of AGNs is called blazars, in which relativistic jets point at a small angle toward the observer. Due to the relativistic beaming, blazars are highly variable sources on short timescales (hours – days) and appear much brighter than they would be if the jets were pointed away from the observer.

**Gamma-ray Bursts** Being the most luminous explosions in the Universe, gamma-ray bursts (GRBs) occur at cosmological distances and are divided according to their duration into short ( $< 2$  s; typically  $\sim 0.3$  s) and long GRBs ( $> 2$  s; typically  $\sim 30$  s duration). The initial, very bright flash, called the *prompt* gamma-ray emission is followed by a less bright but longer-lasting emission, the *afterglow*, which is observed from radio to X-rays, fading with time. GRBs are still poorly understood, so far, only for some long GRBs, an association with the core-collapse supernova events of massive stars has been made. In January 2019, for the very first time, the MAGIC telescopes detected TeV photons from a GRB 4.5 billion light-years away (MAGIC Collaboration et al., 2019).

**Starburst Galaxies** Galaxies with a very high star formation rate (SFR) are called starburst galaxies. In these galaxies, gas densities of the interstellar medium (ISM) are typically much higher than in galaxies with an average SFR. Massive stars with supersonic stellar winds and

supernovae contribute to ISM energetically, thus creating a starburst wind that fills the galactic halo with non-thermal particles and gas, which can be observed also in gamma rays. Two starburst galaxies have been detected by the IACTs so far (NGC 253 and M82, see [Abdalla et al., 2018](#)). Observations of these galaxies at the gamma-ray energies offer insights into non-thermal phenomena associated with hadronic CRs and their relation to the star-formation process.

## 1.4 Detection techniques for high energy gamma rays

Earth's atmosphere is non-transparent to high and very high gamma rays, see Fig. 1.4. The gamma-radiation from astrophysical sources can be detected either directly using space-borne satellites or indirectly from the ground through observation of the extensive air showers developed in the atmosphere. Gamma-ray observatories (see Fig. 1.5) which detect gamma rays indirectly are of two types: Imaging Atmospheric Cherenkov Telescopes (IACTs) and Water Cherenkov Arrays. The main features of direct and indirect techniques are described below.

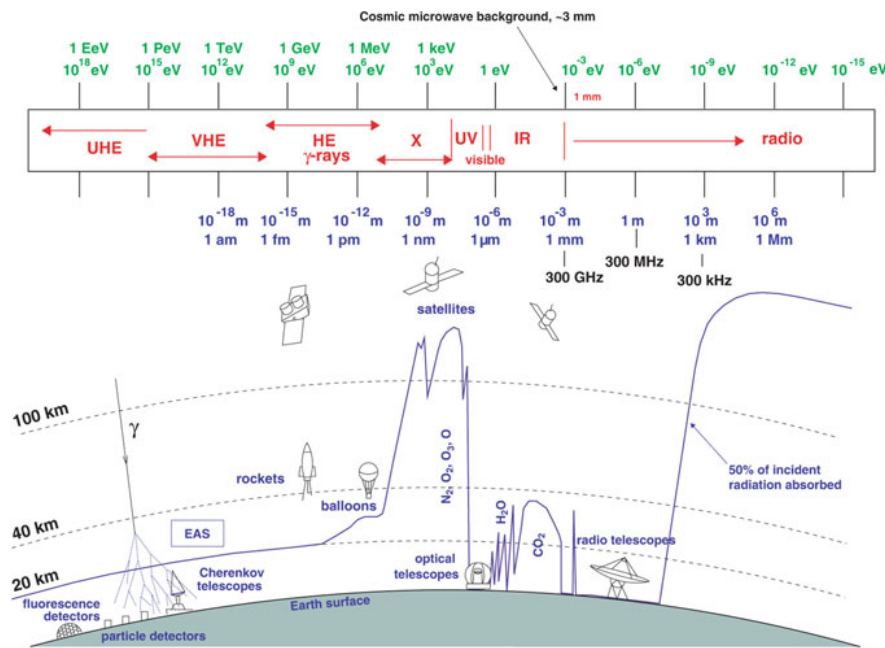


Figure 1.4: Electromagnetic spectrum and the corresponding detection techniques – in space and on the ground. The purple line indicates atmospheric electromagnetic opacity. Figure from ([Lopez-Coto, 2015](#)).

**Satellites** Directly detecting gamma rays via satellite-borne telescopes has its advantages and disadvantages. Satellites provide excellent gamma-hadron separation and excellent energy

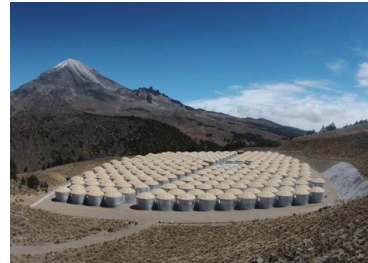
resolution, with small systematic errors. On the other hand, satellites have a reduced collection area ( $\sim 1\text{m}^2$ ) therefore their energy range for detecting gamma rays is from  $\sim 30\text{MeV}$  to  $\sim 300\text{GeV}$ , but effectively to  $\leq 100\text{GeV}$  due to the sparse photon statistics at higher energies. The process of pair production is the dominant mechanism for the detection of gamma rays above  $\sim 30\text{MeV}$ . Fermi Large Area Telescope (*Fermi-LAT*) is a gamma-ray space telescope with angular resolution of  $3.5^\circ$  (at  $100\text{MeV}$  but  $< 0.15^\circ$  for  $E > 10\text{GeV}$ ), and energy resolution of  $< 10\%$ .



(a)



(b)



(c)

Figure 1.5: Gamma-ray observatories: (a) satellite-borne telescope *Fermi-LAT* and ground-based instruments (b) MAGIC and (c) HAWC.

**Imaging Atmospheric Cherenkov Telescopes/Technique (IACT)** The primary gamma ray enters the atmosphere and interacts with the molecules in the air, creating an extensive air shower (EAS) which generates a Cherenkov light flash. These flashes are detected in the IACT's camera, and from the analysis of the image in the camera, the energy, and direction of the primary gamma ray can be reconstructed. With this method, using the atmosphere as a calorimeter, the collection area is increased up to several square kilometres. Therefore, the energy range is also increased considerably, when compared to the direct method via satellite. IACT method will be discussed in detail in Chapter 2.



The energy range between 10 GeV and 100 GeV is an overlapping region between satellites, such as *Fermi*-LAT, and ground-based Cherenkov telescopes. While entirely different detection methods are involved, with a major difference in effective areas, the sensitivity of these two of a kind instruments are similar (differential flux  $\sim 10^{-12}$  erg cm $^{-2}$  for 100 hours of observation and a 10-year *Fermi*-LAT mission). This energy range is interesting because the spectra of numerous galactic source classes show, at this specific range, rising components in energy flux with turn at those or higher energies. The extrapolation of such energy spectra is expected to be wrong and usually multi-instrumental approach is needed. Therefore, a joint fit to spectral points from both experiments, is performed often.

**Water Cherenkov arrays** This kind of particle sampler is using a direct method to detect particles from the extensive air shower (see Chapter 2) reaching the ground, thus provide an insight into the exact moment the shower hits the ground. The energy threshold of this kind of instruments is higher ( $E > 10$  TeV) than of IACT's because only the most energetic showers reach the ground. To efficiently detect the most energetic showers, the instruments are located at much higher altitudes. For example, the High Altitude Water Cherenkov (HAWC, [Tepe & HAWC Collaboration, 2012](#)) detector is situated above 4000 m at the site in Mexico. It is a 100% duty cycle and wide field of view ( $\sim 1$  sr) TeV-range instrument that provides alerts to IACT's instruments for active/flaring states of blazars, etc. HAWC has a modest angular resolution ( $\sim 0.5^\circ$ ) and poor energy resolution, which enables its sensitivity for very extended emission and for mapping the northern sky identifying many steady sources for next generation IACT, like Cherenkov Telescope Array (CTA). The latest, multi-component experiment still under commissioning, the Large High Altitude Air Shower Observatory (LHAASO, [Sciascio, 2016](#)) uses HAWC-like water Cherenkov detectors and a large array of scintillators at a site in China, at the altitude of 4410 m. Observing photons and cosmic rays in the energy range of  $10^{11} - 10^{17}$  will address still unresolved problems in galactic cosmic-ray physics. This detector also has the advantage over current IACTs of a large duty cycle and wide sky coverage, which is useful for continuous monitoring of, e.g., bright AGNs.

## 1.5 Pulsars

### 1.5.1 Discovery and overview

The first observational evidence of the existence of a pulsar was the serendipitous discovery of radio pulsar in 1967 by Jocelyn Bell Burnell and A. Hewish ([Hewish et al., 1968](#)). Initially confused for radio interference, signals were soon resolved as a series of pulses, evenly

distributed every 1.33 seconds. The discovered pulsar was named CP1919 as for Cambridge Pulsar at RA19h19m, see Fig. 1.6.

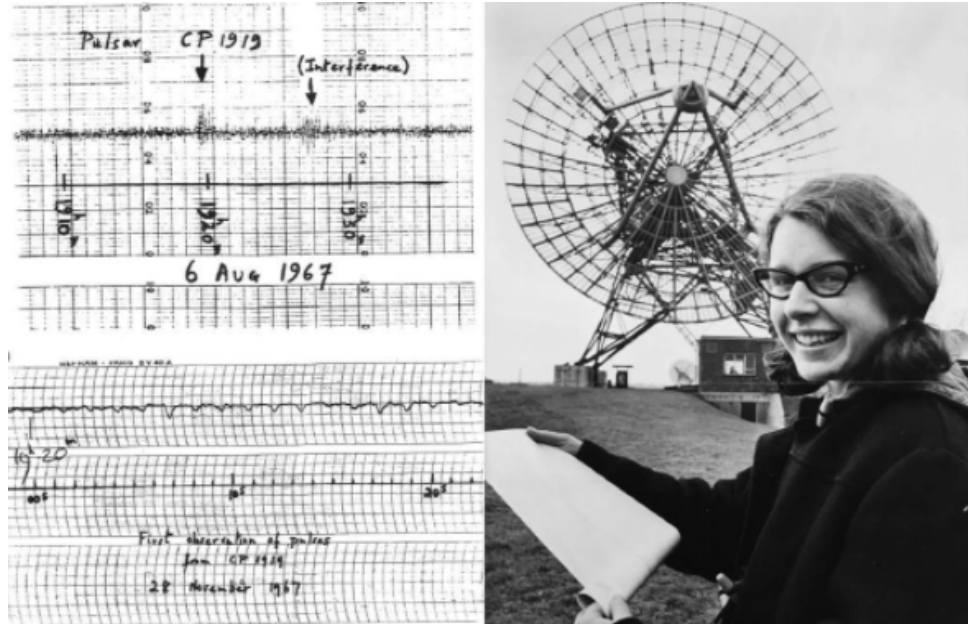


Figure 1.6: Jocelyn Bell (Burnell) pictured at the Mullard Radio Observatory (right) in 1967 with the pulsar chart (left). Image owned by Cavendish Laboratory.

Today, more than 50 years since the discovery of the first pulsar, there are some 2900 radio-emitting pulsars catalogued (Manchester et al., 2005)<sup>7</sup>, with an increasing number of pulsars being detected in other wavebands as well. The population of pulsars is estimated to be between  $10^5 - 10^6$  active pulsars in our Galaxy, with the birth rate of approximately 1 per century. Most of these pulsars are located in the plane of the Milky Way, see Fig. 1.7, within a layer of about 10 kpc from the centre.

From the measurements, pulsars display high proper velocities, originating from their violent births, on average moving away from the Galactic plane at a rate of order  $200 \text{ km s}^{-1}$  (Lyne & Graham-Smith, 2012).

Deduced from observations, pulsars rotational periods lie between 1 ms – 10 s and these are the so-called *normal pulsars* (or *canonical*) pulsars that are powered by rotation. There is also an older and smaller population of pulsars, about 100 known, - the *millisecond pulsars* (MSP) with periods less than 30 milliseconds. These pulsars, also known as recycled pulsars, are old rotating neutron stars that have been spun up or “recycled” by accretion from the companion star. In Fig. 1.8 all pulsars from the ATNF catalogue are shown in  $P - \dot{P}$  diagram according

<sup>7</sup>Catalogue of all pulsars is maintained by the Australia Telescope National Facility (ATNF) and can be found on the web: <https://www.atnf.csiro.au/research/pulsar/psrcat/>.

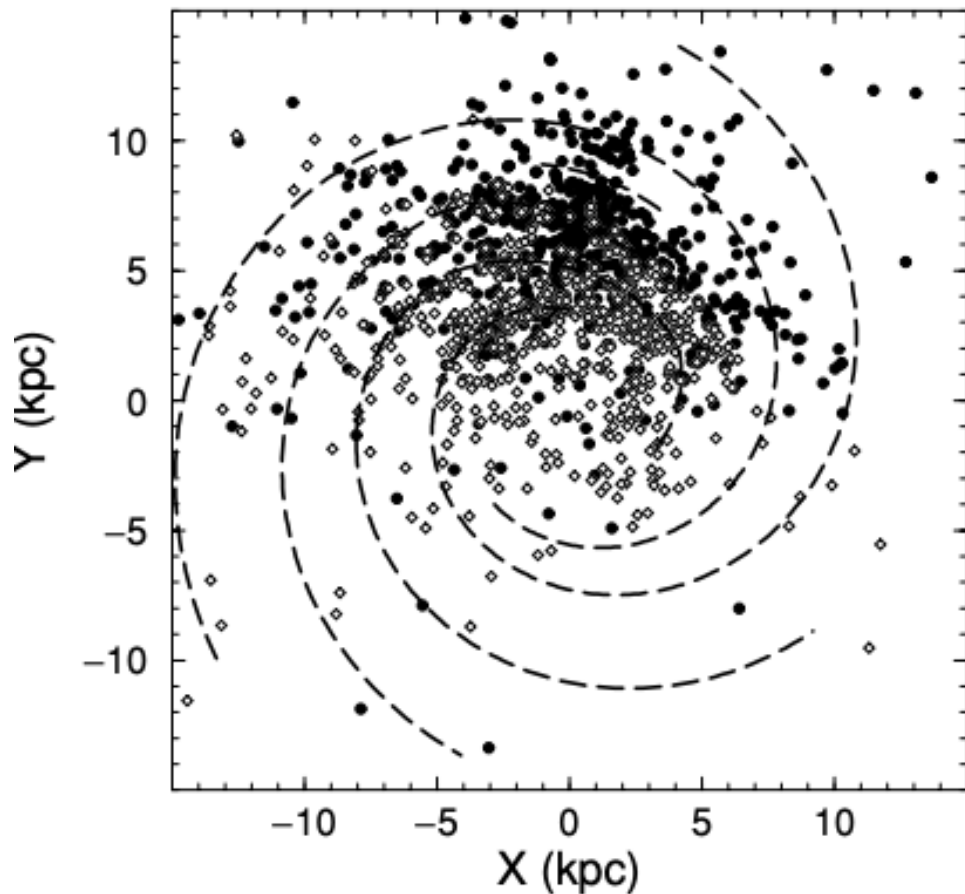


Figure 1.7: Distribution of known pulsars in the Galactic plane, based on distance estimates derived from a model. The spiral arm structure, used in the electron density model, is indicated. The image shows the inner 15 kpc around the Galactic centre. Figure from [Kramer et al. \(2003\)](#).

to their properties. It is observed that pulsars decelerate with time, thus their rotational period increases, where  $\dot{P}$  is subsequently inferred from the technique of pulsar timing. The  $P - \dot{P}$  diagram is a kind of evolutionary tool where the pulsar's life journey can be traced, and it is a good indicator of pulsar age, magnetic field strength and luminosity. Young, energetic pulsars appear in the upper-left corner of the diagram and, as they age, they slow down - evolving over millions of years to become slow pulsars and move to the lower-right corner of the diagram where old pulsars with much weaker magnetic fields reside. When their rate of rotation becomes too slow to power the emission mechanism or their signal is too weak to be detected, they can be no longer seen in the diagram. The millisecond pulsars are placed in the lower-left corner of the diagram. Aside from the classification based on the rotational period, pulsars can be classified as radio-loud or radio-quiet based on whether they are detected in the radio band, respectively.

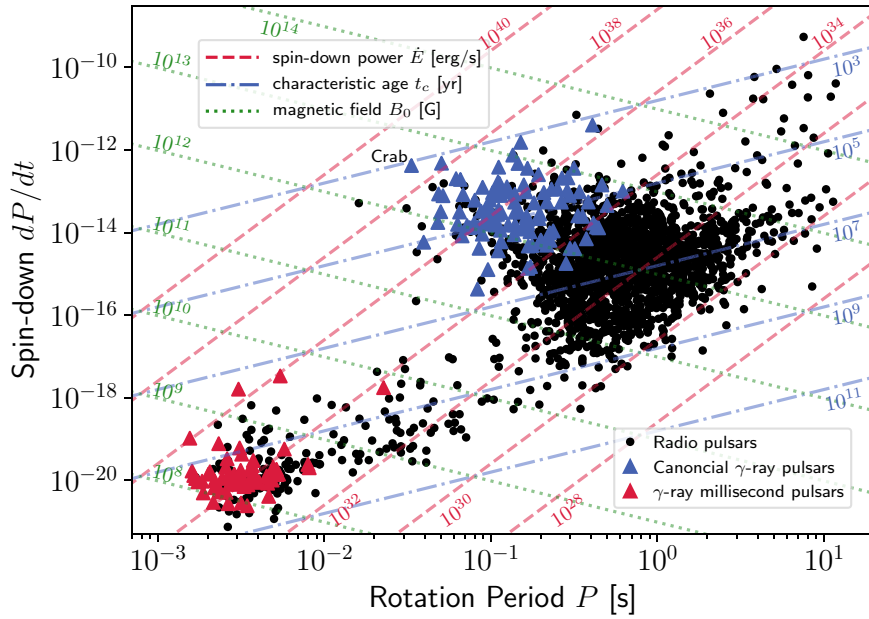


Figure 1.8: Pulsars from the ATNF catalogue are shown in  $P-\dot{P}$  space according to their properties discussed in Sec. 1.5.4. Rotation-powered gamma-ray pulsars are marked with blue, whereas millisecond ones are marked with red triangles. Radio pulsars are depicted as black dots. Figure from Carreto Fidalgo (2019).

## 1.5.2 Neutron stars

After the supernova event, a newly formed neutron star retains only a tiny fraction of a progenitor's radius but, due to the angular momentum conservation, adopts a very high rotational speed. Oppenheimer and Volkoff studied the structure of a star consisting of a degenerate neutron gas back in 1939: they showed that the only important relation for describing the state of this star is a relation between density and pressure, i.e., equation of state. A neutron star's density is similar to that of nuclear matter. The mean density, for some assumed parameters like radius  $r \sim 10\text{km}$  and mass  $1.4M_{\text{Sun}}$  is  $6.7 \times 10^{14}\text{g cm}^{-3}$  which can be compared to the density of a nuclear matter,  $\rho = 2.7 \times 10^{14}\text{g cm}^{-3}$ .

The inner structure and composition of the neutron star is an active research topic. At the surface, a thin atmosphere is assumed (a few cm thick, consisting of light and heavy nuclei) below which not fully degenerated matter shapes an envelope that represents a kind of insulator between the hot interior and the surface of a neutron star. The next layer is the outer crust, which consists of nuclei in a lattice immersed in a quantum liquid of neutrons. Changes in the

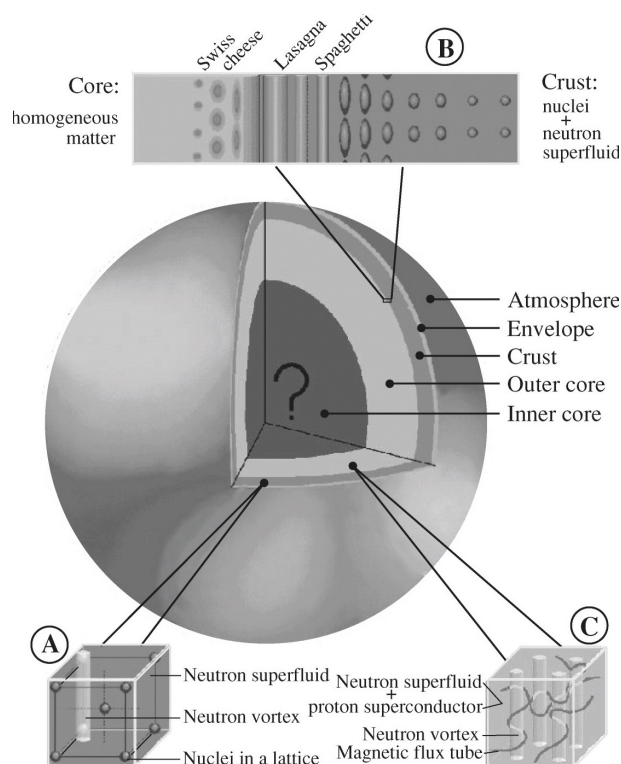


Figure 1.9: Inside the neutron star. The figure is taken from [Page & Reddy \(2006\)](#).

crust are believed to be the cause of a sudden change in a rotational speed of a pulsar, known as a glitch. Then follows the inner crust, the outer core (superconducting neutrons) and the inner core (unknown), see Figure 1.9. For more details on the neutron star's interior, see [Page & Reddy \(2006\)](#).

It was common to think that neutron stars can only be detected as pulsars which were classified, according to the source of energy, into pulsars powered by rotation and the others powered by accretion. The former are detected through the entire electromagnetic spectrum, and the latter are mainly X-ray sources. Today, there are many more objects identified as neutron stars that we know of, like, radio-quiet neutron stars, X-ray dim isolated neutron stars (XDINs), compact central objects (CCO) in SNR, soft gamma-ray repeaters, anomalous X-ray pulsars, etc. In this Thesis, we are only interested in the **rotation-powered** pulsars.

### 1.5.3 Gamma-ray pulsars and observational revolution

Gamma-ray pulsars are the main interest in this Thesis. The launch of the Fermi Gamma-ray Space Telescope in 2008, which carried onboard the Large Area Telescope (LAT) marked the new era for gamma-ray pulsar detection. Prior to *Fermi*-LAT, only 7 gamma-ray pulsars (above

100 MeV) were detected in HE gamma rays with Energetic Gamma Ray Experiment Telescope (EGRET, the precursor of *Fermi*-LAT) whereas *Fermi*-LAT increased that number to about 250, see Fig. 1.10. When the same population of *Fermi*-LAT pulsars is plotted in the  $P - \dot{P}$  diagram (see Fig. 1.8), one can immediately notice that all detected pulsars are young and energetic ones. This is also in agreement with a predictor of gamma-ray detectability, which shows spin-down flux at Earth,  $\dot{E}/d^2$  (see Carrigan et al., 2007) and appears to be a good indicator thus far for selecting a good gamma-emitting pulsar candidate.

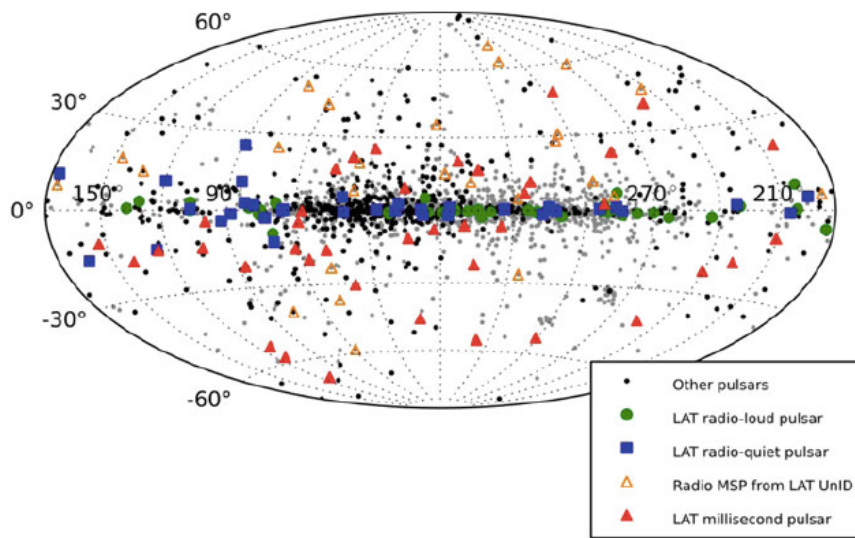


Figure 1.10: The sky-map of known pulsars in Galactic coordinates obtained from *Fermi*-LAT observations where rotation-powered pulsars are divided into radio-loud (green dots) and radio-quiet (blue squares). Figure is taken from Abdo et al. (2013).

Additionally, the great majority of pulsars detected by *Fermi*-LAT show a kind of universal behaviour when their spectra are studied: they all display exponentially cutoff spectra with cutoff energies between few GeV and a few tens of GeV. Early spectral modelling predicted this cutoff with the assumption of curvature radiation, which is believed to be a dominant process in the GeV band. Therefore, it was not expected for pulsars to emit in VHE gamma rays, which is a gamma-domain covered by ground-based instruments, such as Cherenkov telescopes. However, the Crab pulsar was the first pulsar to be detected from the ground with MAGIC telescope in 2008 (Aliu et al., 2008) with emission above 25 GeV, followed by subsequent detections of the same pulsar above 100 GeV (VERITAS Collaboration et al., 2011), 400 GeV (Aleksić et al., 2012), and most recently, above 1.5 TeV (Ansoldi et al., 2016), respectively. In the meantime, H.E.S.S. collaboration detected Vela pulsar up to 100 GeV (H. E. S. S. Collaboration et al., 2018) and recently detected, like for the Crab pulsar, pulsed emission above TeV energies from

Vela as well (H.E.S.S. collaboration, in preparation). The same collaboration detected pulses from PSR B1706-44 (Spir-Jacob et al., 2019) in the GeV range. The MAGIC collaboration followed reporting detection of pulsed emission from the Geminga pulsar (PSR J0633+1746) between 15 GeV and 75 GeV (Acciari et al., 2020) which was the first time a middle-aged pulsar (characteristic age  $\sim 300$  kyr) has been detected at these energies. These pulsars are the brightest sources of gamma rays seen by the *Fermi*-LAT telescope, and thus they were among the first candidates for VHE pulsed emission search. At the beginning of Chapter 4 the main characteristics of these pulsars are given.

### 1.5.4 Pulsar physics

Emission from pulsars is detected over the entire electromagnetic spectrum - from radio up to very high energy gamma rays. As mentioned, most pulsars emit in the radio band. Only about a few tens of pulsars are detected in the optical, infrared or ultraviolet part of the spectrum, about 100 in X-rays and more than 250 in high energy gamma-ray regime (mostly detected with *Fermi*-LAT). However, only 1 (Crab pulsar), and very recently 3 more (Vela, Geminga, PSR B1706-44) have been detected in the **very** high energy gamma-ray regime, i.e., from the ground, with Cherenkov telescopes.

Observations show that the spin period of a rotation-powered pulsar,  $P$ , defined as  $P = 2\pi/\Omega$ , where  $\Omega$  is angular velocity, increases with time, meaning that the pulsar is gradually slowing down and losing its rotational kinetic energy:

$$\frac{dE_{\text{rot}}}{dt} = \frac{d\left(\frac{1}{2}I\Omega^2\right)}{dt} = I\Omega\dot{\Omega} = \frac{4\pi^2 I\dot{P}}{P^3}, \quad (1.9)$$

where  $I$  is the moment of inertia of the neutron star, defined as  $I = 2/5MR^2$ . In the simplest model, this slowdown, or so-called spin-down energy loss,  $\dot{E}$ , is caused by the radiation of the misaligned dipole rotator, meaning that the angle between magnetic and rotational axis,  $\chi$ , is not equal to zero ( $\chi \neq 0$ ). The magnetic dipole moment of the pulsar is equal to:

$$\mathbf{m} = \frac{1}{2}B_P R^3 (\mathbf{e}_z \cos\chi + \mathbf{e}_x \sin\chi \cos\Omega t + \mathbf{e}_y \sin\chi \sin\Omega t), \quad (1.10)$$

where  $B_P$  is the magnetic field strength at the pole and  $R$  is the radius of a neutron star. The  $z$ -axis is in the direction of the rotational axis, and  $\mathbf{e}_{x,y,z}$  are unit vectors in  $x$ -,  $y$ -,  $z$ -direction. In case the magnetic axis is inclined by some angle  $\chi$  from the rotation axis,  $\chi \neq 0$ , rotating magnetic dipole has a component changing in time, and it emits electromagnetic radiation at the rotation frequency  $\Omega$ . We are interested in the power radiated by a rotating magnetic dipole,

$P_{\text{rad}}$  which is defined as:

$$P_{\text{rad}} = \frac{2}{3c^3} (\ddot{\mathbf{m}}_{\perp})^2. \quad (1.11)$$

By equating the energy loss due to radiated power and due to spin-down energy loss in Eq.1.9, we obtain:

$$\frac{dE_{\text{rot}}}{dt} = -\frac{B_p^2 R^6 \Omega^4}{6c^3} \sin^2 \chi. \quad (1.12)$$

Characteristic magnetic field strength,  $B_p$ , can be derived from Eq. 1.9 and Eq. 1.12:

$$\frac{B_p}{\text{gauss}} > 3.2 \times 10^{19} \left( \frac{P\dot{P}}{s} \right)^{1/2}. \quad (1.13)$$

By applying the observationally determined constraints on the pulsar spin period, typically found to be in the range  $\sim 0.03 - 3$  s (Lyne & Graham-Smith, 2012), the characteristic magnetic field strength is expected to be of the order  $10^{11} - 10^{13}$  G, for details see Slane (2017).

However, the model of a pulsar slowdown described above is oversimplified. A more realistic approximation of the pulsar slowing down is to assume that the angular velocity decreases according to the power-law:

$$\dot{\Omega} = -\kappa \Omega^n, \quad (1.14)$$

where  $\kappa$  is a constant and  $n$  is the *breaking index*. In the case where the slowdown is only due to a magnetic dipole breaking, the breaking index is  $n=3$ . Integrating this equation, one obtains a relation between  $\Omega$ ,  $\dot{\Omega}$  and the characteristic age  $\tau$ :

$$\tau = -\frac{\Omega}{(n-1)\dot{\Omega}} \left[ 1 - \left( \frac{\Omega}{\Omega_i} \right)^{n-1} \right]. \quad (1.15)$$

For  $n \neq 1$  assuming  $\Omega_i \gg \Omega$ , one gets the relation for the characteristic age  $\tau$ :

$$\tau = -\frac{1}{n-1} \frac{\Omega}{\dot{\Omega}} = \frac{1}{n-1} \frac{P}{\dot{P}}. \quad (1.16)$$

The characteristic age for magnetic dipole breaking with  $n=3$  is  $\tau = P/(2\dot{P})$ . This is the usual definition used to calculate a characteristic age, but  $n$  may be observable and may differ from 3 (Lyne & Graham-Smith, 2012). For many pulsars, breaking index is smaller than 3 which can be explained by, e.g., particle outflows in the magnetosphere. Only for a few pulsars that



are clearly associated with their supernovae, i.e., with the historical event of known date, the pulsar's true age is known. For the rest of the pulsar population, discrepancies can be significant if  $n$  differs from 3 or if the initial angular velocity,  $\Omega_i$  is overestimated. The spin-down model based on the rotational frequency and its first derivative can only explain the slowdown, but most of the pulsars display timing irregularities, like glitches (sudden increase in rotational frequency) and low-frequency timing noise.

### 1.5.5 Pulse profiles throughout the electromagnetic spectrum

Detected pulsed emission is usually depicted in the characteristic pulsar *light curve*, as in Fig. 1.11, where the variation of light during one rotation of the pulsar is shown.

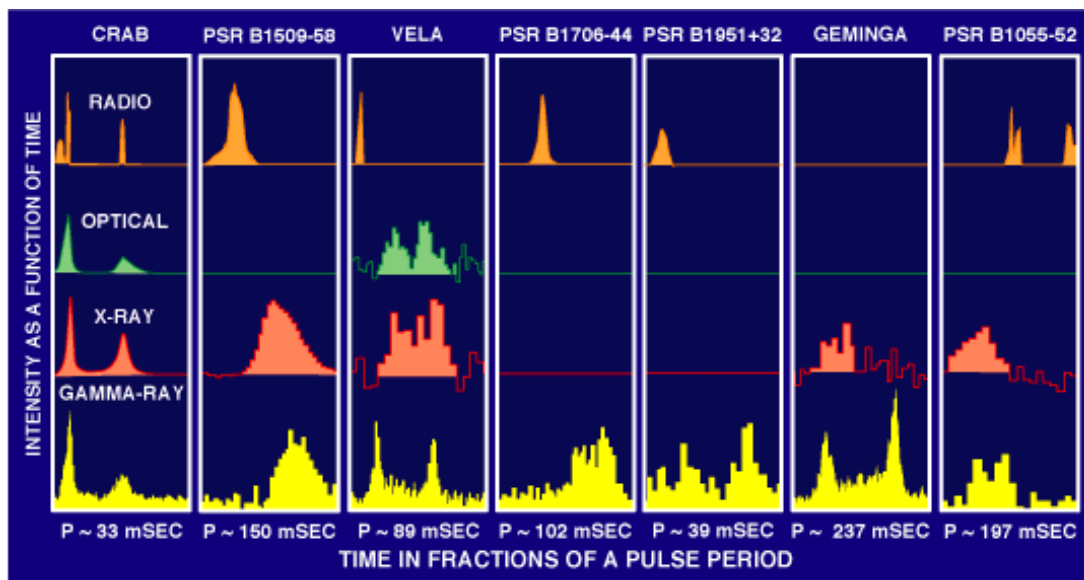


Figure 1.11: The folded light curves of the first seven gamma-ray pulsars (detected at HE gamma rays, up to a few tens of GeV with EGRET satellite) at different energies. A straight line indicates no pulsed emission found. Figure adapted from [Thompson \(2008\)](#) by NASA.

While optical telescopes might record  $>100$  photons per pulse from some pulsar, gamma-ray detectors, on the other hand, might receive one photon per hour because the radiation is recorded as the individual photon. Although producing a pulse profile for higher energies require integration over millions of pulse periods, precise timing over the long observations allows detection of periodicity of the pulsar and construction of the pulse profile. Every light curve is a unique fingerprint of each pulsar. Studying pulse profiles over the whole spectrum is the key to understanding the geometry, electrodynamics, and environment of a pulsar magnetosphere.

For some pulsars, like Crab (see Fig. 1.12) similarities in pulse profiles over the whole

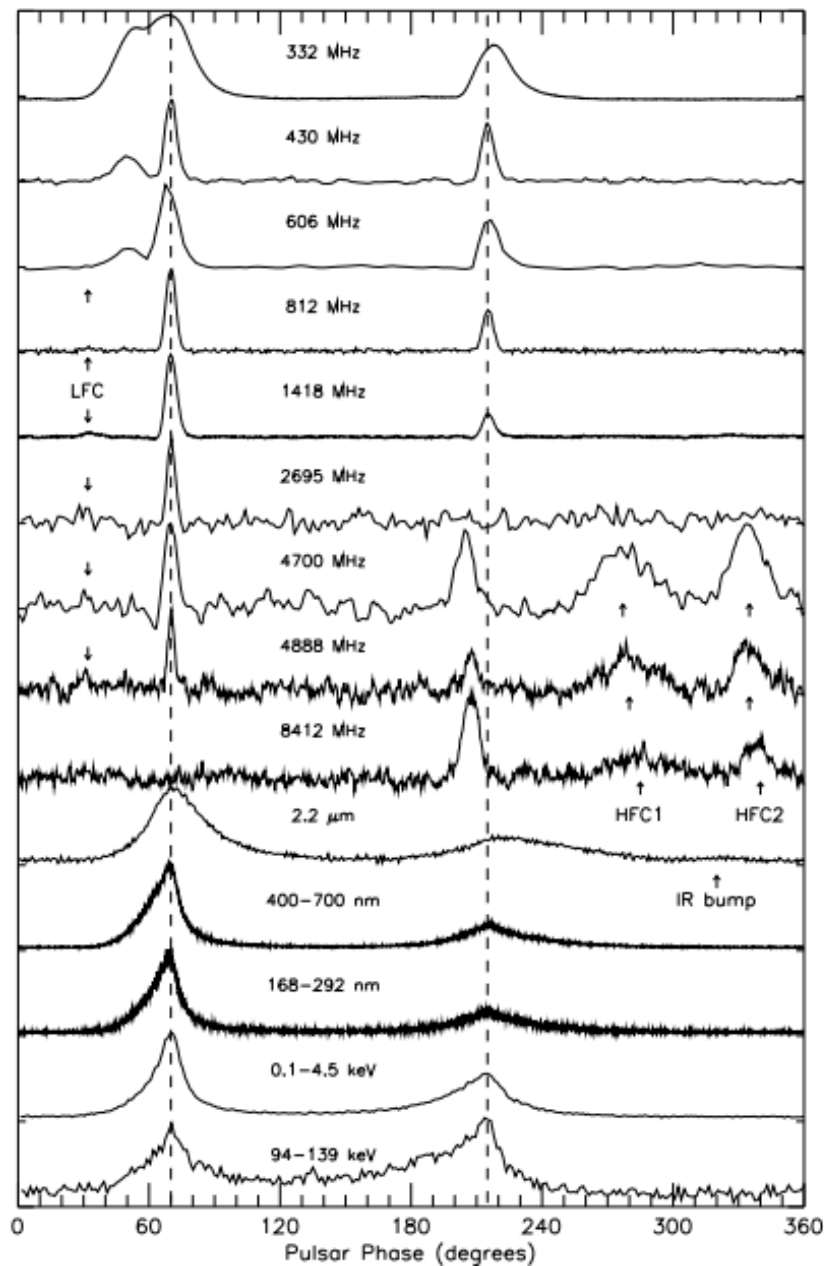


Figure 1.12: Crab pulsar profiles throughout the spectrum (from radio to X-rays). Figure is taken from [Moffett & Hankins \(1996\)](#).

spectrum are striking and this seems to indicate that the closely related populations of particles, located somewhere in the same region, are responsible for the observed pulsed emission. For now, only Crab pulsar, described in detail in Chapter 3, exhibits this kind of pulse profile behaviour throughout the spectrum. The energy-dependent light curves are usually modelled, as a function of geometry, to differentiate between different emission mechanisms and to be

able to constrain the emission geometry by comparing theoretical predictions with the multi-wavelength data. Different particle populations that emit radiation components in accordance with a local magnetic field geometry and electric field spatial distribution are the reason behind unique pulsar light curves that evolve with photon energy. Additionally, it seems the radiation beam emitted far from the star's surface is governed by the relativistic effects since close to the light cylinder, co-rotation speed is  $v \approx c$  (for the light cylinder see the next Section).

Studying pulsar light curves is a subject of extensive theoretical studies. From some models, it can be deduced that the origin of the light curve peaks is, both, altitude- and azimuth-dependent.

### 1.5.6 Pulsar magnetosphere and pulsar emission models

Pulsars are highly magnetized neutron stars. Due to the magnetic flux conservation, its dipole field strengths at the pole, after the star's collapse, reach  $\sim 10^{12}$  Gauss in young pulsars. These huge magnetic fields seem to have little effect on a star's inner structure while outside the star, the magnetic field dominates over all forces, even the gravitational force by a considerable factor (for a pulsar like e.g., Crab):

$$F_{mag}/F_{grav} = \frac{e\Omega r B}{c} / \frac{GMm}{r^2} \approx 10^{12}, \quad (1.17)$$

Thus, the corresponding electric field (above the pole) produced from a rotating magnetic field, has the potential to extract electrons from the surface of the star and fill the pulsar surroundings with plasma.

A pulsar's magnetosphere is a region around the pulsar, filled with magnetized plasma, detained by the pulsar's strong magnetic fields, as shown in Figure 1.13.

The dipole magnetic axis of a pulsar is inclined with respect to the rotational axis, and the combination of these features (the angle of inclination) is at the origin of the pulsed emission. The magnetic field is co-rotating with the star out to the radius, where the co-rotation speed approaches the speed of light. This co-rotation radius, or the so-called, **light cylinder** radius,  $R_L = c/\Omega$ , is shown also in Fig. 1.13. A pulsar model was proposed by Goldreich & Julian (1969), where they showed that a highly magnetized rotating neutron star cannot exist without being surrounded by a plasma. The magnetosphere is highly conductive along, not perpendicular to, the magnetic field lines - just like in a star's interior where there can be no net electric field. In that context, the magnetosphere seems to be an extension of the solid interior. This

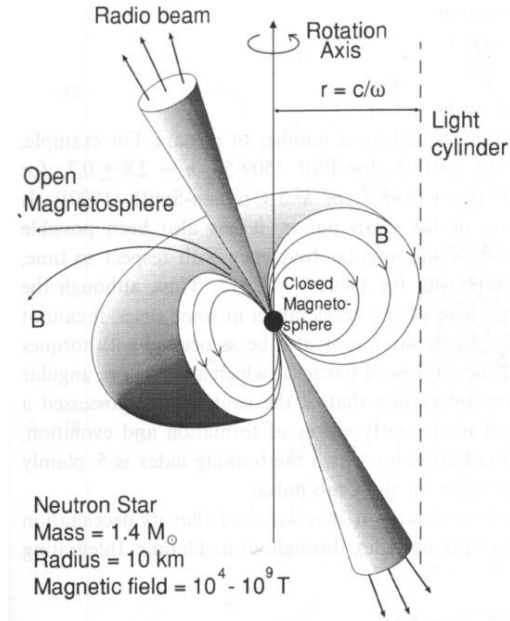


Figure 1.13: Model of a pulsar rotating around its spin axis and emitting beams of radiation along its magnetic axis. Figure is taken from Yuri Lyubarsky.

implies the Lorentz force condition to be satisfied:

$$\mathbf{E} + \frac{\boldsymbol{\Omega} \times \mathbf{r}}{c} \times \mathbf{B} = 0, \quad (1.18)$$

further implying that  $\mathbf{E} \cdot \mathbf{B} = 0$ , i.e., electric and magnetic fields are perpendicular to each other, so charges can move along the magnetic field lines, but at the same time, this implies no acceleration of the electrons can take place. This is referred to as the force-free condition of the magnetosphere. From Gauss' law,  $\rho = \nabla \cdot \mathbf{E}/4\pi$ , one then obtains the charge density  $\rho_{\text{GJ}}$  (details see in [Goldreich & Julian \(1969\)](#)), called Goldreich-Julian density

$$\rho_{\text{GJ}}(r, \theta) = -\frac{\boldsymbol{\Omega} \cdot \mathbf{B}}{2\pi c} \frac{1}{1 - (\Omega r/c)^2 \sin^2 \theta}, \quad (1.19)$$

where  $\rho_{\text{GJ}}$  is given in the polar coordinates,  $\theta$  is the angle with the rotation vector  $\boldsymbol{\Omega}$  and  $c$  is the speed of light. Since the emission is detected, there must be locations where the force-free condition is not satisfied, i.e., where  $\rho \neq \rho_{\text{GJ}}$ . From Eq. 1.19 Goldreich-Julian density is zero when  $\mathbf{B}$  is perpendicular to  $\boldsymbol{\Omega}$ . This region is called a *null charge surface* and marks the place where the space charge density reverses the sign. Charges redistribute themselves in a way that if  $\boldsymbol{\Omega} \cdot \mathbf{m} > 0$  (where  $\mathbf{m}$  is a magnetic moment of a star), electrons co-rotate at the poles and

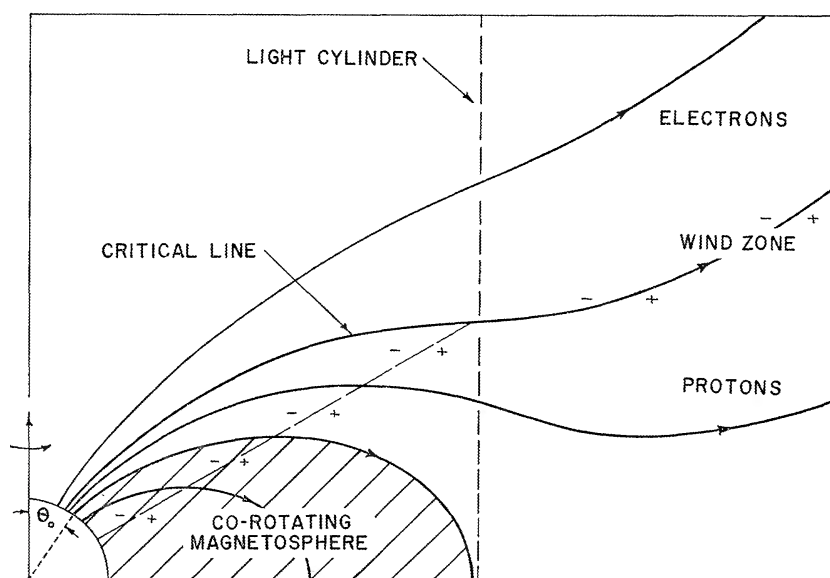


Figure 1.14: Model showing pulsar electrodynamics with the co-rotating magnetosphere and the wind zone proposed by Goldreich & Julian (1969). The model is for an aligned rotator where magnetic and rotational axes are aligned. Pulsar is at the lower left, with the illustrated poloidal magnetic-field structure. The particles attached to the closed magnetic-field lines corotate, and they are within the light cylinder (LC). The open magnetic-field lines are the ones that pass through the LC and charged particles stream out along them. Figure is taken from Goldreich & Julian (1969).

positrons at the equator, while if the sign of  $\mathbf{B}$  is reversed - opposite charge distribution happens. There is an important consequence of the fact that co-rotation of the magnetosphere ends at the light cylinder: magnetic field lines crossing the light cylinder remain open (they can not loop back to the neutron star surface)<sup>8</sup>. Thus, electrons (and positrons) attached to the open magnetic field lines leave the near zone of the pulsar. In this near zone of a pulsar where the co-rotating magnetosphere is, shown in Fig. 1.14, a magnetic field is purely poloidal. This is also a zone where no net currents flow and the field lines are closed. Beyond the light cylinder, a zone called a *wind zone* exists with an open magnetosphere and a toroidal magnetic field structure. For a star to be globally neutral, the pulsar net current must be zero: thus the outgoing flux of electrons must be balanced by the equivalent flux of positrons. If there is a discontinuity in the flow of the opposite charges, a critical field line is defined as the one having the same potential as the outer space far from the pulsar. The Goldreich-Julian model successfully explained some basic concepts of pulsar magnetosphere but produced several inconsistencies, where the most obvious is that the force-free condition implies no particle acceleration is possible. Since the emission

<sup>8</sup>Since  $\nabla\mathbf{B} = 0$ , the open magnetic field lines close themselves but far away from the pulsar where its magnetic field fuses with the interstellar field.

from the pulsar is observed throughout the spectrum, the locations in the magnetosphere exist where this condition is bypassed. The models are trying to constrain the exact location and mechanism where the acceleration is possible.

**Pulsar emission models** There are many model types that try to explain the observed emission from the pulsar, but the most studied ones are the polar cap, the slot gap, the outer gap and the equatorial current sheet. These models differ in the locations and the geometry of the acceleration zone, see Fig. 1.15 and have different implications for gamma-ray emission, especially the higher end of the gamma-ray spectrum.

**Polar cap** are regions around the magnetic poles where open field lines are attached and where large electric fields are induced. According to the polar cap model (Ruderman & Sutherland, 1975), the particles are accelerated at the neutron star surface and the high-energy radiation is generated several stellar radii from the surface due to significant losses of the particle's energy. This would result in a super exponential cutoff in spectra of pulsars, with a cutoff energy below 10 GeV. With the first detection of Crab pulsar above 25 GeV (Aliu et al., 2008) and later above 100 GeV (VERITAS Collaboration et al., 2011), the model was unable to explain very high gamma-ray emission. New models, favouring locations further from the pulsar surface, have emerged.

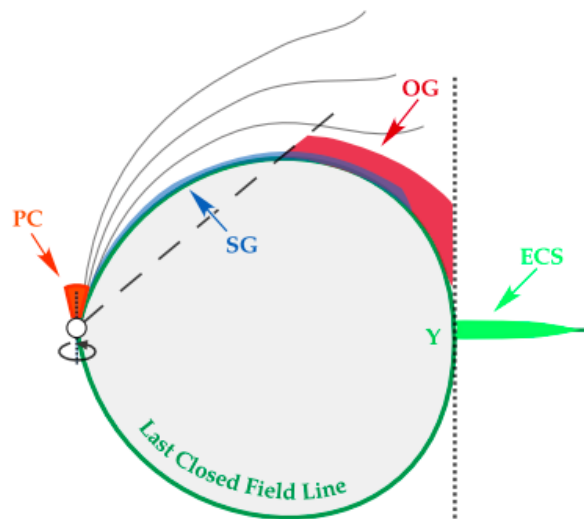


Figure 1.15: Possible emission regions in the pulsar magnetosphere, as theorized in Hirotani (2011). The last closed field line (dark green) meets the light cylinder at the equatorial plane, at the Y point. PC stands for polar cap region; slot gap (SG) is the region along the last closed line. Outer gap (OG) region extends from the null-surface (dashed line) to the LC; equatorial current sheet (ECS) extends from the Y point to the outside of the LC. Figure from Ceribella (2021).

**Outer gaps** are large, almost empty volumes in the magnetosphere, between the null surface ( $\rho = 0$ ) and the last closed field line where the synchrotron emission is likely produced, for details see (Cheng et al., 1986). This model has been successful in reproducing the exponential energy cut-offs in the spectra of several gamma-ray pulsars (Romani, 1996), and is usually used to explain the spectra of *Fermi*-LAT pulsars (Abdo et al., 2013).

**Slot gap** is an elongated region along the last closed field line within the magnetosphere, basically empty of charges, allowing pair-creation (Muslimov & Harding, 2003). However, later studies showed that this model is unsuccessful in reproducing the observed pulsar flux intensities (Hirotani, 2008).

**The equatorial current sheet** is a new class of models which emerged from the Monte Carlo simulations of the pulsar magnetosphere. These simulations show that the pulsar magnetosphere is not so different from the ideal force-free one, with an exception of the equatorial current sheet. For the aligned rotator, the current sheet interacts with the last closed field line at the LC, forming a triple re-connection point known as  $\Upsilon$  point, see Fig. 1.15. Here, at this point, the large electric field accelerates charged particles along the equatorial current sheet. The model can reproduce the spectral lower energy component observed by *Fermi*-LAT via curvature radiation and the very high energy component via inverse Compton scattering, extending up to TeV energies which is observed for Crab pulsar (Ansoldi et al., 2016) and reported for Vela pulsar (Djannati et al. (in prep)) as well.

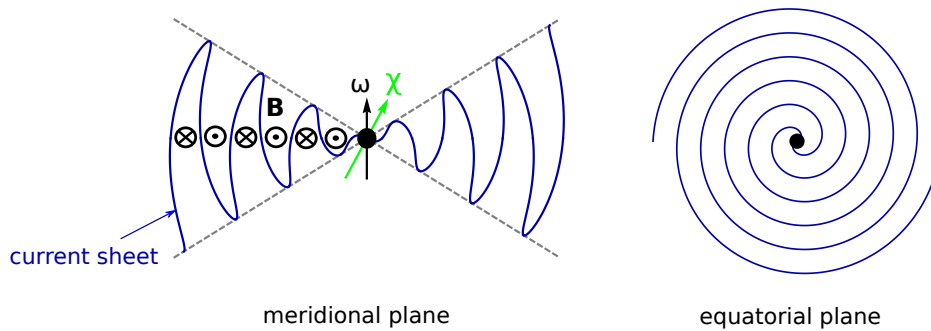


Figure 1.16: Model of a striped wind for an oblique rotator, which encloses the angle  $\chi$  between the rotational and magnetic axes. The undulating current sheet (blue curve) in the meridional plane separates the stripes of opposite magnetic polarity. In the equatorial plane, the current sheet develops an Archimedean spiral. Figure from Mochol (2017).

Another type of emission model, a kind of current sheet model with a more complex morphology, assumes that the acceleration region is beyond the light cylinder. The model of a *striped wind* describes the energy release mechanism that could be related to the specific struc-

ture of the equatorial component of the pulsar wind<sup>9</sup>, see Figure 1.16. As the pulsar rotates, the current sheet sweeps an oscillatory pattern, with the linearly increasing oscillation amplitudes further from the pulsar. The particles accelerated in the current sheet of such a striped wind emit synchrotron and SSC photons, whose spectrum can reach TeV energies, which is seen to be the case for Crab pulsar as well as in millisecond pulsar. Numerical simulations predict spectral hardening at VHE, followed by the cutoff at TeV energies. Thus, further observations of pulsars at VHE are needed to confirm or rule out this emission model. For details of this model see Coroniti (1990) where the model of striped wind originated, also Mochol (2017) and references therein.

Following the first three models, it seems that gamma-ray emission is a result of synchrotron-curvature radiation in one of the gap regions where charged particles follow curved magnetic field lines and radiate. This radiation, limited by the maximum photon energy, predicts an exponentially decaying flux at energies above a few GeV, which is precisely what is observed in most of the pulsars detected with *Fermi*-LAT. However, it seems like only the equatorial current sheet-like scenarios can reproduce the most recent discoveries that are showing detection of pulsed emission even above few TeV with no indication of cutoff energy (for the details, see Sec. 3.1).

### 3D models of pulsar magnetosphere and interpretation of the data

Recent progress in the pulsar magnetosphere simulations pointed out that, for most pulsars, dissipation and particle acceleration occurs near the current sheet outside the light cylinder (for details see Kalapotharakos et al. 2014, 2018). The latest simulations use 3D Cartesian relativistic Particle-In-Cell (PIC) code to build 3D kinetic global model of pulsar magnetosphere, aimed to obtain modelled light curves and spectral energy distributions that successfully reproduce the observed data. These simulations can be considered a new and comprehensive approach to study microphysical conditions but also the global ones, in contrast to MHD models that only capture the global aspects of pulsar magnetosphere (Venter, 2017). The main advantage of PIC simulation is the addition of a self-consistent pulsar magnetosphere, which also makes them computationally challenging.

By simulating realistic trajectories of particles, starting from the stellar surface around the polar cap, the electric field component  $E_{\parallel}$  along the magnetic field line arises in the regions above the polar caps, near the separatrices and near the equatorial current sheets outside the light cylinder, see Fig. 1.17. For the great majority of pulsars, the information on the inclination

---

<sup>9</sup>The striped wind is the pulsar wind in the form of stripes of opposite magnetic polarity, separated by current sheet.



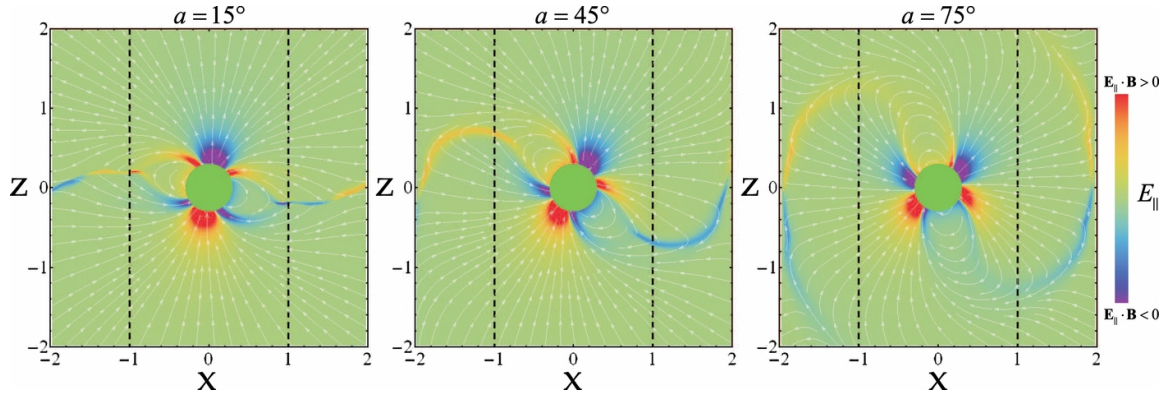


Figure 1.17: Configuration of magnetic field lines for different oblique rotators (inclination angle  $\alpha$  is indicated in the title of each plot) in the poloidal plane ( $\mu, \Omega$ ) obtained from simulations from a dissipative pulsar magnetosphere. The electric field  $E_{\parallel}$  along the magnetic field lines is denoted by the colour scale, and the magnetic field is marked with streamlines. The rotation vector  $\Omega$  is along the Z-axis, where Z and X are given in the units of the light cylinder  $R_{lc}$  marked with a vertical dashed line. Figure is taken from Kalapotharakos et al. (2014).

angle ( $\alpha$ ) or observer angle ( $\zeta$ ) is still unknown, which makes it difficult to determine the best suitable model for a specific pulsar. Thus, a statistical comparison is needed between the results provided by the models and the observational data. The most recent VHE emission modelling (Harding et al., 2021) of the four ground-based detected pulsars, enables one to identify those models that reproduce the observed data more or less successfully. Harding et al. (2021) results seem to suggest that the VHE emission may have various origin, depending on the pulsar under study. While the VHE emission in pulsars, such as Geminga and PSR B1706-44, seem to be an extension of the Fermi spectra to higher energies, in cases such as Crab and Vela pulsars, where pulsed components are detected above 1 TeV, separate higher energy spectral components may be at work that require different emission mechanism.

In the work from Harding et al. (2021), the global magnetosphere fields and multiple emission mechanisms are used. Those models predict three VHE components: synchro-curvature (SC) from primaries whose HE tail can extend to 100 GeV, synchrotron self-Compton (SSC) from pairs that can extend to several TeV and inverse Compton scattering (ICS), originating from primary particles accelerated in the current sheet, that extends beyond 10 TeV, see Fig. 1.18 and 1.19. As a result of these simulations, one can conclude that e.g., for the Crab pulsar the model gives an SSC spectrum that matches the MAGIC VHE points, from 0.1 – 10 TeV well. Therefore, for the Crab pulsar, the MAGIC spectrum is not an extension of the primary SC spectrum (observed in the HE data with the *Fermi*-LAT) while for the Geminga pulsar it is, and

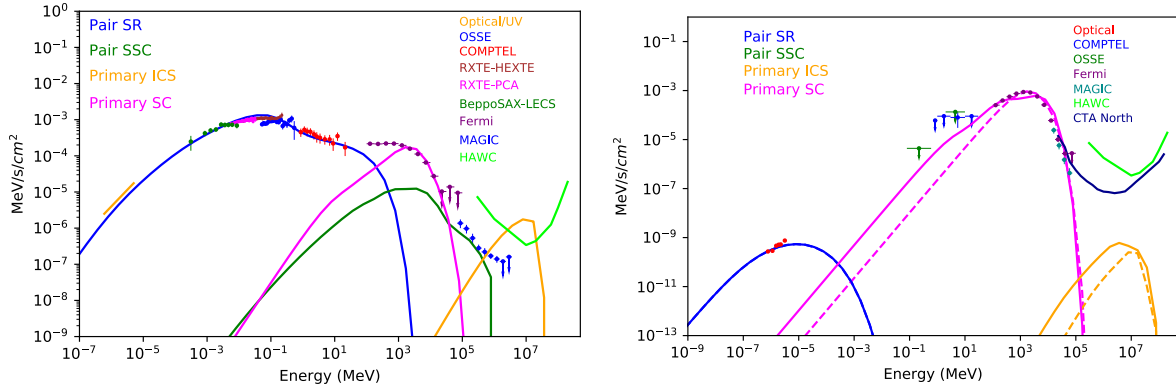


Figure 1.18: Model spectral energy distribution for the Crab pulsar for inclination angle  $\alpha = 45^\circ$ , viewing angle  $\zeta = 66^\circ$  (left), and for Geminga pulsar for inclination angle  $\alpha = 75^\circ$ , viewing angle  $\zeta = 50^\circ$  (right). The viewing angle chosen to best match the Fermi and VHE light curves. Differently coloured lines and points/symbols show results of simulation(s) and observations, as indicated in legends of left and right panels. Figures and data points are from the references in [Harding et al. \(2021\)](#).

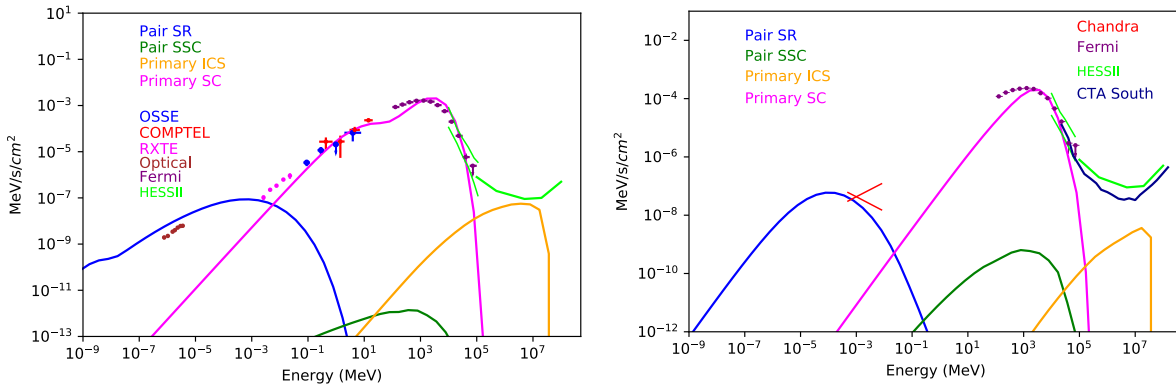


Figure 1.19: Model spectral energy distribution for the Vela pulsar for inclination angle  $\alpha = 75^\circ$ , viewing angle  $\zeta = 50^\circ$  (left), and for PSR B1706-44 for inclination angle  $\alpha = 45^\circ$ , viewing angle  $\zeta = 53^\circ$  (right). Figures and data points are from the references in [Harding et al. \(2021\)](#).

is well explained as primary SC emission with no need for an ICS component. This kind of modelling provides some possible explanations for the observed VHE components and some predictions for future observations.

## 1.6 Pulsar wind nebulae

### 1.6.1 Overview

The extended and luminous nebula forms when pulsar wind expands into its surroundings. This nebula, called the pulsar wind nebula (PWN), see Figure 1.20, also known as a plerion<sup>10</sup>, is continuously powered by electron-positron plasma and magnetic fields from the pulsar, suggesting that most of the pulsar power goes into powering the nebula. The PWN is generated inside the supernova remnant (SNR) and evolves in conjunction with it. In the vicinity of a pulsar, its outflow is cold and radiatively inefficient. The luminous emission of the nebula starts only after the flow is slowed down and energy is converted into particle acceleration, which happens at the termination shock (TS) generated from the interaction between relativistic wind and non-relativistic surrounding medium.

The structure of PWN generally depends on the pulsar power supply and the structure of the ambient medium into which this material is expanding. Specifically: the size, morphology, and spectrum of a PWN are expected to depend on the central engine parameters like pulsar spin-down energy, pulsar velocity, inclination angle between magnetic and rotational axes, as well as on the environmental conditions (ambient pressure, magnetic field and radiation field).

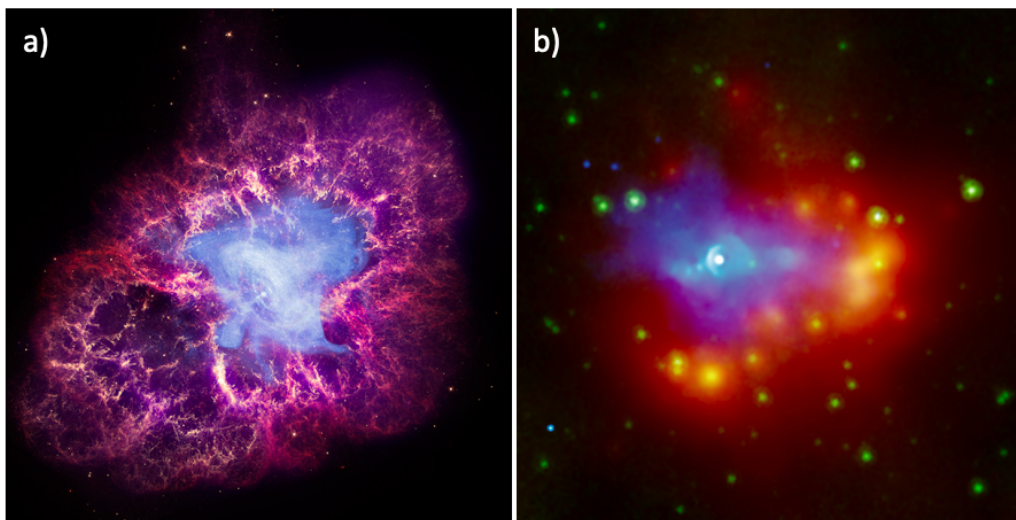


Figure 1.20: Examples of PWN: a) multi-wavelength image of Crab nebula with X-ray emission (blue) from *Chandra*, optical emission (red and yellow) from Hubble Space Telescope, and IR emission (purple) from *Spitzer*; b) multi-wavelength image of G54.1+0.3 with X-ray emission (blue) and IR emission (red-yellow) from the same detectors as in a). Images courtesy NASA/CXO.

<sup>10</sup>The word plerion originates from the Greek word *pleres* meaning full or filled.

The energy in the wind seems to be transported by Poynting flux and deposited at large distances from the pulsar (few parsecs), where energized particles radiate throughout the electromagnetic spectrum, producing synchrotron and inverse Compton (IC) radiation, see Fig. 1.21. The details of this mechanism, as well as the processes that lead to the release of magnetic energy, are still not well understood and are known as the  $\sigma$  **problem**. The  $\sigma$  parameter denotes the ratio between the Poynting flux and the kinetic energy of the wind. At the pulsar, the wind is highly magnetized ( $\sigma \sim 10^3$ ) and it stays such up to the TS, making it unclear where the wind dissipates this electromagnetic energy to the plasma. Additionally, the magnetization parameter  $\sigma$ , obtained from 1D and 2D PWN models, is ambiguous (Kennel & Coroniti, 1984a). It seems small ( $\sigma \sim 10^{-3}$ ) after the particles pass the TS, compared to the value before TS. PWN are fascinating astrophysical objects, as the brightest and closest class of relativistic sources, thus an ultimate laboratory for the physics of relativistic plasmas where acceleration of particles at relativistic shocks can be studied. For current theoretical PWN understanding, the reader is directed to Amato 2020; Gaensler & Slane 2006 and references therein.

## 1.6.2 The evolution of PWNe

The PWN is created inside the SNR and the remnant is surrounded by interstellar medium (ISM), see Figure 1.22. The energy budget of a supernova shock, which drives the expansion of SNR in the ISM, is  $\sim 10^{51}$  ergs. On the other hand, the energy budget of PWN, compared to the former, is negligible  $\sim 10^{49}$  ergs. Therefore, PWN evolution cannot significantly affect the SNR, but the evolution of SNR can have major implications for the PWN (Bucciantini, 2008).

Due to the variety of local conditions, PWNe show a wide distribution of properties. Nevertheless, the first PWN theoretical model, based on relativistic magnetohydrodynamics (MHD) (Coroniti & Kennel, 1985) can explain many of the observed features. Following the 1D model for PWNe, the evolution of these objects is divided into three phases.

**Free expansion phase** The first phase is the *free expansion phase* ( $< 2 - 6$  kyr) when the nebula expands into the cold SN ejecta. The cold pulsar wind produces a TS where the ram pressure of the wind is balanced by the thermal pressure of the PWN. This results in a torus-like structure, which can be seen in an X-ray image of the Crab Nebula. At the TS, particles are thermalized and accelerated, most likely by the Fermi acceleration mechanism or by magnetic reconnection. In comparison with typical pulsar kick<sup>11</sup> velocities that range 50-300 km/s, typical PWN expansion velocity is one order of magnitude greater, so when modelling young PWN one can neglect

---

<sup>11</sup>A pulsar kick is a phenomenon that often causes a neutron star to move with a different, usually substantially greater, velocity than its progenitor star. The cause of pulsar kicks is unknown, but many astrophysicists believe that it must be due to an asymmetry in the way a supernova explodes.

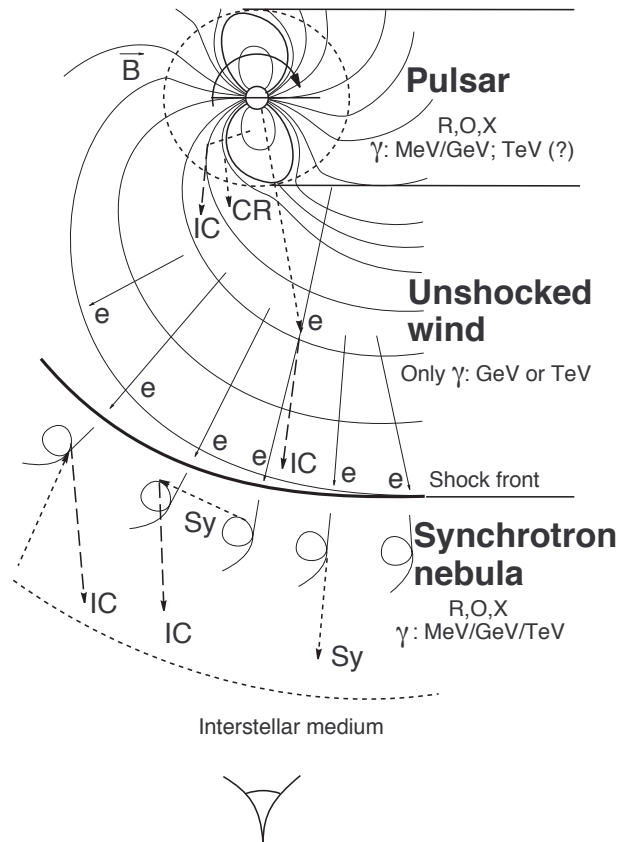
Radiation from a **Pulsar-wind-nebula** complex

Figure 1.21: Sketch of radiation zones in pulsar wind nebula: pulsar and its nebula radiate in a wide energy range, the unshocked wind is assumed to produce only GeV or TeV photons. Figure from [Aharonian & Bogovalov \(2003\)](#).

pulsar kick velocity and locate it in the centre of the nebula. During the free expansion phase, PWN is inside the SNR shell and does not interact with it. At this phase, PWN is growing fast ( $R \sim t^{1/2}$ ), reducing magnetic field strength and synchrotron radiation, while at the same time increasing inverse Compton component (from the accumulated electrons) and then decreasing it very slowly.

**Reverberation phase** The second evolutionary phase starts after a few thousand years and its size is of the order  $\sim 10$  pc. PWN encounters the reverse shock of the SNR (for the SNR evolutionary phases, see Sec 1.7). Now, the evolution of PWN is governed by the more energetic SNR shell and the phase is called the *reverberation phase*: a PWN is subjected to a series of contractions and expansions until the balance is achieved. All these interactions cause the diversity of PWN morphologies in this evolutionary stage. Once the interaction of shocks is over, the PWN continues to expand into the hot shocked SN ejecta. This phase ends some tens of kyr

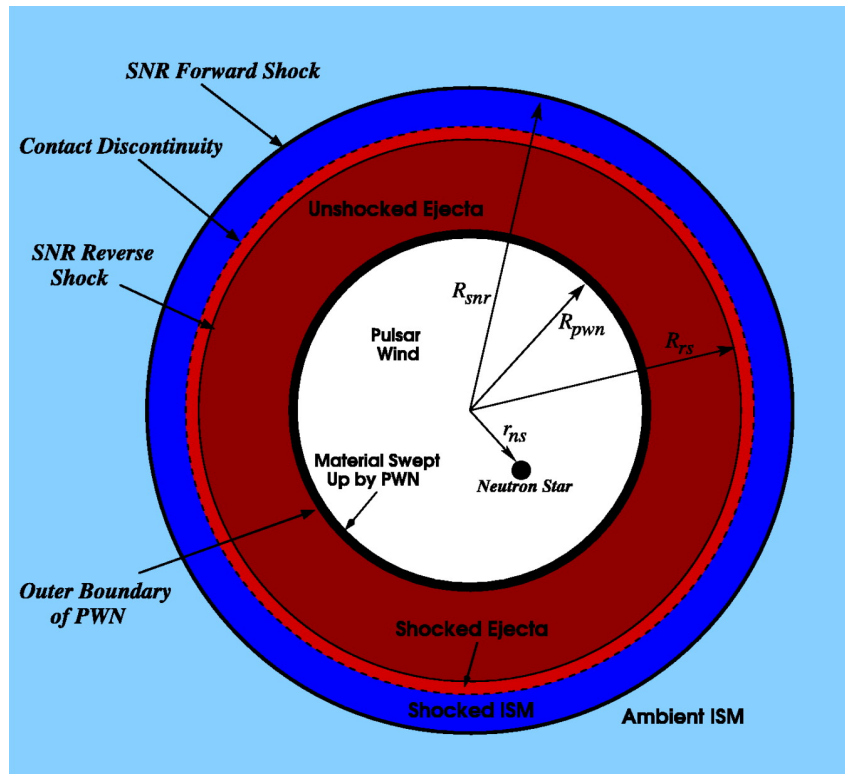


Figure 1.22: The model of a composite SNR with a central neutron star (pulsar) and its nebula. The pulsar produces a cold, ultra-relativistic wind of particles. Wind flows (free expansion) up to the termination shock (denoted with  $R_{pwn}$ , where particles are heated after crossing the shock to produce the shocked wind. The nebula is surrounded by the supernova remnant, itself imprisoned by the ambient medium. Figure adopted from [Gelfand et al. \(2007\)](#)

after the SN explosion.

**Relic phase** During the third phase, called the *relic phase*, a pulsar can drift off from the PWN bubble or even from SNR if it had received a kick during the SN explosion or during the asymmetrical interaction of nebula and SNR reverse shock. Then, the pulsar forms a local plasma bubble and leaves behind the old nebula, now called the relic PWN. This old nebula is IC-dominated due to its much lower magnetization.

### 1.6.3 Observational properties of PWNe

PWNe are observed from the radio to the highest gamma rays and have some common characteristics, such as increased brightness in the centre of the nebula, flat radio spectral index and a steeper index in the X-rays. They are highly polarized with the magnetic field strength in the range from  $\mu\text{G}$  - mG, and young ones (before a PWN interacts with the reverse shock of the

SNR) all have a pulsar in their centre.

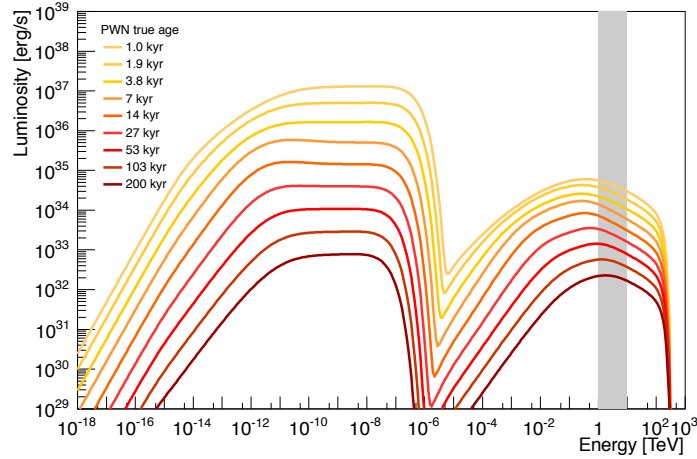


Figure 1.23: Modelled spectral energy distribution (SED) of the generic PWN: time evolution of the SED from 1 kyr - 200 kyr. The left component is the synchrotron and the right one is the Inverse Compton component of the emission. The decline of synchrotron energy flux with the increasing age of the system is more prominent than that of IC component, due to the synchrotron strong dependence on decaying magnetic field strength. Figure from [Abdalla et al. \(2018\)](#).

Synchrotron radiation from relativistic particles coming from the pulsar is responsible for the nebula emission in the radio band all the way up to the X-rays. Observed gamma-ray emission arises from the IC scattering of cosmic microwave background (CMB) photons and the interstellar radiation field. In young PWN, synchrotron self-Compton (SSC) component from synchrotron nebula dominates at VHE. Photons of GeV - TeV energies that are produced in IC scattering from homogenous photon fields (like CMB) carry more information about the electron plasma than the synchrotron photons, which are dependent on variable magnetic fields in the PWN. A characteristic spectrum of PWN is shown in Figure 1.23.

### TeV observations of PWNe

Pulsar wind nebulae are the most numerous galactic source class in the VHE sky. Recent X-rays and TeV observations improved our understanding of the PWNe, where the majority of these objects have been discovered in one of these bands, and many are seen in both. TeV PWNe are observed as extended objects with an angular size of a fraction of a degree, which converts into a size of about 10 pc at a distance of about a few kpcs.

Since most of the spin-down energy that the pulsar deploys to the nebula is in the first few tens of kiloyears it is expected that a bright PWN has a young and energetic pulsar nearby.

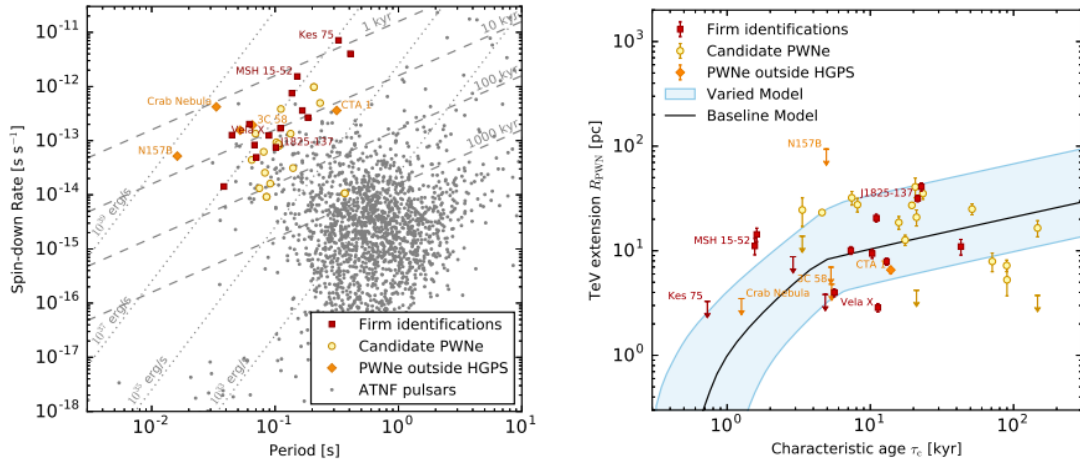


Figure 1.24: Population study shows some trends between pulsars and their nebulae. Left: Spin-down rate,  $\dot{P}$ , and rotational period of pulsars with a firmly identified PWN, candidate PWN and without TeV counterpart (grey dots). Right: PWN extension versus characteristic time  $\tau_c$  where the steeper part corresponds to the free expansion phase and the softer part to the interaction phase, but in general, one PWN expand with time until the age of a few tens of kiloyears. Figure from [Abdalla et al. \(2018\)](#).

The recent population study by H.E.S.S. collaboration ([Abdalla et al., 2018](#)) showed a correlation which confirmed that only young and energetic pulsars grow TeV pulsar wind nebulae that are bright enough for detection with available Cherenkov instruments, see left Figure 1.24. In the same study, several other trends between pulsar and TeV wind nebula parameters are found: TeV luminosity of PWNe decays with time while they expand in (angular) size, see right Fig. 1.24. PWNe, whose pulsars are older than several tens of kyr (meaning that their  $\dot{E} < 10^{36}$  ergs $^{-1}$ ) are currently below the detection limit. Additionally, the power-law relation between TeV luminosity and pulsar spin-down power is estimated from the survey as  $L_{1-10\text{TeV}} \sim \dot{E}^{0.58 \pm 0.21}$ , which is consistent with a theoretical value suggested being around 0.5.

**Unidentified sources as potential pulsar wind nebulae candidates** To associate PWN to a VHE source is often a difficult task as TeV PWNe, especially the evolved ones, have large offsets from the parent pulsar and are poorly resolved by the current instruments. Large offsets are due to the evolution of the SNR blast wave in an inhomogeneous medium or the high velocity of the pulsar. X-ray and gamma-ray observations of PWNe offer insights into their complex morphology: electrons emitting VHE (TeV) gamma rays via inverse Compton scattering are usually less energetic than X-ray-emitting ones (which suffer from severe radiative losses), may survive from the early epochs of the PWN evolution thus form a relic PWN emitting in the TeV energies. Relic PWNe have a very faint (or absent) X-ray counterpart. One-third of the Galactic sources are unidentified TeV sources in the sky. The TeV unidentified sources (UNIDs)



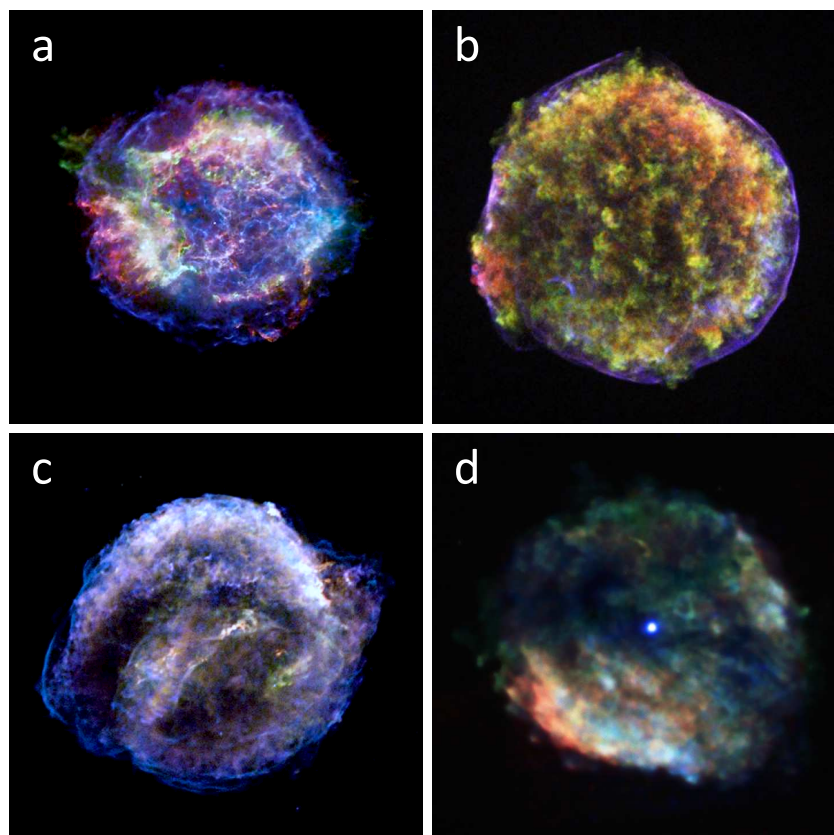


Figure 1.25: Examples of the shell-type SNRs: a) Cassiopeia A b) Tycho's SNR c) Kepler's SNR d) RCW 103. Cas A and RCW are the result of the core collapse SN, while Tycho's and Kepler's are the remnants from SN Type Ia. (NASA)

are the best candidates for finding new PWNe: deeper X-ray observations, energy-dependent morphology studies of TeV source and dedicated pulsar searches within the extent of VHE are crucial to identify PWNe systems.

## 1.7 Short overview of supernova remnants

A supernova (SN) is a powerful stellar explosion which occurs during the last evolutionary stages of a massive star or when a white dwarf is triggered into runaway nuclear fusion. A progenitor star either collapses into a neutron star or a black hole, or it is destroyed. This event is so powerful that the peak optical luminosity of a SN is comparable to that of an entire galaxy, before it fades over a period of weeks or months. Theoretically, there are two basic mechanisms that trigger SN: a detonation of a carbon-oxygen core of a white dwarf as it accretes mass from a companion star and approaches the Chandrasekhar limit or a sudden gravitational collapse of

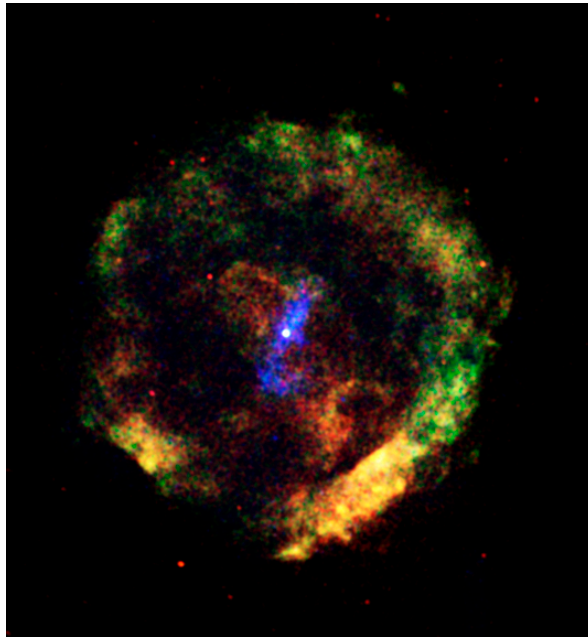


Figure 1.26: G11.2-0.3 is a circularly symmetric supernova remnant with a pulsar at its centre. Chandra's X-ray image shows the pulsar and its pulsar wind nebula seen as high-energy X-rays (blue). A shell of heated gas from the outer layer of the exploded star (the supernova remnant) surrounds the PWN and is visible in the lower X-rays (red and green). Credit: NASA/CXC/Eureka Scientific/M.Roberts et al.

a massive ( $8 M_{Sun} < M < 40 M_{Sun}$ ) star's core. The former mechanism is known as the Type Ia SN, while the latter is classified as Type II (and Ib or Ic). The main difference between the two SN types is the presence of the hydrogen line in the absorption spectrum: if the line is present, SN is classified as Type II, otherwise Type I. Types are also further subdivided according to the presence of other elements or according to their light curves. Core collapse in a massive star occurs when nuclear fusion is no longer able to sustain the core against its gravity. Outer layers of the star are violently expelled during the collapse.

Shell-type SNRs are composed of an expanding SN blast wave that ploughs the ISM and heats the gas to temperatures  $\sim 10^8$  K. The explosion itself releases approximately  $10^{53}$  erg of energy mostly in the form of neutrinos while only 1% of this energy goes to thermal and kinetic energy that drives the expanding remnant. The dynamical evolution of SNR has three stages: I) the free expansion stage, II) the adiabatic or Sedov-Taylor stage and III) the radiative stage. In the free expansion stage, the kinetic energy of the ejecta is governing the evolution of the remnant because the mass of the ejected material is much greater than the mass of the swept-up ISM. Typical velocities for core-collapse SN ejecta are of the order of  $5000 \text{ km s}^{-1}$  (Reynolds, 1998). The second, Sedov-Taylor stage, starts when the pressure of the freely expanding ejecta

is lower than the pressure of the gas heated by the forward shock. This pressure difference forms a reverse shock which now heats the inner ejecta and the outer blast wave continues to expand until it merges with the surrounding ISM. This type of SNRs typically has a symmetric shell morphology, see Figure 1.25. Shell-like remnants emit most of their radiation from a shell of shocked material. A ring-like structure for this type of SNR is observed because when looking at the shell, one sees more hot gas in the line of site at the edges than when looking through the middle. This phenomenon is called *limb brightening*. The Rayleigh-Taylor (RT) instability occurs when two fluids with different densities are in a position where the lighter fluid is pushing the heavier fluid, causing an instability. Water suspended atop the oil layer is a simple example of the RT instability. Composite SNR are the combination of the previous two types: shell-like and a pulsar-powered PWN. The evolution of this system depends on the interaction between the pulsar wind nebula and the reverse shock from the SNR. An example of such a system is a SNR G11.2-0.3, see Fig. 1.26.

## 1.8 This Thesis

In the previous sections, I summarized the current theoretical and observational knowledge of pulsars, putting them into the context of Galactic sources that emit high and very high energy gamma rays. The intriguing and complex system of the pulsar and its nebula can be considered an astronomical laboratory in which the most energetic processes are studied.

In the first part of the Thesis, I am exploring the very high energy emission of gamma-ray pulsars and their nebulae based on the observations performed with the MAGIC telescopes. At the beginning of this research, only one pulsar, the Crab pulsar (PSR J0534+2200), was observed to emit at these gamma-ray energies and the goal was to detect more pulsars like Crab, to better characterize properties of these astrophysical objects and constrain their emission models. The development and construction of the novel hardware component, which lowered the energy threshold of the MAGIC telescopes, enabled the detection of the first pulsar ever detected with the ground-based instrument at VHE (Aliu et al., 2008) and also opened the door for succeeding discoveries. To find a new VHE pulsar, I have first analysed data from the well-known Crab pulsar, to verify the methods and analysis used. Dragonfly pulsar (PSR J2021+3651), as one of the promising candidates for VHE emission, is studied as the second gamma-ray source. Except for young pulsars and their nebulae, I have also studied an unidentified TeV galactic source, HESS J1858+020, which was put forward as an older PWN candidate with a possible offset from the parent pulsar (no obvious pulsar candidate nearby).

In the second part of my Thesis, I have conducted the first deep polarimetric study of Galac-

tic synchrotron emission at low radio frequencies. My study is based on 21 observations of the European Large Area Infrared Space Observatory Survey-North 1 (ELAIS-N1) field using the Low-Frequency Array (LOFAR) at frequencies from 114.9 to 177.4 MHz. Before stacking the data, the observations have to be corrected for the Faraday rotation in the Earth's ionosphere, otherwise the observed polarized emission may be either partially or in exceptional cases fully depolarized. I used the observed polarized diffuse synchrotron emission itself to characterize and additionally to correct for the ionospheric Faraday rotation. Higher signal-to-noise ratio achieved with this method, enables a study of the faint component of the Galactic diffuse emission, which was not visible in a single reference observation. Moreover, applied technique can also be used for studies of the faint polarized sources, including pulsars. The LOFAR telescope usually observes pulsars in a special mode, where a blind periodicity search method is used to search for pulsar candidates. Alternatively, pulsar candidates can be selected using a targeted search, imposing certain criteria, like e.g., high degree of linear or circular polarization, as it was done in the TULIPP (Targeted search, using LoTSS<sup>12</sup> images, for polarized pulsars) survey (Sobey et al., 2022). Thus, combining a targeted search with a described stacking technique which improves sensitivity of the data could be the next step for the future studies of faint pulsars at these low frequencies.

This Thesis is organized as follows. In Chapter 2, the MAGIC telescopes and the main concepts of imaging atmospheric Cherenkov technique, used for data analysis, are described. Chapters 3 and 4 present the results on Crab and Dragonfly pulsars and their respective nebulae. Chapter 5 presents the results on the unidentified TeV HESS J1858+020 source. A method for the detection of faint radio sources (including pulsars) at low radio frequencies with the LOFAR telescope based on the Galactic diffuse emission is explained in Chapter 6. The summary, conclusions, and the outlook of the Thesis are given in Chapter 7.

---

<sup>12</sup>LoTSS stands for LOFAR Two meter Sky Survey

# Chapter 2

## Imaging Atmospheric Cherenkov Technique and MAGIC telescopes

### 2.1 Introduction

In this Chapter I will introduce the MAGIC telescopes, starting from the detection technique used by these ground-based instruments (Sec. 2.2), followed by an overview of the telescopes' hardware components in Sec. 2.3. Furthermore, in Sec. 2.4 the standard analysis chain for MAGIC data is described. An analysis chain is a set of procedures and algorithms applied to the data to detect a gamma-ray source, calculate its spectrum and plot the sky-map. Finally, in Sec. 2.5 the performance of the MAGIC telescopes is summarized.

All data analysed in this Thesis were collected with the MAGIC telescopes, except the data in Chapter 6. The data from Crab and Dragonfly pulsars, described in Chapters 3 and 4 respectively, were observed with the novel Sum-Trigger system (Sec. 2.3.5) and analysed with the standard MAGIC software for pulsar observations. Section 2.4.8 describes how the pulsar light curves are produced. The Dragonfly nebula (studied in Chapter 4) and a pulsar wind nebula candidate, HESS J1858+020 (studied in Chapter 5), are extended sources and were analysed with the MAGIC software analysis chain with few analysis step exceptions explained in Sec. 2.4.10.

### 2.2 Imaging Atmospheric Cherenkov Technique

The Whipple collaboration with its 10m telescope in Arizona (USA) was a pioneer in the very high energy (VHE) gamma-ray astronomy, detecting the first TeV source - the Crab

Nebula in 1989 (Weekes et al., 1989) by using the Imaging Atmospheric Cherenkov Technique/Telescope (IACT). This technique detects the VHE gamma-photons in the energy range of  $\sim 100$  GeV - 100 TeV. There are currently four operating IACT systems: High Energy Stereoscopic System (H.E.S.S., Aharonian et al., 2006) in Namibia, Major Atmospheric Gamma Imaging Cherenkov Telescopes (MAGIC, Aleksić et al., 2016b,a) on the Canary Islands, First G-APD Cherenkov Telescope (FACT, Biland et al., 2014) also on the Canary Islands and Very Energetic Radiation Imaging Telescope Array System (VERITAS, Holder et al., 2008) in Arizona. Around 90% of the VHE sources listed in TeV Gamma-ray source catalogue<sup>1</sup> were discovered by one of the major IACTs. Under construction is also the next generation of telescopes - *Cherenkov Telescope Array (CTA)*<sup>2</sup> (Actis et al. 2011; Cherenkov Telescope Array Consortium et al. 2019) which is being built on the technology of the current generation of IACT but with 10 times greater sensitivity.

Earth's atmosphere is opaque to the gamma rays. A very high energy gamma ray (or cosmic ray) entering the atmosphere, produces a cascade of relativistic charged particles. This phenomenon, called **Extensive Air Shower (EAS)** (Rossi & Greisen, 1941), enables indirect detection of the gamma rays with the ground-based telescope. The relativistic charged particles from the cascade that are faster than light in the air will generate a very short flash of a bluish light called *Cherenkov* radiation. IACT camera detects Cherenkov photons and based on the distribution and arrival times recorded by the high-frequency cameras, one can reconstruct the energy and direction of the primary gamma-ray particle. In contrast to IACT's indirect detection of VHE gamma ray from galactic and extragalactic sources, satellite-borne detectors like *Fermi-LAT* (Atwood et al., 2009) or *AGILE* (Tavani et al., 2008), detect gamma rays directly via pair production. Space detectors have small effective areas of  $\sim 1$  m<sup>2</sup> thus efficiently operate up to  $\sim 10$  GeV. Above that energy range, the photon flux of a typical astrophysical source significantly drops. Unlike satellites, when gamma ray (or cosmic ray) initiates an EAS, the ground-based Cherenkov telescopes use the atmosphere as a calorimeter and because of the shower geometry and mirror sizes have a much larger effective area,  $\sim 10^5$  m<sup>2</sup>. So, the main challenge for the ground-based Cherenkov detectors represents the discrimination between gamma rays and cosmic rays, which both generate EAS.

### 2.2.1 Extensive Air showers

When a high energy cosmic ray enters Earth's atmosphere, it will interact with molecules through electromagnetic or hadronic processes (Nishimura, 1967), which will initiate an exten-

---

<sup>1</sup><http://tevcat.uchicago.edu/>, Wakely & Horan (2008)

<sup>2</sup><https://www.cta-observatory.org>

sive particle air shower - EAS. Depending on the type of the primary particle (which can be a proton, nucleus, an electron, a photon or rarely a positron) the shower will evolve through an electromagnetic cascade or through hadronic processes creating secondary particles. These secondary particles are collimated along the direction of the primary.

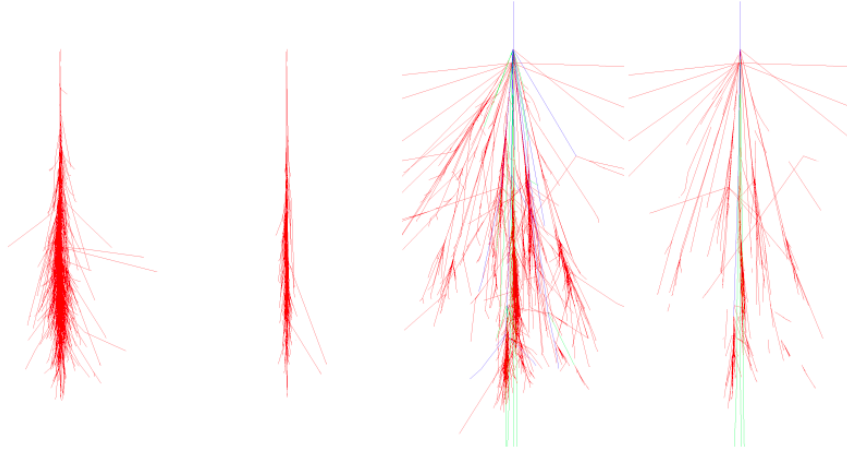


Figure 2.1: Simulations of air showers, from left to right: a) secondaries of a 50 GeV photon primary particle b) same, but only secondaries that produce Cherenkov light are plotted c) secondaries of a 200 GeV proton primary particle d) same, but only secondaries that produce Cherenkov light are plotted. In all figures, the particle type is colour coded: red = electrons, positrons, gamma rays; green = muons; blue = hadrons. Figure is taken from [Hrupec \(2008\)](#).

The EAS initiated by a primary gamma ray evolves through electromagnetic cascades via i) a pair production creating an electron-positron ( $e^\pm$ ) pair in the Coulomb field of atmospheric nuclei, or via ii) bremsstrahlung from  $e^\pm$  in the same Coulomb field producing new very high energy gamma ray. The interaction of the particles depends on the path length and the density of the medium and is expressed by the atmospheric depth,  $X$ , given in the units of  $\text{g cm}^{-2}$ . This parameter indicates the mean amount of matter that an electron must traverse to lose  $1/e$  off its energy via bremsstrahlung. Because the two processes have approximately the same length scale (for a pair production it is  $\frac{7}{9}X$ ) the shower structure is symmetric and narrow and follows the direction of the primary particle ([Groom & Klein, 2000](#)). Figure 2.1 shows simulations of an electromagnetic and hadronic shower initiated by 50 GeV photon and 200 GeV proton. The difference in shower geometries is more pronounced when only secondary particles which produce Cherenkov light are plotted - the hadronic showers are much wider. The shower maximum,  $H_{max}$  is defined as the height above sea level where the number of shower particles reaches maximum.

EAS develops in the atmosphere, which is an inhomogeneous medium, so  $H_{max}$  depends

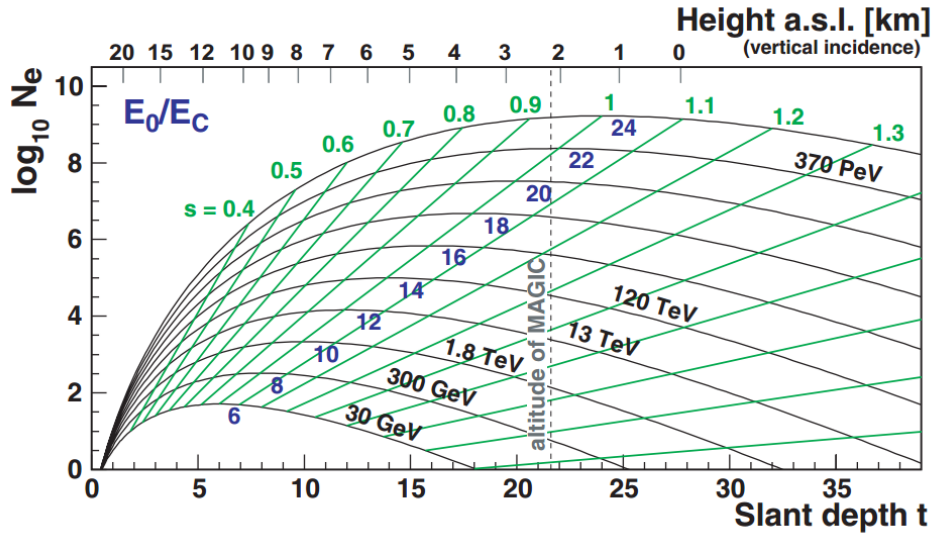


Figure 2.2: Longitudinal development of an EAS initiated by a gamma ray. The number of secondary electrons in relation to radiation length and the height above sea level for different photon energies is shown. The green lines indicate the shower age ( $s=0$  is the start of the shower,  $s=1$  at the shower maximum). The altitude of the MAGIC telescopes is indicated. Figure is taken from [Wagner \(2006\)](#).

(weakly) on the energy of the primary particle  $E_0$ :  $H_{\max} \propto \log(\log(E_0))$ . In Figure 2.2 a size of the electromagnetic shower, characterized by a number of secondary electrons  $N_e$ , is shown. For example, the shower maximum for the primary gamma-ray energy of 100 GeV up to 10 TeV is between 6 - 9 km. After the shower maximum, EAS follows the extinction phase - ionization losses slowly become dominant over the loss via pair production.

If a primary particle entering the Earth's atmosphere is a cosmic ray, it will initiate a hadronic air shower while interacting with nuclei in the atmosphere. The interactions between hadrons produce several types of secondary particles, mainly pions (90%) but also kaons and light baryons ( $p$ ,  $\bar{p}$ ,  $n$ ,  $\bar{n}$ ). Neutral pions  $\pi_0$  have a very short lifetime and decay instantly into two photons inducing an electromagnetic cascade as a sub-shower in a primary hadronic shower, see Figure 2.3. Charged pions  $\pi_{\pm}$  will eventually decay into muons ( $\mu_{\pm}$ ) and neutrinos/antineutrinos ( $\nu$ ,  $\bar{\nu}$ ). Due to the relativistic effects, muons can reach the surface before decaying. Hadronic showers are more complicated and are wider around the shower axis than electromagnetic showers (see the right figure in 2.1).

As mentioned earlier, the main challenge for the IACT experiments is to differentiate between a gamma-ray initiated air shower and one initiated by a cosmic ray which, in this case, represents the background. The background is eliminated by the background rejection method, based on the physical differences between the two types of air showers. Hadronic showers are



much wider and irregular than electromagnetic showers due to the much higher transverse momentum of hadronic interactions and multiple scattering points. Moreover, due to the higher absorption length in the air, hadronic showers develop their shower maxima deeper in the atmosphere compared to electromagnetic showers of the same primary energy (Weekes et al., 1989).

### 2.2.2 Cherenkov radiation

Whenever a charged particle passes through a dielectric medium with a speed greater than the speed of light in the same medium, a characteristic bluish light is emitted. The electromagnetic radiation produced that way is called *Cherenkov* radiation, named after physicist Pavel Cherenkov, who discovered it in 1934. Particles with velocities larger than  $c/n$  ( $c$  is the vacuum speed of light,  $n$  is a refractive index of the medium) polarize the medium which emits the spherical electromagnetic waves along the track of the relativistic particle (see Fig. 2.4). Cherenkov radiation is emitted in a cone at an angle  $\Theta_c$  which can be expressed as  $\cos(\Theta_c) = \frac{1}{n\beta}$ , where  $\beta$  is defined as a ratio between the speed of the particle and speed of the light in vacuum,  $\beta = v/c$ . At the sea level (in the air),  $\Theta_c$  is  $\sim 1.5^\circ$  with linearly decreasing trend so that at  $\sim 30$  km height,  $\Theta_c$  is  $\sim 0.2^\circ$  (de Naurois & Mazin, 2015). The emitted Cherenkov photons are spread

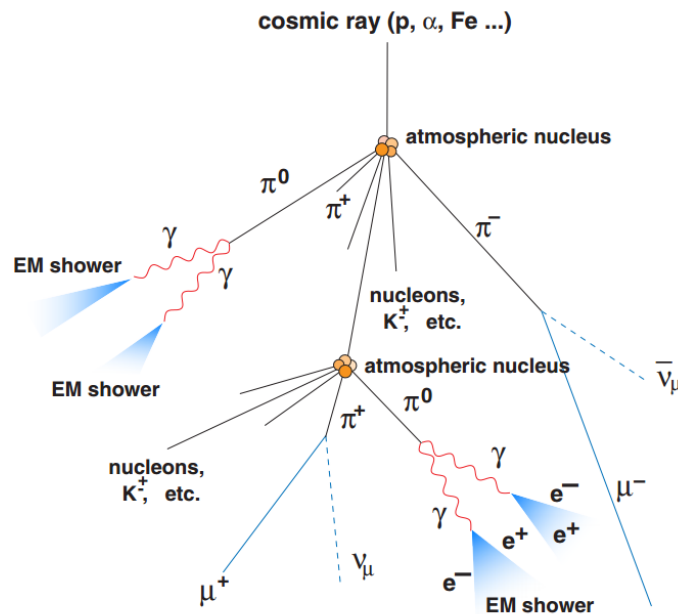


Figure 2.3: Scheme for the development of hadronic shower in the air. Figure is taken from Wagner (2006).

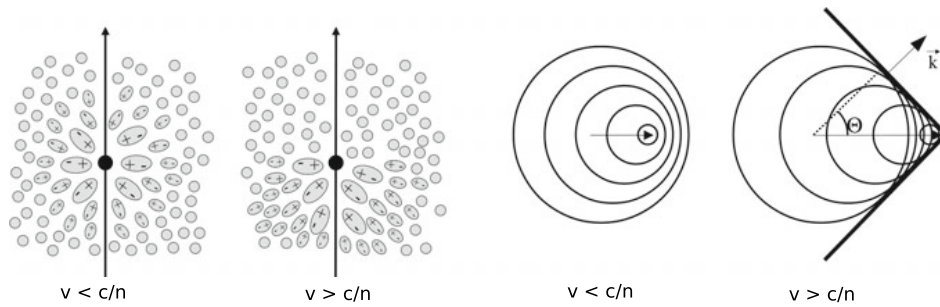


Figure 2.4: Left: Polarization of the medium with refractive index  $n$  when a charged particle passes through. While the particle with  $v < c/n$  produces symmetric polarization of the surrounding medium, particles with  $v > c/n$  are faster than the electromagnetic information that induces the polarization. As a result, a photonic shock wave is produced and is emitted in the narrow cone along the incidental direction of the particle (right). Figure from [de Naurois & Mazin \(2015\)](#).

on the ground over a disc called a light pool. For a vertical incident photon, this light pool has a radius of  $\sim 120$  m, and it is independent of the energy of the primary particle.

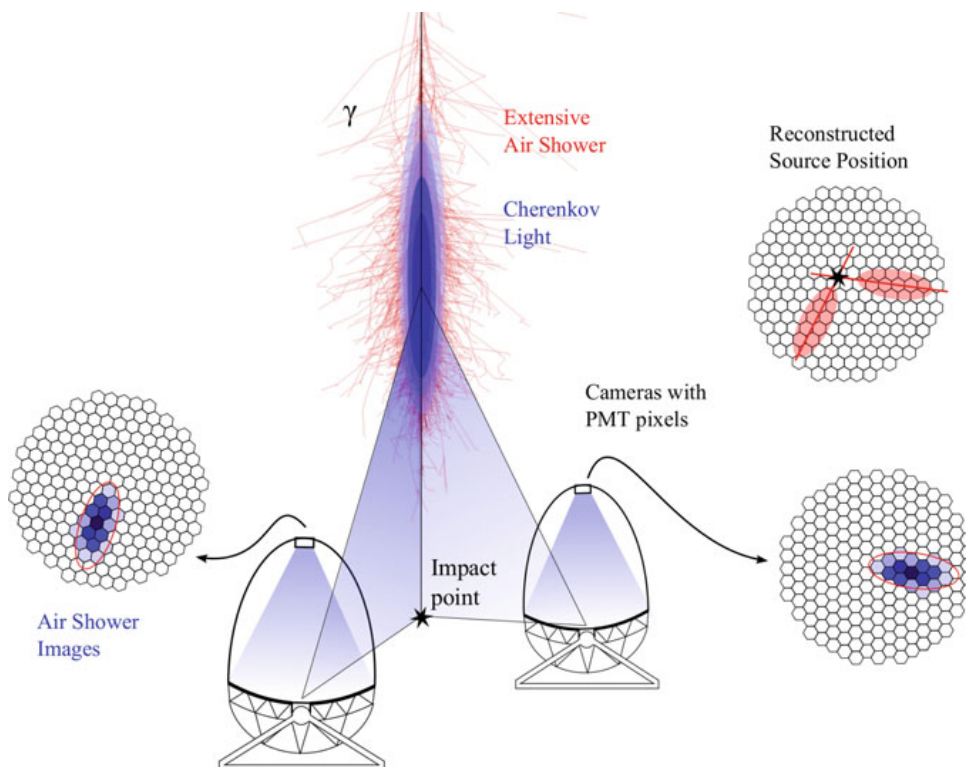


Figure 2.5: IACT technique shown: telescopes detect Cherenkov light from the EAS. Shower images can be combined and stereo image parameters are obtained. Figure is taken from [Fruick \(2015\)](#).

To reconstruct the energy and the direction of the primary gamma ray, Cherenkov light emitted by the secondary particles in the EAS is reflected by the telescope mirrors and focused onto the camera of the telescope(s). The camera of a Cherenkov telescope is typically equipped with hundreds of photodetectors (PMTs). The characteristic image of the photon-induced shower in the camera is ellipse-shaped, with the main axis representing the shower axis, see Figure 2.5.

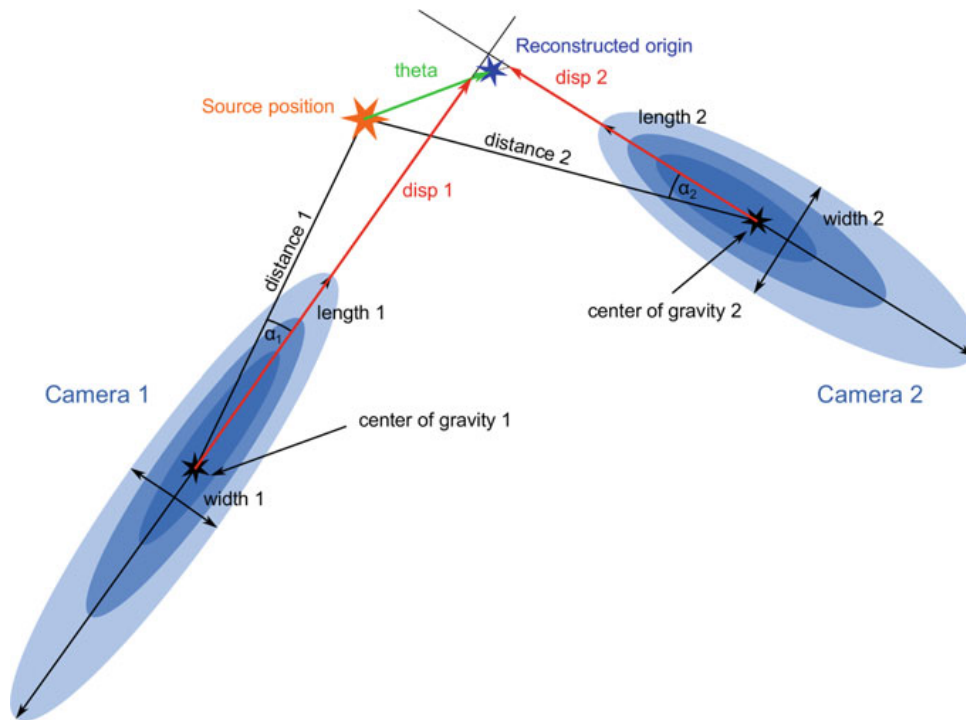


Figure 2.6: Illustration of the reconstruction of the stereo parameters. Two cameras are shown, each with the characteristic image of the same shower. An orange star indicates the source position and a blue star is the reconstructed position. The angular distance between the sky position of the source and the reconstructed direction of the gamma ray is denoted  $\theta$ . Figure is taken from [Fruck \(2015\)](#).

The image is then parameterized by characteristic Hillas parameters ([Hillas, 1984](#)), which differ for hadronic showers and provide the basis for background rejection. As the main axis represents the shower axis, one can estimate the incoming direction of the primary gamma ray. With stereoscopic observation, the reconstruction of the direction of the primary is more precise. For the details of the stereoscopic scheme, see Figure 2.6.



Figure 2.7: The MAGIC telescopes at the Roque de Los Muchachos Observatory, Canary Islands, Spain.  
Credit: Miguel Claro

## 2.3 The MAGIC telescopes: hardware components

The MAGIC (Major Atmospheric Gamma-ray Imaging Cherenkov, [Aleksić et al., 2016b](#)) collaboration operates with two MAGIC telescopes (see [Figure 2.7](#)) located in La Palma, Canary Islands (Spain) at the Roque de Los Muchachos Observatory above 2200 m a.s.l. Originally, one telescope was built in 2002 at the same place where the previous experiment, HEGRA (High Energy Gamma-ray Astronomy) was established. MAGIC I was, at that time, the biggest Cherenkov telescope in the world with the 17-m mirror dish and aimed to lower the energy threshold down to  $\sim 50$  GeV to overlap with space-based observations. With just one telescope in operation, integral flux sensitivity was 1.6% of the Crab Nebula flux in 50 hours of observation ([Aliu et al., 2009](#)). Many new technologies have been developed for the MAGIC construction, including some major innovations concerning support frames of carbon fibre made for a minimum weight and maximum stiffness, fast electronics, automatic controls of different subsystems, detectors that use techniques from accelerator experiments, active mirror surface,

etc. More details can be found on the MAGIC web page<sup>3</sup>. The second telescope, MAGIC II, was built as an improved version of the first telescope and is in operation since 2009 (Aleksić et al., 2012). In the stereo mode, sensitivity improved up to  $(0.76 \pm 0.03)\%$  of Crab Nebula flux for energies greater than 290 GeV in 50 hours of observations.

MAGIC telescopes went through a major upgrade in 2012. Due to the funding constraints at the time of MAGIC I construction, the camera was built combining modules with 1- and 2-inch pixels and the trigger region was restricted to the central region of the field of view (FoV,  $\sim 0.9$  deg). During the upgrade, the MAGIC I camera was replaced by a new one, now equipped with homogeneous 1-inch pixels and with the enlarged trigger region of  $\sim 1.2$  deg, the same as the MAGIC II camera. A better flux sensitivity to the extended sources was expected with the enlargement of the trigger region, where the 1-inch pixel cameras improved the angular resolution and the image parametrization, which resulted in the better reconstruction of the direction of primary shower particle. The readout systems in both telescopes were also changed in the upgrade (for details, see Sec. 2.3.6). This reduced the dead time per event by a factor  $\sim 10$ . Overall, after the major upgrade, integral flux sensitivity of  $(0.66 \pm 0.03)\%$  for the MAGIC telescopes was reached for 50 hours of observations above 220 GeV (Aleksić et al., 2016a).

### 2.3.1 Drive system and structure

MAGIC uses an Altitude-Azimuth mount, running on a circular rail made of steel. The mirror support structure is made from carbon fibre, weighing only 5 tons without mirrors, reinforced with plastic tubes, based on a rod-and-knot system. This design enables a fast response of the telescopes to record signals from the sudden GRB. Azimuthal (altitude) movement is achieved by two (one) electric driving motors and re-orientation of telescopes to any point in the sky is possible in about 40 seconds with average speed. In the case of a GRB, it takes only 25 seconds to reposition the telescope with maximum speed. The camera is mounted on a single aluminium tubular arc, secured against transverse movements by prestressed steel cables. Angular position is cross-checked by the *Starguider camera* mounted in the centre of the mirror dish and described later on. The azimuth (Az) range covers  $-90^\circ$  to  $318^\circ$  and the zenith (Zd) range is available from  $-70^\circ$  to  $105^\circ$ . The Az (Zd) movements of the telescopes are possible due to the three 11 kWh motors. The gamma-ray energy threshold of the telescopes strongly depends on the zenith angle of the observations. For example, high zenith angle observations mean more atmospheric absorption of Cherenkov light, thus to obtain the lowest possible energy

---

<sup>3</sup><https://magic.mpp.mpg.de/newcomers/technical-implementation/>

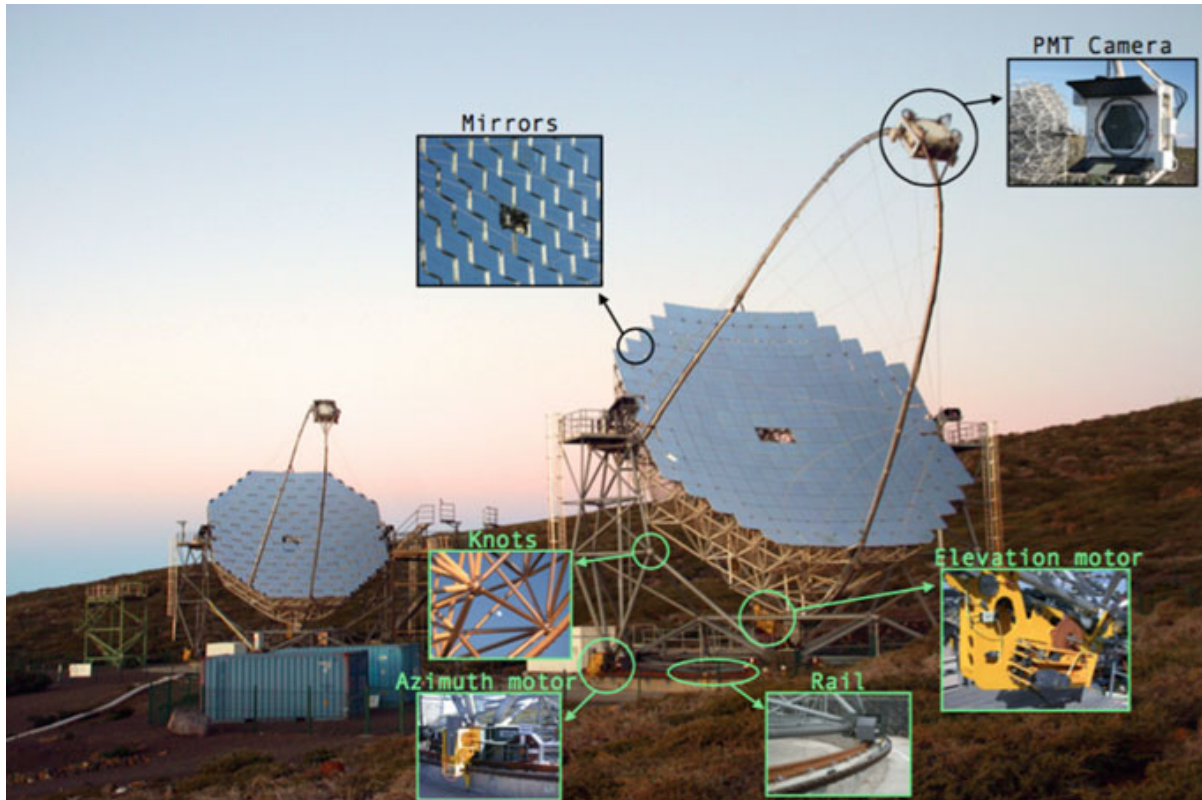


Figure 2.8: The MAGIC telescopes showing insets with the main hardware subsystems. Picture adapted from [Fernandez Barral \(2017\)](#).

threshold, which will be later important for pulsar observations, only events with low zenith angles ( $< 30^\circ$ ) are chosen (for details, see [Aleksić et al., 2016b](#)). The pointing direction of the telescopes is determined by the three 14-bit shaft encoders with an accuracy of  $\sim 0.02^\circ$  and is repeatedly monitored during observations with the *Starguider camera*. This camera is based on the Charge-Coupled Device (CCD) located in the middle of the dish (see Figure 2.8 with telescope's main hardware parts). Thus, the *Starguider camera* is used primarily for pointing corrections, but it also monitors the ratio between the observed and the expected number of stars (from the catalogue) in the field of view. The ratio is used as the information for atmospheric conditions.

### 2.3.2 Mirrors

Both telescopes have an active reflective mirror surface of 236 square meters, and each mirror element is a diamond-milled aluminium with quartz coating (see Fig. 2.9). Four mirror elements are mounted and pre-adjusted on a  $1 \times 1$  m panel. The panels are equipped with a 13 kW

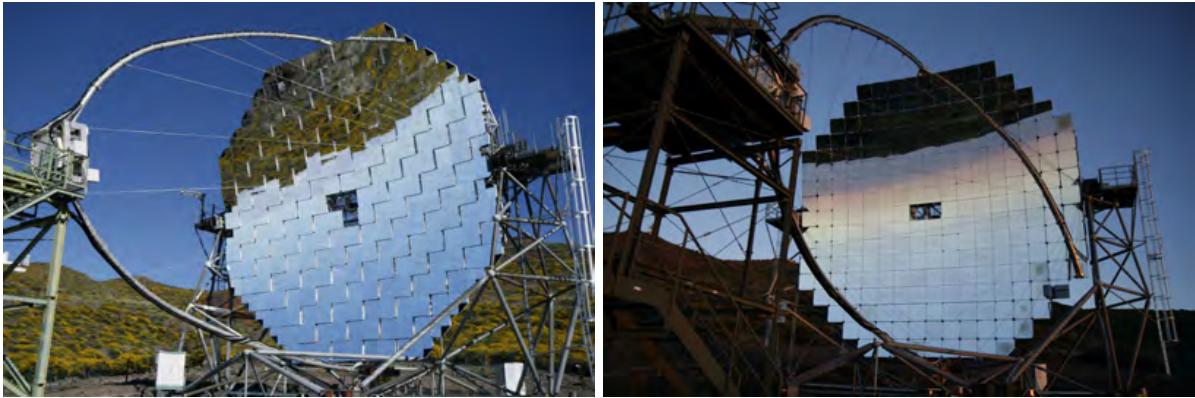


Figure 2.9: The reflecting, parabolic surfaces are composed of mirrors: MAGIC I is on the left and MAGIC II on the right. Credit: R. Wagner.

heating system, which prevents dew deposition and icing of the mirror surface. Each panel has a 3-point mirror mount: one fixed point and two computer-controlled actuators that can move the panel in any direction. Active Mirror Control (AMC) system automatically adjusts the mirror panel orientation and in that way ensures good focusing for each telescope pointing. The focal length and diameter of parabolas are both around 17 m, so the focal length to diameter ratio is  $f/D=1.03$ . The average mirror reflectivity, focused on a spot of 2 cm radius at a wavelength between 290-650 nm, is around 80%.

### 2.3.3 Camera

The MAGIC camera consists of 1039 ultra-sensitive photomultiplier tubes (PMT) which are arranged in a circle of about 1 meter in diameter. The field of view in the sky is thereby 3.5 degrees. Each PMT has a diameter of 25.4 mm and consists of a hemispherical photocathode and 6 dynodes with a hexagonal Winston cone mounted to avoid gaps between the circular pixels (see Figure 2.10). PMTs are constructed in a way to allow observations under moderate moonlight without damaging the dynodes, and their quantum efficiency (QE) has been pushed to or beyond existing limits especially for this experiment. The development of the PMTs for the MAGIC telescopes was crucial for the success of the experiment. The performance of the telescopes has been further improved after the major upgrade (in 2011 and 2012) with the implementation of the next generation of PMTs. The PMTs are Hamamatsu R10408 with the 6-dynode system, whose QE is around 32-34% at 350 nm (Nakajima et al., 2013). The High Voltage (HV) of 1.25 kV is produced by the Direct Current (DC) - DC converter. The calibration of both cameras is done through uniform illumination of the PMTs with well-characterised light pulses of different intensities. The light is produced by a calibration box installed at the centre

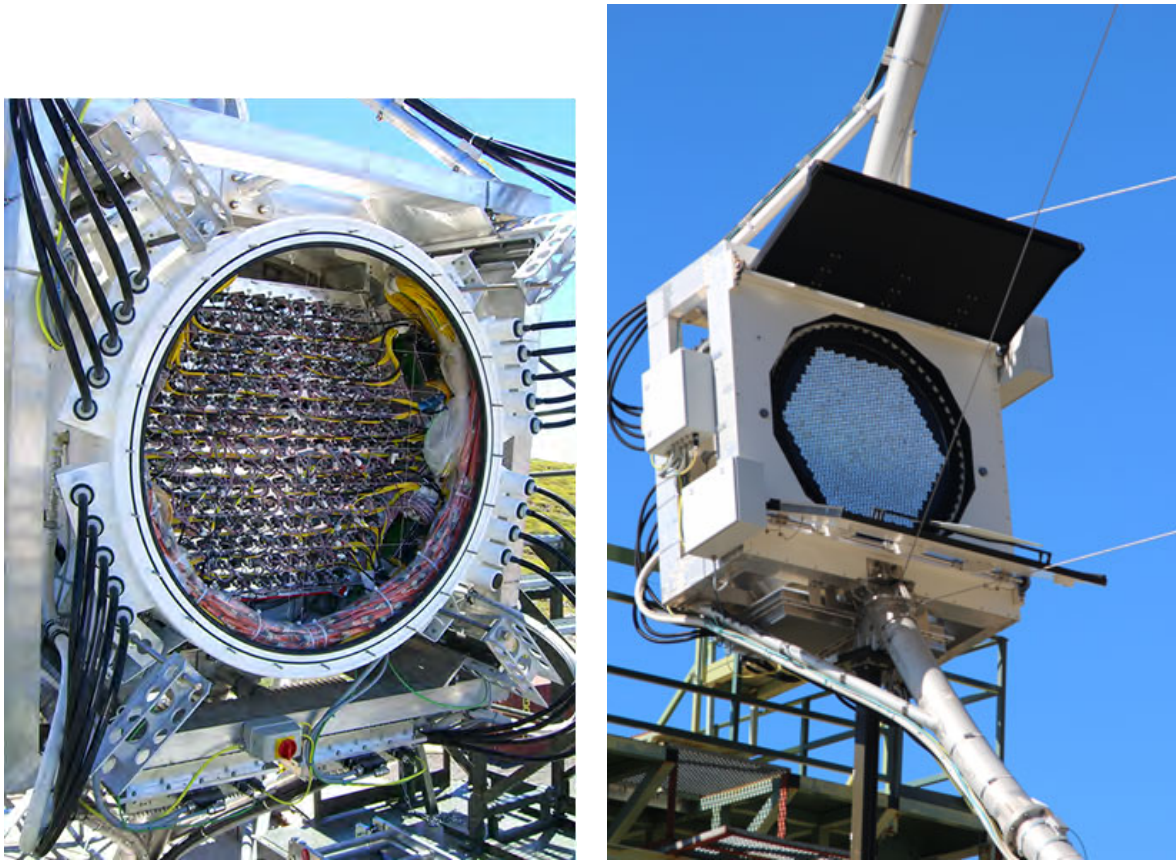


Figure 2.10: MAGIC camera from the backside and from the front. Credit: R. Wagner.

of the mirror dish, about 17 meters away from the camera plane.

### 2.3.4 Receivers and triggers

The electrical signal from PMTs is amplified and transmitted through optical fibres. The fibres, which are 162 m long and protected with UV resistant PVC covers, transmit analogue signals from PMTs to the readout and trigger electronics in a dedicated data acquisition building - counting-house (CH), see Figure 2.8, for the schematic view of data acquisition. Here, the signal is converted back into electric via photodiodes and sent to the trigger and the readout system simultaneously. The key role of the trigger system is to discriminate between the signal and the background.

**Level-0 (L0) trigger** is a digital signal in a channel, generated if a pulse above a certain Discriminator Threshold (DT) is detected. This is strictly related to the Individual Pixel Rate (IPR) of a certain channel.

**Level-1 (L1) trigger** receives the input signals from the L0 trigger (from each pixel, respec-



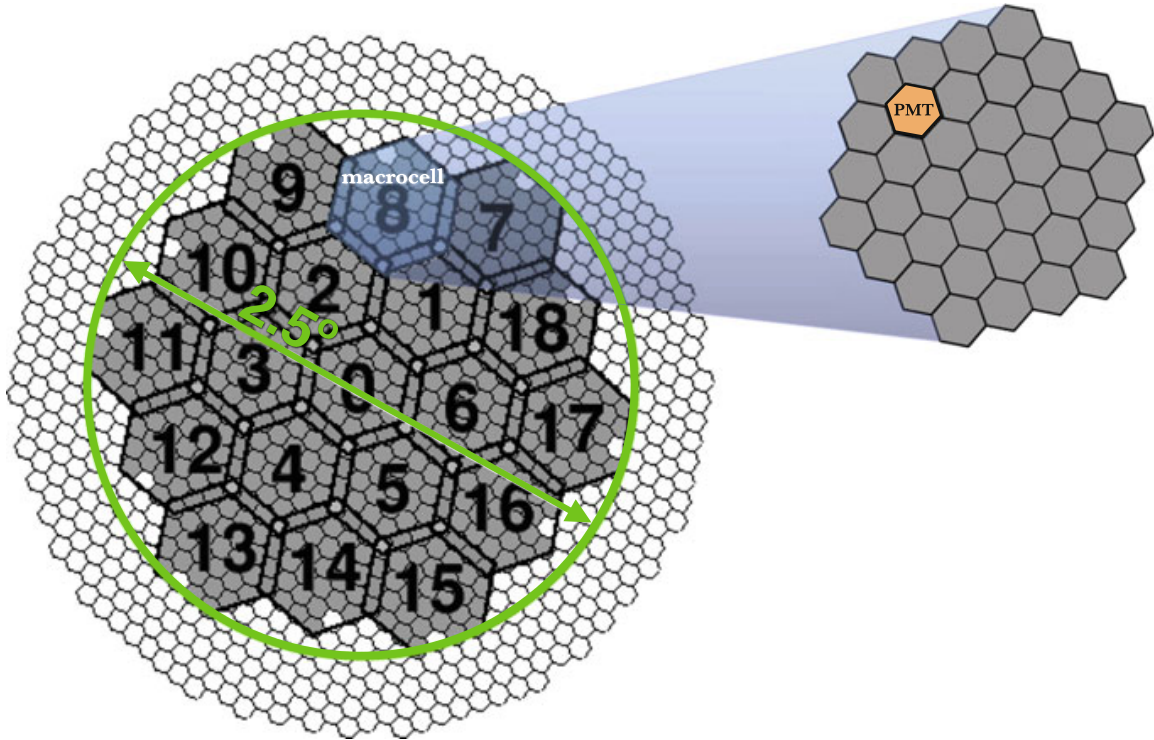


Figure 2.11: The MAGIC camera and the trigger region: distribution of the L1 macrocells, each with 37 PMT pixels equipped with hexagonal Winston cones. The trigger FoV is  $2.5^\circ$  diameter. The figure is taken from [Fernandez Barral \(2017\)](#).

tively) and searches for the time and spatial coincidence between the neighbouring pixels. The L1 trigger works over 19 partially overlapping hexagonal trigger cells, dubbed macrocells (Fig. 2.11), each composed of 37 PMTs. If  $2 \leq n \leq 4$ , neighbouring pixels, defined as  $n$  Next Neighbour (nNN), in any macrocell, contains a signal above the DT, the L1 trigger receives a signal. Hence, to accept the trigger in a macrocell, a pixel that exceeds DT must be in contact with at least other two triggered PMTs. The trigger logic is based on the fact that Cherenkov flashes, produced by the secondary particles in the atmospheric showers, show very tight temporal and spatial correlations, while Night Sky Background (NSB) fluctuations don't. The L1 signal from each macrocell that satisfies the nNN condition is further processed by the Trigger Processing Unit (TPU).

**Level-3 (L3) trigger** applies only for stereo observations. It receives the input from the TPU of each telescope. If only one telescope was triggered, the event is discarded. The stereo coincidence is applied to L1 signals after adding a time delay accounting for the cascade arrival time difference at each telescope. If L1 signals from MAGIC I and II are timed less than 180 ns, then the event is accepted and the readout begins.

### 2.3.5 Sum-Trigger II

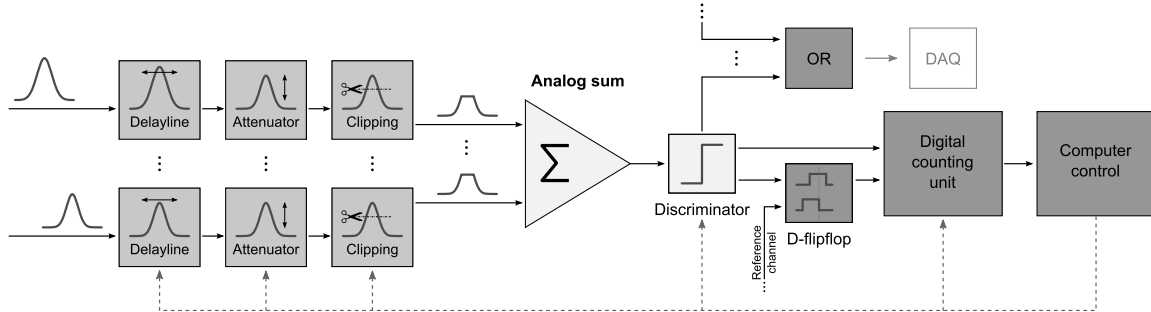


Figure 2.12: The working principle of the Sum-Trigger: clipped channels from a macrocell are summed and then digitized. From [Haefner et al. \(2011\)](#).

For some observations, a low threshold of the telescope is a necessity. For example, due to the absorption of high energetic gamma rays by the extragalactic background light (EBL), distant gamma-ray sources, like high-redshift active galactic nuclei (AGNs) or gamma-ray bursts (GRBs), can only be observed at lower-energy gamma rays. Moreover, pulsars have a very steep gamma-ray spectrum above 10 GeV, so these observations profit from the better performance of the telescopes at lower energies as well. For the reasons mentioned above, a novel trigger dubbed the *Sum-Trigger* was designed and incorporated, at first only for MAGIC I ([Rissi et al., 2009](#)), and afterwards upgraded and installed for both of the telescopes ([Haefner et al. 2011](#); [Dazzi et al. 2021](#)). Sum-Trigger (SumT) II is a conceptually very similar trigger system as Sum-Trigger built for MAGIC I which made the discovery of Crab pulsar above 25 GeV possible ([Aliu et al., 2008](#)). This new analogue trigger system amplifies and sums up the signals in the macrocell of neighbouring pixels using analogue electronics (see Fig. 2.12). What distinguishes the Sum-Trigger from other trigger systems is the discriminator applied to the analogue sum of the pixels and not to each individual pixel. The condition for the standard MAGIC trigger is the threshold of  $\sim 4.5$  photoelectrons (ph.e.), which the three neighbouring pixels containing the signal have to surpass ([Dazzi et al., 2015](#)). The Sum-Trigger's main concept is to divide the camera into macrocells each with 19 pixels, which are partially overlapping. Signals are summed up and the final trigger decision is derived from the summed signals of one patch. Even when dominated by the NSB fluctuations, all pixels within the macrocell are taken into the trigger decision, improving a signal-to-noise ratio. This optimization is performed with the Monte Carlo simulations (trigger geometry, thresholds, etc.) to maximize the detection efficiency for gamma-ray initiated air showers of a few tens of GeV.

The Sum-Trigger II system indeed improved the performance of the MAGIC telescopes at

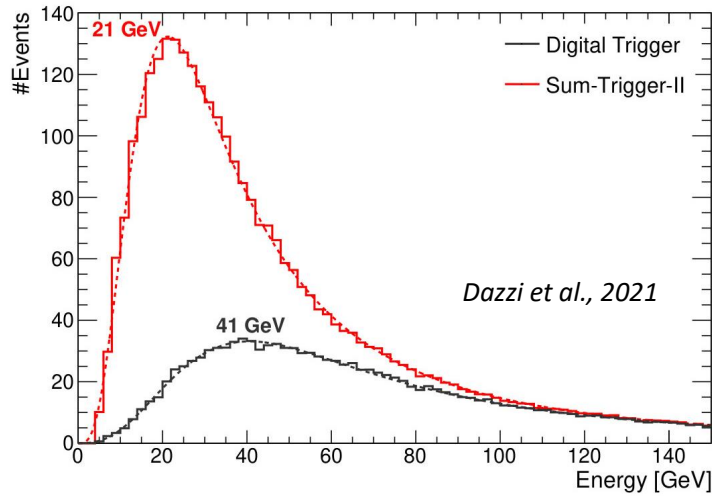


Figure 2.13: Monte Carlo simulations show the energy threshold comparison for the Sum-Trigger and standard, digital trigger. From [Dazzi et al. \(2021\)](#).

energies below 100 GeV. The trigger energy threshold of the novel Sum-Trigger is  $\sim 21$  GeV compared to  $\sim 41$  GeV of the digital trigger ([Dazzi et al., 2021](#)), see Fig. 2.13.

### 2.3.6 The readout electronics

To efficiently detect short (of the order of 1 ns) Cherenkov flashes produced from secondary particles in the EAS and thus decrease the noise exposure, the requirement for the fast time response and a high sampling rate of the system is a priority. The electronic chain of the MAGIC telescopes is schematically shown in Fig. 2.14.

The signal produced in the camera's PMTs is split, with one branch going to the trigger system and the other going to the readout system. The readout system records the signal and passes the information on to the Data Acquisition System (DAQ) if the trigger system detects the gamma-like event. The signal going to the readout system is intentionally delayed a few ns due to the time needed for the trigger response.

Before the upgrade, the readouts of the telescopes were based on a Flash Analogue to Digital Converter (FADCs) and on the Domino Ring Sampler version 2 (DRS2) for the MAGIC I and MAGIC II, respectively. FADC was expensive and bulky, whereas the DRS2 chip was inexpensive but noisy, non-linear and temperature-dependent. During the major upgrade, both trigger systems were exchanged for Domino Ring Sampler version 4 (DRS4) ([Sitarek et al., 2013](#)) and are currently in use. DRS4<sup>4</sup> operate at the sampling speed of 2 GSample/s which

<sup>4</sup><http://drs.web.psi.ch/>

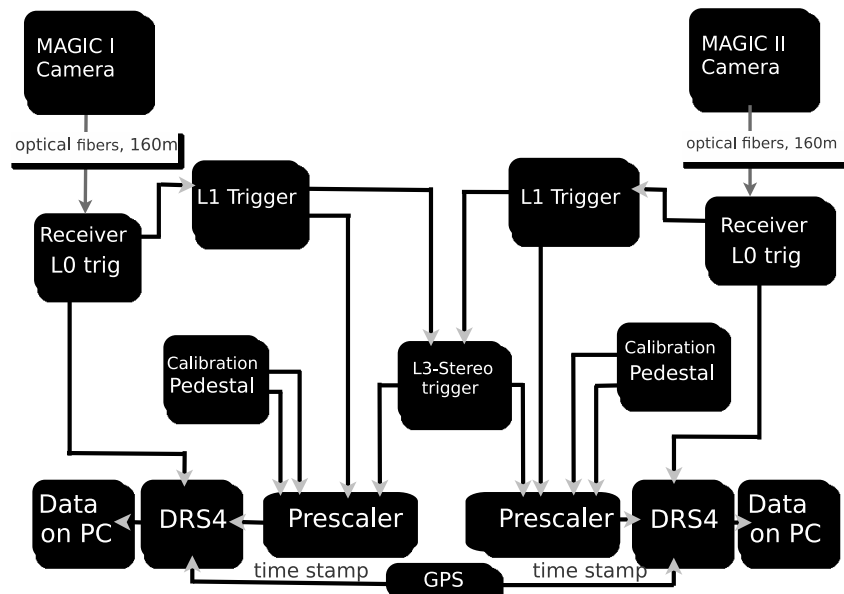


Figure 2.14: Scheme of the electronic chain for the MAGIC telescopes, figure taken from [Sitarek et al. \(2013\)](#)

allows the use of the timing information recorded air showers.

The final data acquisition to the storage disks is done by the DAQ PCs. The signal needs to be calibrated, i.e., it has to be converted to the physical quantity of photoelectrons. The calibration of the readout signals is done with the interleaved calibration laser pulses at 355 nm, and each stored event is marked with the time stamp from the rubidium clock synchronized with the Global Positioning System (GPS).

### 2.3.7 Telescope observations

For the ground Cherenkov telescopes, two observing strategies are commonly employed for astronomical sources: the ON/OFF method and the *wobble* mode method. When observing the source in ON mode, the telescopes are pointing directly at the source, with the source at the camera centre. In OFF observations, the telescopes are pointing to the region of the sky where no source is expected (background) to estimate the signal strength of the source in the ON observations. The OFF region should be relatively close to the source and has to be observed under a similar zenith range as the source.

The second method, the *wobble* or the *false-source tracking* mode, is the observational method where the source is slightly offset from the camera centre, ([Fomin et al., 1994](#)). The

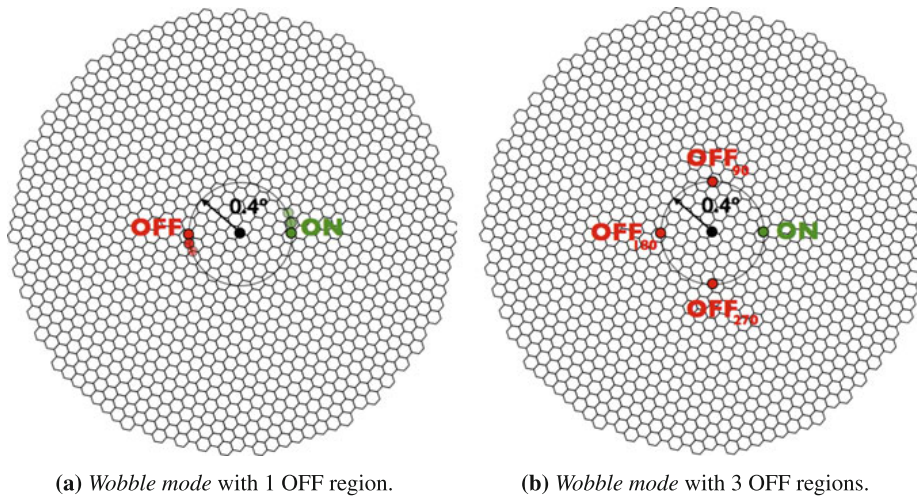


Figure 2.15: The observational *wobble* mode method where the telescopes are not pointing directly (like in ON/OFF observations) but slightly off from the source. The black circle marks the centre of the camera, located at  $0.4^\circ$  from the source - ON region (green circle). Since the source is moving in the sky, it remains placed at this distance from the centre of the camera, resulting in a circular movement around the camera centre. The background is simultaneously observed from one region (left plot) or from three regions (right plot). When using 1 OFF region, it is taken  $180^\circ$  from the source (at the opposite direction from the source), while when using 3 OFF regions the regions are separated the same distance one from the other, all of them  $0.4^\circ$  from the camera centre at the angles  $90^\circ$ ,  $180^\circ$  and  $270^\circ$  counting clockwise from the ON region. Plot taken from [Lopez-Coto \(2015\)](#).

standard offset for MAGIC telescopes is  $0.4^\circ$  and typically 4 wobble positions are used to reduce possible systematics introduced by using one half of the camera for the signal and the other half for the background estimations (the source position in the camera is changed every 20 minutes). The wobble mode method has the advantage over the ON/OFF method as it saves time and ensures identical observing conditions by simultaneous observations of the source and the background (see Fig. 2.15).

## 2.4 MAGIC data analysis

The data collected with the MAGIC telescopes are analysed with the software package MARS (Magic Analysis and Reconstruction Software, [Zanin, R. 2013](#)). This package consists of the container classes for storing data, classes with the analysis algorithms and many executables to run the analysis parts. In this Section, all steps of the MAGIC data analysis chain are described in brief and a scheme is shown in Fig. 2.16. The foremost goals of the MAGIC analysis are a) to detect a gamma-ray signal b) to calculate the energy spectrum of a detected

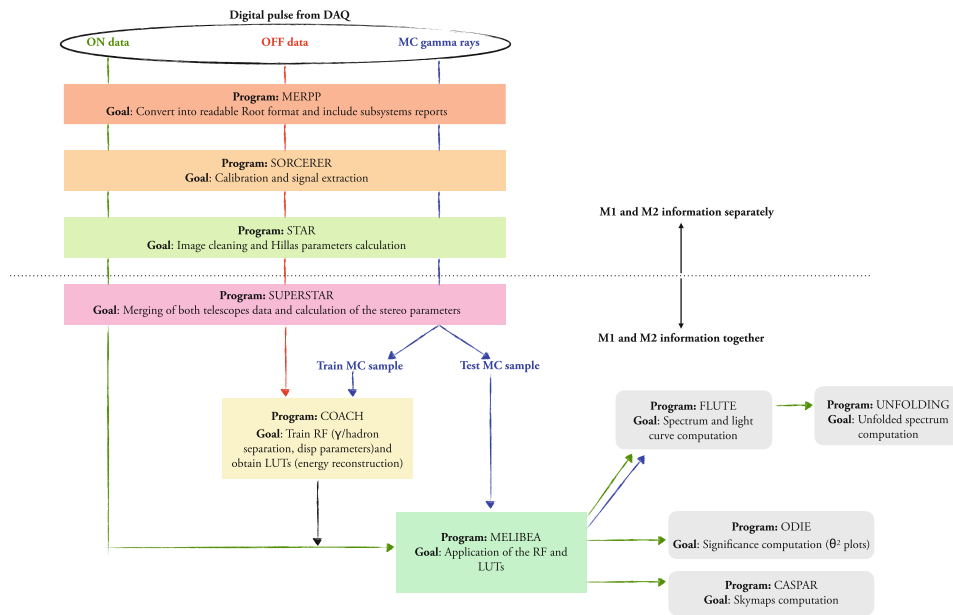


Figure 2.16: The observed data with the MAGIC telescopes is analysed with the software called MARS (Magic Analysis and Reconstruction Software). In the above scheme, all the analysis steps are shown. The figure is taken from [Fernandez Barral \(2017\)](#).

source and c) to produce a gamma-ray skymap/ lightcurve (in case of pulsars). The analysis chain is done in the following sequence:

- **Pre-processing:** Converting RAW files to MARS root format, using the program *Merpp*.
- **Calibration:** PMT signal is converted to photoelectrons and for each signal, the arrival time is estimated, using the program *Sorcerer*.
- **Image cleaning and parametrization:** Using image cleaning algorithms, program *Star* removes NSB photons and extracts signals from the gamma-ray shower with timing and positional information. After cleaning, each event is parametrized with *Hillas parameters*. Stereo image parameters are calculated in the program *SuperStar*.
- **Quality selection:** Data quality selection is performed by the MARS executable *quate*. It calculates the average values of the parameters which are important for signal extraction. With *quate* it is also possible to select the data according to the weather criteria: cloudiness, atmospheric transmission monitored with LIDAR <sup>5</sup>, wind gusts, etc. The analyser

<sup>5</sup>Light Detection And Ranging (LIDAR) is a system that uses laser pulses to determine the distance and properties of clouds and aerosols by measuring the arrival time and intensity of backscattered light. Thereby LIDAR estimates the attenuation of Cherenkov light caused by the clouds, for details see [Fruck et al. \(2014\)](#).

sets quality cuts according to some average values, analysis preferences, etc., and the data which do not satisfy specified criteria are discarded.

- **$\gamma$ /hadron separation and energy reconstruction:** Random Forest (RF) training, Look-up Tables (LUTs) production for energy reconstruction and determining *disp* parameter for the arrival direction. Training of RF requires **Monte Carlo** simulations and some background data with no gamma-like events, using programs *Coach* and *Melibeia*.
- **Arrival Direction Reconstruction and signal extraction:** When RF and LUT are applied to the real data set, via program *Melibeia*, the *hadronness* parameter of each event is computed. Signal significance is obtained from program *Odie*, skymaps are made by program *Caspar*.
- **Spectrum and light curve:** Spectra and light curves are obtained from *Flute*.

### 2.4.1 Pre-processing

To be able to analyse the data written during the observation, one needs to convert the data from that *raw* format into the standard MARS ROOT format. This is done by MARS executable *MERPP* (MERging and Preprocessing Program) which also merges other subsystem reports (e.g., reports from the weather station, LIDAR, the camera reports, the readout reports, etc.) with the data.

### 2.4.2 Calibration

*Sorcerer* (Simple, Outright Raw Calibration; Easy, Reliable Extraction Routines) is the MARS executable used to calibrate the DRS data for MAGIC I and MAGIC II. The goal of the low-level data processing is to obtain information about the arrival times and the number of photoelectrons (charge) for each event from the pixels. First, to extract the light pulses of the PMTs one needs to determine the baseline (see Fig. 2.17) of the readout which is obtained from pedestal events triggered at a fixed frequency (and contains only noise). Then, from integrated light pulse, two quantities are calibrated: FADC counts are converted to photoelectrons (ph.e.) and FADC slices are being connected to an absolute signal timing. The F-Factor method (Mirzoyan, 1997) is used for determining the conversion factor of counts to ph.e. The baseline and conversion factors are updated every  $\sim 30$  s to counteract the changing NSB and electronic instabilities.

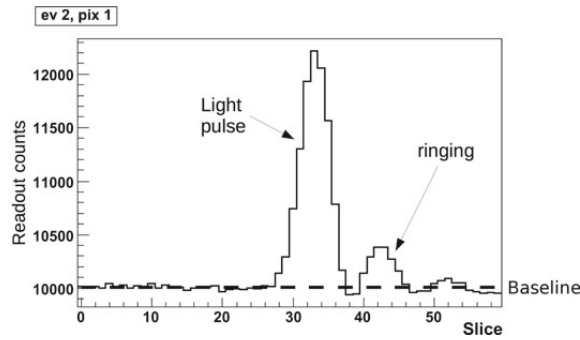


Figure 2.17: An example of the PMT signal digitized by the readout. The readout counts are plotted on the y-axis and on the x-axis are the readout slices. As an artefact of the readout, a so-called *ringing* appears after the light pulse. The readout can also be triggered by the *afterpulses* from PMTs, which are large amplitude signals caused by an ion accelerated back to the PMT’s photocathode. Credit: J. Sitarek.

### 2.4.3 Image cleaning and parameters reconstruction

After the signal extraction and calibration, an image of the shower is obtained. This image still contains the noise from NSB and needs to be cleaned with the proper *image cleaning* algorithm. In this algorithm, only pixels that most probably contain information about the shower are selected. The basic principle used in the cleaning is the fact that Cherenkov photons from EAS are mostly clustered on the camera plane, both spatially and temporally, in contrast with NSB photons which are randomly distributed.

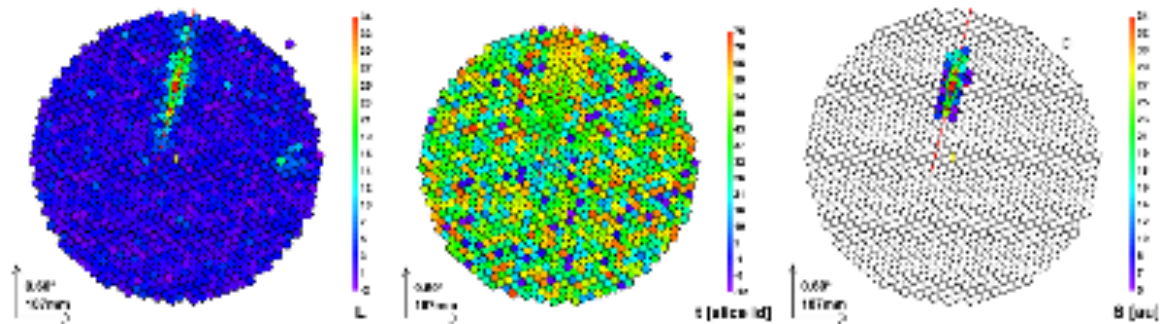


Figure 2.18: Process of an image cleaning: for each event, charges (left) and arrival times (middle) are processed. If a pixel survives an image cleaning algorithm, it is shown in the cleaned image (right). Figure is taken from [Giavitto \(2013\)](#).

For the cleaning, the pixels are classified into three categories: the core pixels, the boundary pixels and the noise pixels. In the *absolute cleaning*, the pixel is classified as a core if its charge is above a certain threshold and its arrival time is within a certain time window. For the pixel to



be a boundary pixel it has to be a neighbouring pixel to at least one core pixel, needs to have a charge above a certain threshold, and its arrival time has to be within some time window (see Fig. 2.18). In the so-called *sum-cleaning*, which is more efficient at lower energies, the core pixels are selected if the clipped sum of  $N$  pixels ( $N=2,3,4$ ) is above a certain threshold and if their arrival time is within a time window from the mean of the corresponding pixels of the same group.

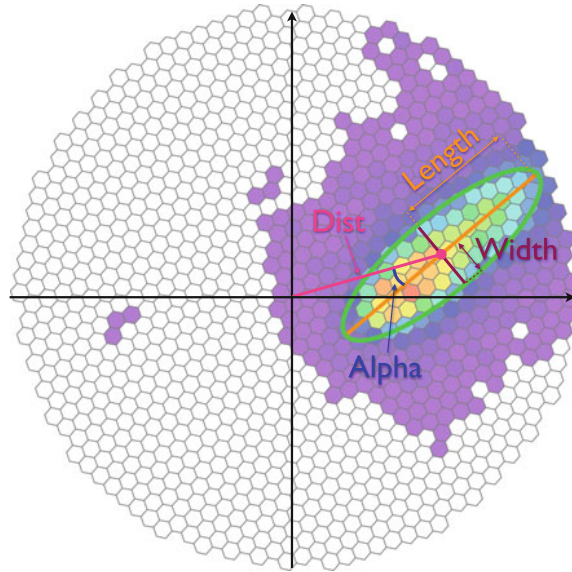


Figure 2.19: The reconstructed image of the shower in the camera is an ellipse which can be parametrized with the specific *Hillas parameters*. This method helps discriminate between gamma-like and hadron-like events. Figure is taken from [Fernandez Barral \(2017\)](#).

When the image cleaning is finished, the parametrization of an image can start. To distinguish gamma-ray showers from hadronic showers in IACTs, [Hillas \(1984\)](#) developed a method that uses a set of parameters, today known as the *Hillas parameters*. The image in the camera, produced by the primary gamma ray in the EAS, has the shape of the ellipse. So, the ellipse is fit to the pixels that pass certain criteria and the momenta of this fit are the above-mentioned Hillas parameters (see Fig. 2.19). The parameters for each event are stored in ROOT files for both telescopes separately. All this is done by the executable *Star*. For the stereo observations, the executable *SuperStar* combines the shower images from both telescopes and calculates stereo parameters. Main image parameters are described below:

- **SIZE**: Parameter roughly proportional to the energy of the primary gamma ray. It is the total charge of the cleaned image.
- **COG**, centre of gravity: The charge-weighted mean position of the image.

- **LENGTH:** The RMS of the charge distribution along the major axis of the image ellipse. It is related to the longitudinal development of the shower.
- **WIDTH:** The RMS of the charge distribution along the minor axis of the ellipse. It is the measure of the lateral development of the shower.
- **CONC:** The sum of the  $N$  brightest pixels in the image divided by SIZE. It gives the compactness of the image, which is larger for EM cascades than for the hadronic showers.
- **LEAKAGE:** The number of charges contained in the two outermost rings of the camera divided by SIZE.
- **DIST:** The angular distance from COG to the assumed source position in the camera. It is an important parameter for the energy and the arrival direction reconstruction because it is directly connected to the impact distance between the shower and the telescope.
- **DISP:** Distance from the COG to a reconstructed source position that lies on a major axis of the corresponding ellipse.
- **THETA:** ( $\theta$ ) Angular distance between the assumed source position and the reconstructed source position.

#### 2.4.4 Gamma Hadron separation and energy reconstruction

For the high-level analysis, we need to determine three main analysis parameters of each recorded event: the energy of the primary gamma ray, the direction of the shower and the *Hadronness* parameter. Hadrons are  $\sim 1000$  times more abundant than gamma rays may produce similar images in the camera. Hence, they present significant background which is rejected efficiently. The *hadronness* parameter estimates the probability that the image in the camera was produced by hadron and takes the value between 0 for unlikely and 1 for certain hadron event. A *hadronness* parameter is computed via **Random Forest** (RF) event classification method. RF is produced using Monte Carlo (MC) simulations of pure gamma-ray showers and the observational data representing hadron sample (data used here is the one with no excess gamma rays detected). RF is 'grown' in the following way: a parameter (like size or length) is chosen randomly and its value is determined in a way to make the best discrimination between gamma rays and hadrons. This process is repeated for each tree, and there are typically 100 trees grown. Then, RF is applied to the observational data where each event needs to pass the decision trees, following a certain path and assigning values 0 or 1. After 100 trees, the *hadronness* parameter

is the sum of results of all individual trees divided by 100. In MAGIC, for stereo data, the RF method is applied in the program *Coach*.

In the same program, energy reconstruction takes place, and this is done via the look-up tables (LUT) based on MC data which are divided into bins of energy according to the value of parameters. In the end, RF and LUT are applied to the real data in the executable *melibea*. The estimated energy  $E_{est}$  is the weighted average (RMS) over both telescopes for the mean  $E_{true}$  value of the LUT bin. Hence, a resolution of the energy reconstruction, which is  $(E_{est} - E_{true})/E_{true}$  is  $\sim 15\%$  in the energy range from 200 GeV up to 1 TeV. For the rest of the energy range (i.e., very high or low energies), the energy is overestimated. For each analysis, there is a value called the energy threshold,  $E_{thr}$ , which is defined as the maximum of the  $E_{true}$  distribution of gamma MC simulated events. The value of  $E_{thr}$ , usually shown as a function of zenith angle, increases rapidly for higher zenith angles, due to the larger absorption of the Cherenkov photons in the atmosphere and dilution of photons reaching the ground over the larger light pool. The threshold is evaluated at different stages of the analysis. After the shower reconstruction which involves the image cleaning and some quality cuts gives  $E_{thr} \sim 70\text{GeV}$ . Below this energy, events are small, therefore harder to reconstruct. Additionally, for lower image sizes, discrimination between gamma ray and hadron is hard.

## 2.4.5 Monte Carlo simulations

Monte Carlo (MC) simulations are a crucial part of the analysis chain because the only way to identify the primary particle is based on the simulations. In the process, simulated events with the pre-known parameters are compared to the shapes of the real air shower images. MAGIC Monte Carlo program consists of 3 subprograms: *Corsika*<sup>6</sup>, *Reflector* and *Camera*. **Corsika** (COsmic Ray Simulations for KAscade), originally developed for the KASCADE experiment in Karlsruhe (Heck et al., 1998), is an MC program for simulating extensive atmospheric showers (EAS) initiated by high energy cosmic particles. The program tracks down the secondary particles in the shower until no more Cherenkov light is produced. Several atmospheric models are implemented in *Corsika* and are used depending on the local site of the observatory. The customized version of *Corsika* for MAGIC is called MAGIC Monte Carlo Software (Mmcs). For the atmospheric model *MagicWinter* atmosphere is used but also density variations of the atmosphere with the altitude and time of the year characteristic for the MAGIC site are taken into account. **Reflector** is a part of the MC program, simulating the atmospheric absorption of Cherenkov photons and the correct reflection by the mirrors onto the camera plane. **Cam-**

<sup>6</sup><https://www.ikp.kit.edu/corsika/70.php>

**era** is also a part of the MAGIC MC program which simulates camera, triggers, and readout electronics.

Two standard types of MC gamma-ray simulations are made for the MAGIC telescopes. The first type is intended for the point-like sources and the second type for the extended or the sources found at different off-axis angles. For the point-like sources, a gamma rays are simulated in a ring of  $0.4^\circ$  radius ( $0.1^\circ$  width) centred in the camera centre, due to observations performed in the *wobble* mode (see left Figure 2.20). These MCs are known as the *ringwobble* MCs.

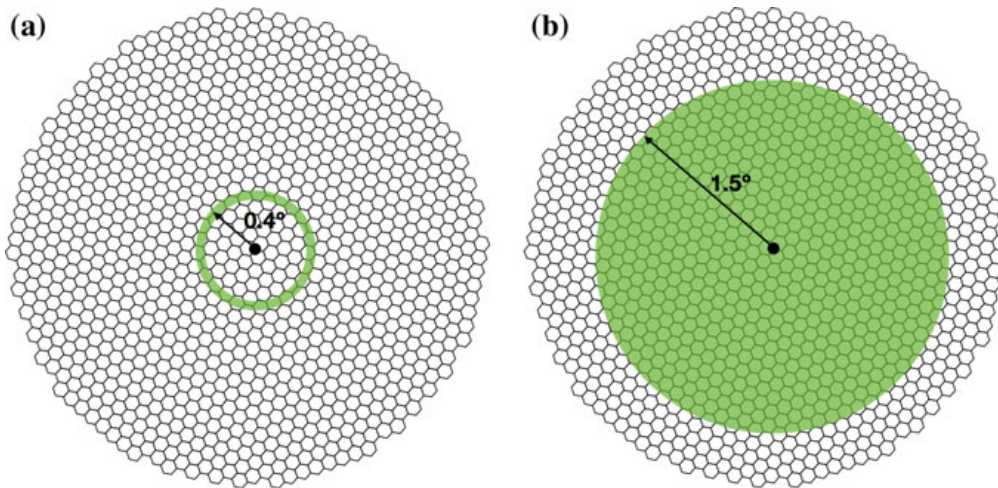


Figure 2.20: Two types of Monte Carlo gamma-ray simulations for the MAGIC telescopes are shown: *ringwobble* (left) and *diffuse* (right) MC. Figure from Lopez-Coto (2015).

For the second type, *diffuse* gamma rays are simulated covering a circle of  $1.5^\circ$  radius (right Fig. 2.20) because the source is simulated in a way that is randomly distributed between  $0$  and  $1.5^\circ$ . Furthermore, to improve the precision of the *diffuse* MC files for the extended source, the *doughnut* MC are used where the source morphology and the correct acceptance is considered. Additionally, the known or assumed source extension is taken into account a priori. For the typical case of a moderately extended, radially symmetric source, the distribution of true gamma-ray directions has the shape resembling that of a doughnut, where the name of the method comes from. If e.g., a source is observed with the offset of  $0.4^\circ$  and has an extension of  $0.2^\circ$  in radius, one needs to select MC between  $0.2^\circ$  and  $0.6^\circ$  from the camera centre, see Fig. 2.21.

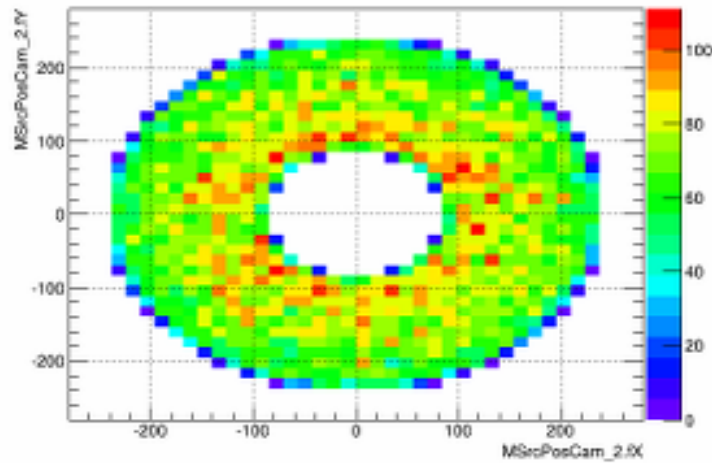


Figure 2.21: *Doughnut* MC for the extended sources (or sources found at different off-axis angles) where the source extension and morphology is assumed a priori for the better precision of the MC files. From the MAGIC wiki pages.

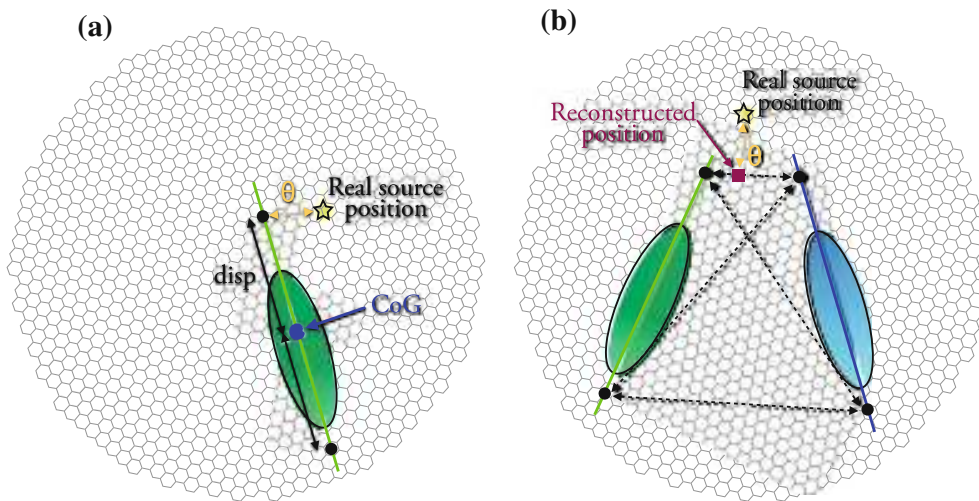


Figure 2.22: *Disp* parameter: a) the shower impact point reconstruction has, in the case of mono observations, two possible degenerate solutions; b) in the case of stereo shower reconstruction, the degeneracy is removed by choosing the closest possible pair. Figure is taken from [Fernandez Barral \(2017\)](#).

## 2.4.6 Arrival reconstruction and signal extraction

Proposed by [Fomin et al. \(1994\)](#) and later revised by [Lessard et al. \(2001\)](#), the so called *Disp* method is widely used in IACT stereo observations. The distance of the impact point from the image CoG along the major axis of the ellipse is called *disp*, see Fig. 2.22. In the case of stereoscopic observations with one image per camera, there are four *disp* distances (estimations) for

the source position (Fig. 2.22 b). To determine the correct arrival direction, distances between these positions are calculated and the smaller one is selected. The *disp* method introduces a new analysis parameter - the angular distance  $\theta$ , which gives the angular distance between a true position of the source and the reconstructed one. The determination of the *disp* parameter can be inferred from the image parameters, but a more efficient approach of estimation is to use the Random Forest (RF) algorithm.

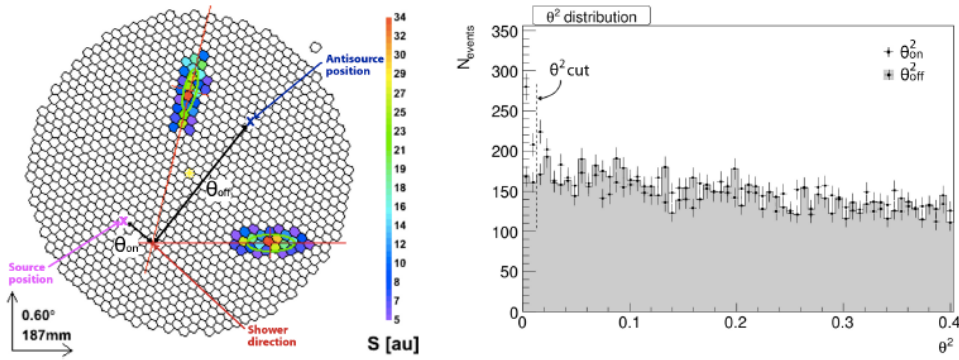


Figure 2.23: Parameter  $\theta$  is defined as the angular distance between the source position and the reconstructed position of the source. Right plot: an example of the  $\theta^2$  distribution, where the vertical dashed line is the cut on the signal region. Figure is taken from [Giavitto \(2013\)](#).

When the parameters like *hadronness*, energy and reconstructed source position for each event are determined, gamma-ray signal in the data can be obtained. First, a cut is applied to a *hadronness* parameter to lower the number of hadron events from the data. There are some standard cuts that maximize the sensitivity depending on the energy. For the stereo observations and the data used in this thesis, the recommended cuts are:

- Low energy ( $E < 200$  GeV): *hadronness*  $< 0.28$  *Size*  $> 60$
- Full range ( $E > 200$  GeV): *hadronness*  $< 0.16$  *Size*  $> 300$
- High energy ( $E > 1$  TeV): *hadronness*  $< 0.1$  *Size*  $> 400$

To extract the signal from the data, the number of gamma-ray events,  $N_{on}$  and the number of the background events,  $N_{off}$  as a function of the squared angular distance from the real source position and the reconstructed one is calculated. The MARS executable *Odie* calculates the  $\theta^2$  distance, hence the significance. The background events are expected to be distributed homogeneously over  $\theta^2$  range and is obtained depending on the pointing mode (ON/OFF mode or *wobble* mode, see Sec. 2.3.7). Besides that, if the source of gamma rays is present it will result in an increase in the excess events towards small  $\theta^2$  values, see Fig. 2.23, suggesting that

the reconstructed and assumed position of the source in the camera are consistent. The excess events are computed as a difference of  $N_{on}$  and  $N_{off}$  (scaled):  $N_{exc} = N_{on} - \alpha N_{off}$ , where  $\alpha$  is the normalization factor accounting for uneven observational time between  $N_{on}$  and  $N_{off}$ . For the *wobble* mode, the observational time is equivalent for ON and OFF, but  $\alpha$  is obtained as  $1/(\text{number of OFFs})$ , (1 or 3 for standard observations). The angular resolution of the telescopes and the source extension are main things responsible for the excess shape. For example, for the Crab nebula, the source extension is negligible compared to the angular resolution. For larger values of  $\theta^2$ , the number of  $N_{on}$  and  $N_{off}$  agree because in both cases events are dominated by the background events. With an upper  $\theta^2$  cut, which is optimized on Monte Carlo or the known gamma-ray sources (like Crab nebula) the signal region is defined from where  $N_{on}$  and  $N_{off}$  are obtained. Once the excess event number is known, the significance of the signal is computed using formula (17) from Li & Ma (1983):

$$\sigma_{LiMa} = \sqrt{2 \left\{ N_{on} \ln \left[ \frac{1 + \alpha}{\alpha} \left( \frac{N_{on}}{N_{on} - N_{off}} \right) \right] + N_{off} \ln \left[ (1 + \alpha) \left( \frac{N_{off}}{N_{on} - N_{off}} \right) \right] \right\}}, \quad (2.1)$$

where  $N_{on}$  and  $N_{off}$  events survived the  $\theta^2$  cut.

### 2.4.7 Spectrum and Light Curve

Differential gamma-ray energy spectrum is defined as

$$F(E) = \frac{dN_\gamma}{dE dA_{eff} dt_{eff}} \quad (2.2)$$

To obtain the spectrum, events are binned in energy and for each energy bin effective area ( $A_{eff}$ ) and effective time ( $t_{eff}$ ) are computed. The number of detected gamma rays, i.e., the number of excess events ( $N_{exc} = N_{on} - N_{off}$ ), is obtained from the  $\theta^2$  distribution or from the phase distribution, in case of pulsars. The effective area,  $A_{eff}$ , is calculated from MC simulations.  $N_{exc,tot}$  simulated gamma rays are produced in the area above the telescope  $A_{sim}$ . After applying cuts to the events, the number of gamma rays that survive is denoted as  $N_{exc,selec}$ . The effective area can be computed via

$$A_{eff} = A_{sim} \epsilon_{gamma} = A_{sim} \frac{N_{exc,selec}}{N_{exc,tot}} \quad (2.3)$$

The ratio of  $N_{exc,selec}$  and  $N_{exc,tot}$  in the above formula can be understood as a shower detection

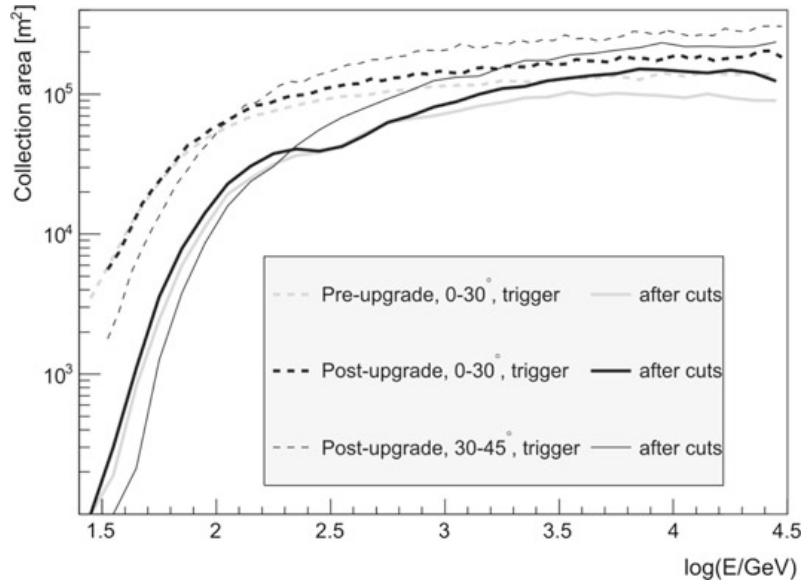


Figure 2.24: Collection area of the MAGIC telescopes at the trigger level (dashed line) and after the cuts (solid lines). Thickness of the line depends on zenith angles. For comparison, the collection area before upgrade is shown with grey lines. Figure taken from [Aleksić et al. \(2016b\)](#).

efficiency of the telescope. The simulated area is a circle, approximately  $r \sim 350$  m, depending on a zenith angle and a type of particle being simulated (protons or gamma rays). So, depending on the energy, the effective area  $A_{eff}$  can reach  $\sim 10^5 m^2$ , as in Fig. 2.24.

The gamma-ray effective time of the observation,  $t_{eff}$ , is calculated from the distribution of the time difference  $dT$  between successive events. The effective time of the observed source is not equal to the elapsed time during observations due to the deadtime for storing events and some gaps during data taking, etc.

Because the instrument, such as the MAGIC telescopes, has finite resolution and unpredictable conditions (i.e., the weather, technical problems, etc.), the measured spectrum is not necessarily the true spectrum of the observed source. These two values are connected with a migration matrix,  $M_{ij}$  in the following formula,

$$g_i = \sum_j M_{ij} f_j, \quad (2.4)$$

where  $g_i$  and  $f_j$  are the number of events in bin  $i$  of  $E_{est}$  and bin  $j$  of  $E_{true}$ . The migration matrix  $M_{ij}$  presents the fraction of events in bin  $j$  of  $E_{true}$  moving into bin  $i$  of  $E_{est}$  due to the finite resolution in energy, and is obtained by the MC simulations. To determine the real spectrum, the matrix needs to be inverted and this procedure is called the *unfolding*. Because  $M_{ij}$  is



not a square matrix, unstable results are obtained from the minimization method ( $\chi_0^2 = \sum_i (g_i - \sum_j M_{ij} f_j)^2$ ). For the regularization, a term  $Reg(\vec{f})$  is added in the formula,

$$\chi^2 = \frac{\omega}{2} (\chi_0)^2 + Reg(\vec{f}), \quad (2.5)$$

where  $\omega$  denotes the strength of the regularization. Program *CombUnfold* in MARS executes unfolding and there are few algorithms that use different regularization terms, such as Tikhonov (Tikhonov et al., 1979), Bertero (Bertero et al., 1988), Schmelling (Schmelling, 1994), all described in Albert et al. (2007). Another way to solve the equation 2.4 is with *forward unfolding*, which is a method more robust than unfolding (spectrum is assumed a priori). Forward unfolding does not provide spectral points but the best fit of the parametrization with corresponding errors, thus should only be used to check the results obtained with other unfolding methods.

### 2.4.8 Special case analysis - Pulsar detection

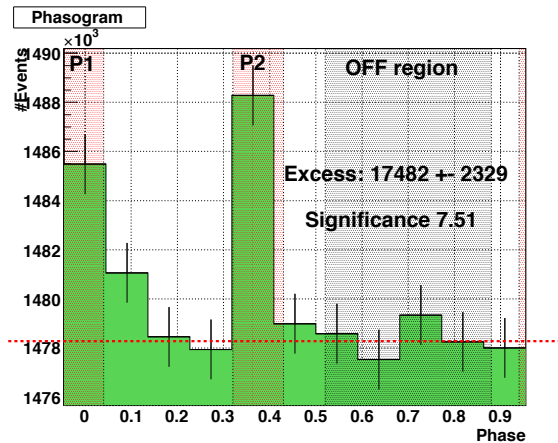


Figure 2.25: Example of signal extraction from a light curve of a pulsar: signal (ON pulse phase) and background (OFF pulse phase). Figure taken from Saito (2011).

At gamma-ray energies, pulsar data are very sparse, so standard search for the signal (using  $\theta^2$  distributions) is not optimal. Instead, the light curve is used for signal extraction, see Fig. 2.25. To detect very high energy gamma-ray emission from pulsars (or, as a matter of fact, pulsed emission in any other part of the spectrum) arrival time information for each event is needed. Therefore, the pulsar signal region is defined, not only in space but also in time, consisting of time intervals around the main pulses (see also Sec 1.5). The background region is defined as time intervals where no signal is expected. For gamma-ray pulsars, the on-pulse

phase interval (i.e., the signal region) can be characterized by one (or a few) prominent and sharp emission peak(s). The off-peak (OP) emission is usually dominated by the background from the surrounding nebula and/or the pulsar itself. The average level of the bridge emission (if present) between two peaks is higher than that of the off-peak phase interval (Pierbattista et al., 2015). The peaks of the known pulsars light curves become sharper with increasing energy (see e.g. Aleksić et al. (2012) for gamma-ray observations). The signal and background time intervals<sup>7</sup> repeat with each pulsar period and can be defined in phase ( $\phi$ ) which represents the fraction of the period of the pulsar. To convert arrival times of the events into a pulse phase  $\phi$ , program TEMPO2<sup>8</sup> is used. It consists of two steps: barycentre correction (removal of the effect of the Earth movement) and phasing. For each gamma-ray event from the pulsar, the recorded gamma-ray arrival time in topocentric coordinates (the observatory's reference system measured in UTC) is transferred to the solar-system barycentric coordinates (SSBC) to correct for the position of the MAGIC telescopes in the solar-system frame of reference. The centre of mass of the Solar system, i.e., the Solar system barycentre (SSB) is an inertial system - it moves uniformly through space. There are four first-order corrections to apply:

$$t_B = t_{UTC} + \Delta_{Roemer} + \Delta_{Einstein} + \Delta_{Shapiro} + \Delta_{TDT-UTC} \quad (2.6)$$

where  $\Delta_{Roemer}$  is the delay due to the geometrical distance between SSBC and the observatory ( $\sim 8$  min);  $\Delta_{Einstein}$  is the effect of the relativistic time dilation and the gravitational redshift (Earth moves in the gravitational well of the Sun,  $\sim 2$  ms);  $\Delta_{Shapiro}$  is the effect due to the non-Euclidean geometry of the space-time around the Sun ( $\sim 0.1$  ms);  $\Delta_{TDT-UTC}$  is the difference between the UTC standard and terrestrial dynamic time (TDT).

The second step in the TEMPO2 program is the phasing of the events. *Phase-folding* a light curve, or pulse profile, denotes filling the histogram with the fractional part of the  $\phi_i$  values. An ephemeris includes the pulsar coordinates, the frequency and its derivatives, also the epoch  $t_0$ , glitch<sup>9</sup> epochs, parameters that describe pulsar motion and more.

The pulsar's rotational phase  $\phi_i(t_i)$  is calculated from a timing model using Taylor series

---

<sup>7</sup>Signal and background regions can be deduced from light curves in other energy bands. In the case where pulsar's peak phase is very energy-dependent, the light curve from the closest energy range is used.

<sup>8</sup>The program is originally developed by Hobbs et al. (2006). Plug-in for the MAGIC data was developed by (Giavitto, 2013).

<sup>9</sup>A glitch is a sudden, irregular change in a pulsar's rotational speed caused possibly due to a starquake and a change in the pulsar's momentum of inertia. This event causes a small increase in the pulsar's rotational speed, thus a small decrease in the pulsar's period. Glitches are relatively rare, for example, the Crab pulsar's average glitch rate is  $\sim 1$  per year.

expansion:

$$\phi = \sum_{n \geq 1} \frac{\nu^{(n-1)}}{n!} (t_B - t_0^n) + \phi_0 \quad (2.7)$$

where  $\nu^{(n-1)}$  is the frequency of  $(n-1)$ -th derivative;  $t_0$  is the epoch of the ephemeris (time of the arrival of one pulse, barycentre corrected);  $\phi_0$  is the phase at the epoch  $t_0$  (usually taken to be 0). This approximation is only valid in a time interval around the epoch  $t_0$ , and the width of the interval depends on the timing noise of the pulsar and timing precision. Different timing models take into account different physical effects.

There are also a few statistical tests used to detect the pulsation:  $\chi^2$  (strongly dependent on the binning of the light curve),  $Z_m^2$  [Buccheri et al. \(1983\)](#) and H-test [de Jager et al. \(1989\)](#) (based on the Fourier decomposition of the signal). These statistical tests can determine the pulsed signal without knowing a priori the signal and background regions, contrary to Li&Ma method (Eq. 2.1, [Li & Ma 1983](#)) where the positions of the peaks are a priori known (used when the strong background is present).

### 2.4.9 Skymaps

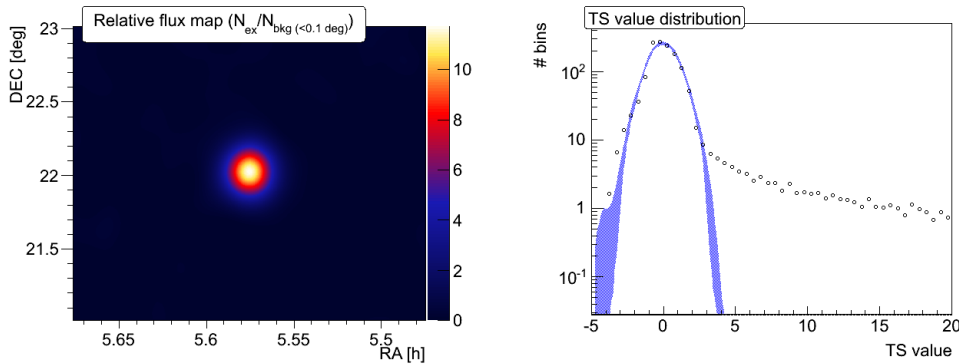


Figure 2.26: Left: Example of the skymap from the Crab Nebula analysis shows clear signal. Right: TS distribution shows a clear deviation from the null hypothesis (blue). Figure taken from [Krause \(2013\)](#).

Since a gamma-ray photon from some source in the sky is not imaged by the MAGIC camera directly but its energy and direction are reconstructed, there are two consequences in this process: 1) gamma-ray photons are recorded one by one, each one having (reconstructed) coordinates in the sky and 2) these coordinates come with an error that results in their random distribution around the true location of the source. This distribution represents the MAGIC

telescopes' resolution, it is called the Point Spread function (PSF), which is different from the PSF of the telescope's optical reflector. The detected number of photons in the image depends on the corresponding sensitivity of the telescope, so the image needs to be normalized. The excess corresponds to the real gamma rays and is obtained by subtracting the ON image of the source by the OFF image, i.e., the background image.

Caspar is the tool in MARS software that produces skymap images, see Fig. 2.26. The skymap is obtained by binning the event arrival directions (after hadronness cut) in sky coordinates. These maps are also used to study the morphology of the extended source or to detect unplanned sources in the FoV of the observation. The main problem is to estimate the background and in the MAGIC experiment the exposure map model of the camera is used: the model is done from the camera half that corresponds to the anti-source position. A test statistic (TS) map is obtained from ON and background maps, where TS value is calculated from Li & Ma equation (see Sec. 2.5, Eq. 2.1). The excess histogram is smoothed by using the instrument's PSF and a Gaussian kernel for smearing the number of excess obtained (the circle displayed on the skymaps represents the total PSF):

$$\sigma_{TOT} = \sqrt{\sigma_{PSF}^2 + \sigma_{kernel}^2} \quad (2.8)$$

### 2.4.10 Notes on the non-standard observations

**Off-axis performance.** Wobble mode with the source offset of  $0.4^\circ$  from the camera centre is mostly used in the MAGIC observations (see Sec. 2.3.7). However, serendipitous sources can occur in the FoV of MAGIC at an angular offset from the pointing direction. The telescope's performance changes with higher offsets from the centre of the FoV (Aleksić et al., 2016b). Nevertheless, after upgrade of the telescopes, the sensitivity at off-sets of  $\sim 1^\circ$  improved by  $\sim 25\%$ , which is more than the global  $15\%$  improvement seen at the standard  $\sim 0.4^\circ$ . In addition, using MC simulations with a diffuse origin for the gamma/hadron separation and direction reconstruction gave better results at large offset angles than MC simulations generated at the standard offset of  $0.4^\circ$ , see Fig. 2.32.

**Off from Wobble Partner.** The method called *OFF from wobble partner* (OfWP) is a method for the background calculation and is especially useful for serendipitous discoveries of sources, scans and for extended sources. While the standard background determination in the wobble mode (Sec. 2.3.7) obtains the background at the same radial distance from the camera as the source position only from the opposite side of the camera, for OfWP this is not the case. For any given source position, the OFF is determined from the same position in the camera as the ON, see Fig. 2.27. The differences in the observation times of each wobble position will

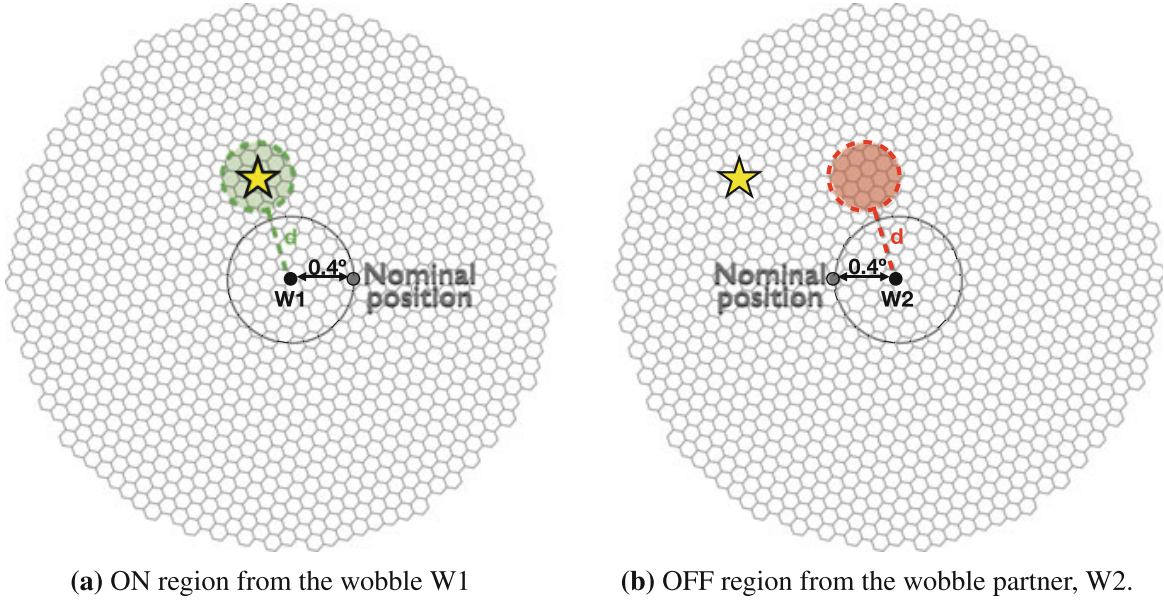


Figure 2.27: Illustration how *Off from Wobble partner* method extracts the background in the case of an arbitrary source position. The black star marks the centre of the camera, located at  $0.4^\circ$  from the nominal source (gray circle). The yellow star marks a source in the FoV aimed for analysis. While in W1 (left plot) the ON region for the source of interest is selected, W2- the wobble partner (right plot) is used to select the OFF region at the same position in the camera at which the source was located when in W1 wobble position. Afterwards, the procedure is repeated, but this time ON is taken from W2 and OFF from W1. Illustration adapted from Lopez-Coto (2015).

be taken into account by scaling the OFF. The method is basically a generalization from the standard OFF calculation to arbitrary source position and non-equal observation times in each wobble positions. The *OfWP* method is well described in Krause (2013).

**Extended sources.** The analysis of the extended source varies from the one for a point-like source: the signal is diluted over the larger part of the sky, so to make a detection, the angular  $\theta^2$  cut needs to be loose and is roughly estimated to be  $\theta_{cut} = \sqrt{\theta_0^2 + \theta_s^2}$ , where  $\theta_0$  is a cut for a point-like source analysis and  $\theta_s$  is a characteristic source size. The looser  $\theta^2$  cut will affect sensitivity in two ways: 1) it will degrade it by a factor of  $\sqrt{\theta_{cut}^2} = \theta_{cut}$  because more background events are accepted, and 2) it will decrease the collection area, which is proportional to  $\gamma$ -rate. However, as it is estimated in Aleksić et al. (2016b) the net degradation in sensitivity is not significant. For the standard observation of sources larger than  $0.4^\circ$  technical difficulties emerge because the source falls into the background estimation region. For the extended sources, *diffuse MC* are used, as described in Section 2.4.5.

The standard *wobble* offset of  $0.4^\circ$  constrains the maximum extension of a source, as shown

in Fig. 2.28. If only 1 OFF is taken, the distance between the centre of the source and the

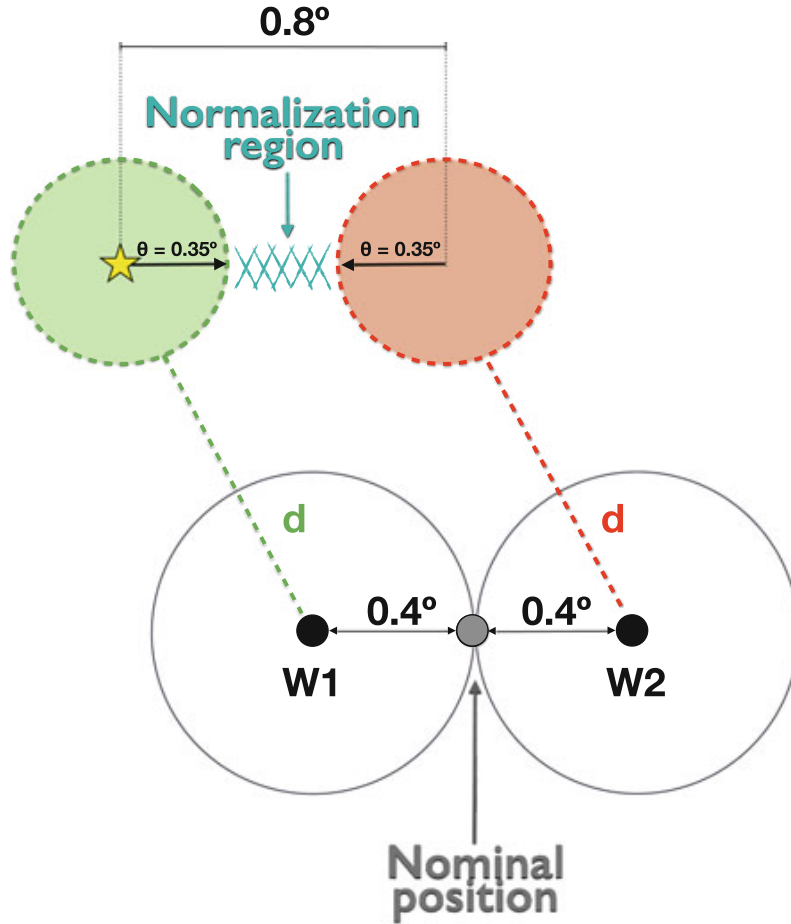


Figure 2.28: Scheme for the maximum possible extension for a source taken in the *wobble* mode with the MAGIC telescopes. Both *wobble* modes are shown here simultaneously. From W1, the ON region (green) is taken while from W2 one obtains the OFF (red) at the same distance,  $d$ , from the camera centre. The normalization region is marked with green crosses between ON and OFF regions. Figure taken from [Fernandez Barral \(2017\)](#).

background region is  $0.8^\circ$ . In addition, the ON region from where the signal is expected depends on intrinsic radius of the source but also on the MAGIC PSF, that is, on the other hand, energy dependent. Thus, the ON region is defined by the  $\theta^2$  cut that is later needed for flux computation and is determined from  $\theta^2 \approx (2 \times R)^2 + (2 \times PSF_{40})^2$ , where  $R$  is the assumed radius of the source and  $PSF_{40}$  is the PSF of the telescopes at the 40% containment determined from e.g., the Crab Nebula sample taken with similar conditions (the same telescope setup, weather, moonlight conditions, etc.) as the data we want to analyse.

## 2.5 MAGIC performance

In this Section, the performance of the stereo MAGIC system is summarized. For a detailed description of all the parameters, see also [Aleksić et al. \(2016b\)](#) and [Aleksić et al. \(2016a\)](#). Sensitivity, energy resolution and angular resolution are all functions of energy and characterize the performance of an astronomical instrument.

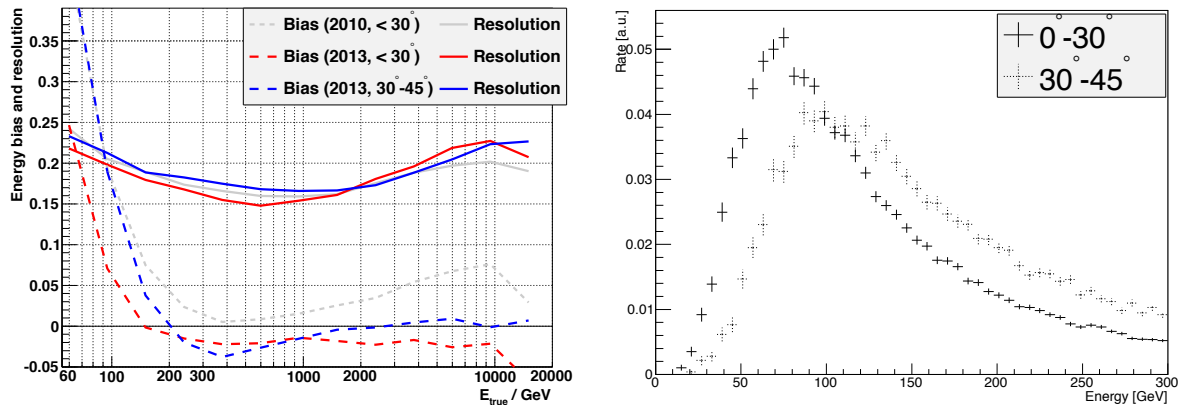


Figure 2.29: Left: energy resolution (solid lines) and bias (dashed lines) evaluated from MC simulations of  $\gamma$  rays. Red lines represent low zenith angle; blue lines medium zenith angle; grey lines are pre-upgrade values. Right: rate of  $\gamma$  rays after quality cuts for low and medium zenith angle. The peak of distribution marks the energy threshold, which is  $\sim 75$  GeV for low zenith angles and  $\sim 100$  GeV for medium zenith angles. Plots taken from [Aleksić et al. \(2016b\)](#).

**Energy resolution** is a measure of how accurately an instrument can determine the real energy of the event. It is calculated as the RMS of the Gaussian for all  $E_{bias}$  in each bin. The current performance of the MAGIC telescopes reaches 15% at a few hundred GeV for the energy resolution, but increases for higher energies due to the higher probability of the image to lay at the edge of the camera and get truncated. For low energies, resolution gets also worse because the reconstruction of the low energy showers is difficult.

**Energy threshold** is defined as the peak of the MC simulated energy distribution for a source which is described with a power-law function with a photon index  $\Gamma = 2.6$ . The distribution is evaluated after quality cuts to account only for the surviving events. The current energy threshold for MAGIC is  $\sim 75$  GeV for a size cut of 50 phe, see Fig. 2.29, [Aleksić et al. \(2016b\)](#).

**Sensitivity** of the MAGIC telescopes is defined as the minimum flux of the source that the telescopes can detect in 50 hours of observation with  $5\sigma$  significance. For a weak source, the significance of excess events,  $N_{exc}$ , over well-known background events,  $N_{bkg}$ , can be computed with the simplified formula  $\text{Significance} = N_{exc} / \sqrt{N_{bkg}}$ . Sensitivity is expressed in C.U. (Crab

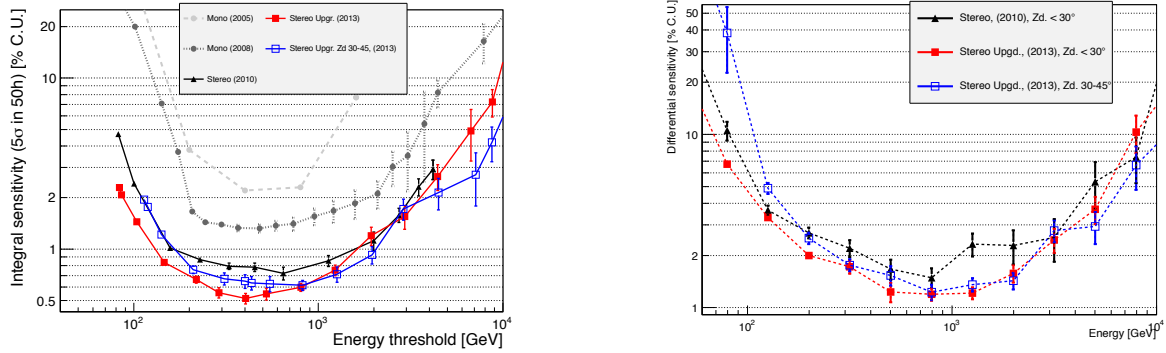


Figure 2.30: MAGIC integral sensitivity as a function of energy threshold (*left*) and differential sensitivity as a function of energy (*right*) for different phases of the MAGIC experiment. Observations in MONO mode (only MAGIC I) are represented in light and dark grey. The black line represents the sensitivity for STEREO observations before the upgrade period. The current performance of the system for low and medium zenith angle is represented with red ( $Zd < 30^\circ$ ) and blue ( $30^\circ < Zd < 45^\circ$ ) lines. Plots were taken from [Aleksić et al. \(2016b\)](#).

Units), which represents the percentage of the Crab Nebula flux. For the observation that lasts for a time  $t$ , the significance for a time  $t_0$  is given by

$$\text{Significance}(t_0) = \frac{N_{\text{exc}} \sqrt{t_0/t}}{\sqrt{N_{\text{bkg}}}} \quad (2.9)$$

The equation 2.9 describes the relation between significance and observational time,  $\sigma \propto \sqrt{t_0}$ . In addition, we can express sensitivity in terms of Crab Nebula flux by assuming the standard deviation where  $t_0 = 50h$  and  $5\sigma$  detection:

$$\text{Sensitivity} = \frac{5\sigma}{\text{Significance}(50)} \times \text{C.U.} \quad (2.10)$$

The sensitivity is more often calculated using already mentioned formula 2.1 from [Li & Ma \(1983\)](#). Expressing the significance in this way is a standard method for VHE  $\gamma$ -astronomy, and the method depends on the number of *Off* positions used for the background estimation.

The sensitivity of an instrument can be integral or differential. The integral sensitivity is obtained by applying the right cuts in the analysis, which give the best sensitivity above a certain threshold. For MAGIC, the best integral sensitivity is  $0.66 \pm 0.03\%$  C.U. for energies above 220 GeV. For the differential sensitivity, the cuts for the best sensitivity are found for each energy bin. The Figure 2.30 shows MAGIC integral and differential sensitivities after the major upgrade of the MAGIC telescopes ([Aleksić et al., 2016b](#)).



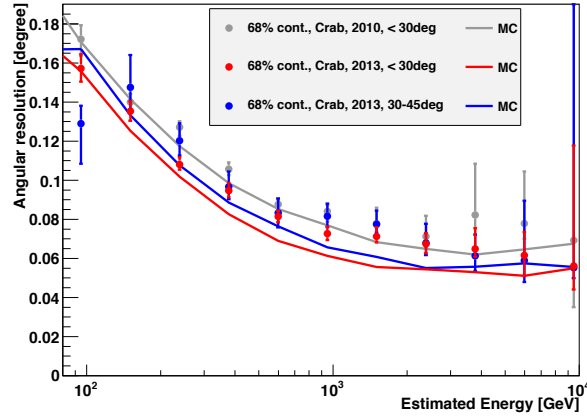


Figure 2.31: Angular resolution of MAGIC telescopes as a function of the estimated energy obtained with the Crab Nebula data sample (points) and MC simulations (solid lines). 2D Gaussian fit with 68% containment radius. Plots taken from [Aleksić et al. \(2016b\)](#).

**Angular resolution** is defined as the standard deviation of a 2-dimensional Gaussian function, fitted to the distribution of the reconstructed event directions of the gamma-ray excess. The angular resolution can be obtained with MC simulations or by observing a strong point source, such as Crab Nebula. In the Fig 2.31 estimated energy as a function of 68% containment radius estimated from both methods. With increasing energy, angular resolution improves due to better reconstruction of larger images. For example, at 250 GeV the angular resolution is  $\sim 0.10^\circ$  while at a few TeV the value reaches  $0.06^\circ$ .

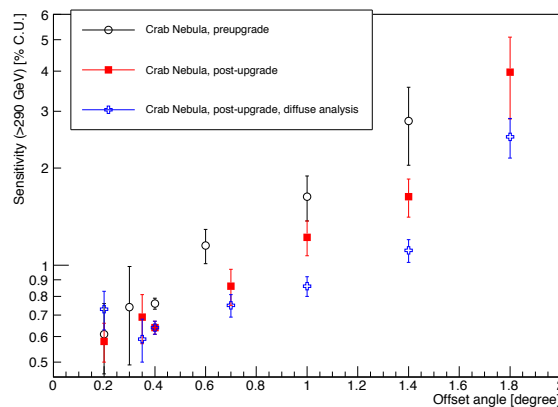


Figure 2.32: Integral sensitivity above 290 GeV for low zenith angle observations at different offsets from the camera centre. Plot from [Aleksić et al. \(2016b\)](#).

### 2.5.1 Upper limits

When no signal is found from the source, upper limits (UL) on the flux are calculated. For this calculation, one needs number of the excess events,  $N_{\text{exc}}$  and number of the background events,  $N_{\text{bckg}}$ . Moreover, one has to assume certain confidence level (C.L.) and contribution from the systematics. The method from [Rolke et al. \(2005\)](#) is used where the maximum number of the expected gamma-ray events,  $N_{\text{UL}}$  is computed and the assumed spectral shape of the source is taken a priori. It is a common practice in gamma-ray astronomy to use a 95% C.L. Specifically for the MAGIC experiment, 30% of the systematic uncertainty is taken into account. The flux of the source is defined as:

$$\phi(E) = K \cdot S(E) = K \cdot \left(\frac{E}{E_0}\right)^{-\Gamma}, \quad (2.11)$$

where  $K$  is the normalization constant (in units of differential flux, e.g.,  $\text{GeV}^{-1}\text{cm}^{-2}\text{s}^{-1}$ ) and  $S$  is the assumed spectral shape (here a power-law). The integral flux above  $E_0$  is:

$$\int_{E_0}^{\infty} \phi(E) dE = K \int_{E_0}^{\infty} S(E) dE = \frac{N_{\text{UL}}}{\int_{E_0}^{\infty} \int_0^{t_{\text{eff}}} A_{\text{eff}}(E) dE dt}, \quad (2.12)$$

where  $t_{\text{eff}}$  is the effective time of the observation and  $A_{\text{eff}}$  is the effective area (obtained from MC simulations). From the above equation, one gets the UL on the integral flux:

$$K_{\text{UL}} < \frac{N_{\text{UL}}}{t_{\text{eff}} \int_{E_0}^{\infty} S(E) A_{\text{eff}}(E) dE}, \quad (2.13)$$

### 2.5.2 Systematic uncertainties

Using the atmosphere as a calorimeter comes along with certain limitations, such as the accuracy of the energy reconstruction and precise absolute pointing. In other words, it is not possible to calibrate IACT telescopes in the laboratory (like it was done with *Fermi*-LAT telescope before its launching) thus they suffer from systematic uncertainties. Some systematic errors affect energy estimation of the primary gamma ray and some affect the estimated flux level. For example, incorrect alignment of the mirrors at the beginning of the observations or a presence of dust on the mirrors can cause light losses and directly affects the energy estimation and is calculated to add  $\sim 10\%$  to the systematic uncertainty. The fluctuations in the weather conditions on a nightly basis (temperature, humidity, cloudiness, etc.) are not incorporated in the MC simulations which use the *Magic Winter* model, so this also affects the estimation of the

gamma-ray energy by the  $\sim 11\%$ . On the other side, there are also systematic errors that affect the flux level, like the background estimation ( $\sim 10 - 15\%$  or  $\sim 1\%$  if using wobble pointing mode) or telescope mispointing ( $\sim 4\%$ ), higher NSB levels ( $\sim 4\%$ ) and MC and data agreement which shows the difference between the MC gamma-ray events and real gamma-ray events and leads to an error for the gamma-hadron separation efficiency and this leads to miscalculation of the collection area. When all the known effects are included, 30% of systematic uncertainty is obtained and included when computing flux or the ULs.

# Chapter 3

## Crab pulsar and its nebula observed at very high gamma-ray energies

### 3.1 Introduction

The Crab nebula, one of the best studied objects in the Very High Energy (VHE;  $E > 100$  GeV) gamma-astronomy, was the first TeV source detected with a ground-based Cherenkov telescope Whipple in 1989, marking the extraordinary breakthrough for the VHE astronomy (Weekes et al., 1989). It is the brightest steady source of TeV gamma rays in the sky and is considered to be a standard candle of gamma-ray astronomy, despite its occasional flares<sup>1</sup>. The nebula's steady brightness across the electromagnetic spectrum is exploited in multiple ways, e.g., to calibrate X-ray and gamma-ray telescopes and to check the instrument performance over time.

The Crab pulsar, located in the centre of this nebula, is a remnant from the supernova explosion observed by Chinese astronomers in 1054 AD, and it is the most powerful known gamma-ray pulsar in the sky. As discussed in Chapter 1, only a few pulsars are detected in the VHE gamma-ray band, compared to a few hundred detected at high energies (HE,  $100 \text{ MeV} < E < 100 \text{ GeV}$ ). After developing a novel electronic trigger system that lowered the energy detection threshold to 25 GeV (Rissi et al., 2009), the MAGIC collaboration detected pulsed emission from the Crab pulsar in 2008 (Aliu et al., 2008). This was the first source of its kind detected at the VHE. Following this discovery, VERITAS collaboration extended the VHE spectrum of

---

<sup>1</sup>An enhancement of gamma-ray flux from the Crab nebula was observed by the *Fermi*-LAT and *Agile* first in February 2009 (for 16 days) and then in September 2010 (for 4 days). During these flares, the nebula's flux increased by a factor of four and six, respectively. Since the flaring lasted for a relatively short time, it is assumed that the enhancement of the gamma-ray flux originates from PeV electrons concentrated in a small region, emitting synchrotron (Abdo et al., 2011).

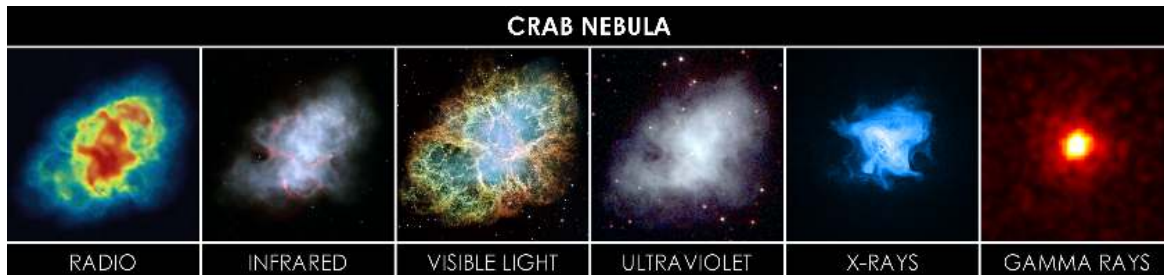


Figure 3.1: An example of pulsar wind nebula (PWN): multi-wavelength image of the Crab nebula. Credits: Radio: NRAO/AUI and M. Bietenholz; NRAO/AUI and J.M. Uson, T.J. Cornwell Infrared: NASA/JPL-Caltech/R. Gehrz (University of Minnesota) Visible: NASA, ESA, J. Hester and A. Loll (Arizona State University) Ultraviolet: NASA/Swift/E. Hoversten, PSU X-ray: NASA/CXC/SAO/F.Seward et al. Gamma: NASA/DOE/Fermi LAT/R

the Crab pulsar up to 400 GeV ([VERITAS Collaboration et al., 2011](#)). The most recent observations by the MAGIC collaboration have extended the spectrum up to 1.5 TeV, finding no indication of cutoff energy ([Ansoldi et al., 2016](#)).

In this Chapter, observations and the analysis of the Crab pulsar and its nebula, previously detected at VHE, are described. To characterize the novel trigger system, described in Sec. 2.3.5, I perform the analysis on  $\sim 9$  hours of Crab data observed by the MAGIC telescopes. The performance check of the telescopes is made by analysing the steady emission from the Crab nebula, the source considered to be a standard candle in VHE. Thus, in the analysis of every VHE source, the analysis of the Crab nebula emission is the initial step. If the Crab nebula analysis from the same period shows the expected results, we can be certain that the hardware modifications did not alter the telescope performance, and we understand systematic uncertainties well. On the other hand, when searching for pulsed emission, the analysis of the best studied Crab pulsar is done along with the analysis of some other pulsar candidate to verify the used methodology. The pulsar analysis is a non-standard where different trigger is used (sumtrigger) and pulsed signal is being searched for not only in space but also in time (for details see Sec. 2.4.8). Based on the results presented in Chapter 3 (this Chapter) I will verify the same method and apply it to the new pulsar candidate – the Dragonfly pulsar in Chapter 4. The Crab pulsar and its PWN are described in Section 3.2. The data set, its analysis and results are presented in Section 3.3. A summary of this Chapter is given in Section 3.4.

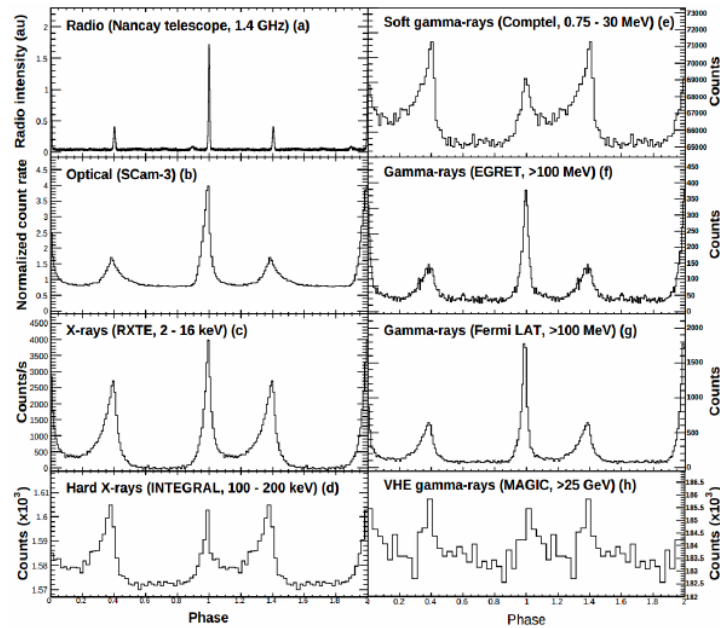


Figure 3.2: The Crab pulsar light curves throughout the electromagnetic spectrum. The image is taken from [Abdo et al. \(2010\)](#).

## 3.2 The source description

### 3.2.1 The Crab pulsar

Crab is one of the youngest (1 kyr) and the most powerful known pulsar in the Galaxy, located at a distance of 2 kpc with a rotational period of 33 ms ([Hester, 2008](#)). It has the highest known spin-down luminosity of  $4.6 \times 10^{38} \text{ erg s}^{-1}$  and its pulsed emission is detected throughout the spectrum, from radio all the way up to VHE gamma rays (see Fig. 3.2). It is also one of the brightest pulsars at high energies. Crab's pulse profile contains three components: two pulses, P1 and P2, separated by  $\sim 0.4$  in phase and observed at all energies, and the bridge<sup>2</sup> component. As reported in [Kuiper et al. \(2001\)](#) and [Saito et al. \(2015\)](#), the emission ratios between two peaks, as well as the ratio between the bridge and P1 component, is energy-dependent. At the radio frequencies, P1 has the highest intensity (and is defined at phase 0) and P2 is the weaker one, whereas at gamma-ray energies P2 becomes dominant above 25-50 GeV and the bridge component is detected up to 150 GeV.

The latest discovery was made by the MAGIC collaboration with almost 320 hours of data. They found the most energetic pulsed emission yet from the Crab pulsar ([Ansoldi et al., 2016](#)),

<sup>2</sup>The bridge emission, first reported in [Fierro et al. \(1998\)](#) and [Kuiper et al. \(2001\)](#) is the additional pulsed emission component in the region between two main pulses.

reaching energies up to 1.5 TeV (see Fig. 3.3). Such energetic photons require a population of parent electrons with a very high Lorentz factor. This marked the Crab pulsar as the most compact TeV accelerator known to date and MAGIC discovery imposed major constraints on the theoretical models, moving the emission region further from the star's surface, up to the light cylinder or even beyond (Bogovalov, 2014).

For the *Fermi*-LAT detected pulsars in the HE regime, their gamma-ray spectra are explained via synchrotron-curvature radiation (Abdo et al., 2013). Electrons and positrons in the pulsar's magnetosphere are confined to magnetic field lines. They follow the curved trajectories and emit curvature radiation. For *Fermi*-detected pulsars, this radiation component ends at GeV energies. Therefore, there is a sharp cutoff in the pulsar spectrum at energies of a few GeV. However, the curvature radiation cannot explain pulsed emission from the Crab pulsar above 1 TeV. Gamma rays at VHE produced closer to the neutron star's surface would be absorbed in the strong magnetic field via pair production process. The emitting region of the detected VHE gamma rays thus must be far from the neutron star surface. Inverse Compton scattering is the most probable mechanism which could explain the recent observations, as discussed in Ansoldi et al. (2016).

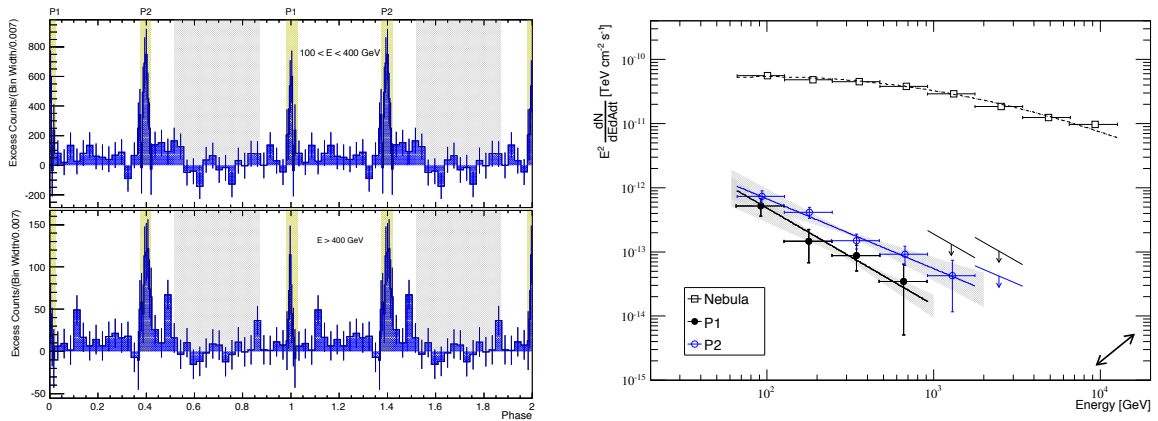


Figure 3.3: Left: Pulse profile of the Crab pulsar for energies up to 400 GeV and beyond. Two rotational cycles are shown. The phase intervals of the two peaks are marked with yellow, off-pulse regions are marked with grey. Right: Phase-folded spectral energy density of the first peak P1 (filled black circle) and the second P2 (open blue circle). The power-law spectrum of P2 extends up to  $\sim 2$  TeV, while P1 diminishes beyond 0.9 TeV. When comparing with the Crab nebula spectrum (open squares) at 1 TeV, one sees that the nebula energy flux is almost 3 orders of magnitude higher than that from the pulsar. For details, see Ansoldi et al. (2016).

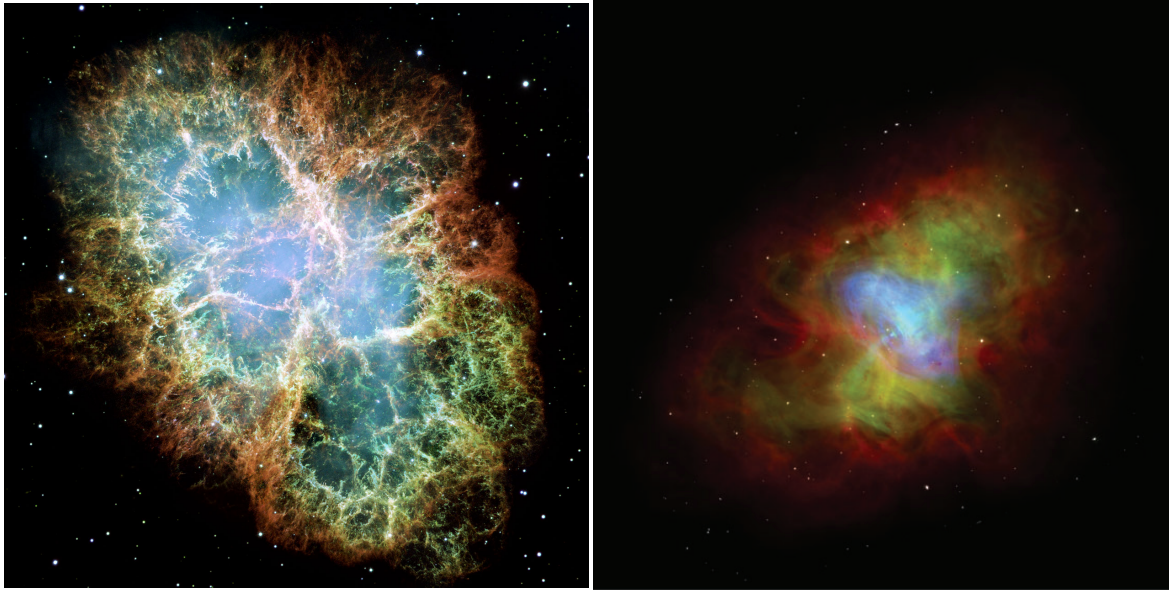


Figure 3.4: Left: This image of the Crab nebula is the most detailed image to date. It was taken with the Hubble Space Telescope WFPC2 camera and assembled from 24 individual exposures, which presents the highest-resolution image of the entire Crab nebula ever made. Credit: NASA, ESA and Allison Loll, Jeff Hester (Arizona State University); acknowledgement: Davide De Martin (ESA, Hubble). Right: The composite image of the Crab nebula showing X-ray image from Chandra satellite in blue, visible light from Hubble in green and a VLA radio image in red. The pulsar is seen in the centre as a bright blue light. Image taken from [Hester \(2008\)](#).

### 3.2.2 The Crab nebula

The Crab nebula is the best-known PWN in our galaxy due to its unique characteristics: it's very young, relatively close, and it is most likely associated with a supernova explosion observed in 1054. This nebula is centrally filled at all wavelengths, which is different from what is observed for other well-known SNRs. For example, Tycho's and Kepler's SNR show a shell morphology with the details described in Sec 1.7.

Energetics of the Crab nebula is governed by a steady injection of magnetic fields and relativistic particles from a central source – a 16th magnitude star in the centre of a nebula, see Fig. 3.4. It was confirmed in the late 1960s that the central star was a pulsar when 33 ms optical and radio pulsations were detected ([Cocke et al. 1969](#); [Staelin & Reifenstein 1968](#)). It was also shown that these pulsations were slowing down at a rate of 36 ns per day. The pulsar in the centre is slowing down, and its spin-down rate implies that its rotational kinetic energy is dissipated at a rate of  $\sim 5 \times 10^{38} \text{ erg s}^{-1}$ . This is similar to the theoretical value of the amount of energy being supplied to the nebula ([Gold, 1969](#)). The pulsar generates a magnetized particle wind, whose ultra-relativistic electrons and positrons radiate synchrotron emission across the elec-



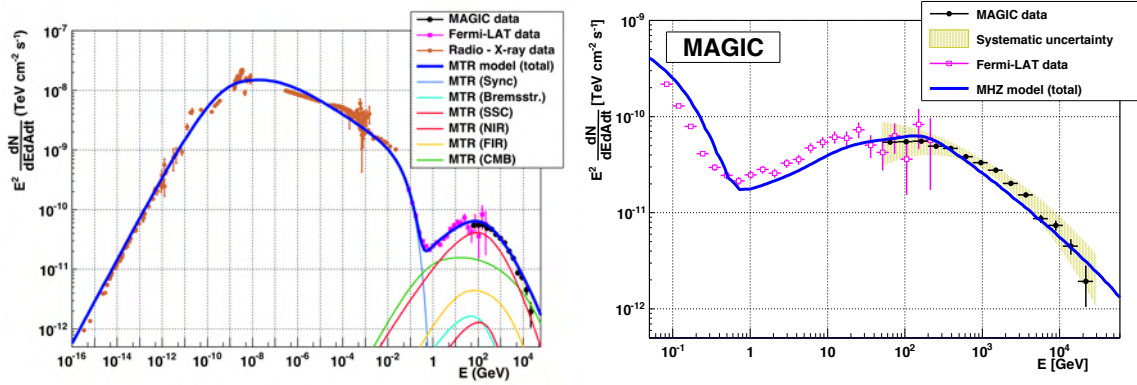


Figure 3.5: Left: The full spectral energy distribution (SED) of the Crab nebula from radio band to the gamma rays. Lines represent the best fit results based on the theoretical models: thin lines represent the individual components of the electromagnetic spectrum, and the thick blue line is the overall emission. Right: SED of the Crab nebula only from the gamma-ray regime: MAGIC and *Fermi*-LAT data (Aleksić et al., 2015).

tromagnetic spectrum (Bucciantini, 2008). The Crab pulsar has emitted the third of its energy budget into its surrounding nebula over the last 950 years. The energy supply of Crab nebula is very different from SNRs' where the dominant energy source was released at the moment of the original SN explosion, providing  $\sim 10^{51}$  ergs of kinetic energy. The Crab nebula that we see is not such freely expanding SNR. Namely, from the spectroscopic studies of the filaments in the Crab, estimated ejecta masses are less than what is expected from ejected mass by a core collapse supernova (Hester, 2008). Furthermore, based on the radial velocity measurements these filaments are found not to be expanding with the typical velocities seen in spectra of SNe,<sup>3</sup> but with significantly smaller velocities that are less than  $1500 \text{ km s}^{-1}$ . Overall, the kinetic energy would sum up to  $\sim 10^{49}$  ergs, which is less than the expected  $10^{51}$  ergs for core-collapse SNe (Hester, 2008). The Crab's outer SNR shell is still undetected, most probably because the SN blast wave has not interacted with enough material to produce a detectable remnant (Hester, 2008).

The magnetohydrodynamic model (Kennel & Coroniti, 1984b) explains steady synchrotron emission of the Crab nebula, observed from radio frequencies up to the soft gamma rays. The Crab nebula spectrum peaks in the optical through the X-ray part of the spectrum (see Fig. 3.5, left panel). Beyond 1 GeV, however, inverse Compton scattering of synchrotron photons on relativistic electrons becomes a dominant part (Atoyan & Aharonian, 1996). Studies of the Crab nebula's spectral index has been done at all wavelengths, and these studies show that the

<sup>3</sup>Typical velocities seen in spectra of young remnant such as Cas A are  $5000 - 10\,000 \text{ km s}^{-1}$ .

index is changing with the wavelength, depending on parent electron populations. In the inner parts of the nebula, the spectrum is harder and softens toward the edge, which is consistent with synchrotron burn-off. The observational evidence for softening of the synchrotron spectrum with the distance from the pulsar comes from the satellite measurements, X-ray torus has a photon index of -1.9 and drops to -4.4 in the nebula's outer regions (see [Hester 2008](#) and the references therein). A possible explanation of the observed spectral index variations in the outer nebula are changes in the particle's magnetically defined path. It is well known that energetic particles can move only along, and not across, the magnetic field lines. This causes the spectral index to change slowly along the field lines, while it changes abruptly across them.

When observed at different wavelengths, the spatial extent of the nebula is also changing, see [Fig. 3.4](#) (right panel). The general trend is that the nebula is smallest at high energies (X-rays) and grows in size when observed at lower energies (radio image). However, the extension of the nebula at very high gamma-ray energies is reported to be 52 arcsec ([H. E. S. S. Collaboration, 2020](#)), which is smaller than measured extension in the ultraviolet (UV) regime but much larger than seen in hard X-rays. This is explained by energetics of parent electrons producing the synchrotron or IC emission: lower energy electrons are emitting the UV synchrotron photons, medium energy electrons are emitting the IC gamma rays and the most energetic from these electrons are producing synchrotron X-ray emission. Thus, when observed at different wavelengths, nebular size matches the energy-dependent radiation losses of the parent electrons, i.e., higher energy electrons suffer more radiation losses thus propagate shorter distances.

### 3.3 Crab pulsar and its nebula observed with the MAGIC telescopes

Crab pulsar was observed with the MAGIC telescopes in January 2015. All data were taken in the stereo mode using SumTrigger II system ([Dazzi et al., 2021](#)) and the *wobble mode*, where the source is offset by  $0.4^\circ$  from the camera centre (see [Section 2.3.7](#)). Crab's coordinates used in the observations are (J2000): RA  $05^{\text{h}} 34^{\text{m}} 31.9^{\text{s}}$ , Dec:  $+22^\circ 00' 52.1''$  and zenith angle range spans from  $5^\circ - 25^\circ$ . Pulsar was observed during the nine days in total (January 13, 15-18 and 21-24, 2015). Due to bad weather or technical difficulties, 3 days were discarded (January 13, 15 and 22, 2015). After the data quality selection, the final data set contains roughly 9.5 hours of the good quality data.

The analysis was performed using the standard MAGIC Analysis and Reconstruction Software – MARS (version 2.14, [Zanin, R., 2013](#)), described in [Section 2.4](#). Standard Monte Carlo

(MC) was used, corresponding to the observational period, ST.03.05<sup>4</sup>. For the OFF data (representing hadron sample with no gamma-signal for growing RF), Dragonfly sumtrigger data from 2014 was used<sup>5</sup>. The phases of all the events were calculated using MAGIC tool *psearch* (Lopez Moya, 2006), based on the publicly available ephemeris (for January 2015) from the Jodrell Bank Observatory<sup>6</sup> (Lyne et al., 1993). For the pulsed emission, *hadronness* and  $\theta^2$  cuts were used and were obtained from *Odie*:  $hadronness < 0.69$  &  $\theta^2 < 0.04$ . To detect pulsar signal, signal and background regions were defined following definitions from Aleksić et al. (2012). Signal regions (ON phases) are  $P1 = [0.983 - 0.026]$  and  $P2 = [0.377 - 0.422]$ , while the background region (or OFF region) is defined as  $Bg = [0.52 - 0.88]$ . These definitions of signal regions are somewhat narrower than the ones used in the GeV range (100 MeV – 10 GeV) by Fierro et al. (1998), but as explained in the Aleksić et al. (2012) paper they are equally valid. The wider intervals give a higher noise contribution, but are free from selection bias, while the narrow intervals have much lower noise, but are affected by a small selection bias. Observations of Crab pulsar by MAGIC and VERITAS telescopes show the tendency of peaks becoming narrower as the energy rises from GeV to beyond 100 GeV. The excess of a signal is much more concentrated with the increasing energy, which results in a narrower peak definition.

#### 3.3.1 Crab pulsar folded light curve

The phase-folded event distribution, i.e., pulse profile, is obtained from the analysis of the data for the energies  $E < 200$  GeV. The significance of the pulsed emission was tested within the *psearch* program (Lopez Moya, 2006) with the  $Z_{10}^2$ -test, H-test and a  $\chi^2$ -test. A priori assumptions about the position and the shape of the pulses in the mentioned tests are not made. This is in contrast to the Li & Ma test significance (see eq.17, Li & Ma, 1983), where the pulse positions are a priori known. Thus, the Li & Ma test for (P1+P2) yields a somewhat higher significance of  $6.0 \sigma$ . The pulse profile is shown in Fig. 3.6. Two peaks (pulses) are clearly detected in the light curve. The first peak, P1, is around the phase 0.0 detected with  $\sim 4 \sigma$  significance and the second peak, P2, is around the phase 0.4, detected with  $\sim 5 \sigma$  significance.

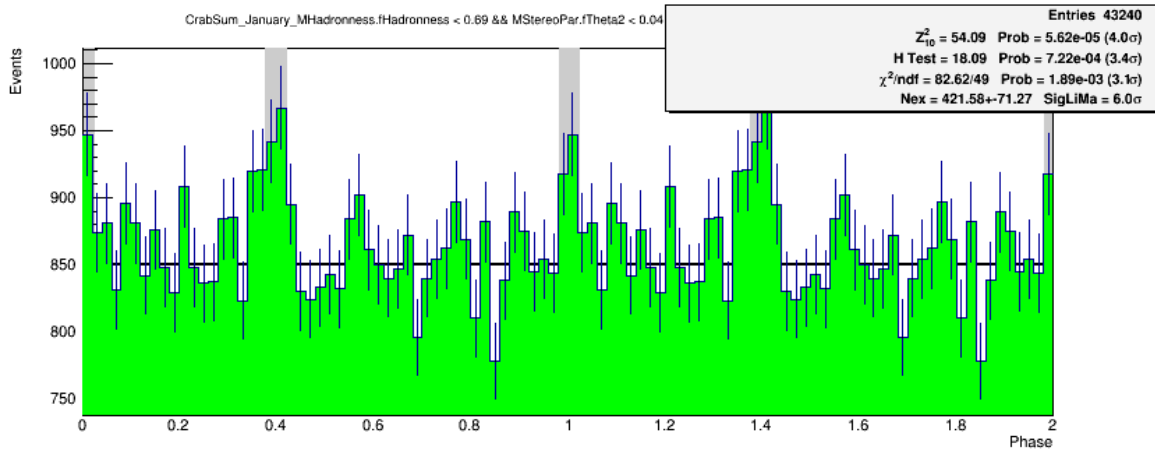


Figure 3.6: Crab pulsar light curve for energies  $E < 200$  GeV. Light curve is folded using monthly ephemeris publicly provided by the Jodrell Bank Observatory (Lyne et al., 1993) covering MAGIC January observations. Two rotation cycles (green histogram) are shown for clarity. Two peak amplitudes (grey shaded area) are visible in the structure that correspond to the P1 and P2 emission: one around 0.0 (P1) and the other around 0.4 (P2). The black line is the constant background level derived from the off-region.

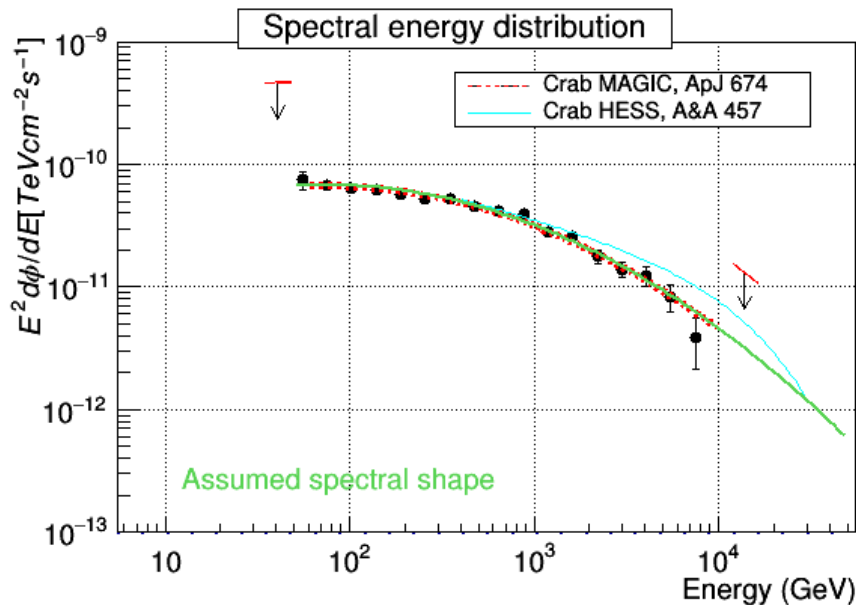


Figure 3.7: The spectral energy distribution of gamma-ray emission of the Crab nebula, obtained from the 9.5 hours of data observed with MAGIC telescopes in January 2015. Black data points represent this work (the upper limits indicated with black arrow) and agree well, within the systematic uncertainties, with the SED computed by H.E.S.S. (turquoise line) and within statistical uncertainties with previous MAGIC work (red dashed line, Albert et al., 2008b).

### 3.3.2 Crab nebula spectral energy distribution

From the same data set used to construct the Crab pulsar folded light curve, the continuous emission from the Crab nebula is studied. The analysis is, once again, performed using MARS (version 2.14, Zanin, R., 2013, see Sec. 2.4) and following the standard analysis pipeline. Although the data are taken with *sumtrigger*, standard Monte Carlo (MC) are used for this analysis (for observational period ST.03.05) since *sumtrigger*-MC were not available at that time. Following the steps described in Albert et al. (2008b), the obtained spectral energy distribution of the Crab nebula is shown in Fig. 3.7. To estimate the emission from the nebula, only photons coming from the off pulse region (in phase:  $B_g = [0.52 - 0.88]$ ) are taken into account. The distribution is given from 60 GeV up to  $\sim 7$  TeV, after analysing 9.5 hours of good quality data. The spectral energy distribution can be fitted by a curved power-law:

$$\frac{dF}{dE} = f_0(E/300 \text{ GeV})^{a+b \log_{10}(E/300 \text{ GeV})}, \quad (3.1)$$

yielding a flux normalization factor  $f_0 = (6.01 \pm 0.12) \times 10^{-10} \text{ cm}^{-2} \text{ s}^{-1} \text{ TeV}^{-1}$ , and parameters  $a = (-2.36 \pm 0.02)$  and  $b = (-0.17 \pm 0.04)$ . The Crab nebula fluxes at energies below  $10^3$  GeV are slowly decreasing with increasing energy while at higher energies, the fluxes start decreasing rapidly. When comparing the Crab nebula spectrum obtained from this work with the one from MAGIC previous results, like Albert et al. (2008a) or with other IACTs, like Aharonian et al. (2006) from HESS, there are slight differences which are due to the fact that the IACT instruments are not absolutely calibrated (see discussion in Sec. 2.5.2) thus suffer from systematic errors. Moreover, it is hard to expect a simple model like a curved power-law to explain broadband emission from likely different particle population in the nebula. For the broadband spectrum modelling of Crab nebula, the reader is referred to Zhang et al. (2020).

Overall, the spectrum of the Crab nebula obtained in this analysis is consistent within the systematic uncertainties with the previous measurements of the Crab nebula performed with other IACTs and within statistical uncertainties with earlier MAGIC results, which is an expected result.

---

<sup>4</sup>MAGIC collaboration internally introduces new analysis periods following significant changes in the telescope performance (i.e., the instrument response function). New Monte Carlo data sets are generated for each analysis period.

<sup>5</sup>The Dragonfly data was used as a hadron sample because no other OFF data taken with *sumtrigger* was available, and the preliminary analysis of the Dragonfly data showed no signal.

<sup>6</sup><http://www.jb.man.ac.uk/research/pulsar/crab.html>

## 3.4 Conclusions

In this Chapter, I demonstrated on the example of the Crab pulsar that the combination of the non-standard sum-trigger system and the pulsar analysis chain is appropriate to study the VHE pulsar candidates. The 9.5 hours of stereo data collected with the MAGIC telescopes show a clear pulsation from the Crab pulsar and a steady emission from the nebula. This expected result confirms that the MAGIC telescopes with the novel trigger system (hardware part) and pulsar analysis chain (software) may be applied to the analysis of similar VHE candidate pulsar, such as the Dragonfly pulsar, presented in the next Chapter.

The MAGIC collaboration recently used a much larger set of data from the Crab pulsar, a total of 320 hours, and discovered a pulsed emission above 1.5 TeV ([Ansoldi et al., 2016](#)). Afterwards, [Harding et al. \(2021\)](#) presented results of the broadband modelling of the Crab pulsar, using Particle-In-Cell (PIC) simulations (see Section 1.5.6), where three different pulsed VHE components are predicted, from which synchrotron self-Compton (SSC) component would best explain the MAGIC result above 1.5 TeV. Their model also predicts an inverse Compton scattering (ICS) component peaking around 10 – 20 TeV that could be detectable with HAWC.

# Chapter 4

## Dragonfly pulsar and its nebula observed at very high gamma-ray energies

### 4.1 Introduction

To better understand the physics behind the observed pulsar's features and its surroundings, more pulsars in the very high energy (VHE) regime needs to be found and used to constrain theoretical models of acceleration mechanisms (see Chapter 1 for more details). According to the *Fermi*-LAT catalogue (Abdo et al., 2013), Dragonfly pulsar (or PSR J2021+3651) is one of the brightest pulsars at 10 GeV in the sky, located in the Cygnus region (RA:  $20^h 21^m 05^s$ , Dec:  $+36^\circ 51' 04''$ ). It was originally discovered at 1.4 GHz with Arecibo radio telescope (Roberts et al., 2002) and timing of this 103.7 ms pulsar shows that it is one of the youngest and most energetic rotation-powered pulsars with its characteristic age of  $\tau = 17$  kyr and its spin-down luminosity of  $3.4 \times 10^{36}$  erg s<sup>-1</sup> (Roberts et al., 2002). A pulsar's surface dipole magnetic field can be estimated using the observational constraints along with the Eq.1.13 and is roughly  $B \approx 3.2 \times 10^{12}$  G. The distance parameter for the Dragonfly pulsar is somewhat questionable. Primarily, the distance of  $\approx 12$  kpc (Roberts et al., 2002) was established by using NE2001 model for the Galactic distribution of the free electrons (Cordes & Lazio, 2002) for the pulsar line of sight and dispersion measure (DM) of  $\approx 370$  pc cm<sup>-3</sup>. First X-ray observations suggested a bit smaller distance of  $\approx 10$  kpc (Hessels et al., 2004). However, a deeper X-ray observations yielded significantly smaller distance of about 3 – 4 kpc (Etten et al., 2008). On the other hand, pulsar polarization rotation measure implies a minimal distance of 5 kpc (Abdo et al., 2009b). Finally, when taking into account an interstellar extinction due to pulsar's specific location, in the crowded Cygnus region, the distance is estimated to be as low as 1.8 kpc (Kirichenko et al., 2015).

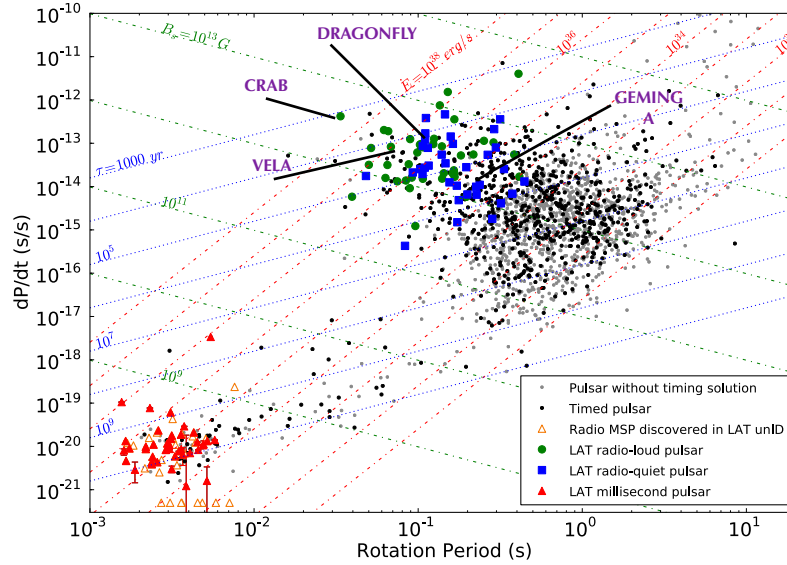


Figure 4.1: Pulsar spin-down rate  $\dot{P}$ , versus the rotation period  $P$ . Different pulsar classes are given in the legend and some ground-detected VHE pulsars and pulsar candidates are indicated in the Figure. Lines of constant characteristic age (blue), magnetic field strength (green) and spin-down luminosity (red) are displayed. Figure adapted from [Abdo et al. \(2013\)](#).

[Carrigan et al. \(2007\)](#) found a clear correlation between the gamma-ray detectability and spin-down flux  $\dot{E}/d^2$ , making the Dragonfly pulsar a promising candidate for the detection in the VHE band, under the assumption of its distance being  $\sim 1.8$  kpc, as indicated by [Kirichenko et al. \(2015\)](#).

Dragonfly, as well as some other pulsars mentioned earlier like Crab, Vela, Geminga, B1706-44, are all pulsars well studied at other energy bands and are plotted in the  $P - \dot{P}$  plane in Figure 4.1. These five pulsars share similar characteristics, which make them good candidates for the detection of the VHE pulsed emission: they are powerful, relatively close, have similar mag-

PULSAR	Crab	Vela	Dragonfly	B1706-44	Geminga
PERIOD (ms)	33	89	103.7	102	237
DISTANCE (in kpc)	2	0.3	1.8	2.3	0.25
AGE $\tau_c$ ( $10^3$ y)	1	11	17	17.5	340
$dE/dt$ ( $\text{ergs}^{-1}$ )	$5 \times 10^{38}$	$7 \times 10^{36}$	$4 \times 10^{36}$	$3.4 \times 10^{36}$	$3.26 \times 10^{34}$
B (in Gauss)	$3.8 \times 10^{12}$	$3.4 \times 10^{12}$	$3.2 \times 10^{12}$	$3 \times 10^{12}$	$1.6 \times 10^{12}$

Table 4.1: Comparing Dragonfly pulsar with all four ground-detected VHE gamma-ray pulsars and their main characteristics: pulsar period (in milliseconds), distance in kiloparsec, age in kiloyears, spin-down luminosity ( $dE/dt$ ) in  $\text{ergs}^{-1}$  and magnetic field strength in Gauss where  $1 \text{ erg} = 1 \times 10^{-7}$  Joules,  $1 \text{ T} = 1 \times 10^4$  Gauss,  $1 \text{ kpc} = 3261.5 \text{ ly}$ ,  $L_{\text{Sun}} = 3.846 \times 10^{33} \text{ ergs}^{-1}$ .



netic field strength (see Table 4.1), and all but Geminga are young (1-10 kyr). Vela pulsar has been the second VHE pulsar found (H. E. S. S. Collaboration et al., 2018), after Crab (see Chapter 3), and detection of Geminga between 15 and 75 GeV followed (Acciari et al., 2020). Pulsar B1706-44 is remarkably similar to Dragonfly, except for being  $\sim 100$  times brighter in the radio band, has recently been detected by the H.E.S.S. collaboration (Spir-Jacob et al., 2019). All of these recent discoveries at VHE were possible due to the improvements in the analysis of the ground-based Cherenkov telescope data, which lowered the energy threshold up to a few tens of GeV. Due to the fact that the emission mechanism at HE and VHE are related, if a source is detected at HE, chances of detecting it at VHE are much higher than for the general population of the same source class. A hint of pulsation above 25 GeV for Dragonfly pulsar was reported in the *Fermi*-LAT catalogue of sources above 10 GeV<sup>1</sup> and further analysed in (Burtovoi et al., 2017), see Fig. 4.2.

If Dragonfly pulsar is emitting at HE, it might be emitting in the VHE range, as well, which would make it detectable by MAGIC telescopes. As a promising VHE pulsar candidate, the Dragonfly pulsar was proposed for the observations with the MAGIC telescopes. These observations are the main topic of this Chapter. Besides the pulsar, the analysis will also include the search for the extended emission from the Dragonfly nebula.

This Chapter is organized as follows: a description of the Dragonfly pulsar and its nebula is given in Sec. 4.2. Section 4.3 describes Dragonfly observations with the MAGIC telescopes, including the telescope set-up. In Section 4.4 light curves for two energy bands are computed to evaluate the significance of the pulsed signal, whereas in Section 4.5 calculations of the SED for the pulsed emission are given. Comparison with the VERITAS results of the same source are presented in Sec. 4.6. Furthermore, the analysis of the extended emission from the Dragonfly nebula is described in Sec. 4.7. Finally, results for Dragonfly pulsar and its nebula are discussed in Section 4.8.

## 4.2 The source description

### 4.2.1 The Dragonfly pulsar

The Dragonfly pulsar has been previously observed with telescopes across the electromagnetic spectrum. Based on the observations with the Arecibo radio telescope, the radio pulse sig-

---

<sup>1</sup>The *Fermi*-LAT catalogue of sources above 10 GeV (Ackermann et al., 2013) can serve as the input for selection of sources which will be observed with ground-based Cherenkov telescopes. Due to the relatively small field of view and overall limited duty cycles of IACTs, the input information from the catalogue is the key to improve efficiency on VHE source detection.

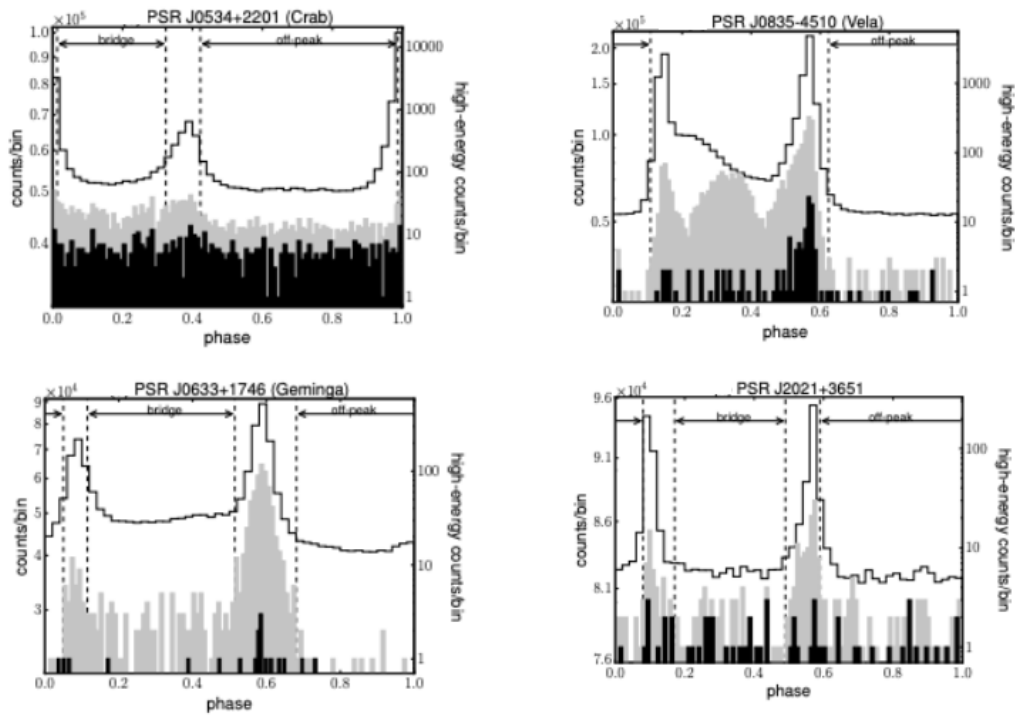


Figure 4.2: Pulse profiles of Crab, Vela, Geminga and PSR J2021+3651 (Dragonfly) produced after folding 5-years of *Fermi*-LAT data, where white, gray and black histograms denote events with energies  $E > 100$  MeV,  $E > 10$  GeV,  $E > 25$  GeV respectively. Vertical dashed lines correspond to the on-peak, off-peak and bridge emission phase intervals for  $E > 10$  GeV. Figure adapted from [Burtovoi et al. \(2017\)](#).

nal of Dragonfly appears to be rather faint ([Hessels et al. 2004](#); [Roberts et al. 2002](#)), as shown in Fig. 4.3. Optical observations with 10.4-m Gran Telescopio Canarias (GTC) showed no detectable counterpart of this pulsar ([Kirichenko et al., 2015](#)). Chandra detected PSR J2021+3651 in X-rays with the  $4\sigma$  significance ([Hessels et al., 2004](#)) based on the period obtained from the radio ephemeris. Thus far, no SNR shell has been observed, which could be used to verify the pulsar’s characteristic age via observation of the Sedov phase (for the SNR evolution phases, see Sec 1.7).

The pulsar was observed and detected in the HE gamma rays with AGILE satellite ([Halpern et al., 2008](#)) and also with *Fermi*-LAT ([Abdo et al., 2009a](#)). Based on the *Fermi*-LAT gamma-ray observations, which used radio pulsar timing information, a double-peaked pulse profile was found with the first peak within the phase interval of  $P1 = [0.13 - 0.20]$  and the second peak within  $P2 = [0.58 - 0.68]$ . Figure 4.4 shows Dragonfly’s pulse profiles across the electromagnetic spectrum: from the radio band to the high-energy gamma rays. From the pulse profile,

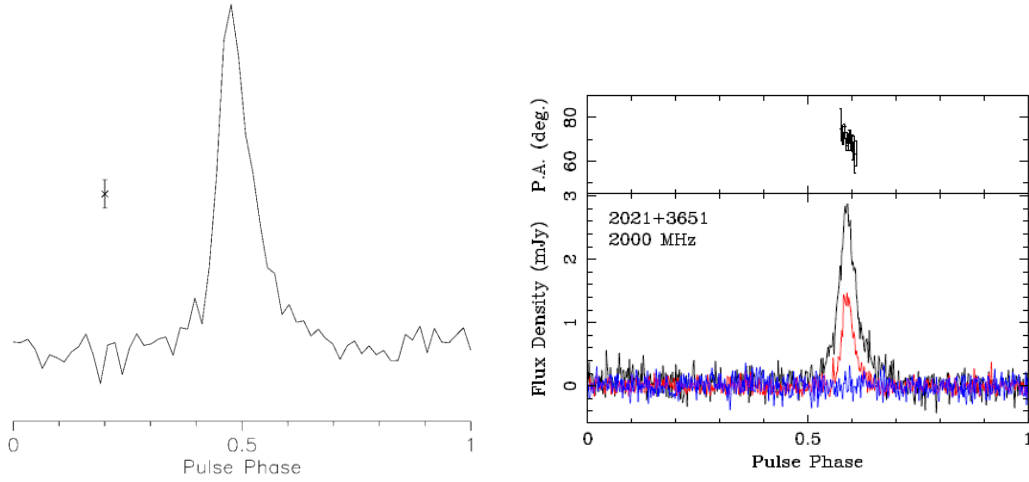


Figure 4.3: Left: 1.4 GHz radio pulse profile for Dragonfly pulsar, with the error bar representing  $1\sigma$  uncertainty. Figure is taken from [Roberts et al. \(2002\)](#). Right: plot shows the polarization- and flux-calibrated profile for the same pulsar measured at Green Bank Telescope. The black line corresponds to the total intensity, the red to linear and the blue to circular polarization; polarization data imply magnetic inclination of  $70^\circ$ , meaning that Dragonfly is close to the orthogonal rotator. Figure taken from [Abdo et al. \(2009a\)](#). Rotation and dispersion measure were determined from the radio observations and suggest a large distance of  $\sim 12$  kpc. Later, optical data showed the distance was overestimated. For details see [Kirichenko et al. 2015](#).

one sees that P1 fades with energy while P2 gives a persistent signal. The highest-energy photon in the shown sample has 12 GeV and is associated with P2 ([Abdo et al., 2009a](#)). The discovery paper at HE ([Abdo et al., 2009a](#)) reports about the bridge emission in the phase interval  $0.26 < \phi < 0.54$ , which can be observed in Fig. 4.4. The off-pulse data show no excess above the background, thus the upper limit on the flux of a PWN of  $< 10\%$  can be established. To constrain the spectral energy distribution (SED) of this pulsar, a power-law is assumed with an exponential cutoff:

$$\frac{dF}{dE} = kE^{-\Gamma} e^{-(E/E_c)}, \quad (4.1)$$

where the three parameters are a normalization factor  $k$  (in units of  $\text{ph cm}^{-2} \text{s}^{-1} \text{MeV}^{-1}$ ), photon index at low energy  $\Gamma$  and the cutoff energy  $E_c$ . Fit is made for photons above 200 MeV and, to reduce the background, the result is extrapolated to 100 MeV.

The results of the fitting, shown in Fig. 4.5, indicate that the SED data are fitted well by the analytic form of Eq. 4.1 with the photon spectrum well described with a photon index  $\Gamma \sim 1.5$  and a cutoff energy of  $\sim 2.4$  GeV. On the grounds of the observed emission beyond 10 GeV and

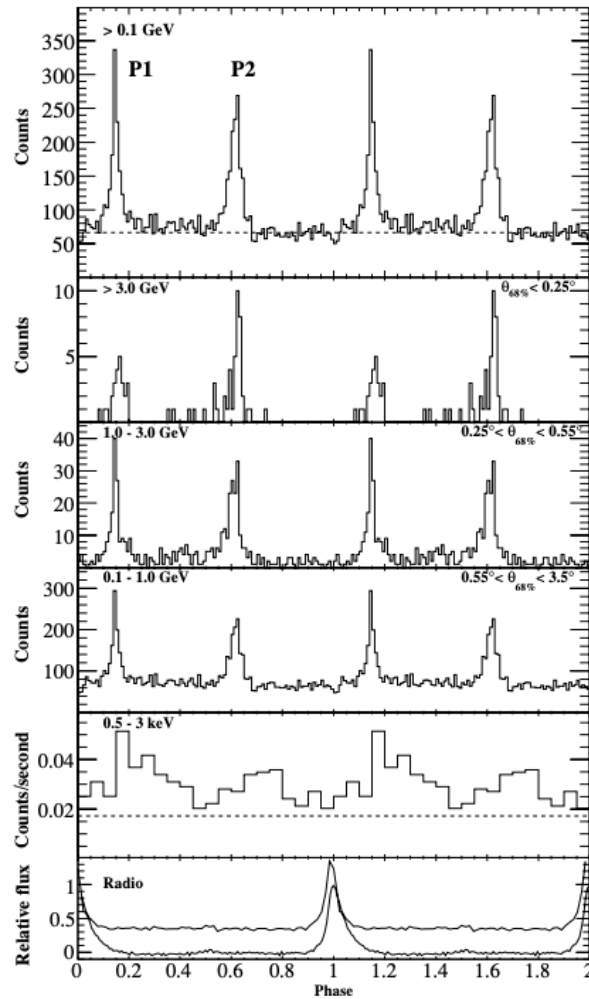


Figure 4.4: Top frames: Dragonfly pulse profile for gamma rays with  $E > 100$  MeV with *Fermi*-LAT; two rotation cycles are shown, the dashed line marks the average number of counts in the OFF region. Three following frames: light curves in specified energy ranges; second frame from the bottom: *Chandra* X-ray light curve; bottom frame: two radio profiles – upper obtained from Green Bank Telescope (1950 MHz) and the lower curve is the total intensity curve obtained from Arecibo. Figure adapted from [Abdo et al. \(2009a\)](#).

the absence of a sharp cutoff, outer gap models for the emission are preferred for this pulsar.

Many *Fermi*-LAT detected pulsars show spectral cutoff at a few tens of GeV: the effect of a spectral cutoff is manifested by the sparse photon statistics above 10 GeV. What is also apparent is the change in the pulse profile at higher energies ( $> 10$  GeV), compared to lower energies ( $< 10$  GeV). It is observed that the pulse widths are narrowing and the height of the first peak is decreasing in significance. This is true for Vela, Crab and Geminga, as well as for some other pulsars. If the pulsar is surrounded by a bright PWN, the gamma-ray emission from the nebula

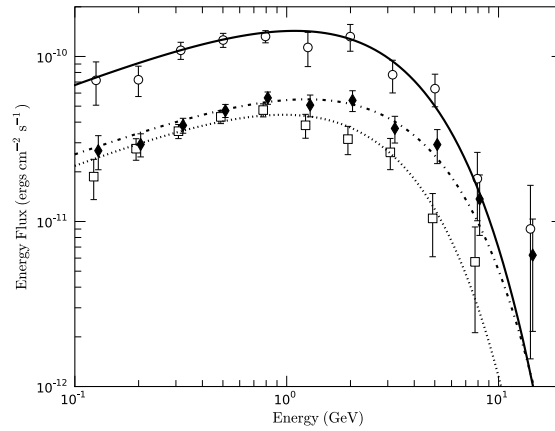


Figure 4.5: SED for PSR J2021+3651 from *Fermi*-LAT data: power-law spectrum with an exponential cutoff was assumed (for P1 – dotted, P2 – dot-dashed, Total pulse – solid). Figure adapted from [Abdo et al. \(2009a\)](#).

can be significant in contrast to the pulsar's, thus representing a significant background. This can limit pulsed emission detection.

#### 4.2.2 The Dragonfly nebula

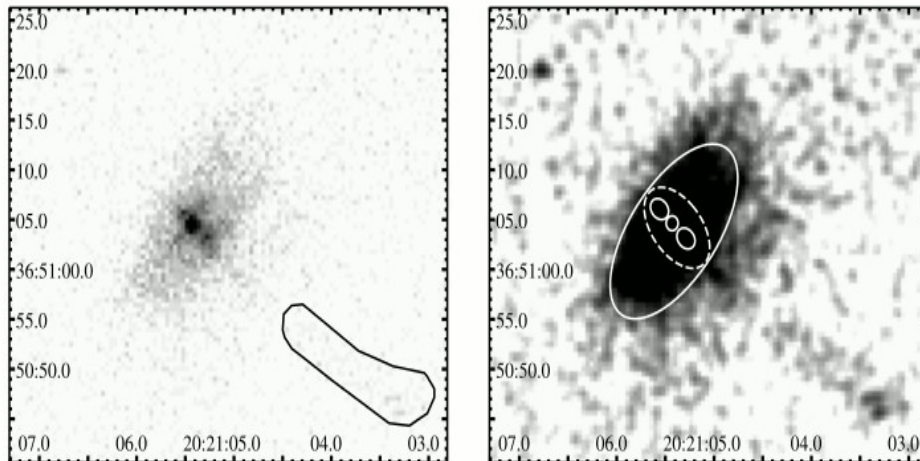


Figure 4.6: Chandra X-ray image of the axisymmetric Dragonfly nebula extending  $20''$  and  $10''$  with two ridges of emission from pulsar. Adapted from [Etten et al. \(2008\)](#).

Dragonfly pulsar is surrounded by a torus-like X-ray PWN, named G75.2+0.1 and detected by Chandra X-ray observatory ([Etten et al., 2008](#)), see Figure 4.6. This nebula is also known

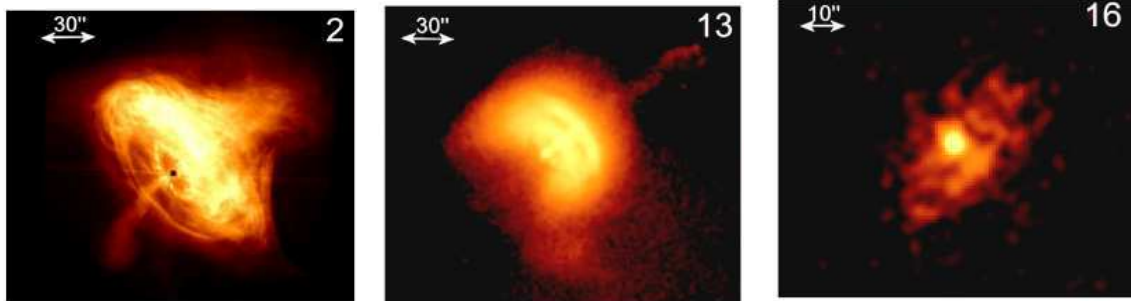


Figure 4.7: Chandra X-ray images of Crab, Vela and Dragonfly nebula, for comparison. Credit: [Kargaltsev et al. \(2015\)](#)

as the Dragonfly nebula, where the name comes from its specific morphology resembling the insect - *dragonfly*.

In X-rays, Dragonfly nebula is characterized with bright inner jets, a double-ridged equatorial inner nebula and a  $\sim 30''$  long polar jet ([Etten et al., 2008](#)). The central nebula is surrounded by the low surface brightness outer nebula, and no clear evidence of a host SNR is seen. The nebula is Vela-like due to the double-torus structure. The Crab and Vela PWNe are considered to be prime examples of torus-jet PWNe, with a distinction in their age (Vela is a factor of ten older) so one can observe evolutionary changes by comparing the two. In addition, Vela is the only other pulsar showing a double ridge<sup>2</sup> morphology in its PWN. Images from Chandra X-ray observatory, Fig. 4.7, show three nebulae powered by Crab, Vela and Dragonfly pulsars. From the X-ray images of the nebula's torus and jets, using a fit to the nebula's structure, the large inclination angle ( $86 \pm 1^\circ$ ) is derived. There is some evidence that pulsars with large misalignment between rotational and magnetic axis power torus-jet PWNe, which may have a crucial role in the morphology formation ([Kargaltsev et al., 2015](#)). In VHE gamma rays, a bright extended ( $\sim 2^\circ$ ) TeV source MGRO J2019+37, with a 20 TeV flux of 80% of those of Crab nebula, is associated with Dragonfly nebula according to the results from the VERITAS collaboration ([Aliu et al., 2014](#)), see Figure 4.8.

Resolving arcminute scale structure at TeV energies for MGRO J2019+37 would help to

<sup>2</sup>For the double-ridge morphology is unclear whether this represents a physical doubling of the equatorial torus or projection (caustic) effects in an optically thin, Doppler boosted pulsar wind is still unclear.

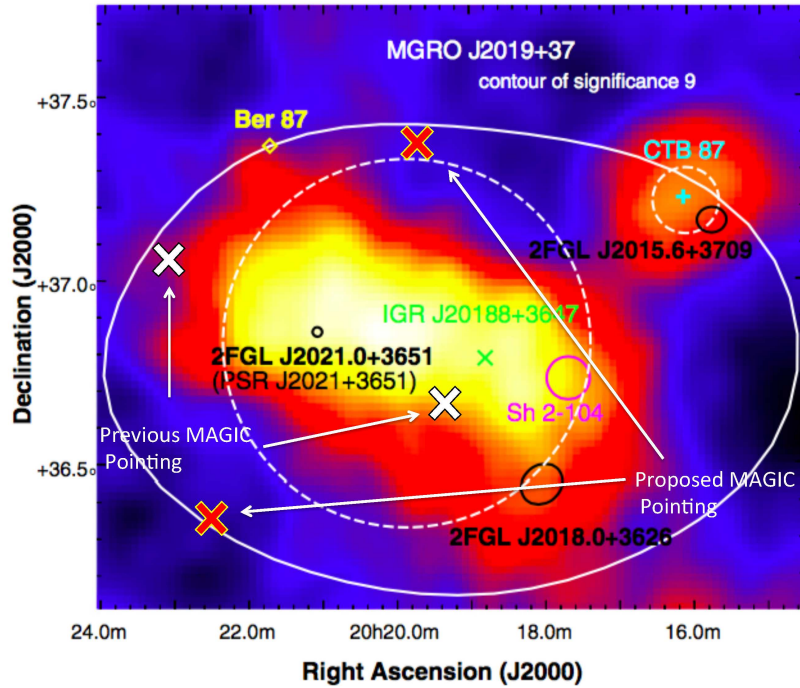


Figure 4.8: VHE gamma-ray excess map of MGRO J2019+37 region (observed by VERITAS) above 600 GeV. Regions used for spectral analysis of VER J2019+368 (and the other sources) are defined by white dashed circles. The locations of possible counterparts are marked using different colours. The contour of significance ( $9\sigma$ ) of MGRO J2019+37 is overlaid in white. Two white “X” indicate the previous MAGIC wobble pointings (from July and August 2014) and two red “X” indicate newly proposed wobble pointing of 0.7 degrees offset from the camera centre. Adapted from [Aliu et al. \(2014\)](#).

identify all the sources contributing to the observed emission. VERITAS resolved the MGRO source into two sources, where the brighter one, VER J2019+368, has a hard spectrum resembling the spectrum of Vela X – a PWN system powered by Vela pulsar. The extended ( $1^\circ$ ) source, VER J2019+368 is a bright source that likely accounts for the bulk of the MGRO J2019+37 emission and is coincident with Dragonfly pulsar.

The emission region contains Dragonfly pulsar and its PWN, but also the HII region Sh 2-104 and a hard X-ray transient IGR J20188+3657 (all potential counterparts of the observed emission are shown in Figure 4.8). The energy spectrum of VER J2019+368 extends from 1 to 30 TeV and is well-fitted by power-law with hard photon index of 1.75, comparable to that observed near Vela-X, ([Aliu et al., 2014](#)). The 1-10 TeV integrated energy flux is estimated to be  $(6.7 \pm 0.5_{\text{stat}} \pm 1.2_{\text{sys}}) \times 10^{-12} \text{ erg cm}^{-2} \text{ s}^{-1}$ .

Energy-dependent morphological studies were not carried out due to the lack of any statistically significant spectral point below 1 TeV. The hard spectrum of the source (spectral index

1.75), which resembles that of Vela-X, and extended VHE morphology in the direction of X-ray nebula favours the scenario where young and energetic pulsar (Dragonfly) is the main contributor to VER J2019+368. But also, other sources (Sh 2-104, 2FGL J2018.0+3626) are physically associated with the VHE emission, so further observations are needed to clarify the overall picture. In addition, a very recent analysis of 300 hours of VHE gamma-ray data taken with VERITAS is showing a  $3\sigma$  hint that emission coming from VER J2019+368 may be the result of two sources: VER J2018+367 and VER J2020+368 that were previously unresolved (Abeysekara et al., 2018).

### 4.3 Dragonfly pulsar and its nebula observed with the MAGIC telescopes

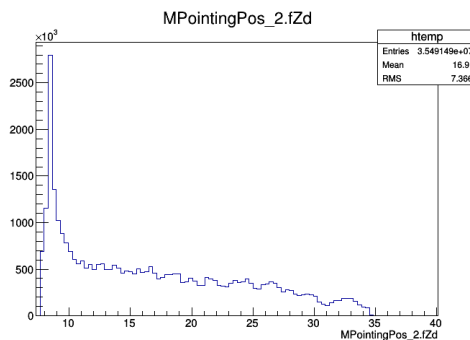


Figure 4.9: Zenith angle distribution of Dragonfly data set taken from July to August 2014.

Dragonfly observations were performed in July and August 2014 with the MAGIC telescopes. Data were taken in the stereo mode using the Sum-Trigger II system, introduced in Section 2.3.5, which lowers the energy threshold in comparison to the standard one, allowing the lower-energy analysis required to study pulsars. This trigger system covers the energy domain which overlaps that of the satellite experiments (see Sec. 1.4). During observations, the standard wobble offset was used, i.e.,  $0.4^\circ$  from the source. Dragonfly’s coordinates were adopted from *Chandra* observations (Hessels et al., 2004): (J2000): RA  $20^{\text{h}} 21^{\text{m}} 05^{\text{s}}$ , Dec:  $+36^\circ 51' 04''$ . Observations were performed under low zenith angles ranging from  $5^\circ$  to  $35^\circ$  (see Figure 4.9) to ensure the lowest possible energy threshold. The Dragonfly pulsar was observed during 18 days in total (July 5,6,8,10,22-31 and August 2-5, 2014). During that period, 35 hours of data



were successfully collected.<sup>3</sup> After quality selection, in which all bad weather data and data affected by the technical problems were discarded,  $\sim 27.6$  hours of good quality data remained for the analysis.

The analysis is performed using the standard MAGIC software, MARS (version 2.14, Zanin, R., 2013), described in Section 2.4. Standard Monte Carlo was used<sup>4</sup>, corresponding to the same observational period as Crab data, ST.03.05<sup>5</sup>, described in previous Chapter. Random forest (RF) was built using data from PSR1957+20 and PSR J2111+460 observations (no signal detected).

## 4.4 Phase calculations for Dragonfly pulsar

The MAGIC telescopes with a GPS receiver recorded the absolute event arrival time of each event, together with the event image. To find the pulsed signal in the data, we need to assign a phase to each event, as explained in Section 2.4.8. For this, we use MAGIC tool *psearch* (Lopez Moya, 2006) with a valid ephemeris corresponding to the observational period. The ephemeris was provided by the *Fermi*-LAT collaboration and is valid in MJD range 54658 – 56947 corresponding to YYYY MM DD: 2008 07 11 – 2014 10 17 period. Using *Fermi*-LAT data, signal (ON) and background (OFF) regions are defined a priori to avoid any selection bias. The light curve above 5 GeV is fitted with Lorentzian and  $\pm 2\sigma$  was used as ON. ON phases are defined as the intervals P1 and P2: [0.08 – 0.15] (P1) and [0.5 – 0.63] (P2), while OFF interval is defined as [0.65 – 0.9], see 4.2. Standard cuts are used for the low  $E_\gamma$ -range ( $50 \text{ GeV} < E < 200 \text{ GeV}$ ): *hadronness*  $< 0.28$ , *size*  $> 60$  and the full  $E_\gamma$ -range ( $E > 200 \text{ GeV}$ ) analysis: *hadronness*  $< 0.16$ , *size*  $> 300$ .

Light curves for both energy bands are computed and shown in Figure 4.10. The significance of the pulsed signal is evaluated in the regions, as defined in Table 4.2, using Eq. 2.1 in (Li & Ma, 1983). No significant pulsation was found from the 27.6 hours of MAGIC Dragonfly data: total significance (P1+P2) was found to be  $-1.9\sigma$  and  $-1.6\sigma$ , respectively.

<sup>3</sup>MAGIC’s time allocation committee (TAC) scheduled 100 hours for the observation of Dragonfly pulsar. Due to the technical malfunction of the telescopes, only 35 hours of data were collected.

<sup>4</sup>It should be noted that the data taken with sumtrigger should be analysed with the appropriate MC for the sumtrigger data, but at the time, we used the best available standard MC.

<sup>5</sup>MAGIC collaboration internally introduces new analysis periods following significant changes in the telescope performance (i.e., the instrument response function). New Monte Carlo data sets are generated for each analysis period.

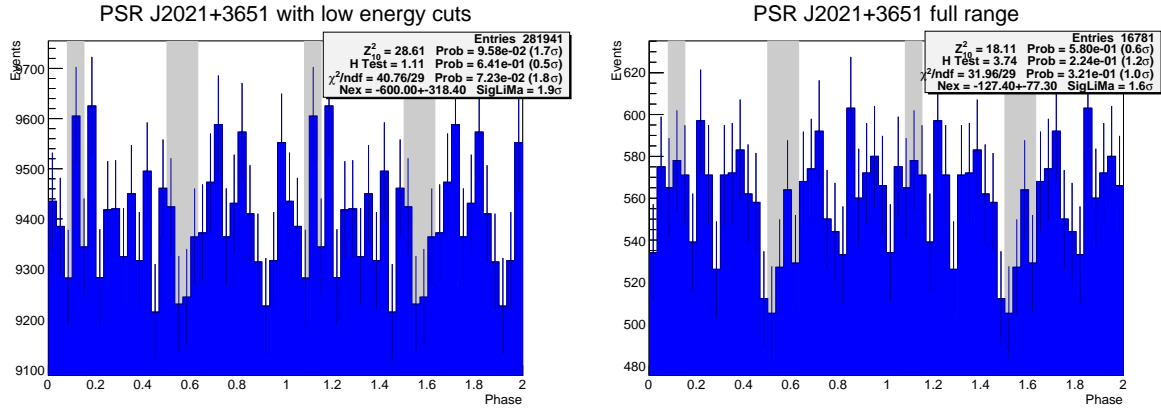


Figure 4.10: Light curves for Dragonfly pulsar obtained with the data from the MAGIC telescopes (this work) for different energy bands. Left to right: low-energy analysis ( $50\text{ GeV} < E < 200\text{ GeV}$ ), full  $E_\gamma$ -range analysis ( $E \geq 200\text{ GeV}$ ). For clarity, two periods are shown. The bin width is 0.03, corresponding to  $\sim 3\text{ ms}$  of Dragonfly rotational period. The shaded area indicates positions of P1 (main pulse) and P2 (interpulse). No significant pulsed emission is detected.

Energy range (GeV)	P1 (0.08 - 0.15)	P2 (0.5-0.63)	P1+P2
50 - 200	$1.9\sigma$	$-1.4\sigma$	$-1.9\sigma$
> 200	$0.22\sigma$	$-0.44\sigma$	$-1.6\sigma$

Table 4.2: Significance computed for the signal regions P1, P2 and the sum of both peaks for the Dragonfly pulsar. The significances were computed using Li&Ma (Li & Ma, 1983).

## 4.5 The spectrum of Dragonfly pulsar

As discussed in Sections 3.2 and 4.1, higher energy cut-off, characteristic for the majority of the high-energy pulsars, is absent in the SED of Dragonfly pulsar based on the previous observations with *Fermi*-LAT at  $E > 100\text{ MeV}$  (Abdo et al., 2009b). In this Section, I combine the data collected with the MAGIC telescopes in 2014 with the multi-year data collected with *Fermi*-LAT to provide a better constraint of the Dragonfly pulsar SED at the very high-energy end.

The SEDs of the pulsed emission of Dragonfly pulsar are presented in Figure 4.11, showing the SEDs of P1 and P2 (left and middle panels) and of the total pulsed emission (right panel). A pulsed signal has not been detected at the hypothesized pulse positions P1 and P2 from the data collected with the MAGIC telescopes. Based on these observations, I present the differential upper limits (see Sec. 2.5.1) for the pulsed emission above 200 GeV. The differential upper limits for the pulsed emission observed with MAGIC are also represented in Fig. 4.11 with black arrows, where we assumed a simple power-law with spectral index  $\Gamma = 4.0$ . SEDs are also computed from the 4.5 years of publicly available *Fermi* data where a power-law is assumed

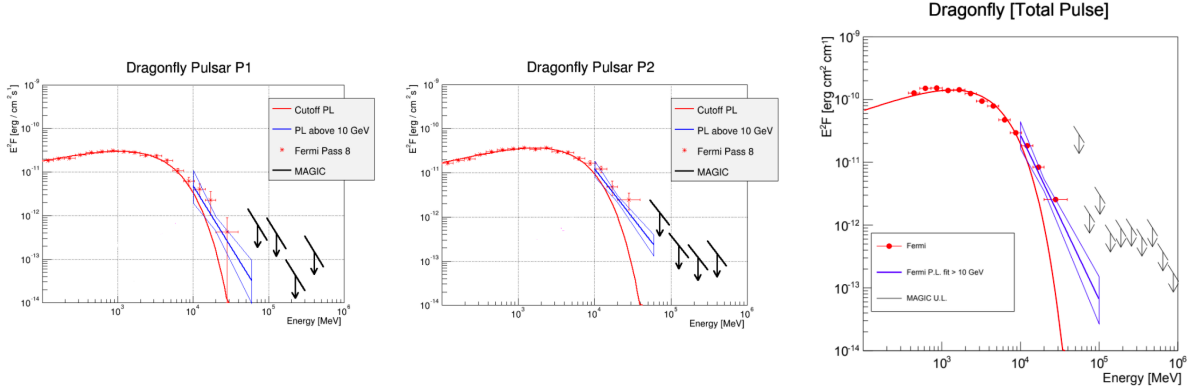


Figure 4.11: Dragonfly SED for the pulsed emission of Dragonfly in terms of P1 (left), P2 (middle) and total pulse (right), respectively. The red line represents the SED computed using 4.5 years of *Fermi*-LAT data (analysis performed by T. Saito), assuming power law spectrum with the exponential cutoff. The blue line is a simple power-law fit to Fermi data above 10 GeV. The statistical error contour from the power-law fit is also plotted. The MAGIC analysis (this work) is done with the assumed spectral index of 4.0 (a simple power-law). The MAGIC upper limits are indicated with black arrows, where a line above an arrow indicates the bin width.

with (for energies,  $0.1 \text{ GeV} < E < 10 \text{ GeV}$ ) and without the cutoff (for energies,  $E > 10 \text{ GeV}$ ). Fermi analysis of the data was performed by Takayuki Saito, a member of the MAGIC collaboration (and also a principal investigator of the Dragonfly observations). Primarily, based on the results from Fermi data analysis up to 10 GeV (Abdo et al., 2009a), a power-law with exponential cutoff is fitted with an assumption of the spectral index  $\Gamma = 4.0$  (marked with a red line in Fig. 4.11). However, motivated by the VHE observations of the Crab pulsar, we also fit a simple power-law (without the cutoff) to the Fermi data above 10 GeV, obtaining the spectral parameters presented in Table 4.3.

Energy range: 0.1 - 100 GeV	P1	P2
$F_0 [10^{-11} \text{ MeV}^{-1} \text{ cm}^{-2} \text{ s}^{-1}]$	$3.44 \pm 0.09$	$3.68 \pm 0.07$
$\Gamma$	$1.65 \pm 0.02$	$1.58 \pm 0.02$
$E_c [\text{GeV}]$	$3.01 \pm 0.15$	$3.97 \pm 0.19$
Energy range: $> 10 \text{ GeV}$	P1	P2
$F_0 [10^{-15} \text{ MeV}^{-1} \text{ cm}^{-2} \text{ s}^{-1}]$	$1.1 \pm 0.5$	$4.1 \pm 1.0$
$\Gamma$	$4.8 \pm 1.2$	$4.2 \pm 0.5$

Table 4.3: Dragonfly’s spectral parameters corresponding to figure 4.11 obtained from *Fermi*-LAT and MAGIC data. For energy range from 0.1 – 100 GeV, power law spectrum with the cutoff was assumed:  $dF/dE = F_0(E/E_0)^{-\Gamma} \exp(-E/E_c)$  with  $E_0=868 \text{ MeV}$  (upper table). For energy range above 10 GeV, simple power law was assumed:  $dF/dE = F_0(E/E_0)^{-\Gamma}$  with  $E_0=20 \text{ GeV}$  (lower table).

## 4.6 Updates on the Dragonfly pulsar

Relatively recently, the VERITAS collaboration presented a study of 13 young and bright gamma-ray pulsars visible in the Northern Hemisphere, including the Dragonfly pulsar (Archer et al., 2019). Using archival VERITAS data, they search for pulsed VHE emission from these pulsars. No significant pulsed emission from Dragonfly was found based on the analysis of 58 hours of observations. Similarly to work presented in Section 4.5, they derived upper limits with 95% confidence level, see Fig. 4.12.

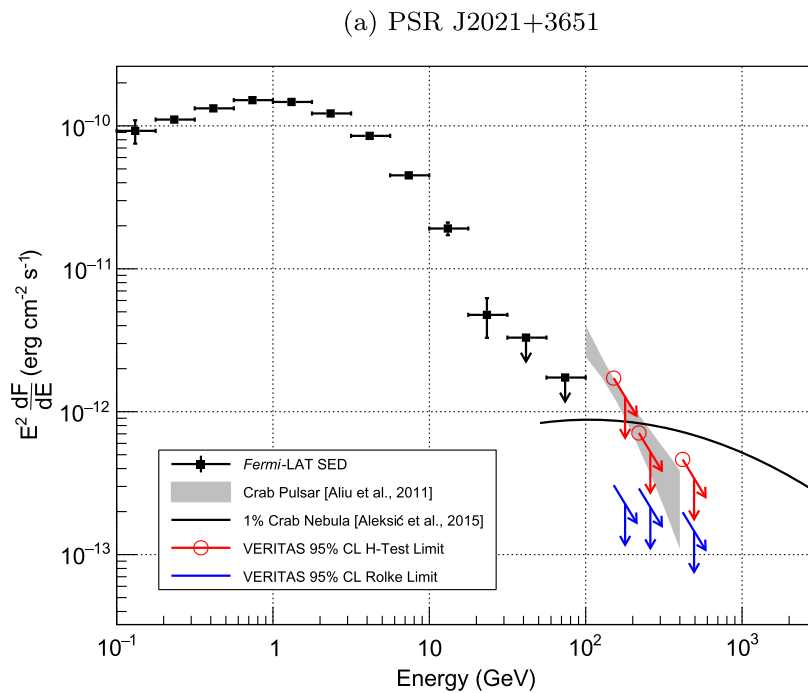


Figure 4.12: *Fermi*-LAT SED for Dragonfly pulsar (marked with black squares) combined with VERITAS differential flux upper limits (H-Test limits: red arrows, Rolke limits: blue arrows). With black solid line 1% Crab Nebula emission is noted, and grey area marks the Crab pulsar SED. Figure from Archer et al. (2019).

Comparing their result with the emission from the Crab pulsar, the upper limits on VHE pulsed emission of the Dragonfly pulsar constrain lower fluxes than those found for the Crab pulsar emission (which is only 1% of the Crab nebula emission, see Fig. 4.12). Derived ULs hint at a potential spectral hardening or possibly an entirely new spectral component in the vicinity or below the level of the limits. Pulsar models described in Chapter 1 (see Sec. 1.5.6) do predict several VHE emission components, one of them being several orders of magnitude below detected flux. If we compare the Dragonfly pulsar with a remarkably similar PSR B1706-

44, which was modelled in [Harding et al. \(2021\)](#) and shown in Fig. 1.19, the SSC radiation from pairs that produces the second VHE component with a broad SED typically peaking at 1-10 GeV, might be a culprit of these derived ULs.

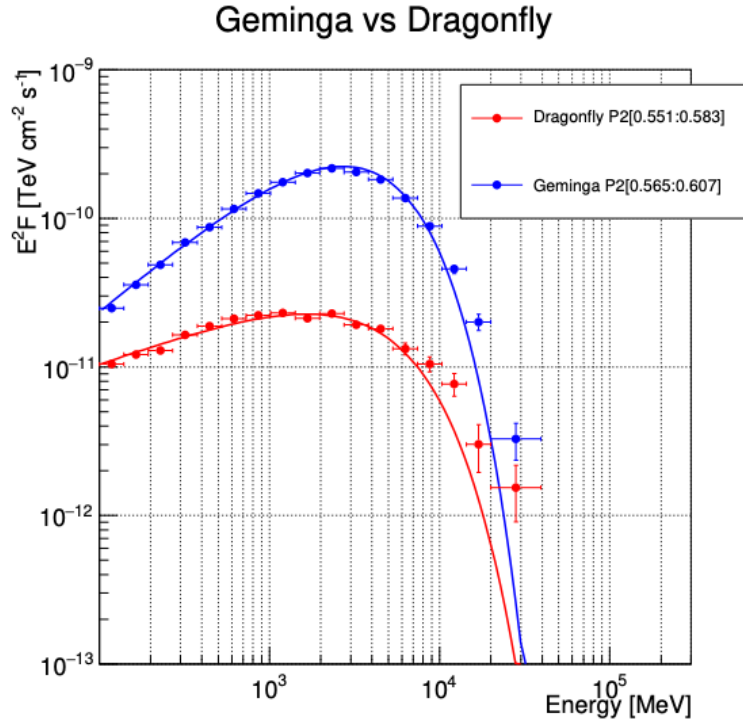


Figure 4.13: The SED of Dragonfly P2 (red) and Geminga P2 (blue) above 100 MeV obtained from *Fermi*-LAT data.

My analysis resulted with no hint of a signal for the pulsed VHE emission from Dragonfly, however upper limits on the VHE emission are constrained and result in fluxes obviously lower than Crab's. These results are independently confirmed by the VERITAS collaboration (with double the observation time). The expected Dragonfly pulsar VHE emission is significantly fainter than the emission from previously detected pulsars at VHE (Crab, Geminga). This could indicate that either the distance parameter for Dragonfly pulsar is underestimated, or some other intrinsic property of this pulsar is the reason for non-detection. The most recent discovery of Geminga pulsar by the MAGIC collaboration ([Acciari et al., 2020](#)) can give us a handle to estimate time needed for Dragonfly pulsar detection with the MAGIC telescopes. For comparison, if we analyse *Fermi*-LAT data (done by T.Saito) and produce SEDs of Geminga P2 and Dragonfly P2, see Fig. 4.13, at 30 GeV it seems that flux of Dragonfly is twice lower than that of Geminga's. Since Geminga is detected in 80 hours with the significance  $6.3\sigma$ , meaning that 50 hours is enough for  $5\sigma$  detection, it can be roughly estimated that  $\sim 200$  hours ( $\sim 50 \text{ hours} \times 2^2$ )

observation of Dragonfly pulsar with the MAGIC telescopes would lead to detection of its VHE pulsed component. A more sophisticated approach is to use the official MAGIC source simulator (*Mss version 1.3*) – a program that takes an assumed spectral shape of the target source and uses MAGIC performance in the range 40 GeV – 16 TeV (Aleksić et al., 2016b) to estimate the signal, i.e., computes the significance of each spectral point according to Eq.17 in Li & Ma (1983). The estimation is shown in the left panel of Fig. 4.14 and confirms an educated guess,

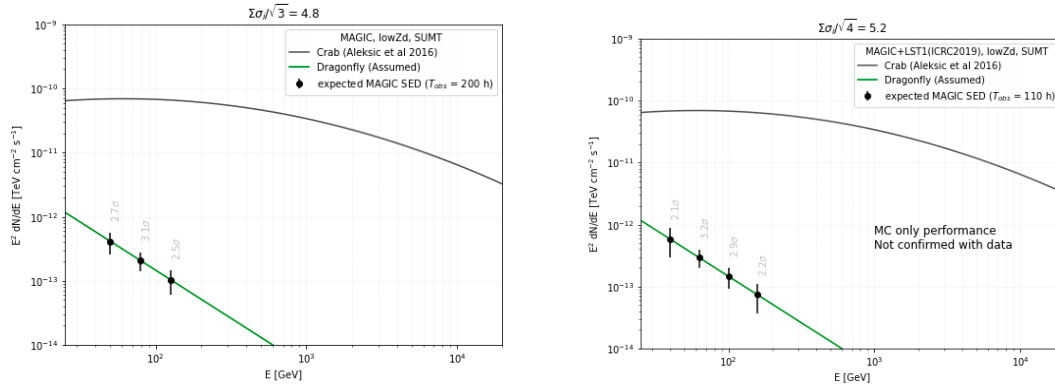


Figure 4.14: Expected Dragonfly’s SEDs produced from the official tool – MAGIC Source simulator for the MAGIC observations (left) and for the CTA (LST) observations (right). The assumed spectrum is a power-law with spectral index of 3.5. The simulator estimates 200 hours of observations are needed for Dragonfly pulsar detection with the MAGIC telescopes, that is 110 hours of CTA with the LST observations.

for the most optimistic case (assumed spectral index greater than -4), that approximately 200 hours of observations are needed for Dragonfly pulsar detection. For the less optimistic case (spectral index less than -4), simulator estimates about 800 hours for detection, which puts this candidate source in the impossible zone for the MAGIC telescopes.

As far as the next-generation telescopes are concerned, Burtovoi et al. (2017) presented prospects of pulsar detection at VHE with the next-generation IACT instrument CTA. They also analysed *Fermi*-LAT data of the chosen high-energy pulsars by fitting the spectra of each pulsar at energies  $E > 10$  GeV with a power-law function (assuming no spectral cut-off) and extrapolating the spectra to VHE range ( $E > 0.1$  TeV) and then simulating CTA observations (Hassan et al., 2015). Dragonfly pulsar, which is among 12 *Fermi*-LAT pulsars simulated, shows no detection, even after 50 hours of such observations. The official MAGIC source simulator where CTA performance (specifically performance for Large Size Telescope, LST with reflector diameter of 23.0 m and a pointing precision of  $< 14$  arcsec) is added from Monte Carlo study estimates, in the optimistic case, 110 hours observations are needed for Dragonfly detection, see right panel of Fig. 4.14, where about 400 hours would be needed if the less optimistic case

is considered.

## 4.7 Searching for an extended emission from Dragonfly’s nebula

To find continuous emission from Dragonfly nebula, the same data set was used as described in Sec. 4.3, in total  $\sim 35$  hours of data collected from July and August 2014. Observations were performed using the standard wobble mode, where the source is offset  $0.4^\circ$  from the camera centre. Although the wobble pointing setup was primarily intended for detection of the point source, the diffuse Monte Carlo simulations were used in the analysis of the 35h observations to search for an extended source, i.e., the Dragonfly nebula.

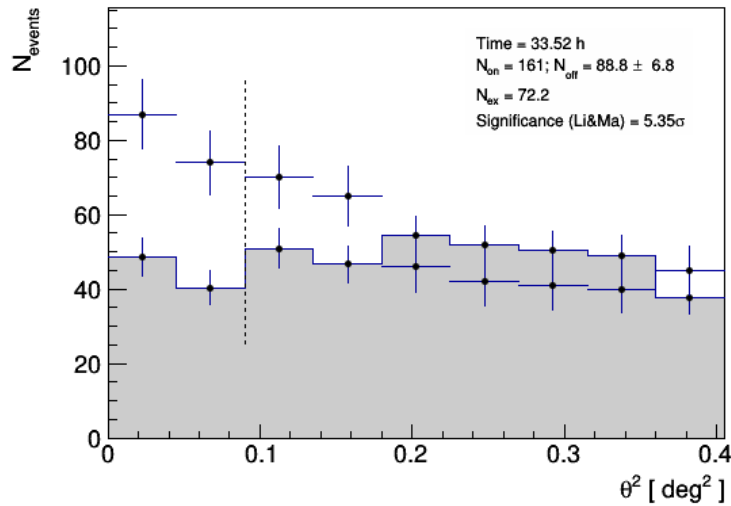


Figure 4.15: Distribution of squared angular distance  $\theta^2$  between the direction of gamma-ray events and the source position where the applied  $\theta^2$  – cut is  $0.09 \text{ deg}^2$  (vertical dashed line). The source position is obtained from skymaps and is found to be RA:  $(20.3156 \pm 0.0067)h$  and Dec:  $(36.8672 \pm 0.0776)^\circ$ . The distribution of  $\theta^2$  for OFF positions is the grey-filled histogram. There is also a negative excess in  $\theta^2$ -range above  $0.2 \text{ deg}^2$  which is the result of unsuitable wobble position, intended for a point source (pulsar observations) and not for the extended source (nebula).

Standard MARS software is used for the detection of the nebula. In the estimated energy range,  $E > 1 \text{ TeV}$  (standard HE cuts) we have a PSF =  $0.039^\circ$  and a smearing kernel of  $0.3^\circ$  (larger smearing kernel to detect the source which corresponds to the assumed source extension (Aliu et al., 2014) with the total PSF= $0.3^\circ$  (for the total PSF estimation see Sec. 2.4.9). The best fit position for the nebula for energies  $E > 1 \text{ TeV}$ , obtained by fitting a two-dimensional

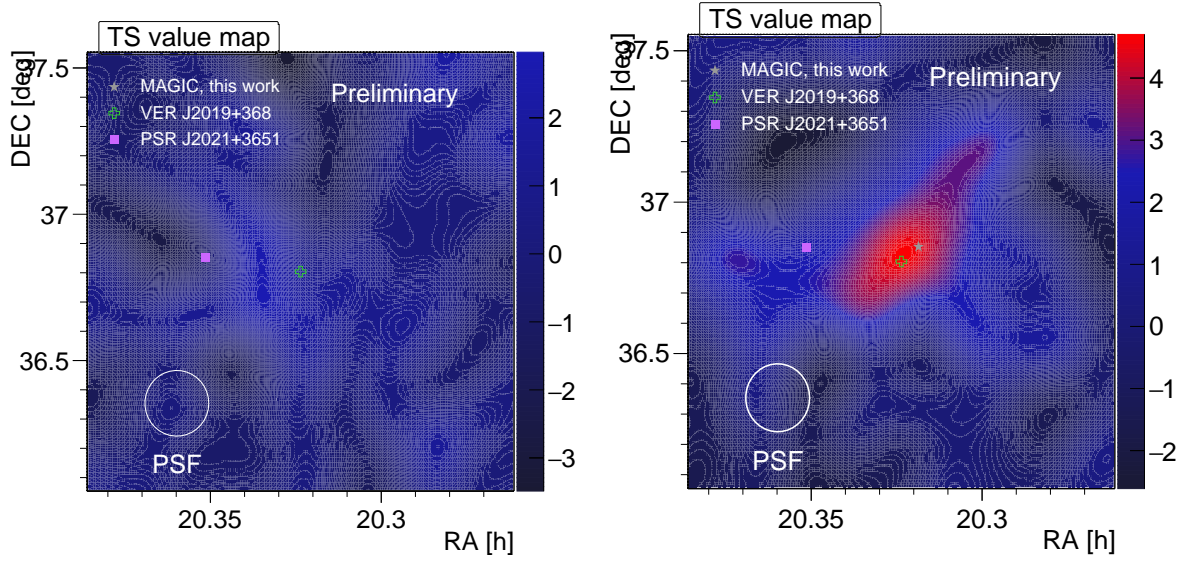


Figure 4.16: Dragonfly nebula Test Significance (TS) maps representing signal significance computed for the source location (grey star), for energies  $100 \text{ GeV} < E < 300 \text{ GeV}$  (left) and above  $5 \text{ TeV}$  (right). The position of the pulsar is indicated by a magenta square, VERITAS coordinates are indicated by the green cross and grey star indicates this work. The white circle indicates the point spread function.

symmetric Gaussian function to the excess map, is found to be RA:  $(20.3156 \pm 0.0067)h$  and Dec:  $(36.8672 \pm 0.0776)^\circ$ . This is compatible with the VERITAS centroid position (Aliu et al., 2014, with  $0.09^\circ$  deviation from this work), used in this analysis as a seed position.

The distribution of squared angular distance,  $\theta^2$  between the direction of gamma-ray events and the source position, is shown in Figure 4.15. To obtain the signal, signal cut of  $\theta^2 = 0.09 \text{ deg}^2$  is used due to the assumed extension of the source taken from Aliu et al. (2014) to be  $0.3^\circ$  and the instrumental PSF =  $0.039^\circ$ . The nebula is detected with  $5.35\sigma$  significance at the high-energy standard cuts.

For all skymaps, a smaller smearing kernel is used ( $0.1^\circ$ ) to see more details in the map. The emission is searched in four different energy ranges:  $100 \text{ GeV} < E < 300 \text{ GeV}$ ,  $E > 500 \text{ GeV}$ ,  $E > 1 \text{ TeV}$  and  $E > 5 \text{ TeV}$ . For different energy ranges, instrumental PSF is different and is estimated from the strong point-like source like Crab Nebula sample (with MARS executable *Odie*) at similar conditions as the data. For  $100 \text{ GeV} < E < 300 \text{ GeV}$ , PSF is estimated to be  $0.051^\circ$ , and for  $E > 500 \text{ GeV}$ , PSF is  $0.039^\circ$ . No emission is found for  $100 \text{ GeV} < E < 300 \text{ GeV}$ , see left plot in the Fig. 4.16. The gamma-ray emission is found for the energies above  $500 \text{ GeV}$  and above  $1 \text{ TeV}$ , respectively. The TS maps (Fig. 4.17) show signal significance around  $6\sigma$  and the relative flux maps with TS contours (Fig. 4.18) show detected emission for the above-mentioned energy ranges, respectively. The peak of the nebula emission above  $500 \text{ GeV}$



#### 4.7. Searching for an extended emission from Dragonfly's nebula

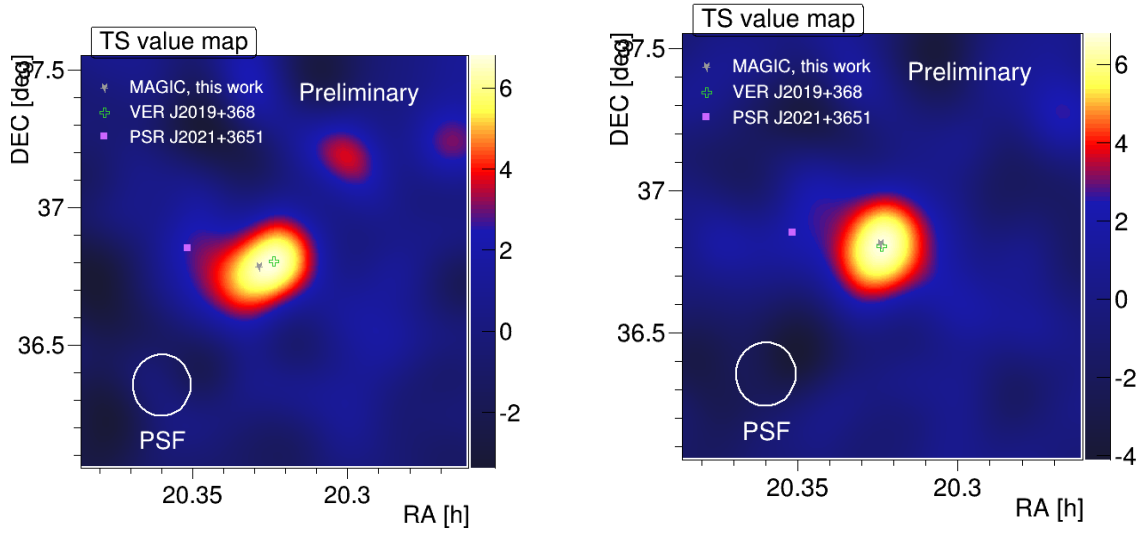


Figure 4.17: Dragonfly nebula Test Significance (TS) maps representing signal significance computed for the source location (grey star), for energies above 500 GeV (left) and above 1 TeV (right). For both energy ranges significance is around  $6\sigma$ . Position of the pulsar is indicated by a magenta square, VERITAS coordinates are indicated by the green cross and grey star indicates this work. The white circle indicates the point spread function.

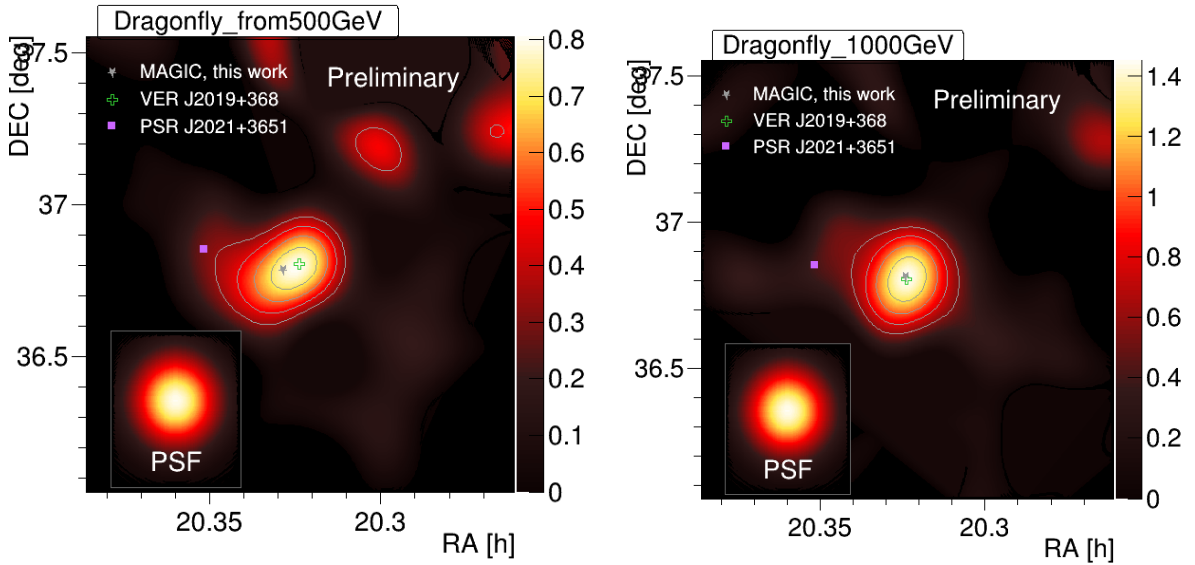


Figure 4.18: Dragonfly nebula gamma-ray flux map in arbitrary units for events with estimated energies above 500 GeV (left) and above 1 TeV (right). Overlaid are test statistic value contours in steps of 1, starting at 3, where the numbers approximately correspond to Gaussian significances. At the bottom-left the instrumental PSF is indicated (after smearing).

(left Fig. 4.18) is located  $\sim 0.27^\circ$  away from the Dragonfly pulsar position and is  $\sim 0.05^\circ$  from VERITAS estimated source position for nebula emission. For the energies above 1 TeV (right Fig. 4.18), the centroid of the emission is estimated only  $\sim 0.005^\circ$  away from the VERITAS source position and a bit more further from the pulsar location ( $\sim 0.32^\circ$ ). Additionally, one observes that the emission above 1 TeV is slightly offset in comparison to the emission above 500 GeV with a hint of a decrease in the emission size with an increase in energy. The hint of the energy-dependant morphology is also reported in [HAWC Collaboration et al. 2021](#). To resolve the obvious energy-dependent morphology, more observations should be performed. For the energies above 5 TeV (see right plot in the Fig. 4.16) there is no significant gamma-ray emission (only a hint) found for this source in this set of data.

## 4.8 Summary and future prospects

The search for pulsed emission from the Dragonfly pulsar with the MAGIC telescopes is motivated by the fact that *Fermi*-LAT reported a hint of a signal from 12 pulsars at energies above 25 GeV, one of them being the Dragonfly pulsar ([Ackermann et al., 2013](#)). Furthermore, Dragonfly pulsar is, like previously detected Crab and Vela pulsars, a highly ranked pulsar in terms of a detectability metric  $\dot{E}/d^2$ , with its high spin-down power (see Table 4.1) and if the last estimated distance of 1.8 kpc ([Kirichenko et al., 2015](#)) is taken into account. Like other gamma-ray pulsars with high  $\dot{E}/d^2$ , it is also associated with the known X-ray PWN – the Dragonfly nebula ([Etten et al., 2008](#)). All mentioned makes the Dragonfly pulsar a promising candidate source for the VHE pulsed emission.

The Dragonfly pulsar was observed during summer 2014 with the MAGIC telescopes. The observations were abruptly interrupted by the technical malfunction of the trigger cooling system, thus collecting 35 hours of data (out of 100 hours granted). The analysed data set showed no significant signal of the pulsed emission from the Dragonfly pulsar. However, these data enabled us to place upper limits on the Dragonfly pulsar SED in the energy range up to 200 GeV. Along with the MAGIC data, the collaborative work included 4.5 years of *Fermi*-LAT data, analysed by T. Saito (PI for Dragonfly observations) which were combined with the VHE upper limits presented in this Chapter. The observations intended for the point source, i.e., the Dragonfly pulsar, were also used to detect the extended emission from the nebula. Although the setup is not optimal, emission from the Dragonfly nebula is detected with the significance over  $5\sigma$ . The nebula signal extends further than the standard wobble setting of 0.4 degrees, and as a consequence, the background (OFF) contains some signal (which can be seen in the  $\theta^2$  range above  $0.2 \text{ deg}^2$  in Figure 4.15). However, despite the positive detection, the flux estimate

and the source extension could not be reliably determined as they would be severely biased by the contamination of the background signal from such an extended source. To have a proper observational set up, a proposal was written for MAGIC observations specifically intended for Dragonfly nebula – this time different wobbles were proposed, so that the signal region does not fall into the off region, as in the previous observations. In Figure 4.8, the gamma-ray excess map of the MGRO J2019+37 region (observed with VERITAS) is shown and also previous and proposed MAGIC wobble settings are indicated. Ultimately, the observations took place, but not enough data (less than  $\sim 7$  hours) was collected for a proper analysis.

Based on the observed upper limits in the VHE domain and considering no hint of the pulsed signal is found in our data set, the Dragonfly pulsar seems to be significantly fainter than the Crab or Geminga pulsars (see discussion in Sec. 4.6). With the result that is independently confirmed by the VERITAS collaboration where they also reported no hint of the signal with double the observational time, I conclude that either the distance parameter for the Dragonfly pulsar  $D \approx 1.8$  kpc, assumed from Kirichenko et al. (2015) and controversial from the start (see Sec. 4.1), might be underestimated or some other intrinsic pulsar property is at the origin. It was expected that the Dragonfly pulsar which is as powerful as Vela would already show a hint of the signal in the 30-hour data set, but this was not the case. Only after the Geminga detection (Acciari et al., 2020) with the MAGIC telescopes could two fluxes be compared and new time estimation for the Dragonfly pulsar could be established. From all the above-mentioned, Dragonfly pulsar will definitely require longer observational times for detection.

As described in Sec. 4.6, it is expected, in the most optimistic case, that roughly 200 hours of observations with the MAGIC telescopes are needed to achieve detection of the Dragonfly pulsed emission. This is double the initially demanded (granted) time. In principle, this could be achieved with repeated observations with MAGIC telescopes or with 110 hours of observations with the Cherenkov Telescope Array North (CTA North, Actis et al., 2011) that should be sensitive enough to resolve the morphology and reveal arcminute-scale structure of the Dragonfly nebula. For the less optimistic case (i.e., harder spectral index), one would need about 800 hours of the observations with the MAGIC telescopes (about 400 hours with CTA) which makes the Dragonfly pulsar a rather improbable candidate.

However, if detected, the Dragonfly pulsar would be the 5th VHE pulsar, which already makes a small population of VHE pulsars. This would allow the preliminary studies on how does the age of the pulsar affect VHE emission, is the second component in the VHE emission always present, how do different pulsars relate to their nebulae, etc. For solid conclusions on the VHE pulsar population, many more candidates needed to be detected, which is the roadmap for instruments like CTA that have a desired sensitivity below 50 GeV.

# Chapter 5

## VHE observations of the unidentified TeV source HESS J1858+020

### 5.1 Introduction

Along with all mentioned galactic sources (see Chapter 1, Sec. 1.3) detected in the VHE gamma-ray band, there are also sources with no obvious catalogued counterpart at longer wavelengths. These, so-called unidentified TeV sources, emit in the VHE band but have not been identified with any particular source class. For now, there are four categories in which a VHE gamma-ray source can be classified in general: active galactic nuclei (AGN), pulsar wind nebula (PWN), supernova remnant (SNR) and X-ray binary (XRB) and all of them are typically detected in the X-ray and radio band. However, the unidentified TeV sources lack X-ray or radio emission components. Since it is very difficult to explain VHE emission without the presence of a lower-energy emission<sup>1</sup>, these sources are either a new class of objects or deeper multi-wavelength observations are needed to detect possible X-ray and radio counterparts.

HESS J1858+020 (RA: 18<sup>h</sup>58<sup>m</sup>20<sup>s</sup>, Dec: 2°05'24'') is an unidentified, extended TeV gamma-ray source that was first discovered by the H.E.S.S. collaboration as part of its Galactic plane survey (Aharonian et al., 2008), see Figure, 5.1. The observed spectrum and size of the source suggest that HESS J1858+020 could be a PWN candidate. The spectrum of HESS J1858+020, reported by the H.E.S.S. collaboration, extends from 0.5 – 50 TeV, follows a power-law with the spectral index  $2.17 \pm 0.12$  and its gamma-ray flux is  $0.6 \times 10^{-12} \text{ TeV}^{-1} \text{ cm}^{-2} \text{ s}^{-1}$  (Aharonian et al., 2008). It is only  $0.7^\circ$  away from a larger and brighter TeV source – HESS J1857+026,

---

<sup>1</sup>VHE gamma rays as tracers of non-thermal particle acceleration are produced by high-energy electrons (leptonic scenario) or protons (hadronic scenario), wherein both cases X-ray and radio emission can occur simultaneously, although in some cases suppression of one or the other can be present.

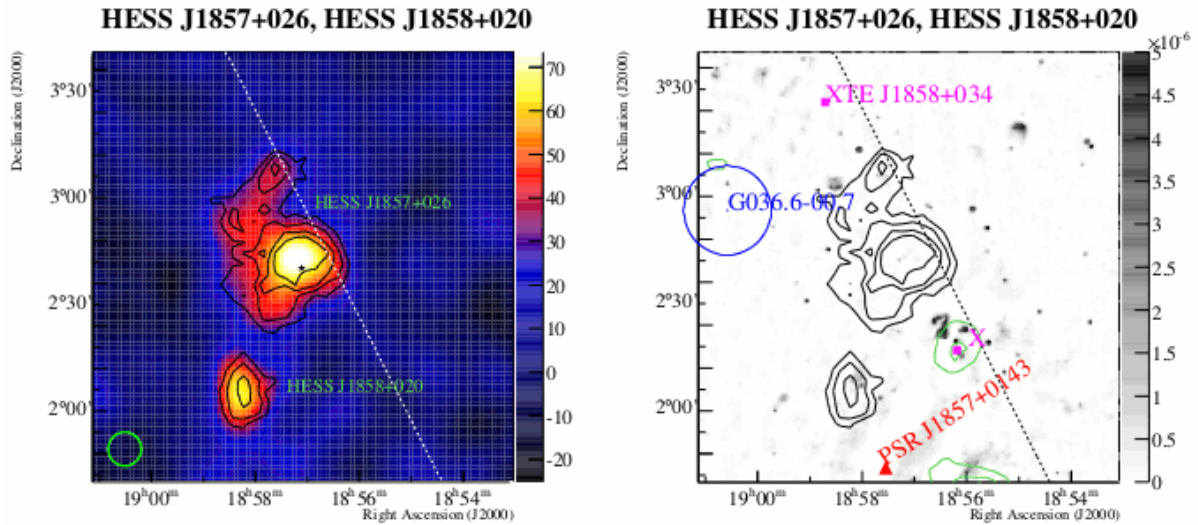


Figure 5.1: Left: VHE gamma-ray image of HESS J1858+020 and a larger nearby source J1857+026. Right: The HESS significance contours (black) and X-ray contours (green) overlaid on a radio image (grey-scale). Figures are taken from [Aharonian et al. \(2008\)](#).

with no significant emission connecting the two sources (see Figure 5.1). HESS J1858+020 is detected with the significance of  $7\sigma$  in 25 hours of observations and shows a slight morphological extension of  $\sim 0.08^\circ$  along the major axis ([Aharonian et al., 2008](#)).

While searching for the counterparts of HESS J1858+020, a radio source G35.6-0.4 (see right panel of Figure 5.1) was detected with VLA Galactic Plane Survey (VGPS) at 1.4 GHz as a middle-aged (30 kyr) SNR ([Green, 2009](#)). It is located north-west of HESS J1858+020 with an estimated distance of 10.5 kpc, shown in the Figure 5.2. Further studies using the Atacama Submillimeter Telescope Experiment (ASTE) in the  $^{12}\text{CO}$  and  $^{13}\text{CO}$  J=3-2 lines found a molecular cloud, IRAS 18558+0201, composed of two clumps, extending near the HESS source central region ([Paron & Giacani 2010; Paron et al. 2011](#)), see Figure 5.3. It was proposed that the detected TeV emission of HESS J1858+020 comes from the molecular gas interacting with cosmic rays accelerated by the shock front of the SNR G35.6-0.4 via hadronic processes. [Torres et al. \(2011\)](#) further investigated the proposed possibility and searched for the GeV counterparts with the *Fermi*-LAT. From the SNR's age, it follows that it could still accelerate protons energetic enough to produce GeV gamma rays. However, no GeV emission was found at that time.

In 2013, more detailed radio and multi-wavelength studies have been performed by [Paredes et al. \(2014\)](#). They observed the source with Giant Meterwave Radio Telescope (GMRT) at 1.4

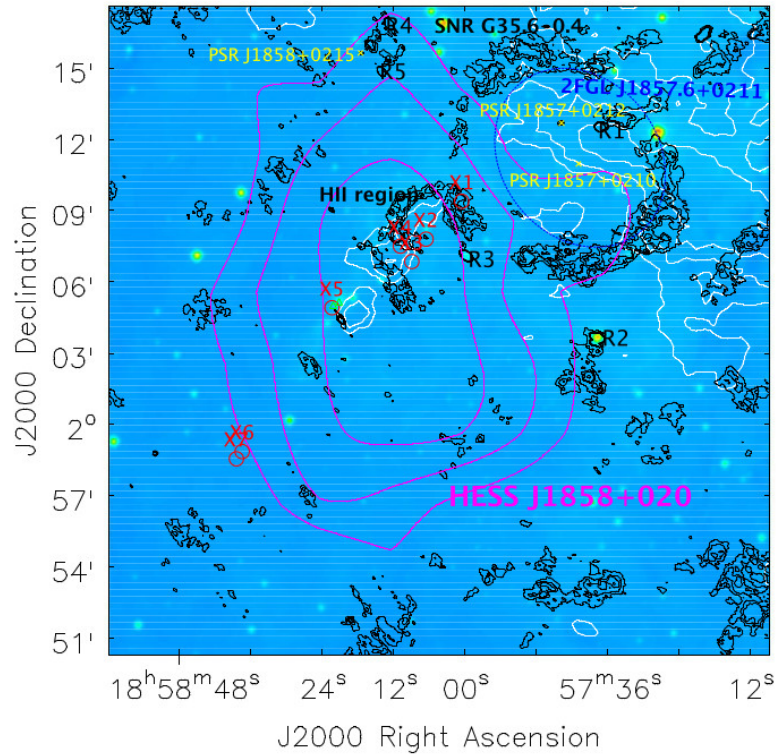


Figure 5.2: Radio image (black contours) of the field containing the unidentified HESS J1858+020 obtained with GMRT at 610 MHz. The HESS significance contours ( $4.5\sigma$  and  $6\sigma$  in magenta) are overlaid. The red circles correspond to X-ray sources. Distinct radio sources are marked with R1, . . . R5, respectively. The shell-like structure of SNR G35.6-0.4 is visible in the upper right region of the Figure. *Fermi*-LAT gamma-ray source 2FGL J1857.6+0211 is marked with a blue ellipse. Three nearby pulsars are marked with the yellow crosses. Figure adapted from [Paredes et al. \(2014\)](#).

GHz and 610 MHz frequencies to obtain deep radio maps of the field with arcsecond detail. No significant radio variability was found. Apart from SNR G35.6-0.4 and the HII region centred at HESS J1858+020, four other radio sources were detected. Two of the radio sources are non-thermal radio sources with an unclear counterpart at other wavelengths, and further observations would be necessary to clarify their physical origin. In the paper, they also explored the IR band using archival data from Wide-field Infrared Survey Explorer (WISE) and the X-ray band by analysing archival Chandra data. Molecular cloud distribution data were obtained from the Galactic Ring Survey ([Jackson et al., 2006](#)). Furthermore, a kinematic distance study of the SNR G35.6-0.4 and its surroundings was performed using 1420 MHz continuum, 21 cm HI spectral line and  $^{13}\text{CO}$   $J = 1 - 0$  line data ([Zhu et al., 2013](#)). The newly established distance for SNR G35.6-0.4 is 3.6 kpc and the new derived mass for the CO molecular cloud is  $600M_{\text{Sun}}$ . With these newly established parameters, the connection between G35.6-0.4 and

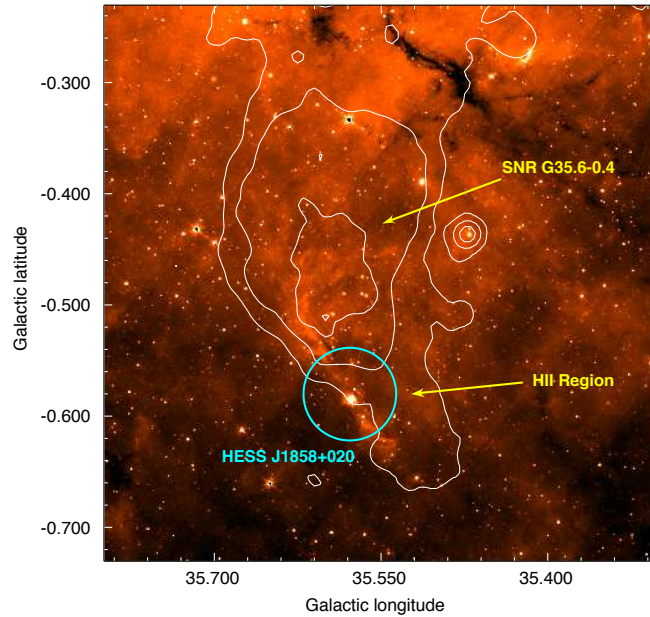


Figure 5.3: Infrared image obtained from Spitzer-IRAC ( $8\mu\text{m}$ ) of the area around SNR G35.6-0.4 with contours of radio continuum emission at 20 cm. The circle represents the position and the extension of HESS J1858+020. SNR is possibly partially superimposed over the HII region. For details, see [Paron et al. \(2011\)](#).

HESS J1858+020 became even more probable.

Three pulsars, PSR J1857+0212, PSR J1857+0210 and PSR J1858+020 are within the field of the SNR. All are older than  $10^5$  yr and, with the estimated distances of 8, 15.4 and 12.4 kpc, were disfavoured for the association with HESS J1858+020 by the newly confirmed SNR's distance of 3.6 kpc. In the 0.4 – 7 keV Chandra data, there are seven X-ray sources detected around HESS J1858+020. None of these seven sources has an IR counterpart and four of them have similar spectra and show hints of a thermal origin of the X-ray emission which, together with the spectral properties, could be an indication that these sources might be embedded proto-stars ([Paredes et al., 2014](#)). Additionally, a new source, 1HWC J1857+023, was detected with High Altitude Water Cherenkov (HAWC) Observatory. It is approximately  $0.4^\circ$  away from both HESS J1857+026 and J1858+020 ([Abeysekara et al., 2016](#)). The differential flux normalization of 1HWC J1857+020 is compatible with the combined flux of the two HESS sources, where J1857+026 has approximately an order of magnitude higher flux.

[Cui et al. \(2021\)](#) performed a deeper *Fermi*-LAT analysis of the two point sources associated with the SNR G35.6-0.4 reported from the latest *Fermi*-LAT catalogue ([Abdollahi et al., 2020](#))

of gamma-ray sources. They used a hadronic model to successfully explain escaping CRs from the SNR and their interaction with molecular clouds producing GeV-TeV emission at the location of HESS J1858+020.

In this Chapter, I will describe the analysis of the HESS J1858+020 archival data collected by the MAGIC telescopes. The source was classified as an unidentified TeV source with no counterparts at lower energies, whereas in the HESS Galactic Survey (Aharonian et al., 2008) it was put forward as a PWN candidate. With a handful of data on our disposal, the goal is to study the source observed with the MAGIC telescopes and to confirm the PWN scenario and possibly study morphology of this slightly extended source. The Chapter is organized as follows: Section 5.2 describes the archival data sets that were the observations performed by the MAGIC telescopes with the HESS J1858+020 in the field of view (FoV). In the Section 5.3, the non-standard analysis of this source is described, followed by the results presented in Section 5.4. The Chapter ends with the Section 5.5 in which conclusion and discussion are given.

## 5.2 The MAGIC observations and data sets

For the analysis of HESS J1858+020, I used two different data sets in which this source was observed indirectly. It was in the FoV of observations targeting HESS J857+026 and SNR W44.

The first data set consists of the MAGIC observations from 2010 where the target was the larger and brighter nearby source, HESS J1857+026. These observations were performed from July to October 2010 (period ST.01.02<sup>2</sup>) with zenith angles between 25° to 36° providing in total 50 hours, see left Figure 5.4. For the exact dates of the observations, see Table 5.1. The HESS J1857+026 source with its coordinates RA : 18<sup>h</sup>57<sup>m</sup>27<sup>s</sup> and Dec : 02°42′60″ was observed in the wobble mode. There were four different pairs of pointing directions symmetric with respect to the source, two of the pairs were 0.4° and 0.5° away from the source direction (see left Figure in 5.4).

From the analysis of the larger source, the MAGIC collaboration revealed an energy-dependent morphology within the HESS J1857+026 and proposed a two-source scenario, whereby one source would be associated with the relic PWN belonging to a nearby pulsar, while the other could be linked with a molecular cloud complex (MAGIC Collaboration et al., 2014). In the same paper, the smaller source HESS J1858+020 (analysed in this Chapter) was also detected,

---

<sup>2</sup>MAGIC collaboration internally introduces new analysis periods following significant changes in the telescope performance (i.e., the instrument response function). New Monte Carlo data sets are generated for each analysis period.



but with low significance due to the low exposure at  $0.5^\circ$  angular distance to the pointing positions (MAGIC Collaboration et al., 2014).

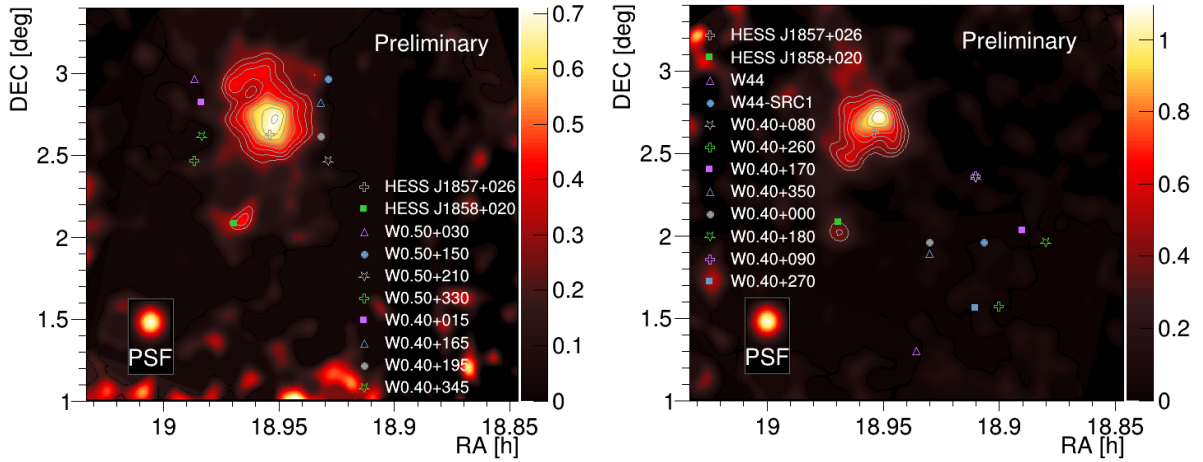


Figure 5.4: MAGIC observations of HESS J1857+026 (left) and W44 (right) where HESS J1858+020 is in the field of view of MAGIC camera. Different wobble positions of the MAGIC camera are marked with different colours and shapes.

The second data set represents the observations of the SNR W44 that took place from April to October 2013 (analysis period ST.03.02) and from April to September 2014 (analysis periods ST.03.03 and ST.03.05) in the zenith range between  $25^\circ$  and  $45^\circ$ , see right Figure 5.4. The SNR W44 region was observed for  $\sim 120$  hours (see Table 5.1 for the exact observational dates) in the wobble mode with an offset of  $0.4^\circ$  between the pointing and the observed W44 SRC1 source with the coordinates RA :  $18^{\text{h}}54^{\text{m}}45^{\text{s}}$ , Dec :  $01^\circ53'59''$  (right Figure 5.4). The region surrounding SNR W44 includes the SNR and two GeV sources detected by *Fermi*-LAT named W44 SRC1 and W44 SRC2 (Uchiyama et al., 2012), with a molecular cloud enclosing the system. The aim of the MAGIC observations was to detect possible VHE emission at the same location where GeV emission (up to  $\sim 100$  GeV) was detected by *Fermi*-LAT, see Fig. 5.5. In the diffusion scenario, hadrons are accelerated at the SNR (W44) shock, after which they escape and diffuse, resulting in a GeV detection offset from the radio SNR shell. MAGIC found no significant VHE ( $> 100$  GeV) signal from W44 SRC1 (Di Tria et al., 2021).

I have combined and analysed these two data sets to study the HESS J1858+020 source. In total, this sums up to 170 hours of archival data.

Target source	RA (h:m:s); DEC(° :':")	Observational dates (YYYY MM DD)
W44	18:56:05 01:23:27	2014 09 13-14; 2014 09 17
W44-SRC2	18:58:00 00:50:24	2014 08 27; 2014 08 29-30; 2014 09 12
HESS J1857	18:57:27; 02:42:60	2010 07 11-18; 2010 08 01-04; 2010 08 06-07; 2010 08 09-10; 2010 08 15; 2010 09 01-06; 2010 09 08-10; 2010 09 28; 2010 09 30; 2010 10 02; 2010 10 04-06; 2010 10 10
W44-SRC1	18:54:45; 01:53:59	2013 04 10; 2013 04 12; 2013 04 14-19; 2013 04 22; 2013 05 06-16; 2013 05 23; 2013 05 31; 2013 06 01-08; 2013 06 10-21; 2013 06 29-30; 2013 07 01-04; 2013 07 07-18; 2013 07 29; 2013 07 31; 2013 08 01-16; 2013 08 29; 2013 08 31; 2013 09 01-07; 2013 09 09-10; 2013 09 12; 2013 09 24; 2013 09 27-30; 2013 10 01; 2013 10 04-06; 2014 04 08-11; 2014 04 25; 2014 04 27-30; 2014 05 01-04; 2014 05 06-12; 2014 05 23-31; 2014 06 01-08; 2014 07 19; 2014 07 23; 2014 07 25; 2014 07 27; 2014 07 29-31; 2014 08 01-03

Table 5.1: Target sources with their coordinates and observational dates

### 5.3 Data analysis of HESS J1858+020

The analysis was done using the MAGIC Analysis Reconstruction Software MARS (version 2.14, Zanin, R., 2013) described in Chapter 2, Sec. 2.4. As already mentioned, HESS J1858+020 was in the FoV of other MAGIC observations and these archival data were used for the analysis. A quality selection was done by discarding the data affected by bad weather or technical problems. After this selection,  $\sim 160$  hours of good quality data remained.

Some parts of this analysis were non-standard. Since the source is extended, the diffuse MC gamma-ray simulations are used, see Sec. 2.4.5 and Sec. 2.4.10. The observations were performed during three different telescope configurations and with different wobble settings, so data are split into separate subsets, accordingly. These subsets are later stacked for final results. The wobble pointings intended for other sources (for W44, W44-SRC1 and HESSJ1857) are used for this analysis, thus the coordinates of HESS J1858+020 are shifted from the camera

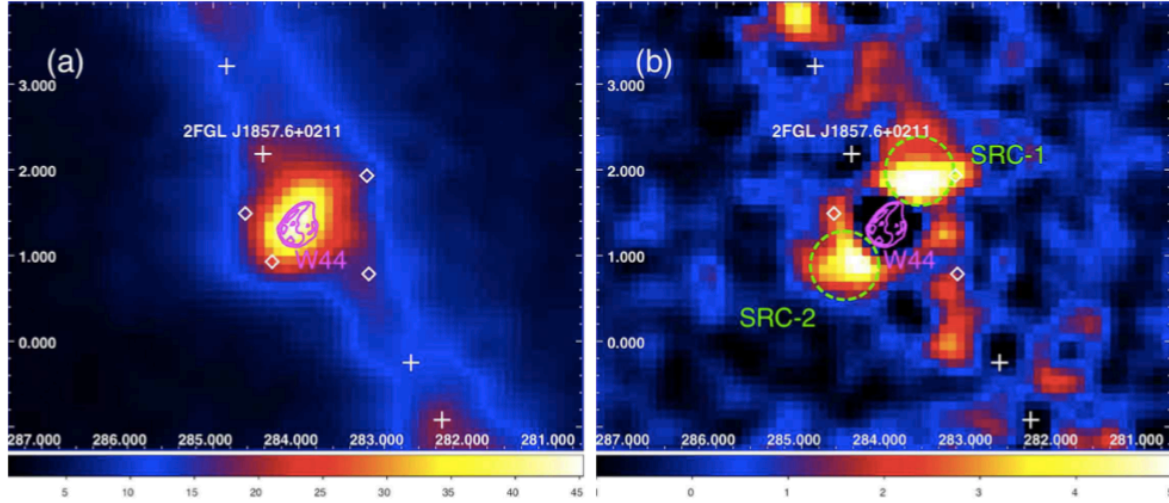


Figure 5.5: Left: *Fermi*-LAT  $\gamma$ -ray count map for 2-100 GeV in units of counts per pixel in celestial coordinates (J2000) showing SNR W44 and its surrounding area. Right: The difference between the count map (left) and the best-fit model which includes diffuse emission, other sources, and SNR W44 represented by the radio map). SRC-1 and SRC-2 are areas of  $\gamma$ -ray excess emission, located in the vicinity of W44 (green contours represent a 10 GHz radio map of SNR W44). Figure is taken from [Uchiyama et al. \(2012\)](#).

centre by a different distance than the standard  $0.4^\circ$  for each wobble position. In this case, to evaluate the background correctly, a non-standard method, called *Off from wobble partner* (OfWP) is used and is explained in Sec. 2.4.10. To account for possible differences in the effective observation time of each wobble position, the background is scaled by the observation time ratio of the wobble position used to extract the ON and the one used to extract the OFF data. Table 5.2 gives an overview of calculated distances (in degrees) between the camera centre and HESS J1858+020 for W44-SRC1 data for each wobble position. Table 5.3 gives the same overview but for HESS J1857+026 data taken in 2010 with different wobble pointings. Since the analysis uses many wobble positions, care was taken not to use OFF if it falls into the signal region (either of HESS J1858 or HESS J1857). For example, in the right panel of Figure 5.4, the light blue empty triangle (or also the grey filled circle) is used around the SNR W44 source as ON data and all the other wobbles as OFF, except the grey empty star and the empty magenta cross, for which the corresponding OFF would fall too close to the other source, HESS J1857. The MAGIC sensitivity decreases with a higher angular offset from the pointing direction (details in Section 2.5), which is the case for this data set. Thus, more data will be required for the source detection, in comparison to H.E.S.S. observations that were specifically aimed for HESS J1858+020.

W44-SRC1 DATA	RA (h)	DEC (deg)	Distance [°]
W0.40+080	18.91	2.35	0.86
W0.40+260	18.90	1.57	0.9
W0.40+170	18.88	2.03	1.27
W0.40+350	18.93	1.89	0.5
W0.40+000	18.93	1.96	0.53
W0.40+180	18.89	1.96	1.28
W0.40+090	18.91	2.36	0.92
W0.40+270	18.91	1.56	1.02

Table 5.2: Distance (in degrees) between the MAGIC camera centre and the HESS J1858+020 source at 8 different wobble positions intended for W44 observations.

HESS J1857+026 DATA	RA (h)	DEC (deg)	Distance [°]
W0.40+015	18.98	2.82	0.77
W0.40+195	18.93	2.61	0.7
W0.40+165	18.93	2.82	0.86
W0.40+345	18.98	2.61	0.58
W0.50+030	18.98	2.97	0.9
W0.50+150	18.93	2.97	1.02
W0.50+210	18.93	2.47	0.64
W0.50+330	18.98	2.47	0.47

Table 5.3: Distance (in degrees) between the MAGIC camera centre and the HESS J1858+020 source at 8 different wobble positions intended for HESS J1857+026 observations.

The analysis is performed with the assumption of the extended source, as the extension was reported by [Aharonian et al. \(2008\)](#). The  $\theta^2$  cut for the extended source (described in Sec. 2.4.10, subsection *Extended sources*) is determined in such a way that the ON and OFF regions do not overlap and that there is enough distance between these regions to perform the normalization for gamma rays and the background. For this particular analysis, signal cut is taken to be  $\theta^2 = 0.03 \text{ deg}^2$  after taking into account the assumed radius of the source (value taken from the HESS observations, that is  $\sim 0.08 \text{ deg}$ , [Aharonian et al. 2008](#)) and corresponding PSF. The instrumental PSF is computed from the Crab Nebula sample (with MARS executable *Odie*) at similar conditions as the data and the values are given in Table 5.4 according to the observational periods. For the stacked data, the highest value of PSF is taken, that is  $0.05 \text{ deg}$ . Thus, signal cut yields  $\theta^2 \sim (2 \times 0.08)^2 + (2 \times 0.05)^2 \sim 0.03 \text{ deg}^2$ .

Diffuse-gamma Monte Carlo (MC) data, described in Sec. 2.4.5, were used to calculate the spectrum.

Simulated gamma-ray data are matched with the observational conditions: *doughnut* MC is constructed according to the source's assumed extension and to the distance of the source to the centre of the camera (see, for example, Fig. 5.6).

PERIOD	Zenith range (deg)	PSF (deg)
ST0302	26-44	0.05
ST0303	26-46	0.04
ST0305	27-32	0.048
ST0102	25-35	0.05

Table 5.4: Point Spread Function (PSF) of the MAGIC telescope for the corresponding observational periods.

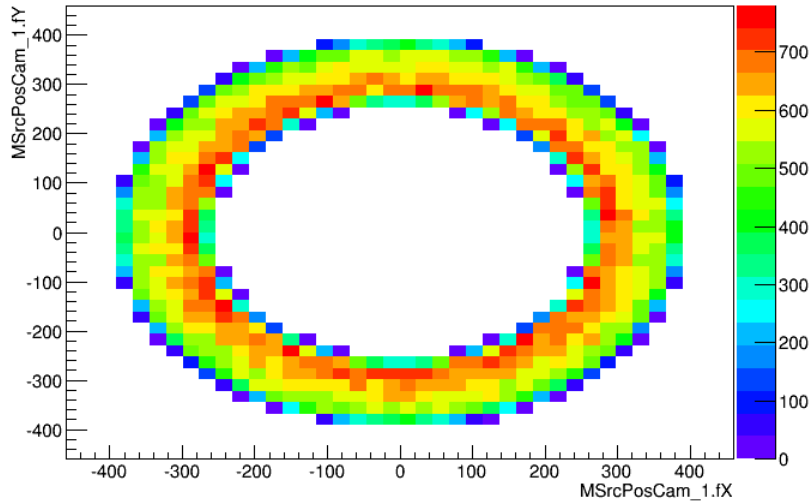


Figure 5.6: *Doughnut* Monte Carlo produced for the HESS J1858+020 source. MC were adjusted for the assumed extension of the source, which is taken from Aharonian et al. (2008) to be 0.08 deg. This particular MC is produced for the period ST0302 and for the wobbles with the same and similar distances from the camera centre (wobble positions 270, 260, 170 and 180).

## 5.4 Results of the analysis on HESS J1858+020

### 5.4.1 Detection of HESS J1858+020

For the detection of HESS J1858+020, I used the full range of  $E_\gamma$ -energies ( $E > 200$  GeV). Test Statistic (TS) value map and gamma-ray flux map are obtained (see Figure 5.7). TS value contours are in steps of  $2\sigma$  starting with  $5\sigma$ , and they are approximately consistent with the Gaussian significance. TS value of the fitted position is  $> 9\sigma$ . The total PSF shown in all skymaps is the sum in quadrature of the instrumental angular resolution and the applied smearing, which is in this case 0.071 deg.

The distribution of the squared angular distance between gamma-ray events and the position of HESS J1858+020 is shown in Figure 5.8. To obtain the signal, signal cut of  $\theta^2 = 0.03 \text{ deg}^2$

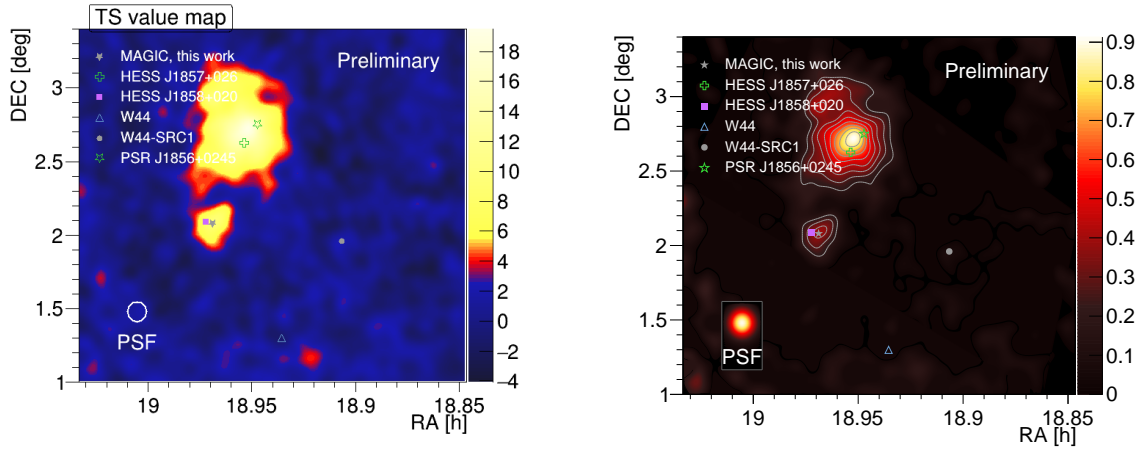


Figure 5.7: Detection of the HESS J1858+020 (this work). Left: Test statistic (TS) value map (full  $E_\gamma$ -range  $E > 200$  GeV). TS value of the fitted position is  $9.67\sigma$ . The source HESS J1858 is marked with the grey star (this work); Right: gamma-ray flux skymap (in arbitrary units) showing morphology of HESS J1858+020. Fitted source extension is  $0.08 \pm 0.03$  deg. Overlaid TS contours start at  $5\sigma$  and are in steps of  $2\sigma$  and roughly correspond to Gaussian significances. In the bottom-left the instrument's PSF (0.05 deg) is shown along with the applied smearing kernel of the same value which gives the total PSF=0.071 deg

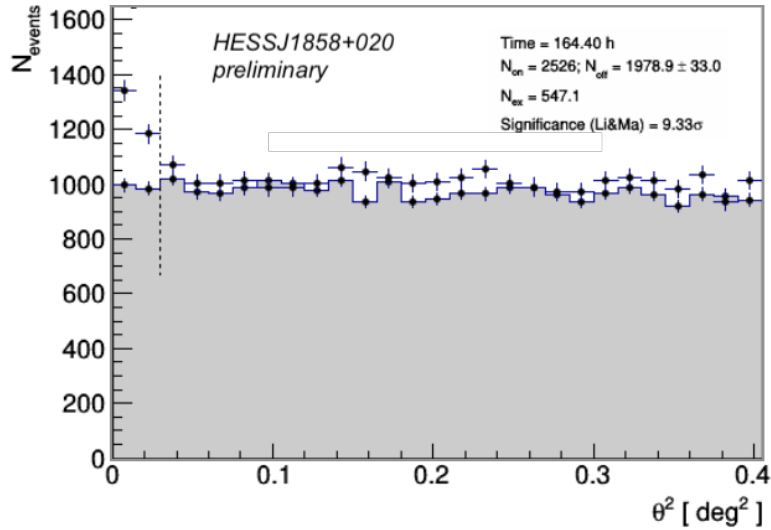


Figure 5.8: Distribution of squared angular distance  $\theta^2$  between gamma-ray events and the position of HESS J1858+020 where the applied  $\theta^2$ -cut is  $0.03 \text{ deg}^2$  (black vertical dashed line). The distribution of  $\theta^2$  for OFF positions is a grey-filled histogram. The normalization range used for the background estimation is  $(0.06 - 0.12) \text{ deg}^2$ . There is a signal enhancement at  $\theta^2 > 0.14 \text{ deg}^2$  due to a neighbouring bright source, HESS J1857+026.

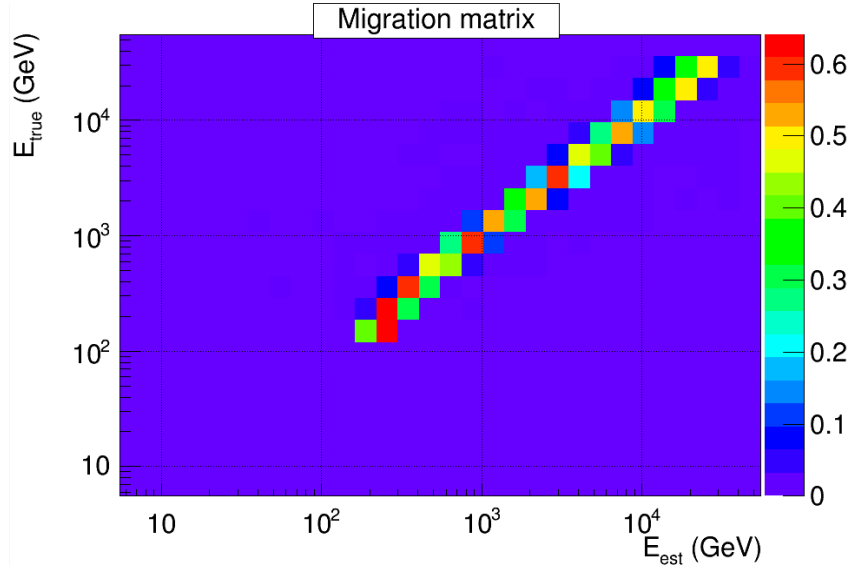


Figure 5.9: The migration matrix shows the relation between the reconstructed and the true energy. For the points above 10 TeV, MC statistics is too low: the real data in the  $E_{est}=20$  TeV bin would contain events with real energy above 30 TeV, which is not simulated. The estimated flux would contain a systematic error.

is used, as explained in the previous section. For the background estimation, a  $\theta^2$  range of  $0.06 - 0.12 \text{ deg}^2$  is used. The signal fades out above  $0.04 \text{ deg}^2$  but appears again above  $\theta^2 > 0.14 \text{ deg}^2$  due to the bright nearby source HESS J1857+026.

For the given energy range,  $E > 200$  GeV, the instrumental PSF is  $0.05^\circ$  and is folded (smeared) with the Gaussian kernel of the same value ( $0.05^\circ$ ) to achieve a PSF with a Gaussian shape. Thus, the total PSF is  $0.071^\circ$ , where the number corresponds to a  $1\sigma$  value of the symmetric 2D Gaussian function. The centroid of the emission is estimated by fitting a Gaussian function to the relative flux map and from this analysis, the coordinates of the detected source are RA :  $18^{\text{h}}58^{\text{m}}8^{\text{s}}$  and Dec :  $02^\circ04'48''$  which is in good agreement with the HESS result (Aharonian et al., 2008). An intrinsic source extension is also measured from the fit, after removing the combined effect of the instrument PSF and smearing, and yields  $0.08 \pm 0.03 \text{ deg}$ , which is also in good agreement with Aharonian et al. (2008).

### 5.4.2 The spectrum of HESS J1858+020

The first statistically significant point in SED was obtained for the energy bin starting around 300 GeV. The OfWP method is obviously not optimal for lower energies because the source is far away from the camera centre, where the sensitivity drops. On the other hand, for the point(s) above 10 TeV, Monte Carlo statistics is too low, i.e., MC data were truncated at the energy of 30

TeV. In the Figure 5.9 migration matrix is shown and one can see that real data in the  $E_{est}=20$  TeV bin will contain events with real energy above 30 TeV, which will be absent in the MC, and therefore the estimated flux would have a systematic error in it.

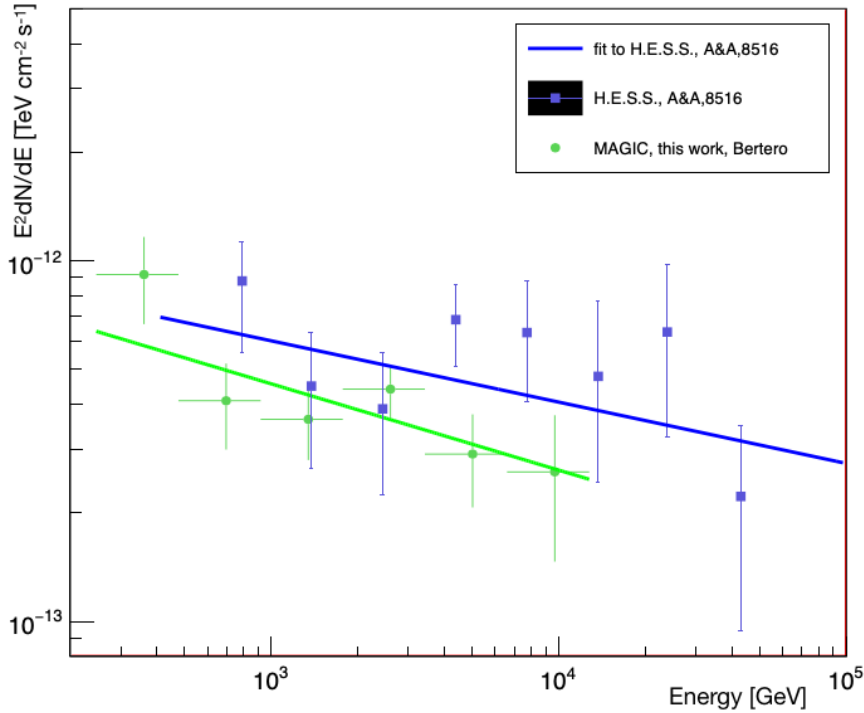


Figure 5.10: Spectral energy distribution of HESS J1858+020 obtained from MAGIC data (this work, green dots with power-law fit marked with green solid line). MAGIC measured the spectrum between 300 GeV and 10 TeV. SED from HESS (Aharonian et al., 2008) of the same source with a power-law fit (blue solid line) is included for comparison.

The spectrum is derived requiring larger air showers, i.e., putting Hillas parameter size cut to 400. Hadronness cuts were obtained from efficiency and minimum  $\theta^2$  cut used is 0.03. To obtain the SED for the source, program *Flute* (described in Section 2.4.7) was run for each wobble separately in OfWP mode, taking care that neither OFF falls into the signal region of both sources. All results were combined for unfolding to account for the finite energy resolution and bias. The differential energy spectrum between 300 GeV and 10 TeV is computed and shown in Figure 5.10 and is well described by a power-law function  $dN/dE = N_0[(E/1 \text{ TeV})]^{-\Gamma}$  with  $N_0 = (4.7 \pm 0.6) \times 10^{-13} \text{ TeV}^{-1} \text{ cm}^{-2} \text{ s}^{-1}$  with a photon index of  $\Gamma = 2.29 \pm 0.13$ .



## 5.5 Discussion and conclusions

The analysed source, HESS J1858+020, was present in the FoV of the previous MAGIC observations dedicated to W44 and HESS J1857+026, respectively. These observations were performed using the false-source tracking mode, i.e., *wobble mode*. In the Figure 5.4, all wobble pointings used in the MAGIC observations are shown. Since observations were not aimed at HESS J1858+020 coordinates, the distance between the camera centre and J1858+020 is larger than the standard offset for all wobble pointings. Tables 5.2 and 5.3 summarize these distances. To account for the new distances, the *Off from Wobble partner* method was used (Krause, 2013). After quality selection, 160 hours of data remained.

The very high energy gamma-ray emission is detected from HESS J1858+020 with a significance of  $> 9\sigma$  above 250 GeV. Its differential energy spectrum between 300 GeV and 10 TeV is shown in Figure 5.10 with a power-law fit. The SED computed from HESS observations is also included, for comparison.

When comparing spectral results obtained from this analysis and the one from HESS (Aharonian et al., 2008), spectral points at some energies do not overlap, which is expected to some degree. To begin with, 25 hour observations of HESS J1858+020 with the HESS telescopes are compared to 160 hours of data collected with the MAGIC telescopes where this source was in the field of view of other observations. Much more data in the latter analysis resulted in a slightly smaller error bars. The first point of the SED from the MAGIC analysis is computed for 300 GeV and analysis extends up to 10 TeV, as opposed to SED from HESS starting at 500 GeV and extending to 50 TeV. Energy density spectra for HESS J1858+020 shown in Fig 5.10 have comparable spectral parameters:  $N_{0,\text{MAGIC}} = (4.7 \pm 0.6) \times 10^{-13} \text{ TeV}^{-1} \text{ cm}^{-2} \text{ s}^{-1}$  and  $\Gamma_{\text{MAGIC}} = 2.29 \pm 0.13$  compared to  $N_{0,\text{HESS}} = (6 \pm 1) \times 10^{-13} \text{ TeV}^{-1} \text{ cm}^{-2} \text{ s}^{-1}$  and  $\Gamma_{\text{HESS}} = 2.17 \pm 0.12$ . In general, the absolute energy scale of each IACT (HESS, MAGIC, or VERITAS) is difficult to determine because many systematic effects are involved that affect it (like variable atmospheric transmission, mirror reflectivity, PMTs' functionalities, for details see Aleksić et al. 2016b). Since the two SEDs are from different IACTs, the differences are most likely due to uncertainty in the absolute energy scale determination. Discrepancies could also emerge (although less likely) from different zenith angle distributions (no information about this for the HESS analysis) or from the fact that in my analysis I have used several observational periods, each having their MC simulations, that were combined in the final result and that directly may impact the SED (see Sec. 2.5). Nevertheless, when comparing fluxes for both analysis, they are within  $1 - 2\sigma$  for all points and HESS spectral index is  $1\sigma$  within the MAGIC one, concluding that the two SEDs are compatible.

The analysis presented here shows limitations when applied to the extended and off-centred sources, like HESS J1858+020. For this reason, it was unfeasible to study the morphological features of this slightly extended source, as well as to reach energies below 300 GeV. A new analysis method, called the *Likelihood method*, was recently developed in MAGIC (Vovk et al., 2018) and is intended specifically for extended, morphologically complex and off-centred sources. To obtain more information on the morphology of HESS J1858+020 and its SED below 300 GeV, this new method could be applied in the future.

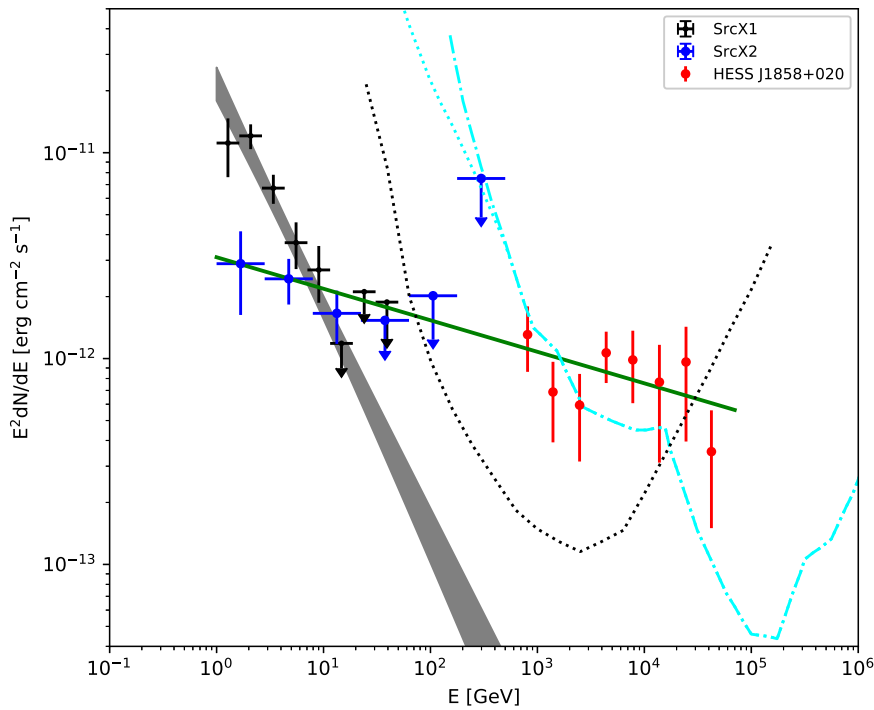


Figure 5.11: The SED of HESS J1858+020. Blue, black and red dots show the hard (SrcX2) and soft *Fermi*-LAT (SrcX1) and HESS GeV observations, respectively. The solid green line is the joint fit for the *Fermi*-LAT data of SrcX2 and HESS data of HESSJ1858+020. Figure is taken from Cui et al. (2021).

Results for the HESS J1858+020 source obtained from the archival MAGIC data confirmed the already published HESS results. However, due to the limitations caused by the large distance between the camera centre and the targeted source, no further details could be deduced from the performed analysis in spite of the large data set (160 hours).

In their recent work, Cui et al. (2021) found a hard GeV source in the close vicinity of HESS J1858+020 and a nearby molecular complex. The spectrum of this complex connects smoothly with the one found by HESS (Aharonian et al., 2008, and see Fig. 5.11), and then also with

the MAGIC spectrum. This indicates that the scenario, in which CRs from the nearby SNR G35.6-0.4 escape and interact with the molecular complex, is the most plausible to explain the observed excess of gamma rays. The GeV-TeV emission of this source can be explained with certain assumptions in their hadronic model, namely taking a middle-aged SNR (the middle-age scenario is favoured because it is more likely that the middle-age SNR releases low-energy CRs) and a much smaller diffusion coefficient than the Galactic one to be able to confine the CRs to SNR-cloud complex (for details, see [Cui et al. 2021](#)). In the light of these results, HESS J1858+020 is most likely not a PWN. More sensitive X-ray observations are necessary to check for the missing diffuse X-ray emission. Additionally, future observations with CTA or LHAASO (see Sec. 1.4) could be able to resolve morphological features of these interesting sources in the TeV energy range in more detail.

# Chapter 6

## Searching for the very faint radio emission

### 6.1 Introduction

Detection of the diffuse low-frequency radio emission from our Galaxy by K. Jansky, explained as synchrotron emission years later, has revealed the presence of the interstellar magnetic fields (IMFs). Relativistic cosmic-ray electrons, originating from astrophysical sources like supernova remnants (SNRs), produce synchrotron polarized emission when accelerated by IMFs. Since IMFs cannot be directly measured, but are permeated in the multiphase interstellar medium (ISM), by studying properties of the ISM we can indirectly learn about the magnetic fields. Diffuse polarized emission travelling through ISM experiences Faraday rotation, which causes the frequency-dependent rotation of its polarization angle. The effect is stronger at longer wavelengths due to  $\lambda^2$  dependency, which makes low-frequency observations around 150 MHz the most suitable. The emission observed along a line of sight (LOS) is a superposition of the emission at all distances with different Faraday depths. The rotation measure (RM) synthesis ([Brentjens & de Bruyn, 2005](#)) is a method that enables discernment of the polarized emission by the degree of Faraday rotation it has experienced. In this way, Faraday depth cubes are created, outlining the diffuse polarized emission as a function of sky coordinates and Faraday depth.

ISM can also be studied through pulsars, which are the most polarized known objects in the universe, henceforth their emission is also subjected to the Faraday rotation. From this effect, one can deduce pulsar's RM, a quantity proportional to free-electron density and component of the magnetic field along the LOS. Detection of pulsars at radio frequencies offers a deeper insight to the galactic pulsar population of neutron stars, but also provides with the LOS information valuable for probing the Galactic interstellar medium (ISM) in three dimensions ([Sobey et al., 2019](#)).

Diffuse polarized synchrotron emission from our Galaxy, mapped through the Faraday to-

mography, is the dominant component that makes 70% of overall astrophysical foregrounds and is barely studied at the frequency range of 115 – 180 MHz. This frequency range is accessible to the latest generation of low-frequency radio telescopes such as the LOw Frequency ARray (LOFAR, [van Haarlem et al. 2013](#)) and the Murchison Widefield Array (MWA, [Tingay et al. 2013](#)). So far, Galactic polarized emission studies were done mostly at higher radio frequencies (> 1GHz, [Reich 2006](#)) or at 325 MHz with the Westerbork Synthesis Radio Telescope (WSRT) where they reported some unusual polarized structures with no counterpart in total intensity ([Schnitzeler et al., 2009](#)). Polarized diffuse galactic emission is interesting due to various polarized structures that seem to be from Faraday rotation effects in the ISM. Only a few studies were done in the frequency range 115-180 MHz ([Iacobelli et al. 2013](#); [Van Eck et al. 2017](#); [Jelić et al. 2015](#)). LOFAR is the best suitable instrument for this kind of studies due to its wide frequency coverage and good angular resolution. It is a radio interferometer utilizing a new-generation phased-array design to explore the low-frequency radio sky (10 – 240 MHz) in the Northern Hemisphere, built by Netherlands Institute for Radio Astronomy, ASTRON. It achieves the resolution of  $\approx 1 \text{ rad m}^{-2}$  in Faraday depth with an antenna network extending mainly through the Netherlands, but also across eight other European countries, see Fig. 6.1. The novel feature of this instrument is its non-mechanical pointing system, enabling efficient observations at the same time in multiple directions. The pointing system works in a way that the radiation is detected from the whole observable sky at the same time, and the pointing is performed electronically towards a targeted source. The project is carried out through a number of key science projects, including a series of ongoing LOFAR surveys. The LOFAR Two-meter Sky Survey (LoTSS, [Shimwell et al., 2017, 2019, 2022](#)) and LOFAR Low Band Antenna Sky Survey (LoLSS, [de Gasperin et al., 2021](#)) are the wide-area surveys at 120 – 168 MHz and 42 – 66 MHz, respectively. The LoTSS survey aims to cover the whole northern sky with its first data release (DR1) covering  $424 \text{ deg}^2$  with up to  $6''$  resolution and  $71 \mu\text{Jy}/\text{beam}$  median sensitivity ([Shimwell et al., 2019](#)), and the second release (DR2) containing full polarization data ([Shimwell et al., in prep](#)). The two mentioned surveys are complemented by a few deeper fields, known as the LoTSS-Deep Fields ([Tasse et al., 2021](#); [Sabater et al., 2021](#)) and the LoLSS-Deep Fields ([de Gasperin et al., 2021](#)). The deep fields are selected in regions covered by a wealth of multiwavelength data and the first data release includes the Boötes, Lockman Hole, and European Large Area Infrared Space Observatory Survey-North 1 (ELAIS-N1) fields. These data sets make it possible to probe a new, fainter population of radio sources, dominated by star-forming galaxies and radio-quiet active galactic nuclei ([Smolčić et al., 2017](#); [Novak et al., 2018](#); [Kondapally et al., 2021](#)) but can also be used for probing a faint population of pulsars, specifically. Pulsars are detected mostly as galactic sources that emit throughout the electro-



Figure 6.1: The LOFAR stations across Europe (left) and LOFAR's central station, the so-called "superterp" (right). Images taken from <https://science.astron.nl/>.

magnetic spectrum and are described in Sec. 1.5 where it was pointed out that majority of pulsar population is discovered only at radio wavelengths. However, pulsars are generally weak radio sources with pulsed flux densities ranging from 0.0001 to 5 Jy with a median of 0.01 Jy at a frequency of 400 MHz with a steep spectrum index ( $S_\nu \propto \nu^\alpha$ ;  $-4 < \alpha < 0$ ;  $\alpha_{mean} = -1.8$ , [Stappers et al. 2011](#) and references within). Although most pulsars are intrinsically brightest at frequencies below 300 MHz, the majority of detected and studied pulsars are from frequency ranges of 300 - 2000 MHz due to unfavourable effects of the ISM on the pulsed signal<sup>1</sup>, the effect of the galactic synchrotron emission<sup>2</sup> and due to ionospheric effects (see section below) which all become worse towards lower frequencies. The LOFAR telescope successfully overcomes these observational challenges (detail description in [Stappers et al., 2011](#)). Most radio pulsars have been discovered in blind surveys, where large sky areas are monitored in high-time and -frequency resolution. The LOFAR Tied-Array All-Sky Survey (LOTAAS) is a blind pulsar search conducted at low-frequencies (135 MHz) that has discovered 74 pulsars to date ([Sanidas et al., 2019](#)). Alternatively, the pulsar population can also be probed using targeted surveys with predefined criteria, in contrast to all-sky periodicity searches. Since pulsars universally show high degree of linear or circular polarization, steep spectrum ( $\alpha < 2$ ) and/or high variability, these criteria can be used to efficiently extract pulsar candidates from interferometric images like in this specific survey “Targeted search, using LoTSS images for polarized pulsars” (TULIPP, [Sobey et al., 2022](#)).

The feasibility of the stacking technique was first demonstrated by [Herrera Ruiz et al.](#)

<sup>1</sup>Free electrons in the ISM between the observer and the pulsar affect the pulsed signal to be dispersed and scattered.

<sup>2</sup>The diffuse synchrotron emission has a strong frequency dependence,  $\nu^{-2.6}$ , and is a significant component at low frequencies.

(2021), where an analysis was done on polarized radio sources in the LoTSS Deep Fields. They used six eight-hour observations of the ELAIS-N1 field at low-resolution (20'') (Sabater et al., 2021), and detect three polarized sources in the single observation, with the number increasing by more than a factor of three for the stacked data, yielding a surface density of polarized sources of one per 1.6 deg<sup>2</sup>. In a follow-up study, Piras et al. (in prep.) expand on this approach by stacking 19 eight-hour LoTSS-Deep Field observations re-imaged at higher angular resolution (6''). This results in further decrease in the detection threshold, an increase in a number of detected polarized sources, and better characterization of their counts at low radio frequencies. When stacking, polarization data need to be first properly calibrated and corrected for the Faraday rotation in the Earth's ionosphere (Murray & Hargreaves, 1954; Hatanaka, 1956).

### The effect of the ionosphere on the low frequency data

In the frequency range at which LOFAR interferometer operates, ionosphere has a certain effect on the observations which has to be corrected for. The ionosphere is the ionized layer of gas between  $\sim 50$  and 1000 km altitude over Earth's surface. It is an inhomogeneous atmospheric layer with variable electron density that depends on the period of the day/night but also on sunspot activity, time of year or geomagnetic latitude. Photo-ionization processes (at UV and short X-rays) and injection of charged particles from the solar wind ionize this part of the atmosphere. Daytime ionization is balanced by the recombination at night. Ionospheric Faraday rotation is a time- and direction-dependent propagation effect proportional to the integral along the LOS of the product of the total electron content (TEC) of plasma in the ionosphere and a projection of the geomagnetic field,  $B_{\text{geo}}$ , to the LOS towards the observed field of view (FoV). It is characterized by the ionospheric rotation measure ( $RM_{\text{ion}}$ ), which, in the thin-shell model, can be approximated as (e.g. Sotomayor-Beltran et al., 2013)

$$\frac{RM_{\text{ion}}}{[\text{rad m}^{-2}]} = 0.26 \times \frac{\text{TEC}_{\text{LOS}}}{[\text{TECU}]} \frac{B_{\text{geo,LOS}}}{[\text{G}]}, \quad (6.1)$$

where  $\text{TEC}_{\text{LOS}}$  is the total electron content, measured in TEC units (1 TECU =  $10^{16}$  electrons  $\text{m}^{-2}$ ), at the ionospheric piercing point of the LOS. A typical  $RM_{\text{ion}}$  is 0.5 – 2  $\text{rad m}^{-2}$  (Sotomayor-Beltran et al., 2013; Jelić et al., 2014, 2015) at moderate geographical latitudes during nighttime. Daytime values are higher due to solar irradiation and an increase in TEC. The TEC decreases after the sunset due to recombination of plasma in the ionosphere.

Given that ionospheric Faraday rotation changes the polarization angle  $\theta$  of the observed emission on timescales smaller than the total integration time of observation, the observed polarized emission may be incoherently added during the synthesis, resulting in partial, or, in excep-

tional cases, full depolarization. Ionospheric depolarization effects are mostly relevant at lower radio frequencies, as Faraday rotation is inversely proportional to a square of the frequency ( $\Delta\theta \sim RM_{\text{ion}}\nu^{-2}$ ). At 150 MHz, a change in the ionospheric Faraday rotation of  $\sim 0.8 \text{ rad m}^{-2}$  results in a  $180^\circ$  rotation of the polarization vector and therefore full depolarization.

The LOFAR observations are usually corrected for the ionospheric Faraday rotation in a direction-independent manner by combining global geomagnetic field models with Global Navigation Satellite System (GNSS) observations of the ionospheric TEC (Sotomayor-Beltran et al., 2013; Mevius, 2018). This was first tested on the LOFAR commissioning observations of the ELAIS-N1 field (Jelić et al., 2014), and since then, it is widely used in polarization studies with LOFAR (e.g. Jelić et al., 2015; Van Eck et al., 2017; Turić et al., 2021; Erceg et al., 2022). Depending on the source of the TEC data, the estimated uncertainty in the calculated ionospheric Faraday rotation is within a factor of a few of  $0.1 \text{ rad m}^{-2}$  at time intervals of 15 minutes to two hours.

Recently, de Gasperin et al. (2018) showed that LOFAR Low Band Antenna (LBA) station-based gain phase can be decomposed into a few systematic effects related to clock delays and ionospheric effects and used directly to obtain independent measurements of the absolute TEC. The LOFAR measured TEC values are within 10% of the satellite-based measurements and have two orders of magnitude better time resolution. This has enabled a new, efficient, unified calibration strategy for LOFAR LBA (de Gasperin et al., 2019). However, further detailed analysis of systematic uncertainties related to ionospheric Faraday rotation corrections is needed, as well as, an assessment of the method for LOFAR High Band Antenna (HBA) observations and direction-dependent effects.

The six ELAIS-N1 observations analysed by Herrera Ruiz et al. (2021) were corrected for the ionospheric Faraday rotation by the satellite-based TEC measurements (Sabater et al., 2021). To check how well they were corrected relatively to each other, Herrera Ruiz et al. (2021) compared the observed Faraday depth of the bright reference source in each observation and found a relative difference varying from  $-0.12$  to  $+0.05 \text{ rad m}^{-2}$ . Then they calculated the difference in the observed polarization angle, corrected each observation accordingly and stacked the data.

A complementary method to check for a relative alignment between the observations concerning the Faraday rotation in the ionosphere is based on using the polarized diffuse Galactic synchrotron emission (Lenc et al., 2016; Brentjens, 2018). This type of emission is ubiquitous at low radio frequencies (e.g. Erceg et al., 2022, and references therein) and allows analysis over a larger portion of the field of view compared to using a single reference polarized source. Ionospheric Faraday rotation corrections obtained in such a way should improve the accuracy of corrections and allow the analysis of differential variations across the field.



In this work, I use the polarized diffuse synchrotron emission to study the ionospheric Faraday rotation corrections in 21 LOFAR observations of the ELAIS-N1 field. Also, very low-resolution images (4.3') are stacked to study the faint component of the diffuse polarized emission in the ELAIS-N1 field, whose bright component was observed in the commissioning phase of the LOFAR (Jelić et al., 2014). This Chapter is organized as follows. LOFAR observations and related data products are described in Sec. 6.2. Section 6.3 presents the analysis of the ionospheric Faraday rotation corrections. Section 6.4 describes the methodology for stacking the very low-resolution data. The final stacked Faraday cube is presented and analysed in Sec. 6.5. The newly detected faint polarized emission is discussed in Sec. 6.6. Summary and conclusions are presented in Sec. 6.7. Results from this Chapter are accepted in A&A: Šnidarić, I., Jelić, V., Mevius, M., et al., *LOFAR Deep Fields: Probing faint Galactic polarized emission in ELAIS-N1*<sup>3</sup>.

## 6.2 Data and processing

In this section, I describe the LoTSS-Deep Fields observations and the derived data products used in this Chapter. I also give an overview of the used Rotation Measure (RM) synthesis technique and its parameters used to create Faraday cubes.

### 6.2.1 LoTSS-Deep Fields observations and very low-resolution images

The ELAIS-N1 data analysed in this Chapter are part of the LoTSS-Deep Fields Data Release 1 (Sabater et al., 2021). 21 out of 27 observations are used, which were of good quality (ten observations from Cycle 2 and 11 observations from Cycle 4, IDs 009–018, 020–024, 026–028, 030–032 in table 1 in Sabater et al., 2021), see Table 6.1. The data were taken with the LOFAR HBA from May 2014 to August 2015 (under project codes LC2\_024 and LC4\_008), covering the frequency range from 114.9 to 177.4 MHz divided into 320 frequency sub-bands. The observing time of each observation was between five and eight hours, taken during nighttime and symmetric around transit. The array was used in the HBA DUAL INNER configuration (van Haarlem et al., 2013). The HBA antennas of each core station are clustered in two groups of 24 tiles of 16 dual-polarized antennas. Each cluster of 24 tiles was then treated as an independent HBA core station. The remote stations have one group of 48 HBA tiles of 16 dual-polarized antennas. They were reduced to inner 24 tiles, to have the same shape and number of tiles as the dual core HBA stations. This provided a uniform general shape of the primary beam over

<sup>3</sup><https://doi.org/10.1051/0004-6361/202245124>

ID	LOFAR ID	Cycle	Date	Obs. time
009	L229064	2	2014-05-19 19:49:19	28 805.8
010	L229312	2	2014-05-20 19:46:23	28 805.8
011	L229387	2	2014-05-22 19:30:00	28 805.8
012	L229673	2	2014-05-26 19:30:00	28 805.8
013	L230461	2	2014-06-02 19:30:00	28 805.8
014	L230779	2	2014-06-03 19:30:00	28 805.8
015	L231211	2	2014-06-05 19:30:00	28 805.8
016	L231505	2	2014-06-10 19:50:00	26 406.0
017	L231647	2	2014-06-12 19:50:00	25 198.0
018	L232981	2	2014-06-27 20:05:58	17 998.6
020	L345624	4	2015-06-07 20:11:00	27 606.3
021	L346136	4	2015-06-14 18:31:32	27 606.3
022	L346154	4	2015-06-12 20:11:00	27 606.3
023	L346454	4	2015-06-17 20:11:15	27 606.3
024	L347030	4	2015-06-19 17:58:00	27 606.3
026	L347494	4	2015-06-26 20:11:00	27 606.3
027	L347512	4	2015-06-29 20:11:00	27 606.3
028	L348512	4	2015-07-01 20:11:00	24 001.3
030	L366792	4	2015-08-07 18:11:00	27 606.3
031	L369530	4	2015-08-22 16:11:00	27 606.3
032	L369548	4	2015-08-21 16:11:00	27 606.3

Table 6.1: ELAIS-N1 observations. The table is marked with the following columns (i) ID - Internal ID code of the data set; (ii) LOFAR observation ID - standard LOFAR ID; (iii) Cycle - observing LOFAR cycle; (iv) Date - Date and time of the beginning of the observations; (v) Obs. time - Duration of the observations in seconds. The Figure is taken from (Sabater et al., 2021).

the entirety of the LOFAR stations in the Netherlands. The phase centre of the main target field was at RA  $16^{\text{h}}11^{\text{m}}00^{\text{s}}$  and Dec  $+55^{\circ}00'00''$  (J2000).

Cycle 2 data were taken and pre-processed jointly with the LOFAR Epoch of Reionization Key Science Project team in a slightly different way than Cycle 4 data. This created a difference in frequency configurations of the final data products of the two cycles. Here, a brief overview of the main processing steps and relevant differences for each cycle are given, while details are provided in Sabater et al. (2021).

The pre-processing of the data included averaging in time and frequency. Before averaging, the Cycle 2 data were automatically flagged for radio-frequency interference (RFI) using AOFlogger (Offringa et al., 2012). The first two and the last two frequency channels were then removed from each 64-channel sub-band to minimize the band-pass effects. The remaining 60 channels were averaged to 15 channels per sub-band. The Cycle 4 data were originally averaged by the observatory to 16 channels per sub-band, without discarding the channels at edges of each sub-band. After that, they were flagged for the RFI. The data from both cycles were averaged in time to 2 s. The direction-independent calibration was done using the PREFACTOR pipeline

(van Weeren et al., 2016; de Gasperin et al., 2019), which corrects for the polarization phase offset introduced by the station calibration table, the instrumental time delay associated with clocks in the remote stations, the amplitude bandpass, and ionospheric direction-independent delays and Faraday rotation.

The ionospheric Faraday rotation corrections were done by `RMextract` (Mevius, 2018), which combines the satellite-based TEC measurements and the global geomagnetic field models to predict the corrections. The ionosphere was modelled as a single phase screen above the array, taking into account its spatial structure. The  $RM_{\text{ion}}$  corrections were calculated for each LOFAR station separately, however the model does not allow for direction-dependent corrections within the field of view. Moreover, the model uses a thin screen approximation. The contribution from the plasmasphere to the total integrated electron content along the LOS can be significant (up to 40% at moderate geographical latitudes, Yizengaw et al., 2008). Since the GNSS data include the full integrated electron density, including the plasmaspheric contribution, and the magnetic field contribution from the higher layers is significantly smaller, the derived RM values using a thin screen model are likely an overestimate of the ionospheric Faraday rotation. Figure 6.2 shows calculated values for the LOFAR station CS002, as an example. The curves are given for different nights as a function of the observing time at 30-minute intervals. The absolute  $RM_{\text{ion}}$  values are between 0.5 and 3  $\text{rad m}^{-2}$ , while their relative variations during observations are on average  $0.9 \pm 0.3 \text{ rad m}^{-2}$ .

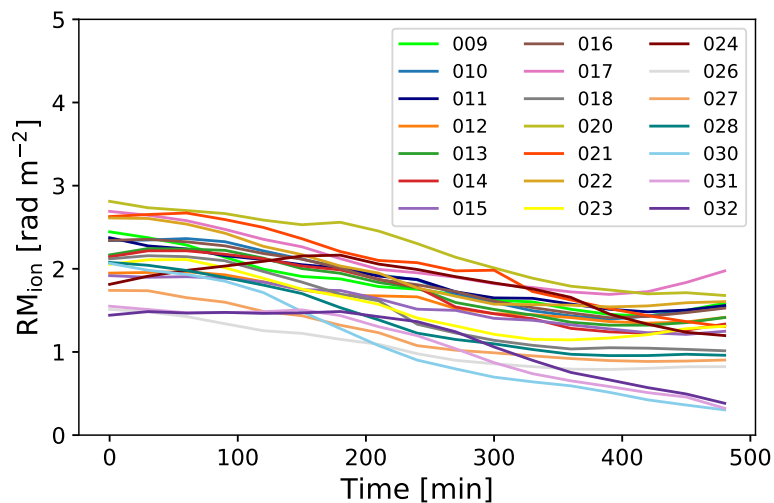


Figure 6.2: Calculated  $RM_{\text{ion}}$  corrections given at 30-minute intervals for different observations using the satellite-based TEC measurements and the global geomagnetic field model. The observed decrease of  $RM_{\text{ion}}$  during each nighttime observation is due to recombination of plasma in the ionosphere, which happens after the sunset and decreases the TEC throughout night.

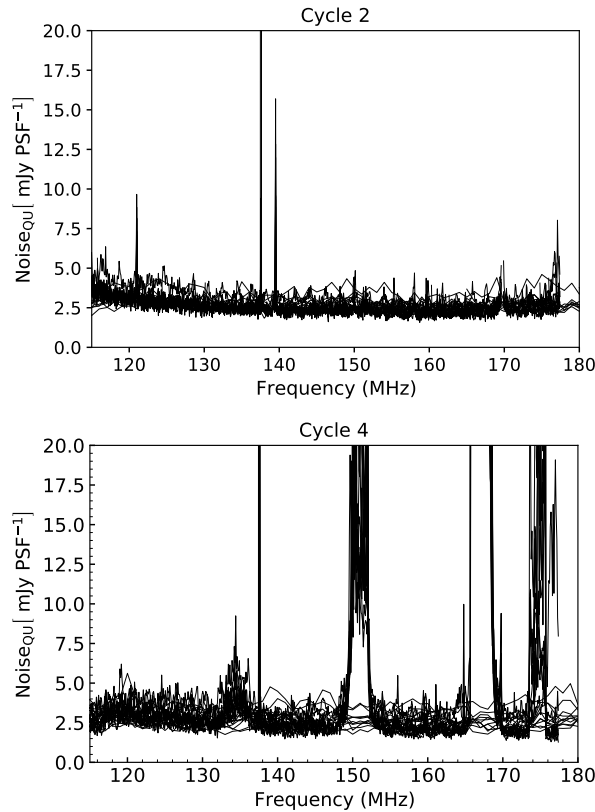


Figure 6.3: Noise in Stokes QU data cubes for observations from Cycle 2 (top plot) and Cycle 4 (bottom plot) as a function of frequency. Cycle 4 data are much more affected by broad RFI than Cycle 2 data, due to DABs and DVBS.

The final step of processing included the direction-dependent calibration done by the DDF pipeline (Tasse et al., 2021) and imaging of the data in full Stokes parameters (I, Q, U, and V). In this work, I used very low (vlow) resolution (4.3') Stokes QU data cubes (Sabater et al., 2021). They are split in 800 or 640 frequency channels of 73.24 kHz or 97.66 kHz width in the case of Cycle 2 or 4 data, respectively, due to their different frequency configurations.

Figure 6.3 shows the noise in Stokes QU data cubes as a function of frequency. The noise at each frequency was calculated as a standard deviation in the corner of the primary-beam-uncorrected image (farthest out of the primary beam), where no polarized emission is present. The noise in Stokes Q and U is comparable. Cycle 4 data are much more affected by broad RFI (Offringa et al., 2013) at frequencies around 134, 151, 167, and 174 MHz than Cycle 2 data. These RFIs are due to man-made wireless applications such as digital audio/video broadcasts (DABs/DVBs). Over the observed frequency range, a typical noise at frequencies not affected by the RFI is  $\sim 3.3$  mJy PSF $^{-1}$  in Cycle 2 data and  $\sim 2.7$  mJy PSF $^{-1}$  in Cycle 4 data. A small difference between the two cycles arises from their different frequency configurations and hence

frequency channel widths.

### 6.2.2 RM synthesis and Faraday depth cubes

The Faraday data cubes of the ELAIS-N1 deep field observations were created for the analysis. They were produced by applying the RM synthesis technique (Burn, 1966; Brentjens & de Bruyn, 2005) to Stokes QU frequency data cubes. This technique decomposes the observed polarized emission by the amount of Faraday rotation of its polarization angle,  $\theta$ , experienced at wavelength  $\lambda$ :

$$\frac{\Delta\theta}{[\text{rad}]} = \frac{\Phi}{[\text{rad m}^{-2}]} \frac{\lambda^2}{[\text{m}^2]}. \quad (6.2)$$

The quantity  $\Phi$  is called Faraday depth, and it is defined as

$$\frac{\Phi}{[\text{rad m}^{-2}]} = 0.81 \int_0^d \frac{n_e}{[\text{cm}^{-3}]} \frac{B_{\parallel}}{[\mu\text{G}]} \frac{dl}{[\text{pc}]}, \quad (6.3)$$

where  $n_e$  is the density of thermal electrons and  $B_{\parallel}$  is the magnetic field component parallel to the LOS. The integral is taken over the path length  $dl$  from the source ( $l = 0$ ) to the observer ( $l = d$ ). If the magnetic field component is pointing towards the observer, the value of the Faraday depth is positive and vice versa. Equation 6.3 and the sign convention related to the magnetic field component along the LOS are in agreement with the correct sense of Faraday rotation discussed by Ferrière et al. (2021).

For a given location in the sky, the RM synthesis gives us the distribution of the observed polarized emission in Faraday depth. This so-called Faraday spectrum is the Fourier transform of the complex polarization of the observed signal,  $P(\lambda^2) = Q(\lambda^2) + iU(\lambda^2)$ , from  $\lambda^2$ - to  $\Phi$ -space (Brentjens & de Bruyn, 2005):

$$F(\Phi) = \frac{1}{W(\lambda^2)} \int_{-\infty}^{+\infty} P(\lambda^2) P^*(\lambda^2) \exp^{-i2\Phi\lambda^2} d\lambda^2, \quad (6.4)$$

where  $W(\lambda^2)$  is the non-zero-weighting function, usually taken to be 1 at  $\lambda^2$  where measurements are taken and 0 elsewhere. If the RM synthesis is applied over a sky area, we can study the morphology of the observed polarized emission at different Faraday depths, to perform the so-called Faraday tomography. Characteristics of the  $\lambda^2$  distribution constrain scales in Faraday depth that we can probe when performing the RM synthesis. A resolution in Faraday depth is inversely proportional to the spectral bandwidth ( $\Delta\lambda^2$ ) as  $\delta\Phi \approx 2\sqrt{3}/\Delta\lambda^2$  and corresponds to the width of the rotation measure spread function (RMSF, Brentjens & de Bruyn, 2005). The maximum detectable Faraday scale is inversely proportional to the smallest ( $\lambda_{\min}^2$ ) measured  $\lambda^2$

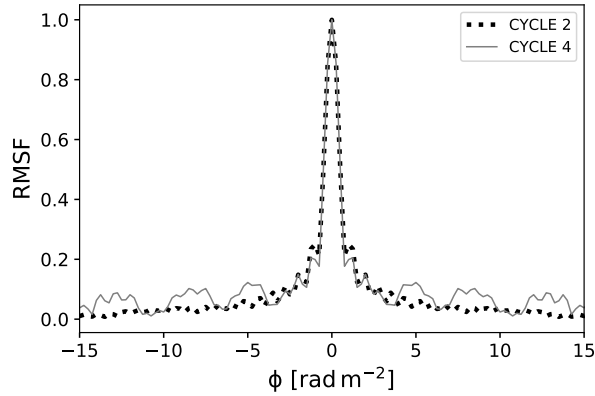


Figure 6.4: RMSF for 10 observations in Cycle 2 (dashed) and 11 observations in Cycle 4 (solid line) of the ELAIS-N1 field.

as  $\Delta\Phi_{\text{scale}} \approx \pi/\lambda_{\text{min}}^2$ .

I used the publicly available code `rm-synthesis`<sup>4</sup> and applied it to Stokes Q and U images, which had comparable noise levels ( $< 7.5 \text{ mJy PSF}^{-1}$ )<sup>5</sup> in the frequency data cube of each observation. The frequency channels with noise  $> 7.5 \text{ mJy PSF}^{-1}$  were flagged. The resulting Faraday cubes covered Faraday depths from  $-50$  to  $+50 \text{ rad m}^{-2}$  in  $0.25 \text{ rad m}^{-2}$  steps, given the expected Faraday depth range of the observed emission in this field (from  $-10$  to  $+13 \text{ rad m}^{-2}$  Jelić et al., 2014). The resolution in Faraday depth was  $\delta\Phi = 0.9 \text{ rad m}^{-2}$  for all observations. The side lobes of the RMSF in Cycle 4 data were higher than in Cycle 2 data (see Fig. 6.4) due to the gaps at frequencies contaminated by the broad RFIs (see Fig. 6.3). Because the resolution in Faraday depth is comparable to the maximum detectable Faraday scale ( $\Delta\Phi = 1.1 \text{ rad m}^{-2}$ ), we are only sensitive to Faraday-thin structures ( $\lambda^2\Delta\Phi \ll 1$ ) or the edges of Faraday-thick structures ( $\lambda^2\Delta\Phi \gg 1$  Brentjens & de Bruyn, 2005).

The noise in the Faraday cubes for the different observations is given in Table 6.2. The noise was estimated as the standard deviation of an image given in the polarized intensity at Faraday depth of  $-50 \text{ rad m}^{-2}$  and multiplied by a factor of  $\sqrt{2}$ . At this Faraday depth, polarized emission is not observed, and the image is dominated by noise. The factor  $\sqrt{2}$  addresses the Rician distribution of the noise in the polarized intensity, which roughly corresponds to a normally distributed noise in Stokes Q and U (e.g. Brentjens & de Bruyn, 2005). A mean value of the noise in Cycle 2 observations is  $91 \pm 10 \text{ } \mu\text{Jy PSF}^{-1} \text{ RMSF}^{-1}$  and in Cycle 4 observations is  $121 \pm 26 \text{ } \mu\text{Jy PSF}^{-1} \text{ RMSF}^{-1}$ . Higher noise in Faraday cubes of Cycle 4 data is due to a

<sup>4</sup><https://github.com/brentjens/rm-synthesis>

<sup>5</sup>The noise threshold of  $7.5 \text{ mJy PSF}^{-1}$  is estimated based on the noise characteristics in Stokes QU data cubes of Cycle 2 observations. It corresponds to the mean value of it plus six times its variations measured by the standard deviation at frequencies not affected by the RFI.

ID	Cycle	Noise [ $\mu\text{Jy PSF}^{-1} \text{RMSF}^{-1}$ ]	$\Delta\Phi_{\text{shift}}$ [rad/m <sup>2</sup> ]
009	2	106	$-0.159 \pm 0.007$
010	2	94	$-0.065 \pm 0.005$
011	2	88	>1
012	2	84	$0.053 \pm 0.007$
013	2	88	$0.002 \pm 0.006$
014	2	82	'reference'
015	2	84	$0.010 \pm 0.005$
016	2	86	$0.003 \pm 0.005$
017	2	85	$0.010 \pm 0.006$
018	2	112	$0.052 \pm 0.005$
020	4	107	$-0.033 \pm 0.005$
021	4	91	$-0.021 \pm 0.004$
022	4	133	$0.020 \pm 0.004$
023	4	111	$0.011 \pm 0.004$
024	4	102	'reference'
026	4	112	$0.033 \pm 0.005$
027	4	112	$0.017 \pm 0.004$
028	4	179	$0.045 \pm 0.006$
030	4	164	$0.114 \pm 0.005$
031	4	103	$0.080 \pm 0.004$
032	4	111	$0.101 \pm 0.004$

Table 6.2: Calculated noise in the Faraday cubes given for different observations and their relative shift in Faraday depth ( $\Delta\Phi_{\text{shift}}$ ) with respect to the reference observation (calculated in Sec. 6.3). An ID of each observation corresponds to the one given in Table 1 in Sabater et al. (2021).

larger number of frequency channels in this cycle affected by RFI (see Fig. 6.3). Observation 014 has the lowest noise among both Cycle 2 and 4 observations, and observation 021 has the lowest noise among Cycle 4 observations. Hence, the 014 observation is chosen, as a reference for Cycle 2. For Cycle 4 I take for consistency the same reference observation (024) as in Herrera Ruiz et al. (2021), which is the second-best observation in terms of the noise in this cycle. The same reference observation for both cycles cannot be chosen because of their different frequency configurations.

I used publicly available code `rmclean3d` from `RM-Tools`<sup>6</sup> (Purcell et al., 2020) to deconvolve the Faraday cubes for the side lobes of the RMSF. The code is based on RM-CLEAN algorithm described in Heald et al. (2009). A threshold of five times the noise in the Faraday cube is used during the RM-CLEAN process.

<sup>6</sup><https://github.com/CIRADA-Tools/RM-Tools>

### 6.2.3 Comparison with a previous LOFAR commissioning observation

The ELAIS-N1 field was observed previously with LOFAR during its commissioning phase (Jelić et al., 2014). That observation was done in a limited frequency range from 138 MHz to 185 MHz. Here, a comparison is made between that observation and observations used in this work. The comparison is done using Faraday cubes in the polarized intensity.

Noise in a Faraday cube of the commissioning observation (a single 8h synthesis) was  $300 \mu\text{Jy PSF}^{-1} \text{RMSF}^{-1}$  (Jelić et al., 2014). This is around 3.6 times higher than the noise in the individual Faraday cubes presented in this work. The difference arises from the limited available frequency bandwidth during the commissioning phase of LOFAR and the use of a simpler calibration strategy that addressed only direction-independent effects.

The commissioning observation of the ELAIS-N1 field revealed polarized diffuse emission over a wide range of Faraday depths ranging from  $-10$  to  $+13 \text{ rad m}^{-2}$  (Jelić et al., 2014), given a resolution of  $1.75 \text{ rad m}^{-2}$  in Faraday depth. The most prominent features of that emission are seen in the left image of Fig. 7 in Jelić et al. (2014), showing the highest peak value of the Faraday depth spectrum at each pixel (RA, Dec). The mean surface brightness of that emission is  $2.6 \text{ mJy PSF}^{-1} \text{RMSF}^{-1}$ . The same figure also shows the Faraday depth of each peak in an image presented on the right.

The same images are constructed for the observations analysed in this work. The images for the observation that has the lowest noise level (014) are presented in Fig. 6.5 as an example. Images for all other observations are very similar to these. The observed diffuse emission in the left image of Fig. 6.5 shows morphological similarity with the one detected in the commissioning observation (see left image in Fig. 7 in Jelić et al., 2014). The observed morphological features appear much sharper despite comparable angular resolution in both observations. This is due to almost two times better resolution in Faraday depth than in the commissioning observation. As a consequence, the observed emission suffers less from depolarization, as is the case, for example, for a filamentary structure oriented north-south in the central part of the image. The filament is depolarized in the commissioning observation, while it is visible in observations presented in work. Due to a better signal-to-noise ratio, there is also more emission visible towards the edges of the image, where the emission is attenuated by the LOFAR primary beam. The mean surface brightness of the observed emission in the central part of the image is  $3.0 \text{ mJy PSF}^{-1} \text{RMSF}^{-1}$ , which is a bit brighter than in the commissioning observation. The emission appears in a range of Faraday depths from  $-16$  to  $+14 \text{ rad m}^{-2}$ , starting at slightly smaller and ending at slightly larger Faraday depths than in the commissioning observation. Further discussion on characteristics of the observed emission are in Sec. 6.5.2.



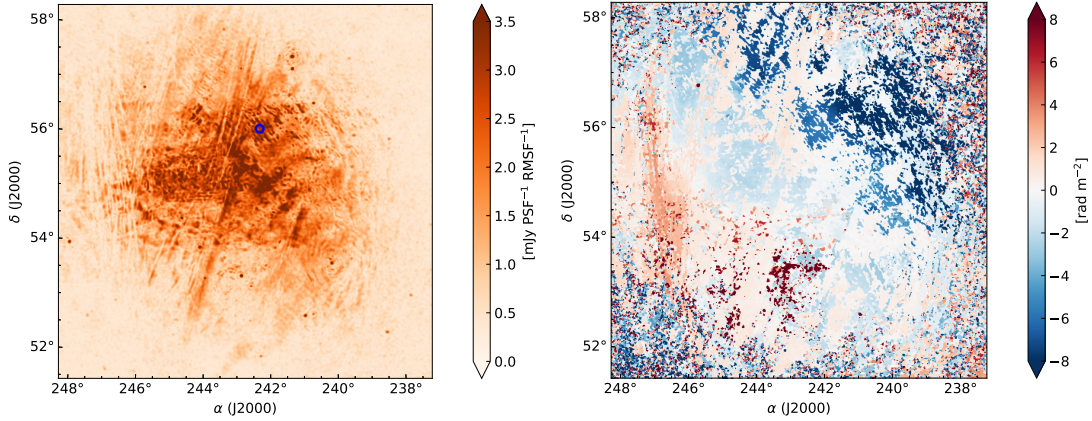


Figure 6.5: Image of the highest peak of the Faraday depth spectrum in the polarized intensity (left) and a corresponding image of a Faraday depth of the highest peak (right) for the observation with the lowest noise (014, the reference observation for Cycle 2). The blue circle in the left image marks a randomly chosen location for which a Faraday spectrum is presented in Fig. 6.6.

## 6.3 Ionospheric Faraday rotation corrections

### 6.3.1 Analysis of a relative shift in Faraday depth between different observations

Data analysed in this work were corrected for the ionospheric Faraday rotation by the satellite-based TEC measurements (see Sec. 6.2.1). To check how well the data are corrected, I make a relative comparison between each observation and the reference observation by cross-correlating Faraday cubes.

Instead of explicitly cross-correlating Faraday cubes of two observations ( $a$  and  $b$ ) as in Jelić et al. (2015), it is computationally more efficient to use the Fourier transform’s cross-correlation property. I calculate the cross-correlation function by effectively performing RM-synthesis on  $P_a(\lambda^2)P_b^*(\lambda^2)$ , as proposed by Brentjens (2018) and implemented in the above-mentioned publicly available code `rm-synthesis`. Using this code, the cross-correlation function is evaluated for Faraday depths between  $-5$  and  $+5$   $\text{rad m}^{-2}$  in  $0.01$   $\text{rad m}^{-2}$  steps. I expect the relative shift between the observations to be  $\lesssim 1$   $\text{rad m}^{-2}$ .

The applied method is illustrated in Fig. 6.6 by giving examples of Faraday spectra in the polarized intensity for two observations (009 and 014; left image) and the modulus of their evaluated complex cross-correlation function  $\zeta$  (right image). Faraday spectra are taken for a random (RA, Dec) pixel in the cube (marked with a blue circle in Fig. 6.5), where the observed emission is relatively bright. To find a Faraday depth of the cross-correlation function’s peak, I

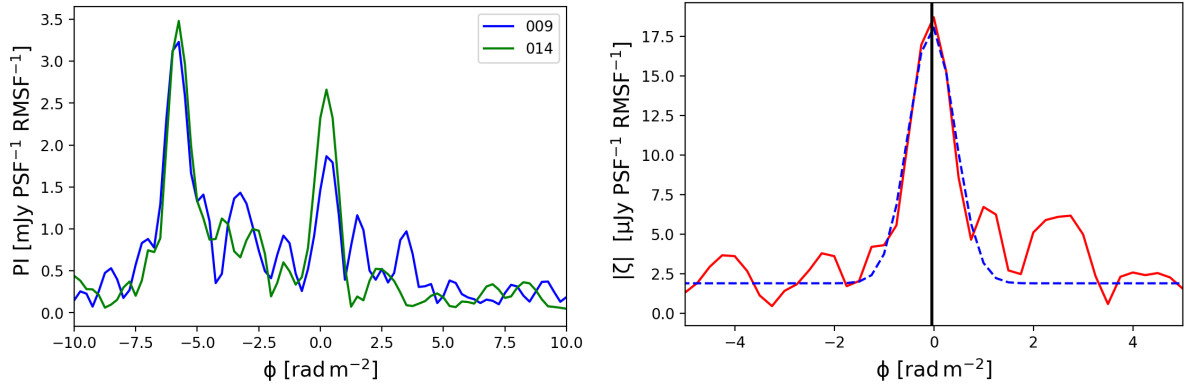


Figure 6.6: Left panel: Example of a Faraday spectrum given in the polarized intensity for the 009 observation (blue line) and the reference (014) observation at a randomly chosen location marked with a blue circle in Fig. 6.5 (RA  $242^{\circ}18'03.60''$  and Dec  $56^{\circ}08'16.80''$ ). Right panel: Calculated modulus of the complex cross-correlation function  $|\zeta|$  (red line) for the given Faraday spectra, fitted with a Gaussian (blue dashed line) to estimate the misalignment between the two observations (black vertical line) at this specific location.

fit a Gaussian to the peak. At this specific position in the image, the Faraday spectrum of the 009 observation is shifted by  $-0.047 \pm 0.006 \text{ rad m}^{-2}$  with respect to a reference (014) observation.

To find a common shift in Faraday depth across the field of view, the complex cross-correlation functions are averaged for all pixels (RA, Dec), where the observed emission in a reference observation has the highest peak value of the Faraday depth spectrum at least ten times larger than the noise ( $\geq 82 \text{ mJy PSF}^{-1} \text{ RMSF}^{-1}$ ). This will improve the signal-to-noise ratio and therefore the location of the main peak of the cross-correlation function. When averaging, the assumption is that the variation of shifts in Faraday depth across the field of view is much smaller than the width of the main peak of the RMSF ( $\ll 0.9 \text{ rad m}^{-2}$ ).

Figure 6.7 shows the calculated modulus of the averaged complex cross-correlation function for observations 009 and 014 (magenta solid line). The same figure also gives variations of the cross-correlation function across the field of view as measured by a standard deviation (cyan dashed line). Then, I fit a Gaussian to the peak and find that the 009 observation is shifted by  $-0.159 \pm 0.007 \text{ rad m}^{-2}$  with respect to the reference observation.

Calculated relative shifts in Faraday depth for all other observations are given in Table 6.2. There is no significant difference in misalignment between the two cycles. The observations are on average misaligned by  $\pm(0.046 \pm 0.042) \text{ rad m}^{-2}$  with respect to the reference observation. The only exception is 011 observation, which shows a misalignment larger than  $1 \text{ rad m}^{-2}$  and is analysed in detail in the Sec. 6.3.2.

The estimated misalignments are comparable to the one found in the analysis of five LO-

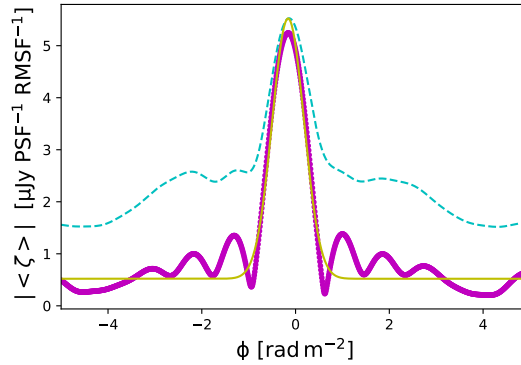


Figure 6.7: Calculated modulus of the averaged complex cross-correlation function for observations 009 and 014 (solid magenta line) and variations of the cross-correlation function across the field of view as measured by a standard deviation (dashed cyan line). A misalignment between two observations is determined by fitting a Gaussian to the peak (solid yellow line).

FAR observations of the 3C 196 field ( $0.1 \pm 0.08 \text{ rad m}^{-2}$ ; Jelić et al., 2015). This verifies the reliability of ionospheric Faraday rotation corrections estimated using the satellite-based TEC measurements. The related uncertainties are mostly connected to daily systematic biases in the TEC measurements of  $\sim 1$  TEC unit, translating to an error in the ionospheric rotation measure of  $\sim 0.1 \text{ rad m}^{-2}$ . The misalignment for observations 020, 027, 028, 030, and 031 are in agreement with the one estimated by Herrera Ruiz et al. (2021) within the errors. Herrera Ruiz et al. (2021) based their analysis using a single Faraday spectrum at the location of the peak pixel of the reference polarized source, while here all pixels are used which show bright polarized diffuse emission. Therefore, estimated errors in this work are  $\sim 5$  times smaller than in their work.

### 6.3.2 Restoring 011 observation using Galactic polarized emission

The 011 observation shows the largest shift with respect to the reference observation ( $\gtrsim 1 \text{ rad m}^{-2}$ ) among all observations analysed in this work. The Faraday cube is inspected for this observation in the polarized intensity. There is almost no emission visible in the Faraday cube in comparison to the reference observation. An example is given in Fig. 6.8 (left image) at Faraday depth of  $-2.25 \text{ rad m}^{-2}$ . The same figure (middle image) shows an image of the reference observation but at a Faraday depth of  $-3.25 \text{ rad m}^{-2}$  to account for a relative misalignment between the two observations in Faraday depth. The lack of the observed polarized emission shows that  $RM_{\text{ion}}$  corrections were not applied properly to the data due to some unfortunate processing error. This is confirmed by inspection of the processing log files.

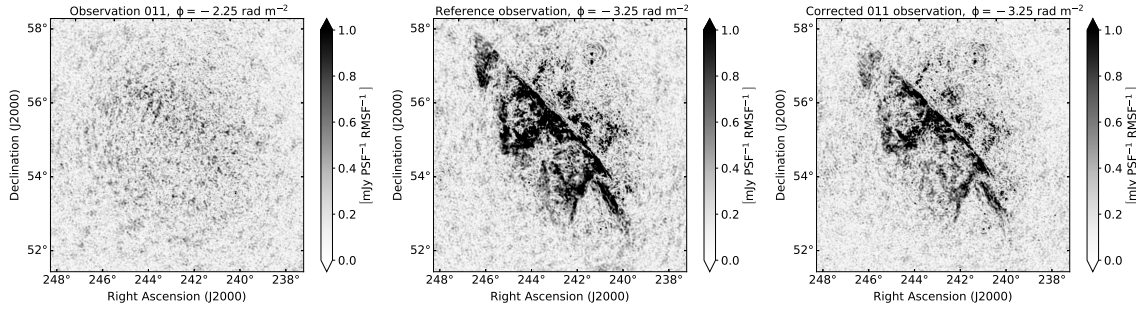


Figure 6.8: Example of an image in Faraday cube given in the polarized intensity at  $-2.25 \text{ rad m}^{-2}$  for the 011 observation (left image), which is not properly corrected for the  $RM_{\text{ion}}$ . There is almost no emission visible in comparison to the reference (014) observation (middle image), whose image is given at  $-3.25 \text{ rad m}^{-2}$  to account for a relative misalignment of  $+1.0 \text{ rad m}^{-2}$  between the two observations. The polarized emission is visible in the restored Faraday cube of the 011 observation (right image), which is corrected using the estimated  $\Delta\Phi_{\text{shift}}$  given in Fig. 6.9.

The calculated  $RM_{\text{ion}}$  correction for this observation is  $2.4 \text{ rad m}^{-2}$  at the beginning of the observation, and then it decreases to  $1.5 \text{ rad m}^{-2}$  within the first 430 minutes. This relative change of  $0.9 \text{ rad m}^{-2}$  is enough to fully depolarize the signal at 150 MHz (see Sec. 6.1), if we do not correct the data for it. In the remaining 50 minutes of the observation, it increases again to  $1.6 \text{ rad m}^{-2}$ .

To restore the polarized signal in 011 observation, we test if the observed polarized emission itself can be used to account for the ionospheric Faraday rotation correction that should be applied to the data. We first re-image the eight-hour 011 observation by creating 48 Stokes QU images of 10-minute intervals of the observation. Then, for each 10-minute interval, we find its relative shift in Faraday depth with respect to the full eight-hour reference observation by following the methodology described in Sec. 6.3.

Figure 6.9 shows the results (thick solid black line) which are compared with the corrections calculated using the satellite-based TEC measurements (black dashed line). The two curves are showing the same trend. A systematic shift of  $\sim 0.3 \text{ rad m}^{-2}$  between the two curves is due to the different nature of these two methods. The satellite-based corrections give absolute  $RM_{\text{ion}}$ , while the corrections based on the observed polarized emission give relative values with respect to the used reference observation ( $\Delta\Phi_{\text{shift}}$ ).

Test is also made for any angular variations of  $\Delta\Phi_{\text{shift}}$  across the field of view. This is done by splitting the frequency cube spatially into quadrants and then repeating the procedure to find a relative time varying shift for each quadrant separately. The results are over-plotted in Fig. 6.9 with thin solid coloured lines. The northwest (NW) and the southeast (SE) quadrants show relative shifts which are consistent with the result of the full cube. Larger values are found

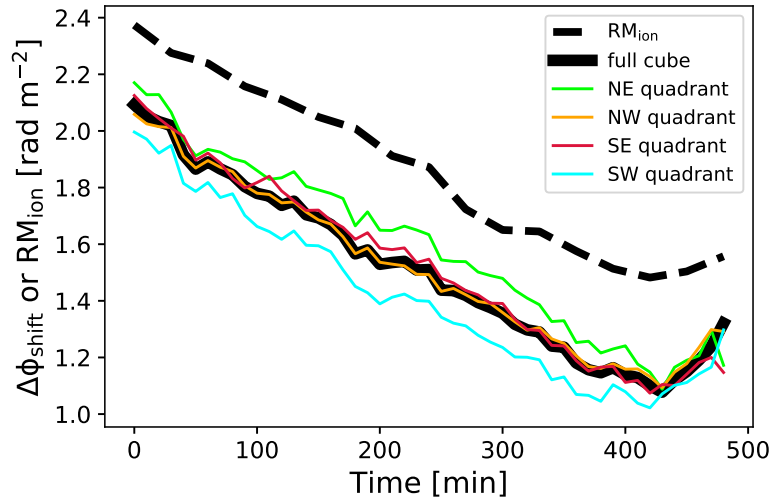


Figure 6.9: Estimated relative shifts in Faraday depth ( $\Delta\Phi_{\text{shift}}$ ) of each 10-minute interval of the 011 observation with respect to the full eight-hour reference (014) observation (thick solid black line). The calculated  $RM_{\text{ion}}$  corrections based on the satellite TEC measurements are plotted with thick dashed black line. The thin solid colored lines give the  $\Delta\Phi_{\text{shift}}$  in the field of view quadrants.

in the northeast (NE) quadrant, on average, the shifts are larger by  $0.096 \text{ rad m}^{-2}$  than the one from the full cube. In the southwest (SW) quadrant, they are smaller by  $0.1 \text{ rad m}^{-2}$ . This points to a relative spatial gradient of  $\sim 0.2 \text{ rad m}^{-2}$  in NE-SW direction across the field of view.

The observed polarization angle of each 10-minute interval is ‘de-rotated’ by its estimated shift across the full image with respect to the reference observation ( $\Delta\Phi_{\text{shift}}$ ). This is done by multiplying the complex polarization given at each wavelength (frequency) by  $\exp^{-i2\Delta\Phi_{\text{shift}}\lambda^2}$ . Then, all corrected 10-minute intervals are combined to get Stokes QU cube over the full eight-hour synthesis and use the RM synthesis to get the final restored Faraday cubes of the 011 observation.

The polarized emission is now visible in the restored Faraday cubes. An example of polarized intensity is shown in Fig. 6.8 (right image) at Faraday depth of  $-3.25 \text{ rad m}^{-2}$ . Observed morphology of polarized emission in the restored 011 observation and the reference observation are visually very similar. To quantify this similarity, the Pearson correlation coefficient is calculated between the images of the highest peak value of the Faraday depth spectrum in the polarized intensity of the two observations and a ratio of their peak intensity distributions. In the calculation only the inner  $3^\circ \times 3^\circ$  of the images are used. We get a correlation coefficient of 0.95, and find that polarized emission in the restored cube is  $(73 \pm 14)\%$  of that in the reference observation. The majority of the emission and its morphology is restored.

To increase even further the percentage of the recovered brightness of the observed emission,

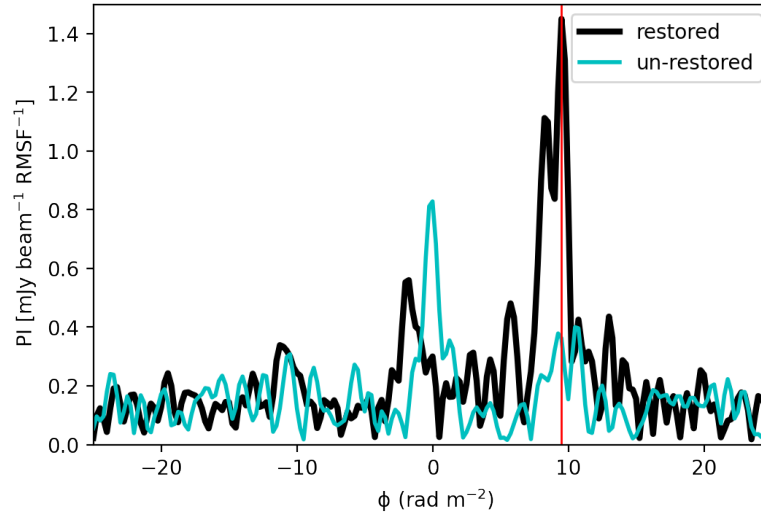


Figure 6.10: Primary beam uncorrected Faraday spectrum at a location of a polarized source (ID 01 in [Herrera Ruiz et al., 2021](#)) in the high-resolution restored (solid black line) and unrestored (solid cyan line) Faraday cube of the 011 observation. The source should be present at Faraday depth of  $+(9.44 \pm 0.03) \text{ rad m}^{-2}$  (red vertical line), as reported by [Herrera Ruiz et al. \(2021\)](#).

we would need to address the depolarization that happens within the timescale of 10 minute intervals. To achieve that, we could re-image the eight-hour observation to even smaller time intervals, for example of 1 minute. However, the signal-to-noise ratio in that case would be a limiting factor for our methodology, making it out of the scope of current work.

Furthermore, we assess if the estimated shifts can be applied to the high-resolution images ( $6''$ ) of the same observation. We re-image in 10-minute intervals a small part of the high-resolution data centred at a polarized source at RA  $16^{\text{h}}24^{\text{m}}32^{\text{s}}$  and Dec  $+56^{\circ}52'28''$  ([Herrera Ruiz et al., 2021](#), source with ID 01). Then, we ‘de-rotate’ the observed polarization angle of each 10-minute interval by the shift estimated using the very low-resolution data, combine high-resolution 10-minute intervals to the full eight-hour synthesis frequency cube and apply the RM synthesis to it. The resulting primary beam uncorrected Faraday spectrum at a location of the polarized source is presented in Fig. 6.10 (black line). The source appears at Faraday depth of  $\sim 9.5 \text{ rad m}^{-2}$ , as expected. Its recovered peak polarized flux is 43% of the value reported by [Herrera Ruiz et al. \(2021\)](#), once we take into account the primary beam correction at the location of the source (a factor of  $2.3\times$ ). The same figure also shows the Faraday spectrum before the ionospheric corrections are applied (cyan line), where the source is fully depolarized. A successful detection of the source demonstrates a potential of using the very low-resolution data to correct the high-resolution data. This method is computationally more efficient than the one that uses the high-resolution data only.

## 6.4 Stacking a very low-resolution data

To stack images of different observations together, we first need to ‘de-rotate’ the observed polarization angle of each observation by its estimated shift with respect to the reference observation ( $\Delta\Phi_{\text{shift}}$ , see Table 6.2). We multiply the complex polarization  $P_i(\lambda^2) = Q_i(\lambda^2) + iU_i(\lambda^2)$  given at each wavelength (frequency) by  $\exp^{-i2\Delta\Phi_{\text{shift}}\lambda^2}$ :

$$\tilde{P}_i(\lambda^2) = \tilde{Q}_i(\lambda^2) + i\tilde{U}_i(\lambda^2) = (Q_i(\lambda^2) + iU_i(\lambda^2))\exp^{-i2\Delta\Phi_{\text{shift}}\lambda^2}. \quad (6.5)$$

This way, the correction is applied to the whole Faraday spectrum simultaneously.

We then stack all corrected images of each observing cycle by calculating the weighted average at each wavelength (frequency):

$$P_{\text{combined}}(\lambda^2) = \frac{\sum_i \tilde{Q}_i(\lambda^2)w_i^{\tilde{Q}}(\lambda^2)}{\sum_i w_i^{\tilde{Q}}(\lambda^2)} + i \frac{\sum_i \tilde{U}_i(\lambda^2)w_i^{\tilde{U}}(\lambda^2)}{\sum_i w_i^{\tilde{U}}(\lambda^2)}, \quad (6.6)$$

where  $w_i^{\tilde{Q},\tilde{U}}(\lambda^2)$  is a wavelength (frequency) dependent weight for each observation defined as the inverse of the variance of the noise in Stokes Q and U images. We recall that the noise in Stokes Q and U were comparable and were calculated in the corner of each image where the polarized emission was not present. We are not able to stack the data from two cycles directly because of their different frequency channel widths (see Sect. 6.2.1). They are combined at a later stage in Faraday depth. Figure 6.11 shows a number of images per frequency channel used in the final stacked data cube for Cycle 2 and Cycle 4. There are on average nine images added per frequency channel in Cycle 2 and 11 images in Cycle 4.

Images of observation 011 are not used for the stacked data cube of Cycle 2 because of their relatively bad quality compared to the images of all other observations. This choice does not have any significant impact on the final result. Once the data of each observing cycle are stacked, the RM synthesis is applied.

The noise in the stacked Faraday cube of Cycle 2 data is  $32 \mu\text{Jy PSF}^{-1} \text{RMSF}^{-1}$  and of Cycle 4 data is  $40 \mu\text{Jy PSF}^{-1} \text{RMSF}^{-1}$ . In both cases, this is  $\sim 3$  times less than the mean value of noise in Faraday cubes of individual observations ( $91 \pm 10 \mu\text{Jy PSF}^{-1} \text{RMSF}^{-1}$  and  $121 \pm 26 \mu\text{Jy PSF}^{-1} \text{RMSF}^{-1}$ , respectively). The noise in the stacked Faraday cube is reduced by a square root of the number of observations that are stacked, as expected.

We calculate the cross-correlation between the stacked Faraday cubes of two cycles as a function of a displacement in Faraday depth to check for their alignment. We consider only Faraday spectra that have a peak flux in the polarized intensity  $\geq 82 \text{ mJy PSF}^{-1} \text{RMSF}^{-1}$ , the

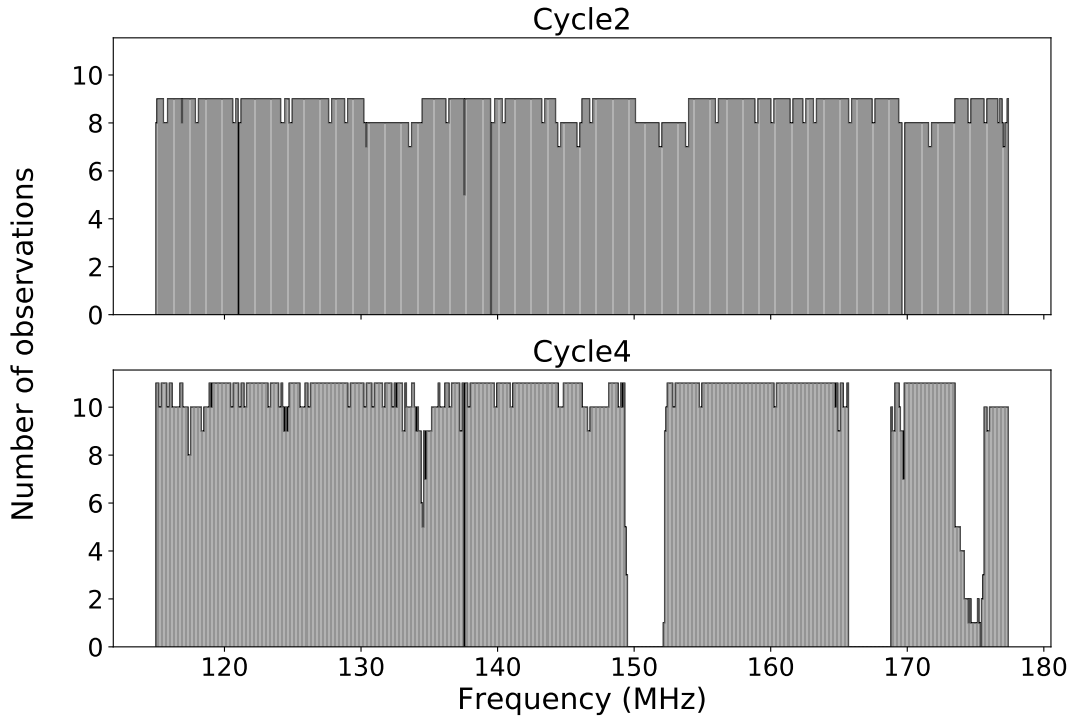


Figure 6.11: Number of observations per frequency channel used in the stacked data cube from Cycle 2 (upper plot) and Cycle 4 (lower plot) data. Although the data cover the same frequency range, they have different frequency configurations and hence a different number of frequency channels (see Sec. 6.2.1).

same limit as the one used in Sec. 6.3. The resulting cross-correlation functions are then averaged, and their common peak is fitted with a Gaussian. The two cubes are aligned in Faraday depth within the error of the fit, and can be combined directly to the final Faraday cube.

We combine the stacked Faraday cubes of two cycles by calculating the weighted average in Faraday depth:

$$P_{\text{combined}}(\Phi) = \frac{\sum_i Q_i(\Phi)w_i^\Phi}{\sum_i w_i^\Phi} + i \frac{\sum_i U_i(\Phi)w_i^\Phi}{\sum_i w_i^\Phi}, \quad (6.7)$$

where  $w_i^\Phi$  is a Faraday depth independent weight for each Faraday cube defined as the inverse of the variance of the noise in Stokes Q and U Faraday cubes. The noise in the Faraday cube is estimated as the standard deviation of an image given in Stokes Q and U at  $-50 \text{ rad m}^{-2}$ . This is the Faraday depth, where we do not observe any polarized emission and the image is dominated by noise.



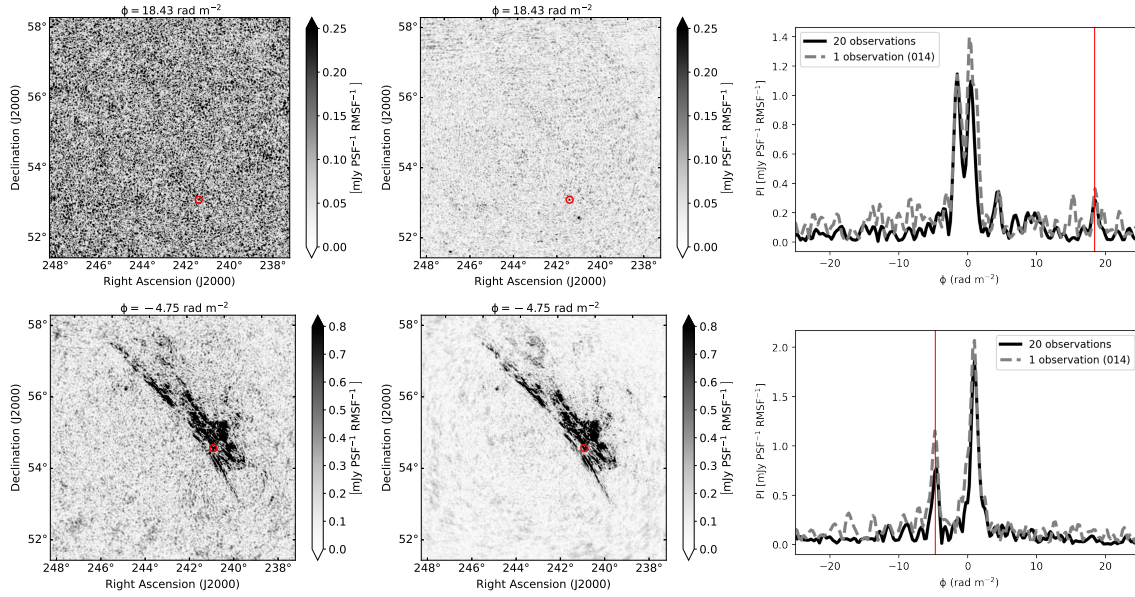


Figure 6.12: Example of a successful (upper panels) and an unsuccessful detection of a polarized source (lower panels) in the presented Faraday cubes (sources with ID 10 and 07 in [Herrera Ruiz et al., 2021](#), respectively). Polarized intensity images in the reference (014, left images) and in the final stacked Faraday cube (middle images) are given at the closest available Faraday depth, such as that of the source. The location of the source in each image is marked with the red circle, while the corresponding Faraday spectra are given in plots on the right. A reported Faraday depth of the sources by [Herrera Ruiz et al. \(2021\)](#) are marked with vertical red lines.

## 6.5 The final stacked Faraday cube

The final stacked Faraday cube combines images of 20 ELAIS-N1 LoTSS-Deep Fields observations,  $\sim 150$  hours of data in total. The cube covers Faraday depths from  $-50$  to  $+50 \text{ rad m}^{-2}$  in  $0.25 \text{ rad m}^{-2}$  steps. The resolution in Faraday depth is  $0.9 \text{ rad m}^{-2}$ , as defined by the resolution of the stacked Faraday cubes of the two observing cycles. The final image noise is  $27 \mu\text{Jy PSF}^{-1} \text{ RMSF}^{-1}$ , which is  $\sim \sqrt{20}$  smaller than the mean value of noise in Faraday cubes of every individual observation in the two cycles, as expected.

In the following two subsections, we first cross-check if we detect the radio sources presented in catalogues by [Herrera Ruiz et al. \(2021\)](#) and [Piras et al. \(in prep.\)](#) and then we analyse and discuss the observed diffuse Galactic polarized emission.

### 6.5.1 Cross-checking the detection of the radio sources

We use the catalogues of the polarized sources provided by [Herrera Ruiz et al. \(2021\)](#) and [Piras et al. \(in prep.\)](#) to check how many of them we detect in our final stacked Faraday cube.

The purpose of this comparison is only to verify our stacking method on very low-resolution data. It is not meant to provide in-depth analysis of the polarized sources. This is done in [Herrera Ruiz et al. \(2021\)](#) and [Piras et al. \(in prep.\)](#) using the high-resolution data (20'' and 6'', respectively), which are better suited for such analysis than a very low-resolution data (4.3') used in this work.

We extract the Faraday spectra and inspect the images in our final polarized intensity cube at locations of polarized sources provided in the catalogues. We have clear detection of 9 out of 10 radio sources from [Herrera Ruiz et al. \(2021, table 2, ID 01–06 and 08–10\)](#), while 1 of them (ID 07) is difficult to identify due to the presence of the diffuse polarized emission in our Faraday cube. Two examples are given in Fig. 6.12 for sources with IDs 10 and 07. In the first example, the source is not contaminated by diffuse emission. There is a clear signature of it in the Faraday spectrum of the stacked data. This source is however difficult to detect in the reference observation due to poorer signal-to-noise ratio than in the stacked data. In the second example, we don't find the signature of the source neither in the stacked data, nor in the reference observation, due to contamination by diffuse polarized emission that dominates the image and the Faraday spectrum at the location of the source.

A preliminary catalogue of [Piras et al. \(in prep.\)](#) contains 16 additional polarized radio sources compared to the catalogue of [Herrera Ruiz et al. \(2021\)](#). We have detected 7 of these additional sources, while others are contaminated by polarized diffuse emission and could not be discerned.

The rotation measures of successfully detected sources in our final cube are in agreement with the values provided in the catalogues, taking into account a resolution in Faraday depth of  $0.9 \text{ rad m}^{-2}$  and a difference in angular resolution of the used data. The polarized radio source catalogues are based on high-resolution LoTSS data (20'' and 6''), while in our work we use very low-resolution LoTSS data (4.3'). Therefore, morphologies of polarized sources are mostly not resolved in our data. If a source is unresolved in our data, while in reality, it has for example two lobes (see a source with ID 07, Fig. 7 in [Herrera Ruiz et al., 2021](#)) whose RMs do not differ more than a resolution of the data in Faraday depth, we observe its rotation measure as an averaged value of the two lobes and additionally weighted by their relative brightness.

## 6.5.2 Faint diffuse Galactic polarized emission

We detect diffuse polarized emission in the final stacked Faraday cube over a range of Faraday depths from -16 up to +18  $\text{rad m}^{-2}$  (see Fig. 6.13). Its brightest and prominent morphological features were already detected by [Jelić et al. \(2014\)](#), but over a smaller Faraday depth range, starting from -10 to +13  $\text{rad m}^{-2}$ , and with a poorer resolution of  $1.75 \text{ rad m}^{-2}$ . Here we give a

description of all morphological features observed in our final stacked cube.

From  $-16$  to  $-4$   $\text{rad m}^{-2}$  there is a northwest to southeast gradient of emission. It starts as a small-scale feature in the northwest part of the image, and then it grows diagonally across the centre of the image to an extended northeast-southwest structure. Its mean surface brightness is  $3.1 \mu\text{Jy PSF}^{-1} \text{RMSF}^{-1}$ . From  $-4$  to  $-0.5$   $\text{rad m}^{-2}$  there is a diffuse emission whose morphology is more patchy, but it spreads over the full field of view. It has mean surface brightness of  $3.5 \mu\text{Jy PSF}^{-1} \text{RMSF}^{-1}$ . A conspicuous, stripy morphological pattern of diffuse emission with north to south orientation dominates in the eastern part of the image from  $+0.5$  up to  $+4$   $\text{rad m}^{-2}$ . Its mean surface brightness reaches  $4.3 \mu\text{Jy PSF}^{-1} \text{RMSF}^{-1}$ . Towards higher Faraday depths, structures become very patchy, emission gets fainter, and then it disappears completely at  $+18$   $\text{rad m}^{-2}$ . The mean surface brightness of this faint emission is  $0.4 \mu\text{Jy PSF}^{-1} \text{RMSF}^{-1}$ .

We construct Faraday moments to make a comparison between the observed diffuse emission in the final stacked cube and the reference (014) observation. Faraday moments provide statistical description of Faraday tomographic cubes, as introduced by [Dickey et al. \(2019\)](#). The zeroth Faraday moment,  $M_0$ , is the polarized intensity  $PI(\Phi)$  integrated over the full Faraday depth range, given in units of  $\text{mJy PSF}^{-1} \text{RMSF}^{-1} \text{rad m}^{-2}$ . It gives the total polarized brightness of the emission in the Faraday cube. The first Faraday moment,  $M_1$ , is the polarized intensity weighted mean of Faraday spectra in units of  $\text{rad m}^{-2}$ . It measures a mean Faraday depth at which the brightest emission is observed. Finally, the second Faraday moment,  $M_2$ , is the intensity-weighted variance of Faraday spectra, whose square root gives the spread of the spectrum in units of  $\text{rad m}^{-2}$ . Its square root measures a range of Faraday depths over which the brightest emission is observed. The Faraday moments are defined as

$$M_0 = \sum_{i=1}^n PI_i \cdot \Delta\Phi, \quad (6.8)$$

$$M_1 = \frac{\sum_{i=1}^n PI_i \cdot \Phi_i}{\sum_{i=1}^n PI_i}, \quad (6.9)$$

and

$$M_2 = \frac{\sum_{i=1}^n PI_i \cdot (\Phi_i - M_1)^2}{\sum_{i=1}^n PI_i}, \quad (6.10)$$

where  $\Delta\Phi$  is a step in Faraday depth. The Faraday moments are calculated only for emission whose brightness is larger than a defined threshold to exclude noise-dominated areas in the data. We use a threshold of  $m_P + 5\sigma_P$ , where  $m_P$  is the polarized intensity bias and  $\sigma_P$  is noise in the polarized intensity.

Figure 6.14 shows the calculated Faraday moments, both for the reference (upper images)

## Chapter 6. Searching for the very faint radio emission

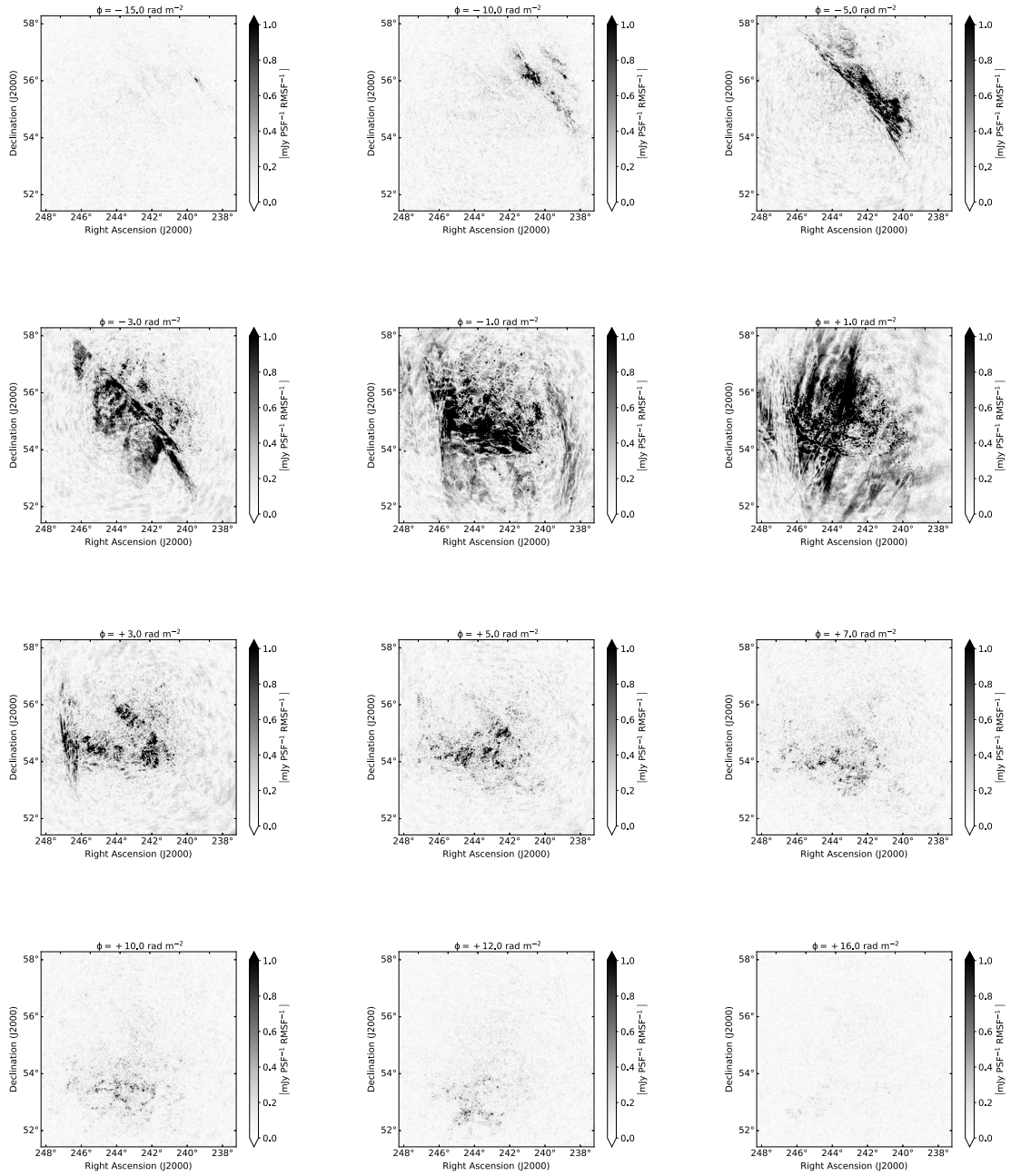


Figure 6.13: Images of the ELAIS-N1 field in the polarized intensity given at Faraday depths of  $-15.0$ ,  $-10.0$ ,  $-5.0$ ,  $-3.0$ ,  $-1.0$ ,  $+1.0$ ,  $+3.0$ ,  $+5.0$ ,  $+7.0$ ,  $+10.0$ ,  $+12.0$  and  $+16.0 \text{ rad m}^{-2}$  of the final stacked Faraday cube. The cube is based on  $\sim 150$  hours of the LOFAR observations in the frequency range from 114.9 to 177.4 MHz. Angular resolution of the images is  $4.3'$ . These are primary beam uncorrected images with the noise of  $27 \mu\text{Jy PSF}^{-1} \text{ RMSF}^{-1}$ .

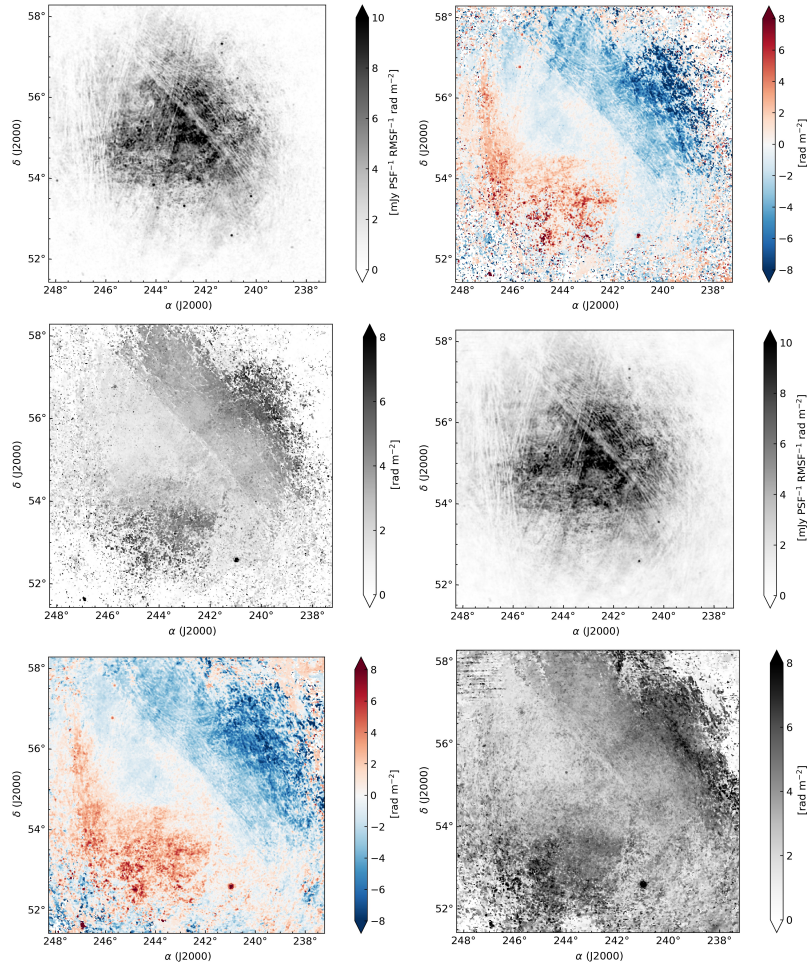


Figure 6.14: Moments of the reference (014) (upper images) and the final stacked Faraday cube (lower images). The left images give  $M_0$ , the middle ones show  $M_1$ , and the right images give  $\sqrt{M_2}$ .

and the final stacked Faraday cube (lower images). There is around 15% more integrated emission in the stacked cube than in the reference observation, as measured by the  $M_0$ . This is due to a better signal-to-noise ratio in the stacked cube and contribution of the detected faint emission to the  $M_0$ . The first Faraday moments do not differ much, as they are mostly driven by the brightest emission, which is the same in both cases. However, mean values of the  $M_1$  are  $-0.85 \text{ rad m}^{-2}$  and  $-0.65 \text{ rad m}^{-2}$  for reference and stacked cube respectively, indicating that there is on average more emission at positive Faraday depths in the stacked cube than in the reference cube. The  $\sqrt{M_2}$  shows the most noticeable differences. The measured spread in Faraday depth is on average 42% larger in the stacked than the reference cube. This is again due to faint emission at larger Faraday depths, which does not contribute to the second moment of the reference observation.

Examples of the faint emission, which is only clearly detected in the stacked cube, are

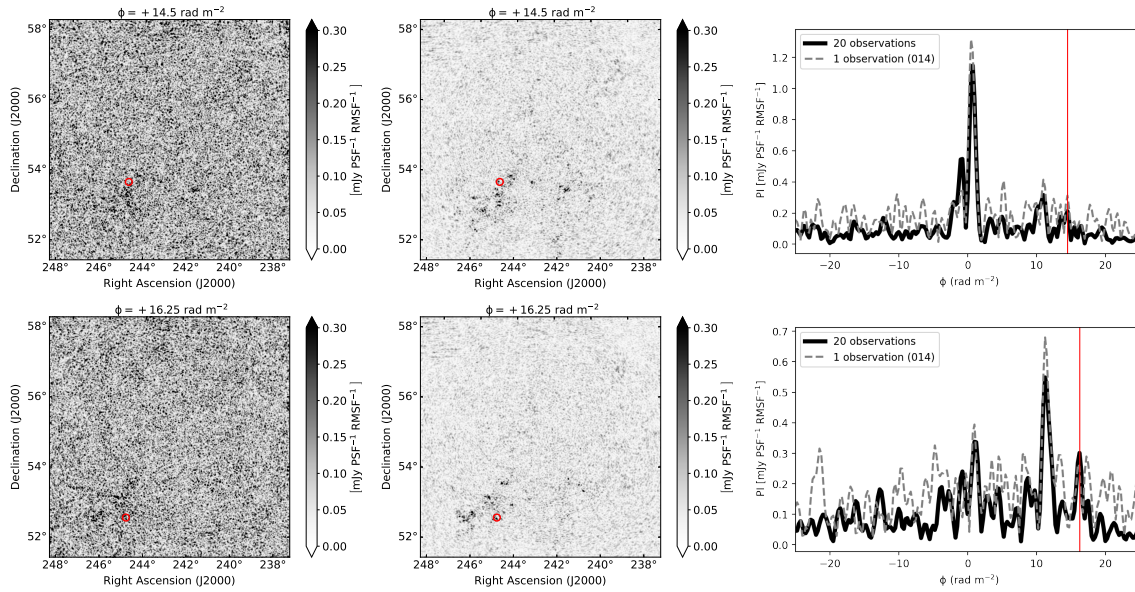


Figure 6.15: Examples of the faint Galactic polarized emission, which is only clearly detected in the final stacked Faraday cube. The images are given in the polarized intensity at Faraday depths of  $+14.5$  (upper images) and  $+16.25$   $\text{rad m}^{-2}$  (lower images) for the reference (left images) and the final stacked cube (middle images). The corresponding Faraday spectra at a location of the red circle in the images are given in plots on the right.

shown in Fig. 6.15. The images are given at Faraday depths of  $+14.5$  (upper images) and  $+16.25$   $\text{rad m}^{-2}$  (lower images). The images in the first panels are shown for the reference cube, while in the second panels for the final stacked cube. The third panels show the corresponding Faraday spectra at a location of the red circle in the images. The brightness of the faint emission is comparable to the noise in the reference cube and therefore is not detected there.

## 6.6 Discussion on the faint polarized emission newly detected

The diffuse polarized emission detected in the final stacked Faraday cube has the mean polarized intensity of  $10 \text{ mJy PSF}^{-1} \text{ RMSF}^{-1} \text{ rad m}^{-2}$ , as measured in the central region of the  $M_0$  (see bottom left image in Fig. 6.14). This translates to a mean brightness temperature of  $\sim 9.5 \text{ K}$ <sup>7</sup>.

The  $M_0$  of the final stacked Faraday cube is recalculated by restricting it to Faraday depths  $\geq +13 \text{ rad m}^{-2}$  to estimate the mean brightness temperature of the newly detected faint emission at higher Faraday depths. We get its mean polarized intensity to be of  $0.5 \text{ mJy PSF}^{-1} \text{ RMSF}^{-1}$

<sup>7</sup>The intensity of  $1 \text{ mJy PSF}^{-1} \text{ RMSF}^{-1} \text{ rad m}^{-2}$  corresponds to a brightness temperature of  $\sim 0.95 \text{ K}$  at  $144 \text{ MHz}$ , a frequency that corresponds to the weighted average of the observed  $\lambda^2$  used in RM synthesis.

rad m<sup>-2</sup>, which is  $\sim 0.475$  K. Although this faint emission is not contributing more than  $\sim 5\%$  to the total observed polarized emission, its relevance comes from the fact that it is present at Faraday depths at which the emission was not observed before. It increases the range of Faraday depths, usually characterized by  $\sqrt{M_2}$ , over which the emission is detected in this field with LOFAR. This is especially important for the interpretation of the LOFAR observations in terms of an extent of the probed volume along the LOS and underlying distribution of synchrotron emitting and Faraday rotating regions.

Depolarization effects associated with Faraday rotation are significant at low-radio frequencies. Only a few percent of the intrinsically polarized synchrotron emission is observed with the LOFAR (Jelić et al., 2014, 2015; Van Eck et al., 2017, 2019; Turić et al., 2021). The questions that arise are where along the LOS does depolarization happen and from where does the observed emission originate from. The idea is that we observe mostly close-by emission, while far-away emission gets depolarized in the magneto-ionic medium on the way to us. However, determining this from the LOFAR observations only is very difficult. A Faraday depth is not necessarily a good proxy for the distance. We need to take into consideration the full-complexity of the magnetic fields, its possible reversals and the multiphase nature of the interstellar medium. This is challenging, but it has been attempted recently in a number of the multi-tracer and -frequency studies of the LOFAR observations (Zaroubi et al., 2015; Van Eck et al., 2017; Jelić et al., 2018; Bracco et al., 2020; Turić et al., 2021; Erceg et al., 2022) and by using the magneto-hydrodynamical simulations (Bracco et al., 2022). For example, Erceg et al. (2022) was comparing the Faraday moments of the LOFAR observations of around 3100 square degrees in the high-latitude outer Galaxy to the high-frequency polarization data (DRAO GMIMS, Dickey et al., 2019) and to the Galactic Faraday Sky map (Hutschenreuter et al., 2022). The latter compliments the low- and high-frequency observations, as it represents the total RM yielded from the Galaxy. It is constructed using the observed RM of a large sample of extragalactic polarized sources, including the one in the LoTSS polarized source catalogue (O’Sullivan et al., 2023).

Erceg et al. (2022) found a correlation between the Galactic Faraday Sky map and the LOFAR first Faraday moment image. However, the ratio of the two can not be explained by a simple model of a Burn slab (Burn, 1966), which seems to be applicable to the high-frequency data (Ordog et al., 2019). A Burn slab assumes a mixture of uniform synchrotron-emitting and Faraday-rotating regions along the LOS and predicts a ratio of 2 between the modelled total Galactic RM and the observed polarized emission. The observed LOFAR Faraday spectra are more complex to understand, highlighting the high level of complexity of the LOS distribution of synchrotron emission and Faraday rotation.

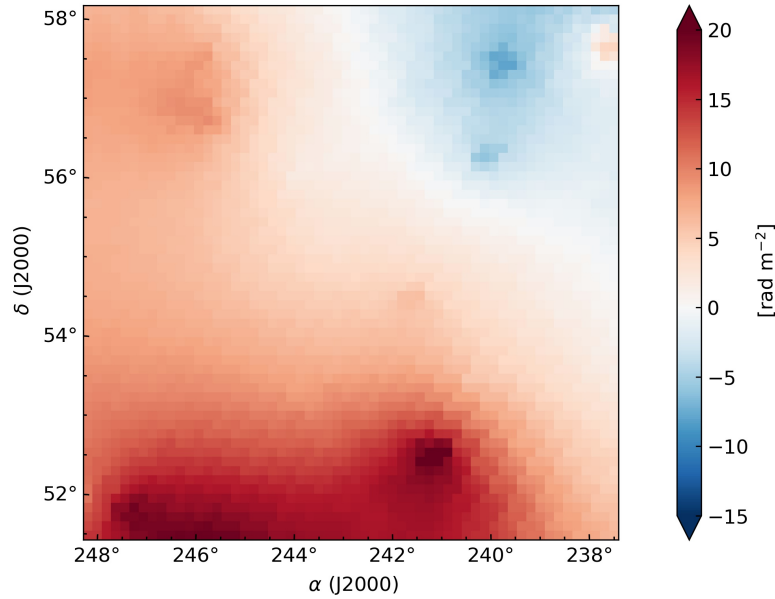


Figure 6.16: The total Galactic RM in the area of the ELAIS-N1 field, extracted from the publicly available the Galactic Faraday Sky map by [Hutschenreuter et al. \(2022\)](#).

We compare the  $M_1$  of our stacked Faraday cube with the Galactic Faraday Sky map ([Hutschenreuter et al., 2022](#)). Figure 6.16 shows a cut-out of this map in the area of ELAIS-N1 field. A visual comparison with the middle bottom panel of Fig. 6.14 shows that the northwest to a southeast gradient in the first moment is also present in the Galactic Faraday sky map. The values are more negative around the northwest corner of the image, then diagonally towards the centre of the image they increase towards zero, and then they increase to more positive values towards the southeast corner of the image. This gradient implies a bending magnetic field in a southeast to a northwest direction. The magnetic field mostly points towards us in the southeast corner of the image, in the central part of the image is mostly in the plane of the sky and then in the northwest corner points away from us.

Comparable negative values towards the northwest corner of the image between the two maps means that we are probing the same volume of the magneto-ionic medium. On the contrary, larger positive values of Galactic Faraday Sky towards the southeast corner of the image than in the first moment means that we are not probing the same volume. Emission which comes from further away is either depolarized in LOFAR observations or it is Faraday thick, as discussed by [Erceg et al. \(2022\)](#) in a broader discussion of Faraday moments in the high-latitude outer Galaxy. Moreover, from the same work (see fig. 5, 8, 9 and 10 in [Erceg et al., 2022](#)), it is clear that the ELAIS-N1 field is just at the edge of a region associated with the polarized emission from the radio Loop III. The observed gradient is perpendicular to the shape of the



loop, and probably it is associated to it. The same is true for the emission which is observed in the surrounding area of the ELAIS-N1 field.

Faraday depths at which we observe the diffuse emission in the ELAIS-N1 field are comparable or smaller than the total Galactic RM in the same area. Therefore, the observed diffuse emission is probably Galactic, including its newly detected faint component.

## 6.7 Summary and conclusions

We used 21 LOFAR HBA observations of the ELAIS-N1 field (about 150 hours of data) to conduct currently the deepest polarimetric study of Galactic synchrotron emission at low-radio frequencies. The analysis was performed on a very low-resolution (4.3') Stokes QU data cubes produced as part of the LoTSS-Deep Fields Data Release 1 (Sabater et al., 2021). A stacking technique was developed to improve sensitivity of the data based on diffuse polarized emission. The outcomes of this analysis follow:

1. We verified the reliability of the absolute ionospheric Faraday rotation corrections estimated using the satellite-based TEC measurements to be of  $\sim 0.05 \text{ rad m}^{-2}$ . We also demonstrated that diffuse polarized emission itself can be used to account for the relative ionospheric corrections with respect to some reference observation.
2. We showed the feasibility of the developed stacking technique by combining 20 single night observations into one 150 hours data set. The resulting Faraday cube has a noise of  $27 \mu\text{Jy PSF}^{-1} \text{ RMSF}^{-1}$  in polarized intensity, which is an improvement of  $\sim \sqrt{20}$  in comparison with noise in an individual 5 – 8h long observation.
3. The rotation measures of successfully detected polarized sources in our final Faraday cube are in agreement with the values provided in the catalogues by Herrera Ruiz et al. (2021) and Piras et al. (in prep.), which are based on the higher angular resolution LoTSS Deep Field data (20'' and 6', respectively).
4. We have detected a faint component of diffuse polarized emission in the stacked cube at high Faraday depths, ranging from +13 to +17  $\text{rad m}^{-2}$ , which is not detected in the commissioning observation by Jelić et al. (2014). The brightness temperature of this emission is  $\sim 475 \text{ mK}$ , which is almost an order of magnitude fainter than the brightest emission observed in this field.

5. The observed northwest to southeast gradient of emission in Faraday depth we associate with a bending magnetic field across the field of view. It is probably connected to the radio Loop III, as the ELAIS-N1 field is just at the edge of it.

Presented stacking technique provides a valuable tool and gives perspective for the future deep polarimetric studies of Galactic synchrotron emission at low-radio frequencies with LOFAR, the Square Kilometre Array and its other precursors. For example, it can be applied to other LoTSS Deep Fields (Lockman Hole and Boötes), as well as, to the Great Observatories Origins Deep Survey - North (GOODS-N) field. It is also of importance for cosmological studies, where the polarized emission of the Milky Way is the foreground contaminant. For instance, if one wants to measure magnetic field properties in the cosmic web (e.g. [Carretti et al., 2022](#)), it is crucial to have an independent measurement of the Galactic contribution to the total Faraday rotation observed toward extragalactic sources. Moreover, successful extraction of the cosmological signal from the cosmic dawn and epoch of reionization also relies on good knowledge of the foreground emission, including the Galactic polarized emission (e.g. [Jelić et al., 2010](#); [Asad et al., 2015](#); [Spinelli et al., 2019](#)).

# Chapter 7

## Thesis summary and outlook

This research is a study of pulsars and their surrounding nebulae as Galactic sources emitting very high energy (VHE,  $E > 100$  GeV) gamma rays detected with the ground-based Cherenkov telescopes. As opposed to high energy (HE,  $100 \text{ MeV} < E < 100 \text{ GeV}$ ) sky where large number of pulsars are found ( $> 250$ ) and constitute a separate class of Galactic gamma-ray sources, only Crab pulsar was found to emit VHE pulsation at the time this research started. Thus, one of the aims of this research was to find another pulsar with similar characteristics, emitting at VHE. Spectra of HE pulsars detected by satellites are characterized by a simple power-law with exponential cutoff, likely caused by the curvature radiation at energies of a few GeV. At very high energies, where statistics is sparse for satellites, there is an energy domain that has recently been accessed by the ground-based Imaging Atmospheric Cherenkov Telescopes (IACT) such as Major Atmospheric Gamma-ray Imaging Cherenkov (MAGIC). This overlapping energy region between satellites and IACTs, where some of the important spectral features appear, hasn't been accessible by any instrument for some time. However, the implementation of the novel trigger system in MAGIC, specially designed to lower the trigger threshold, enabled the detection of the first VHE pulsar - the Crab pulsar, detected at energies above 25 GeV which was direct proof of concept. Considering the latest reports on the pulsed emission from Crab reaching energies even above few TeV with no indication of a cutoff energy, this could indicate that there is an additional higher-energy spectral component present, caused by a different emission mechanism. VHE observations are thus crucial to help understand why, for some pulsars, this emission in the VHE band is just an extension of the spectra detected at HE, and for other there seem to be another higher-energy spectral component with different emission mechanism. VHE observations are also important to understand the extension of the pulsar spectrum at the highest energies. In Chapters 3 and 4, I studied two pulsars, Crab and Dragonfly, where the former was already well known and detected throughout the electromagnetic spectrum and the

latter is proposed as a promising candidate for the pulsed VHE emission with the hint of signal above 25 GeV reported by the *Fermi*-LAT satellite. Crab pulsar analysis in this research serves as a verification for the method applied in the search for the pulsed VHE emission from Dragonfly. Dragonfly pulsar is one of the youngest and most energetic rotation-powered pulsars. Its distance is somewhat controversial, with the last estimation yielding a distance of 1.8 kpc. Due to some technical difficulties, the Dragonfly observations with the MAGIC telescopes resulted in a total of  $\sim 27$  hours of good data, instead of the scheduled 100 hours. Dedicated data analysis showed no significant detection from the Dragonfly pulsar, however 95% confidence level upper limits were constrained. Independent analysis from other collaboration later confirmed no signal from this pulsar with double the observational time. If the fluxes of other detected VHE pulsars are compared with the Dragonfly's, I conclude that the Dragonfly pulsar is a much fainter source. This may imply either that the distance parameter is underestimated or some intrinsic property of this pulsar is different. From the extrapolation of the Fermi spectrum for Dragonfly, it follows that it would actually need, in the optimistic scenario, approximately 200 hours of observations with the MAGIC telescopes for a statistically significant detection. Subsequently, the next-generation instrument, Cherenkov Telescope Array (CTA) would require approximately 110 hours observational time for detection of this source. Furthermore, in the cases of Crab, Vela and Geminga pulsars detected at VHE, it is observed that the pulse widths are narrowing and peak's heights are decreasing with increasing energy, so if the pulsar is surrounded by the bright pulsar wind nebula (PWN), the nebula can present significant background and can limit pulsed emission detection. The Dragonfly pulsar is surrounded by the nebula, which is one of the brightest sources in the star-forming Cygnus region, studied also in this Thesis. Taking the same data used for the point source, the extended nebula was detected and there is also a hint of energy-dependent morphology. However, no statistically significant morphological details could be constrained for the Dragonfly nebula due to inadequate pointing settings. Besides young PWNe, in Chapter 5 I studied an unidentified extended TeV source, HESS J1858+020, that was put forward as an old relic PWN. Estimation of the source extension and the source detection were successful, however the source could not be resolved with the applied method. Detection of the VHE gamma-ray emission from new pulsars and their nebulae proved to be more challenging than expected, and thus longer observations are needed. For morphological studies of extended or off-centred sources, the analysis relying on the standard methods is inadequate, so new adjusted analysis methods should be used. Next-generation CTA and other future experiments should provide better data revealing richer physics.

Besides energetic gamma-rays, in this Thesis I also investigated diffuse polarized synchrotron emission from our Galaxy at low radio frequencies (115 – 180 MHz) which is sparsely

---

studied at this frequency range. Using observed Galactic polarized emission as a way of self-calibration with respect to some reference observation, I developed a stacking method for deep polarimetric study of the faint component of the Galactic diffuse emission and for detection of faint radio sources, such as pulsars. Pulsars can be relatively easily detected in radio catalogues due to their high degree of polarization, steep spectrum and variability, however the detection of radio pulsars from the presented study was out of the scope for this Thesis. Chapter 6 presents deep polarimetric observations of Galactic synchrotron emission in the European Large Area ISO Survey-North 1 (ELAIS-N1) field, a part of the LOFAR Two-metre Sky Survey (LoTSS) Deep Fields Data Release 1 using the Low Frequency Array (LOFAR) interferometer. Stokes Q and U data cubes of 20 observations were stacked in the combined cube, where the rotation measure (RM) synthesis was utilized for decomposition of the distribution of polarized structures in Faraday depth and cross-correlation RM synthesis for alignment of different observations in Faraday depth. In total, 150 hours of the ELAIS-N1 observations were put together to produce the deepest Faraday cube at low frequencies to date, covering  $\sim 36 \text{ deg}^2$  of the sky with a noise level of  $27 \mu\text{Jy PSF}^{-1} \text{ RMFS}^{-1}$  in polarized intensity. This is an improvement in noise by a factor of approximately the square root of the number of stacked data cubes ( $\sim \sqrt{20}$ ) as expected, compared to the one in a single data cube based on five-to-eight-hour observations. As a result, a faint component of diffuse polarized emission was detected in the stacked cube, which was not observed previously. Additionally, the reliability of absolute ionospheric Faraday rotation (FR) corrections estimated using the satellite-based total electron content (TEC) measurements was verified, as well as the reliability of the relative ionospheric FR corrections estimated using the diffuse polarized emission with respect to some reference observation. The future prospects could include stacking more observations when available for even deeper study of the ELAIS field or/and the method could be applied to other LOFAR deep fields as well.

# Bibliography

- Abdalla H., et al., 2018, *Astron. Astrophys.*, 612, A2, *The population of TeV pulsar wind nebulae in the H.E.S.S. Galactic Plane Survey*
- Abdo A. A., et al., 2009a, *ApJ*, 700, 1059, *Pulsed Gamma-rays from PSR J2021+3651 with the Fermi Large Area Telescope*
- Abdo A. A., et al., 2009b, *The Astrophysical Journal*, 708, 1254, *FERMI Large Area Telescope Observations Of the Crab Pulsar and Nebula*
- Abdo A. A., et al., 2010, *ApJ*, 708, 1254, *Fermi Large Area Telescope Observations of the Crab Pulsar And Nebula*
- Abdo A. A., et al., 2011, *Science*, 331, 739, *Gamma-ray flares from the crab nebula*
- Abdo A. A., et al., 2013, *ApJS*, 208, 17, *The Second Fermi Large Area Telescope Catalog of Gamma-Ray Pulsars*
- Abdollahi S., et al., 2020, *The Astrophysical Journal Supplement Series*, 247, 33, *Fermi large area telescope fourth source catalog*
- Abeysekara A. U., et al., 2016, *ApJ*, 817, 3, *Search for TeV Gamma-Ray Emission from Point-like Sources in the Inner Galactic Plane with a Partial Configuration of the HAWC Observatory*
- Abeysekara A. U., et al., 2018, *ApJ*, 861, 134, *A Very High Energy  $\gamma$ -Ray Survey toward the Cygnus Region of the Galaxy*
- Acciari V. A., et al., 2020, *Astronomy & Astrophysics*, 643, L14, *Detection of the geminga pulsar with magic hints at a power-law tail emission beyond 15 gev*
- Ackermann M., et al., 2013, *The Astrophysical Journal Supplement Series*, 209, 34, *The First FERMI-LAT Catalog Of Sources above 10 GeV*
- Actis M., et al., 2011, *Experimental Astronomy*, 32, 193–316, *Design concepts for the cherenkov telescope array cta: an advanced facility for ground-based high-energy gamma-ray astronomy*
- Aharonian F., Bogovalov S., 2003, *New Astronomy*, 8, 85, *Exploring physics of rotation powered pulsars with sub-10 gev imaging atmospheric cherenkov telescopes*
- Aharonian F., et al., 2006, *Astronomy & Astrophysics*, 457, 899–915, *Observations of the crab nebula with hess*
- Aharonian F., et al., 2008, *A&A*, 477, 353, *HESS very-high-energy gamma-ray sources without identified counterparts*
- Albert J., et al., 2007, *Nuclear Instruments and Methods in Physics Research A*, 583, 494, *Unfolding of differential energy spectra in the MAGIC experiment*
- Albert J., et al., 2008a, *Nuclear Instruments and Methods in Physics Research A*, 588, 424, *Implementation of the Random Forest method for the Imaging Atmospheric Cherenkov Telescope MAGIC*
- Albert J., et al., 2008b, *The Astrophysical Journal*, 674, 1037, *Vhe  $\gamma$ -ray observation of the crab nebula and its pulsar with the magic telescope*
- Aleksić J., et al., 2012, *A&A*, 540, A69, *Phase-resolved energy spectra of the Crab pulsar in the range of 50-400 GeV measured with the MAGIC telescopes*
- Aleksić J., et al., 2015, *Journal of High Energy Astrophysics*, 5-6, 30, *Measurement of the crab nebula spectrum over three decades in energy with the magic telescopes*
- Aleksić J., et al., 2016a, *Astroparticle Physics*, 72, 61, *The major upgrade of the MAGIC telescopes, Part I: The hardware improvements and the commissioning of the system*

- Aleksić J., et al., 2016b, *Astroparticle Physics*, 72, 76, *The major upgrade of the MAGIC telescopes, Part II: A performance study using observations of the Crab Nebula*
- Alessandro De Angelis M. P., 2018, *Introduction to particle and astroparticle physics*, 2 edn. Undergraduate Lecture Notes in Physics, Springer, Cham, doi:10.1007/978-3-319-78181-5
- Aliu E., et al., 2008, *Science*, 322, 1221–1224, *Observation of pulsed  $\gamma$ -rays above 25 gev from the crab pulsar with magic*
- Aliu E., et al., 2009, *Astroparticle Physics*, 30, 293, *Improving the performance of the single-dish Cherenkov telescope MAGIC through the use of signal timing*
- Aliu E., et al., 2014, *The Astrophysical Journal*, 788, 78, *Spatially resolving the very high energy emission from MGRO j2019+37 with VERITAS*
- Amato E., 2020, *The theory of pulsar wind nebulae: recent progress* (arXiv:2001.04442)
- Ansoldi S., et al., 2016, *A&A*, 585, A133, *Teraelectronvolt pulsed emission from the Crab Pulsar detected by MAGIC*
- Archer A., et al., 2019, *The Astrophysical Journal*, 876, 95, *A search for pulsed very high-energy gamma-rays from 13 young pulsars in archival veritas data*
- Asad K. M. B., et al., 2015, *Polarization leakage in epoch of reionization windows: I. lofar observations of the 3c196 field*, doi:10.48550/ARXIV.1503.01644
- Atoyan A. M., Aharonian F. A., 1996, *MNRAS*, 278, 525, *On the mechanisms of gamma radiation in the Crab Nebula*
- Atwood W. B., et al., 2009, *ApJ*, 697, 1071, *The Large Area Telescope on the Fermi Gamma-Ray Space Telescope Mission*
- Bertero M., Brianzi P., Pike E. R., Rebolia L., 1988, *Proceedings of the Royal Society of London Series A*, 415, 257, *Linear Regularizing Algorithms for Positive Solutions of Linear Inverse Problems*
- Biland A., et al., 2014, *Journal of Instrumentation*, 9, P10012–P10012, *Calibration and performance of the photon sensor response of fact — the first g-apd cherenkov telescope*
- Blandford R. D., Ostriker J. P., 1978, *ApJ*, 221, L29, *Particle acceleration by astrophysical shocks.*
- Blasi P., 2013, *The Astronomy and Astrophysics Review*, 21, *The origin of galactic cosmic rays*
- Bogovalov S. V., 2014, *Monthly Notices of the Royal Astronomical Society*, 443, 2197, *Magnetocentrifugal acceleration of bulk motion of plasma in pulsar magnetosphere*
- Bracco A., Jelić V., Marchal A., Turić L., Erceg A., Miville-Deschênes M. A., Bellomi E., 2020, *A&A*, 644, L3, *The multiphase and magnetized neutral hydrogen seen by LOFAR*
- Bracco A., et al., 2022, *A&A*, 663, A37, *First look at the multiphase interstellar medium using synthetic observations from low-frequency Faraday tomography*
- Breed M., Venter C., Harding A. K., 2016, arXiv e-prints, p. arXiv:1607.06480, *Very-high energy emission from pulsars*
- Brentjens M. A., 2018, in *Astrophysics and Space Science Library*. p. 159, doi:10.1007/978-3-319-23434-2\_10
- Brentjens M. A., de Bruyn A. G., 2005, *A&A*, 441, 1217, *Faraday rotation measure synthesis*
- Buccheri R., et al., 1983, *A&A*, 128, 245, *Search for pulsed  $\gamma$ -ray emission from radio pulsars in the COS-B data.*
- Bucciantini N., 2008, in Bassa C., Wang Z., Cumming A., Kaspi V. M., eds, *American Institute of Physics Conference Series Vol. 983, 40 Years of Pulsars: Millisecond Pulsars, Magnetars and More*. pp 186–194 (arXiv:0710.0397), doi:10.1063/1.2900139
- Burn B. J., 1966, *MNRAS*, 133, 67, *On the depolarization of discrete radio sources by Faraday dispersion*
- Burtovoi A., Saito T. Y., Zampieri L., Hassan T., 2017, *MNRAS*, 471, 431, *Prospects for the detection of high-energy ( $E \gtrsim 25$  GeV) Fermi pulsars with the Cherenkov Telescope Array*
- Carreto Fidalgo D., 2019, *Revealing the Most Energetic Light from Pulsars and Their Nebulae*. Springer Theses, Springer, doi:10.1007/978-3-030-24194-0
- Carretti E., et al., 2022, *MNRAS*, 512, 945, *Magnetic field strength in cosmic web filaments*

## Bibliography

---

- Carrigan S., Hinton J. A., Hofmann W., Kosack K., Lohse T., Reimer O., 2007, *Establishing a connection between high-power pulsars and very-high-energy gamma-ray sources* (arXiv:0709.4094)
- Ceribella 2021, Dissertation, Technische Universität München, München
- Cheng K. S., Ho C., Ruderman M., 1986, ApJ, 300, 500, *Energetic Radiation from Rapidly Spinning Pulsars. I. Outer Magnetosphere Gaps*
- Cherenkov Telescope Array Consortium et al., 2019, *Science with the Cherenkov Telescope Array*, doi:10.1142/10986.
- Cocke W. J., Disney M. J., Taylor D. J., 1969, Nature, 221, 525, *Discovery of Optical Signals from Pulsar NP 0532*
- Cordes J. M., Lazio T. J. W., 2002, arXiv e-prints, pp astro-ph/0207156, *NE2001.I. A New Model for the Galactic Distribution of Free Electrons and its Fluctuations*
- Coroniti F. V., 1990, ApJ, 349, 538, *Magnetically Striped Relativistic Magnetohydrodynamic Winds: The Crab Nebula Revisited*
- Coroniti F. V., Kennel C. F., 1985, in Kafatos M. C., Henry R. B. C., eds, *The Crab Nebula and Related Supernova Remnants*. pp 25–36
- Cui Y., Xin Y., Liu S., Tam P. H. T., Pühlhofer G., Zhu H., 2021, A&A, 646, A114, *HESS J1858+020: A GeV-TeV source possibly powered by cosmic rays from SNR G35.6-0.4*
- Dazzi F., Herranz Lazaro D., Lopez M., Nakajima D., Rodriguez Garcia J., Schweizer T., 2015, arXiv e-prints, p. arXiv:1508.05255, *Performance studies of the new stereoscopic Sum-Trigger-II of MAGIC after one year of operation*
- Dazzi F., et al., 2021, IEEE Transactions on Nuclear Science, pp 1–1, *The stereoscopic analog trigger of the magic telescopes*
- Di Tria R., et al., 2021, in Proceedings of 37th International Cosmic Ray Conference — PoS(ICRC2021). p. 642, doi:10.22323/1.395.0642
- Dickey J. M., et al., 2019, ApJ, 871, 106, *The Galactic Magneto-ionic Medium Survey: Moments of the Faraday Spectra*
- Erceg A., et al., 2022, A&A, 663, A7, *Faraday tomography of LoTSS-DR2 data. I. Faraday moments in the high-latitude outer Galaxy and revealing Loop III in polarisation*
- Etten A. V., Romani R. W., Ng C.-Y., 2008, The Astrophysical Journal, 680, 1417, *Rings and jets around PSR j2021+3651: The dragonfly nebula*
- Fermi E., 1949, Phys. Rev., 75, 1169, *On the origin of the cosmic radiation*
- Fernandez Barral A., 2017, PhD thesis, -, <http://www.tdx.cat/handle/10803/457715>
- Ferrière K., West J. L., Jaffe T. R., 2021, MNRAS, 507, 4968, *The correct sense of Faraday rotation*
- Fierro J. M., Michelson P. F., Nolan P. L., Thompson D. J., 1998, ApJ, 494, 734, *Phase-resolved Studies of the High-Energy Gamma-Ray Emission from the Crab, Geminga, and VELA Pulsars*
- Fomin V. P., Stepanian A. A., Lamb R. C., Lewis D. A., Punch M., Weekes T. C., 1994, Astroparticle Physics, 2, 137, *New methods of atmospheric Cherenkov imaging for gamma-ray astronomy. I. The false source method*
- Fruck C., 2015, PhD thesis, Max Planck Institut Für Physik, München
- Fruck C., Gaug M., Zanin R., Dorner D., Garrido D., Mirzoyan R., Font L., 2014, *A novel lidar-based atmospheric calibration method for improving the data analysis of magic* (arXiv:1403.3591)
- Gaensler B. M., Slane P. O., 2006, Annual Review of Astronomy and Astrophysics, 44, 17–47, *The evolution and structure of pulsar wind nebulae*
- Gelfand J. D., Gaensler B. M., Slane P. O., Patnaude D. J., Hughes J. P., Camilo F., 2007, The Astrophysical Journal, 663, 468–486, *The radio emission, x-ray emission, and hydrodynamics of g328.4+0.2: A comprehensive analysis of a luminous pulsar wind nebula, its neutron star, and the progenitor supernova explosion*
- Giavitto G., 2013, PhD thesis, Universitat Autònoma de Barcelona, Barcelona
- Gold T., 1969, Nature, 221, 25, *Rotating Neutron Stars and the Nature of Pulsars*
- Goldreich P., Julian W. H., 1969, ApJ, 157, 869, *Pulsar Electrodynamics*
- Green D. A., 2009, MNRAS, 399, 177, *Re-identification of G35.6-0.4 as a supernova remnant*



- Groom D., Klein S., 2000, *The European Physical Journal C - Particles and Fields*, 15, 163, *Passage of particles through matter*
- H. E. S. S. Collaboration 2020, *Nature Astronomy*, 4, 167, *Resolving the Crab pulsar wind nebula at teraelectron-volt energies*
- H. E. S. S. Collaboration et al., 2018, *A&A*, 620, A66, *First ground-based measurement of sub-20 GeV to 100 GeV  $\gamma$ -Rays from the Vela pulsar with H.E.S.S. II*
- HAWC Collaboration et al., 2021, arXiv e-prints, p. arXiv:2101.01649, *Spectrum and Morphology of the Very-High-Energy Source HAWC J2019+368*
- Haefner D., Schweizer T., Dazzi F., Corti D., 2011, *Proceedings of the 32nd International Cosmic Ray Conference, ICRC 2011*, 9, *New improved sum-trigger system for the magic telescopes*
- Halpern J. P., et al., 2008, *The Astrophysical Journal*, 688, L33, *Discovery of high-energy gamma-ray pulsations from PSR j2021+3651 with AGILE*
- Harding A. K., Venter C., Kalapotharakos C., 2021, in *Proceedings of 37th International Cosmic Ray Conference — PoS(ICRC2021)*. p. 930, doi:10.22323/1.395.0930
- Hassan T., et al., 2015, *Second large-scale monte carlo study for the cherenkov telescope array* (arXiv:1508.06075)
- Hatanaka T., 1956, *PASJ*, 8, 73, *The Faraday Effect in the Earth's Ionosphere with Special Reference to Polarization Measurements of the Solar Radio Emission*
- Heald G., Braun R., Edmonds R., 2009, *A&A*, 503, 409, *The Westerbork SINGS survey. II Polarization, Faraday rotation, and magnetic fields*
- Heck D., Knapp J., Capdevielle J. N., Schatz G., Thouw T., 1998, *CORSIKA: a Monte Carlo code to simulate extensive air showers*.
- Herrera Ruiz N., et al., 2021, *Astronomy & Astrophysics*, 648, A12, *Lofar deep fields: probing a broader population of polarized radio galaxies in elais-n1*
- Hessels J. W. T., Roberts M. S. E., Ransom S. M., Kaspi V. M., Romani R. W., Ng C.-Y., Freire P. C. C., Gaensler B. M., 2004, *The Astrophysical Journal*, 612, 389, *Observations of PSR j2021+3651 and its x-ray pulsar wind nebula g75.2+0.1*
- Hester J. J., 2008, *ARA&A*, 46, 127, *The Crab Nebula : an astrophysical chimera*.
- Hewish A., Bell S. J., Pilkington J. D. H., Scott P. F., Collins R. A., 1968, *Nature*, 217, 709, *Observation of a Rapidly Pulsating Radio Source*
- Hillas A. M., 1984, *ARA&A*, 22, 425, *The Origin of Ultra-High-Energy Cosmic Rays*
- Hirovani K., 2008, *The Astrophysical Journal*, 688, L25–L28, *Outer-gap versus slot-gap models for pulsar high-energy emissions: The case of the crab pulsar*
- Hobbs G. B., Edwards R. T., Manchester R. N., 2006, *MNRAS*, 369, 655, *TEMPO2, a new pulsar-timing package - I. An overview*
- Holder J., et al., 2008, in Aharonian F. A., Hofmann W., Rieger F., eds, *American Institute of Physics Conference Series Vol. 1085*, American Institute of Physics Conference Series. pp 657–660 (arXiv:0810.0474), doi:10.1063/1.3076760
- Hrupec D., 2008, PhD thesis, University of Zagreb, Zagreb
- Hutschenreuter S., et al., 2022, *A&A*, 657, A43, *The Galactic Faraday rotation sky 2020*
- Iacobelli M., Haverkorn M., Katgert P., 2013, *A&A*, 549, A56, *Rotation measure synthesis at the 2 m wavelength of the FAN region: unveiling screens and bubbles*
- Jackson J. M., et al., 2006, *ApJS*, 163, 145, *The Boston University-Five College Radio Astronomy Observatory Galactic Ring Survey*
- Jelić V., Zaroubi S., Labropoulos P., Bernardi G., de Bruyn A. G., Koopmans L. V. E., 2010, *MNRAS*, 409, 1647, *Realistic simulations of the Galactic polarized foreground: consequences for 21-cm reionization detection experiments*

## Bibliography

---

- Jelić V., et al., 2014, A&A, 568, A101, *Initial LOFAR observations of epoch of reionization windows. II. Diffuse polarized emission in the ELAIS-N1 field*
- Jelić V., et al., 2015, A&A, 583, A137, *Linear polarization structures in LOFAR observations of the interstellar medium in the 3C 196 field*
- Jelić V., Prelogović D., Haverkorn M., Remeijn J., Klindžić D., 2018, A&A, 615, L3, *Magnetically aligned straight depolarization canals and the rolling Hough transform*
- Kalopotharakos C., Harding A. K., Kazanas D., 2014, The Astrophysical Journal, 793, 97, *Gamma-ray emission in dissipative pulsar magnetospheres: from theory to fermi observations*
- Kalopotharakos C., Brambilla G., Timokhin A., Harding A. K., Kazanas D., 2018, The Astrophysical Journal, 857, 44, *Three-dimensional kinetic pulsar magnetosphere models: Connecting to gamma-ray observations*
- Kargaltsev O., Cerutti B., Lyubarsky Y., Striani E., 2015, Space Science Reviews, 191, 391–439, *Pulsar-wind nebulae*
- Kennel C. F., Coroniti F. V., 1984a, ApJ, 283, 694, *Confinement of the Crab pulsar's wind by its supernova remnant.*
- Kennel C. F., Coroniti F. V., 1984b, ApJ, 283, 694, *Confinement of the Crab pulsar's wind by its supernova remnant.*
- Kirichenko A., et al., 2015, The Astrophysical Journal, 802, 17, *Optical Observations of PSR J2021+3651 in the Dragonfly Nebula with the GTC*
- Kondapally R., et al., 2021, A&A, 648, A3, *The LOFAR Two-meter Sky Survey: Deep Fields Data Release 1. III. Host-galaxy identifications and value added catalogues*
- Kramer M., et al., 2003, Monthly Notices of the Royal Astronomical Society, 342, 1299–1324, *The parkes multi-beam pulsar survey - iii. young pulsars and the discovery and timing of 200 pulsars*
- Krause J. D. G., 2013, PhD thesis, LMU München: Fakultät für Physik, München
- Kuiper L., Hermsen W., Cusumano G., Diehl R., Schönfelder V., Strong A., Bennett K., McConnell M. L., 2001, Astronomy & Astrophysics, 378, 918–935, *The crab pulsar in the 0.75-30 mev range as seen by cgro comptel*
- Lenc E., et al., 2016, ApJ, 830, 38, *Low-frequency Observations of Linearly Polarized Structures in the Interstellar Medium near the South Galactic Pole*
- Lessard R. W., Buckley J. H., Connaughton V., Le Bohec S., 2001, Astroparticle Physics, 15, 1, *A new analysis method for reconstructing the arrival direction of TeV gamma rays using a single imaging atmospheric Cherenkov telescope*
- Letessier-Selvon A., Stanev T., 2011, Reviews of Modern Physics, 83, 907, *Ultrahigh energy cosmic rays*
- Li T. P., Ma Y. Q., 1983, ApJ, 272, 317, *Analysis methods for results in gamma-ray astronomy.*
- Longair M. S., 2011, *High Energy Astrophysics*
- Lopez-Coto R., 2015, PhD thesis, Universitat Autònoma de Barcelona
- Lopez Moya M., 2006, PhD thesis, Madrid U.
- Lyne A., Graham-Smith F., 2012, *Pulsar astronomy*, 4 edn. Cambridge Astrophysics, Cambridge University Press, doi:10.1017/CBO9780511844584
- Lyne A. G., Pritchard R. S., Graham Smith F., 1993, MNRAS, 265, 1003, *23 years of Crab pulsar rotational history.*
- MAGIC Collaboration et al., 2014, A&A, 571, A96, *MAGIC reveals a complex morphology within the unidentified gamma-ray source HESS J1857+026*
- MAGIC Collaboration et al., 2019, Nature, 575, 455, *Teraelectronvolt emission from the  $\gamma$ -ray burst GRB 190114C*
- Manchester R. N., Hobbs G. B., Teoh A., Hobbs M., 2005, The Astronomical Journal, 129, 1993–2006, *The australia telescope national facility pulsar catalogue*
- Mevius M., 2018, *RMextract: Ionospheric Faraday Rotation calculator* (ascl:1806.024)
- Mirzoyan R., 1997, in International Cosmic Ray Conference. p. 265
- Mochol I., 2017, Astrophysics and Space Science Library, pp 135–159, *Pulsar striped winds*
- Moffett D. A., Hankins T. H., 1996, ApJ, 468, 779, *Multifrequency Radio Observations of the Crab Pulsar*

- Murray W. A. S., Hargreaves J. K., 1954, *Nature*, 173, 944, *Lunar Radio Echoes and the Faraday Effect in the Ionosphere*
- Muslimov A. G., Harding A. K., 2003, *ApJ*, 588, 430, *Extended Acceleration in Slot Gaps and Pulsar High-Energy Emission*
- Nakajima D., et al., 2013, in *International Cosmic Ray Conference*. p. 3044
- Nishimura J., 1967, *Handbuch der Physik*, 46, 1, *Theory of Cascade Showers*
- Novak M., Smolčić V., Schinnerer E., Zamorani G., Delvecchio I., Bondi M., Delhaize J., 2018, *A&A*, 614, A47, *Constraints on submicrojansky radio number counts based on evolving VLA-COSMOS luminosity functions*
- O’Sullivan S. P., et al., 2023, *MNRAS*, 519, 5723–5742, *The Faraday Rotation Measure Grid of the LOFAR Two-metre Sky Survey: Data Release 2*
- Offringa A. R., van de Gronde J. J., Roerdink J. B. T. M., 2012, *A&A*, 539, A95, *A morphological algorithm for improving radio-frequency interference detection*
- Offringa A. R., et al., 2013, *A&A*, 549, A11, *The LOFAR radio environment*
- Ordog A., Booth R., Van Eck C., Brown J.-A., Landecker T., 2019, *Galaxies*, 7, 43, *Faraday Rotation of Extended Emission as a Probe of the Large-Scale Galactic Magnetic Field*
- Page D., Reddy S., 2006, *Annual Review of Nuclear and Particle Science*, 56, 327–374, *Dense matter in compact stars: Theoretical developments and observational constraints*
- Paredes J. M., Ishwara-Chandra C. H., Bosch-Ramon V., Zabalza V., Iwasawa K., Ribó M., 2014, *A&A*, 561, A56, *Deep GMRT radio observations and a multi-wavelength study of the region around HESS J1858+020*
- Paron S., Giacani E., 2010, *A&A*, 509, L4, *Identifying the counterpart of HESS J1858+020*
- Paron S., Giacani E., Rubio M., Dubner G., 2011, *A&A*, 530, A25, *Study of the molecular clump associated with the high-energy source HESS J1858+020*
- Pierbattista M., Harding A. K., Grenier I. A., Johnson T. J., Caraveo P. A., Kerr M., Gonthier P. L., 2015, *Astronomy & Astrophysics*, 575, A3, *Light-curve modelling constraints on the obliquities and aspect angles of the youngfermipulsars*
- Purcell C. R., Van Eck C. L., West J., Sun X. H., Gaensler B. M., 2020, *RM-Tools: Rotation measure (RM) synthesis and Stokes QU-fitting*, *Astrophysics Source Code Library*, record ascl:2005.003 (ascl:2005.003)
- Reich W., 2006, *arXiv e-prints*, pp astro-ph/0603465, *Galactic polarization surveys*
- Reynolds S. P., 1998, *The Astrophysical Journal*, 493, 375, *Models of synchrotron x-rays from shell supernova remnants*
- Rissi M., Otte N., Schweizer T., Shayduk M., 2009, *IEEE Transactions on Nuclear Science*, 56, 3840, *A new sum trigger to provide a lower energy threshold for the magic telescope*
- Roberts M. S. E., Hessels J. W. T., Ransom S. M., Kaspi V. M., Freire P. C. C., Crawford F., Lorimer D. R., 2002, *The Astrophysical Journal*, 577, L19, *PSR j2021+3651: A young radio pulsar coincident with an unidentified EGRET -ray source*
- Rolke W. A., López A. M., Conrad J., 2005, *Nuclear Instruments and Methods in Physics Research Section A: Accelerators, Spectrometers, Detectors and Associated Equipment*, 551, 493–503, *Limits and confidence intervals in the presence of nuisance parameters*
- Romani R. W., 1996, *ApJ*, 470, 469, *Gamma-Ray Pulsars: Radiation Processes in the Outer Magnetosphere*
- Rossi B., Greisen K., 1941, *Reviews of Modern Physics*, 13, 240, *Cosmic-Ray Theory*
- Ruderman M., Sutherland P., 1975, *Astrophysical Journal - ASTROPHYS J*, 196, 51, *Theory of pulsars - polar caps, sparks, and coherent microwave radiation*
- Sabater J., et al., 2021, *A&A*, 648, A2, *The LOFAR Two-meter Sky Survey: Deep Fields Data Release 1. II. The ELAIS-N1 LOFAR deep field*
- Saito T., 2011, PhD thesis, Max Planck Institut Für Physik
- Saito T. Y., Bonnefoy S., Hirotani K., Zanin R., 2015, *Detection of vhe bridge emission from the crab pulsar with the magic telescopes (arXiv:1502.02757)*

## Bibliography

---

- Sanidas S., et al., 2019, A&A, 626, A104, *The LOFAR Tied-Array All-Sky Survey (LOTAAS): Survey overview and initial pulsar discoveries*
- Schmelling M., 1994, Nuclear Instruments and Methods in Physics Research A, 340, 400, *The method of reduced cross-entropy A general approach to unfold probability distributions*
- Schnitzeler D. H. F. M., Katgert P., de Bruyn A. G., 2009, A&A, 494, 611, *WSRT Faraday tomography of the Galactic ISM at  $\lambda \sim 0.86$  m. I. The GEMINI data set at  $(l, b) = (181^\circ, 20^\circ)$*
- Sciascio G. D., 2016, *The Ihaaso experiment: from gamma-ray astronomy to cosmic rays* (arXiv:1602.07600)
- Shimwell T. W., et al., 2017, A&A, 598, A104, *The LOFAR Two-metre Sky Survey. I. Survey description and preliminary data release*
- Shimwell T. W., et al., 2019, A&A, 622, A1, *The LOFAR Two-metre Sky Survey. II. First data release*
- Shimwell T. W., Hardcastle M. J., Tasse C., Best P. N., Röttgering H. J. A., et al. 2022, A&A, Forthcoming article, *The LOFAR Two-metre Sky Survey. II. First data release*
- Sitarek J., Gaug M., Mazin D., Paoletti R., Tesaro D., 2013, Nuclear Instruments and Methods in Physics Research Section A: Accelerators, Spectrometers, Detectors and Associated Equipment, 723, 109, *Analysis techniques and performance of the domino ring sampler version 4 based readout for the magic telescopes*
- Slane P., 2017, *Pulsar Wind Nebulae*. p. 2159, doi:10.1007/978-3-319-21846-5\_95
- Smolčić V., et al., 2017, A&A, 602, A2, *The VLA-COSMOS 3 GHz Large Project: Multiwavelength counterparts and the composition of the faint radio population*
- Sobey C., et al., 2019, MNRAS, 484, 3646, *Low-frequency Faraday rotation measures towards pulsars using LOFAR: probing the 3D Galactic halo magnetic field*
- Sobey C., et al., 2022, A&A, 661, A87, *Searching for pulsars associated with polarised point sources using LOFAR: Initial discoveries from the TULIPP project*
- Sotomayor-Beltran C., et al., 2013, A&A, 552, A58, *Calibrating high-precision Faraday rotation measurements for LOFAR and the next generation of low-frequency radio telescopes*
- Spinelli M., Bernardi G., Santos M. G., 2019, MNRAS, 489, 4007, *On the contamination of the global 21-cm signal from polarized foregrounds*
- Spir-Jacob M., Djannati-Ataï A., Mohrmann L., Giavitto G., Khélifi B., Rudak B., Venter C., Zanin R., 2019, arXiv e-prints, p. arXiv:1908.06464, *Detection of sub-100 GeV gamma-ray pulsations from PSR B1706-44 with H.E.S.S*
- Staelin D. H., Reifenstein E. C., 1968, Science, 162, 1481, *Pulsating radio sources near the crab nebula*
- Stappers B. W., et al., 2011, A&A, 530, A80, *Observing pulsars and fast transients with LOFAR*
- Tasse C., et al., 2021, A&A, 648, A1, *The LOFAR Two-meter Sky Survey: Deep Fields Data Release 1. I. Direction-dependent calibration and imaging*
- Tavani M., et al., 2008, Nuclear Instruments and Methods in Physics Research A, 588, 52, *The AGILE space mission*
- Tepe A., HAWC Collaboration 2012, in Journal of Physics Conference Series. p. 052026, doi:10.1088/1742-6596/375/1/052026
- Thompson D. J., 2008, Reports on Progress in Physics, 71, 116901, *Gamma ray astrophysics: the egret results*
- Tikhonov A., Arsenin V., Ya V., 1979, Nauka, *Methods of Solution of Ill-Posed Problems*
- Tingay S. J., et al., 2013, PASA, 30, e007, *The Murchison Widefield Array: The Square Kilometre Array Precursor at Low Radio Frequencies*
- Torres D. F., Li H., Chen Y., Cillis A., Caliendo A. G., Rodríguez-Marrero A. Y., 2011, MNRAS, 417, 3072, *Cosmic rays in the surroundings of SNR G35.6-0.4*
- Turić L., et al., 2021, A&A, 654, A5, *Multi-tracer analysis of straight depolarisation canals in the surroundings of the 3C 196 field*
- Uchiyama Y., Funk S., Katagiri H., Katsuta J., Lemoine-Goumard M., Tajima H., Tanaka T., Torres D. F., 2012, ApJ, 749, L35, *Fermi Large Area Telescope Discovery of GeV Gamma-Ray Emission from the Vicinity of SNR W44*

- VERITAS Collaboration et al., 2011, *Science*, 334, 69, *Detection of Pulsed Gamma Rays Above 100 GeV from the Crab Pulsar*
- Van Eck C. L., et al., 2017, *A&A*, 597, A98, *Faraday tomography of the local interstellar medium with LOFAR: Galactic foregrounds towards IC 342*
- Van Eck C. L., et al., 2019, *A&A*, 623, A71, *Diffuse polarized emission in the LOFAR Two-meter Sky Survey*
- Venter C., 2017, *New advances in pulsar magnetosphere modelling* (arXiv:1702.00732)
- Vovk I., Strzys M., Fruck C., 2018, *A&A*, 619, A7, *Spatial likelihood analysis for MAGIC telescope data. From instrument response modelling to spectral extraction*
- Wagner R. M., 2006, PhD thesis, Max Planck Institut Für Physik, München
- Wakely S. P., Horan D., 2008, in *International Cosmic Ray Conference*. pp 1341–1344
- Weekes T. C., et al., 1989, *ApJ*, 342, 379, *Observation of TeV gamma rays from the Crab nebula using the atmospheric Cerenkov imaging technique*
- Yizengaw E., Moldwin M., Galvan D., Iijima B., Komjathy A., Mannucci A., 2008, *Journal of Atmospheric and Solar-Terrestrial Physics*, 70, 1541, *Global plasmaspheric tec and its relative contribution to gps tec*
- Zanin, R. 2013, in *Proceedings, 33rd International Cosmic Ray Conference (ICRC2013): Rio de Janeiro, Brazil, July 2-9, 2013*. p. 0773
- Zaroubi S., et al., 2015, *MNRAS*, 454, L46, *Galactic interstellar filaments as probed by LOFAR and Planck*.
- Zhang X., Chen Y., Huang J., Chen D., 2020, *Monthly Notices of the Royal Astronomical Society*, 497, 3477–3483, *Modelling the broadest spectral band of the crab nebula and constraining the ion acceleration efficiency*
- Zhu H., Tian W. W., Torres D. F., Pedalletti G., Su H. Q., 2013, *ApJ*, 775, 95, *A Kinematic Distance Study of the Planetary Nebulae-Supernova remnant-H II Region Complex at G35.6-0.5*
- de Gasperin F., Mevius M., Rafferty D. A., Intema H. T., Fallows R. A., 2018, *A&A*, 615, A179, *The effect of the ionosphere on ultra-low-frequency radio-interferometric observations*
- de Gasperin F., et al., 2019, *A&A*, 622, A5, *Systematic effects in LOFAR data: A unified calibration strategy*
- de Gasperin F., et al., 2021, *Astronomy & Astrophysics*, 648, A104, *The lofar lba sky survey*
- de Jager O. C., Raubenheimer B. C., Swanepoel J. W. H., 1989, *A&A*, 221, 180, *A powerful test for weak periodic signals with unknown light curve shape in sparse data*.
- de Naurois M., Mazin D., 2015, *Comptes Rendus Physique*, 16, 610, *Ground-based detectors in very-high-energy gamma-ray astronomy*
- van Haarlem M. P., et al., 2013, *A&A*, 556, A2, *LOFAR: The LOw-Frequency ARray*
- van Weeren R. J., et al., 2016, *ApJS*, 223, 2, *LOFAR Facet Calibration*

# Curriculum vitae

Iva Šnidarić was born in 1983 in Banja Luka. In 2002 she finished Fifth gymnasium in Zagreb that specializes in science and mathematics. In 2009 she graduated Physics at the Department of Physics, Faculty of Science at the University of Zagreb. The subject of her diploma thesis was "Influence of the atmospheric transparency on observations by Cherenkov telescopes" done at the Ruđer Bošković Institute (RBI) under supervision of dr. sc. Tihomir Surić. In the fall of 2010 she entered a PhD program at the same faculty and a year later she was employed as an assistant at RBI, Division of Experimental Physics in the Laboratory for Astroparticle Physics and Astrophysics where she started to work on her doctorate, under supervision of dr. sc. Tihomir Surić. Iva became a full member of the international collaboration MAGIC in 2011 and formally joined Croatian MAGIC consortium. She was a collaborator on the following projects funded by Croatian Science Foundation: Very High Energy Gamma Ray Astronomy with the MAGIC telescopes (project id: 09/176) and Very High Energy Gamma Ray Astronomy with MAGIC and CTA (project id: 9782). During her PhD she participated in the operation and data taking with the MAGIC telescopes, and she attended number of schools and workshops (like Novicosmo school in Rabac; SAAS-Fee course in Les Diablerets, software schools/workshops organized by the MAGIC collaboration in Berlin, Padova, Barcelona, Madrid, Munich). She was also a guest visiting the Max Planck Institute for Physics in Munich for several times (11/2010, 05/2011 and 05/2014) working on a collaborative tasks with other MAGIC colleagues. In addition, she also joined LOFAR collaboration and collaborated with dr. sc. Vibor Jelić who became her second thesis supervisor. She presented her work on both intra-national and international conferences (Croatian MAGIC consortium meetings, HAD scientific meeting, HFD meetings, MAGIC General meeting; Annual meeting of the LOFAR Magnetism Key Science Project).

Iva's main field of research are pulsars and pulsar wind nebulae at the very high gamma-ray energies. Another field of research she investigated deals with polarimetric (radio) observations at very low energies accessible with the LOFAR telescope. Iva is a co-author on 113 scientific publications and a lead author on one scientific publication.

## Published work

### Accepted for publication

Šnidarić, I., Jelić, V., Mevius, M., et al., accepted for publication in *A&A*, *LOFAR Deep Fields: Probing faint Galactic polarized emission in ELAIS-N1*. doi:10.48550/arXiv.2303.13152

### Published

Bracco A., Ntormousi E., Jelić V., Padovani M., Šiljeg B., Erceg A., Turić L., Šnidarić I., et al., *First look at the multiphase interstellar medium using synthetic observations from low-frequency Faraday tomography*, 2022, *A&A*, 663, A37. doi:10.1051/0004-6361/202142453

Iva is a co-author on many publications of the MAGIC collaboration and the complete list of publications can be found here: <https://www.bib.irb.hr/pregled/profil/30592>.